

1998

Tomography applied to Lamb wave contact scanning nondestructive evaluation

James Christopher P. McKeon
College of William & Mary - Arts & Sciences

Follow this and additional works at: <https://scholarworks.wm.edu/etd>



Part of the [Aerospace Engineering Commons](#), and the [Applied Mechanics Commons](#)

Recommended Citation

McKeon, James Christopher P., "Tomography applied to Lamb wave contact scanning nondestructive evaluation" (1998). *Dissertations, Theses, and Masters Projects*. Paper 1539623370.
<https://dx.doi.org/doi:10.21220/s2-zy7f-z633>

This Dissertation is brought to you for free and open access by the Theses, Dissertations, & Master Projects at W&M ScholarWorks. It has been accepted for inclusion in Dissertations, Theses, and Masters Projects by an authorized administrator of W&M ScholarWorks. For more information, please contact scholarworks@wm.edu.

INFORMATION TO USERS

This manuscript has been reproduced from the microfilm master. UMI films the text directly from the original or copy submitted. Thus, some thesis and dissertation copies are in typewriter face, while others may be from any type of computer printer.

The quality of this reproduction is dependent upon the quality of the copy submitted. Broken or indistinct print, colored or poor quality illustrations and photographs, print bleedthrough, substandard margins, and improper alignment can adversely affect reproduction.

In the unlikely event that the author did not send UMI a complete manuscript and there are missing pages, these will be noted. Also, if unauthorized copyright material had to be removed, a note will indicate the deletion.

Oversize materials (e.g., maps, drawings, charts) are reproduced by sectioning the original, beginning at the upper left-hand corner and continuing from left to right in equal sections with small overlaps. Each original is also photographed in one exposure and is included in reduced form at the back of the book.

Photographs included in the original manuscript have been reproduced xerographically in this copy. Higher quality 6" x 9" black and white photographic prints are available for any photographs or illustrations appearing in this copy for an additional charge. Contact UMI directly to order.

UMI[®]

Bell & Howell Information and Learning
300 North Zeeb Road, Ann Arbor, MI 48106-1346 USA
800-521-0600

NOTE TO USERS

Copyrighted materials in this document have not been filmed at the request of the author. They are available for consultation at the author's university library.

202-233

This reproduction is the best copy available.

UMI

TOMOGRAPHY APPLIED TO LAMB WAVE CONTACT
SCANNING NONDESTRUCTIVE EVALUATION

A Dissertation

Presented to The Faculty of the Department of Applied Science

The College of William and Mary

In Partial Fulfillment

Of the Requirements for the Degree of

Doctor of Philosophy

By

James C. P. McKeon

August 1998

UMI Number: 9936907

Copyright 1998 by
McKeon, James Christopher P.

All rights reserved.

UMI Microform 9936907
Copyright 1999, by UMI Company. All rights reserved.

This microform edition is protected against unauthorized
copying under Title 17, United States Code.

UMI
300 North Zeeb Road
Ann Arbor, MI 48103

Copyright

by

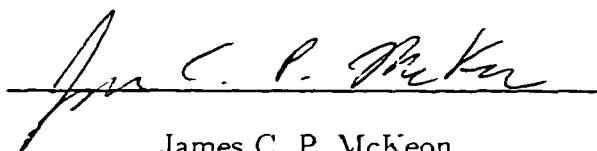
James C. P. McKeon

1998

APPROVAL SHEET

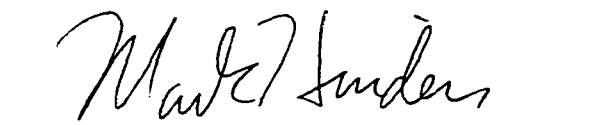
This dissertation is submitted in partial fulfillment
of the requirements for the degree of

Doctor of Philosophy.

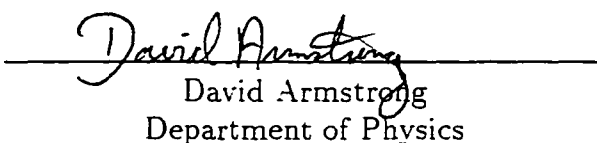


James C. P. McKeon

Approved. August 1998



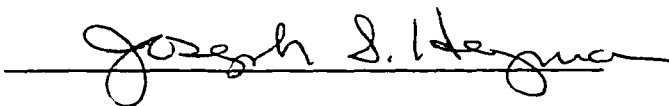
Mark K. Hinders



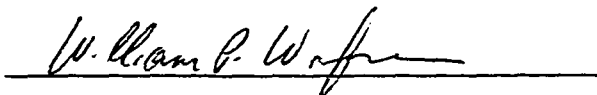
David Armstrong
Department of Physics



Dennis Manos



Joseph Heyman



William Winfree

Dedicated to
my family,
for always encouraging me
to strive for my best,
and
Tracey,
for helping me to attain it.

Contents

Acknowledgments	vii
List of Figures	viii
Abstract	xii
Chapter 1 Introduction	2
Chapter 2 Literature Review	5
2.1 Review of Lamb Wave Literature	5
2.2 Review of Tomography Literature	37
2.3 Discussion	54
Chapter 3 Theory and Experimental Results	56
3.1 Lamb Wave Scanning	56
3.2 Parallel Projection Tomography	78
3.3 Cross Borehole Tomography	88
3.4 Discussion	106
Chapter 4 Scattering Theory	113
4.1 Theory of Kane and Mindlin	114
4.2 Scattering From Cylindrical Inclusions	116
4.3 Results of the Scattering Theory	154
Chapter 5 Discussion and Future Work	195
Appendix A Characterization of the ART Algorithm	201

Appendix B Diffraction Tomography	234
Appendix C S_0 Scattering Between Adjacent Plates	240
Bibliography	245
Vita	296

Acknowledgments

I would like to thank my advisor, Dr. Mark Hinders, for his insight, advice and encouragement. The years that I have spent at William and Mary as a graduate student have been full of exciting research and learning both in and out of the classroom. Thank you for making my graduate studies so valuable and so fun. I would also like to thank the members of my committee for their reading and criticism of this document. They include Dr. Dennis Manos of the Department of Applied Science, Dr. David Armstrong of the Department of Physics, Dr. Joseph Heyman of NASA-Langley, and Dr. William Winfree of NASA-Langley. I am also indebted to the Office of Naval Research, NASA-Langley, and the Virginia Space Grant Consortium for their support of this research.

I would also like to thank the Department of Applied Science for all of the classes, talks, and demonstrations that I was able to attend, and for the many valuable conversations that I had with the faculty and my fellow students. I would especially like to thank Kathee Card for all of her help over the four years that I have been here. Thank you also to the Department of Physics for the use of their computing, copying, and machine shop facilities.

Finally, I would like to express my most sincere thanks to my family for all of their support and encouragement over the years, and I would especially like to thank my wife, Tracey, for putting up with me over the last few months and helping me to finish. Without your love and support, I could not have done this.

List of Figures

3.1	Coordinate system for Lamb wave propagation in an elastic layer.	60
3.2	Symmetric and Asymmetric motion of a plate for S_0 and A_0 Lamb wave propagation respectively.	62
3.3	Dispersion curves of the A_0 , S_0 , A_1 , and S_1 Lamb wave modes in aluminum.	65
3.4	Typical Lamb wave waveform obtained at a fd value of 1.51 MHz-mm.	68
3.5	Typical Lamb wave waveform obtained at a fd value of 2.42 MHz-mm.	69
3.6	Dispersion curves of the Lamb wave modes in aluminum are shown over the frequency-thickness range where only the S_0 and A_0 modes propagate appreciably.	71
3.7	Experimental frequency data obtained from a single scan on an aluminum plate with a 2.54cm diameter 50% thinning region.	73
3.8	Experimental frequency data obtained from a single scan on an aluminum plate with a 2.54cm diameter 50% thinning region after the plate has been rotated by 90°	74
3.9	Normalized experimental frequency data obtained along the 0° orientation after all values outside of the defined flaw region have been set to zero.	75
3.10	Normalized experimental frequency data obtained along the 90° orientation after all values outside of the defined flaw region have been set to zero.	76
3.11	Image corresponding to the two-dimensional array produced by multiplying the processed 0° and 90° data sets.	77
3.12	The geometry for parallel-projection tomography is shown here schematically for the case of seven parallel rays at four orientations.	79
3.13	The parallel projection scanning system is shown here schematically.	81
3.14	The projection at some angle θ along some line $x \cos \theta + y \sin \theta = t$ passing through an object function $f(t, s)$ is shown.	83
3.15	PPT reconstruction contour plot of a 2.45 mm thick aluminum plate with a 20 cm^2 region of 50% thickness reduction is shown here.	86

3.16	The scanning geometry and raypaths for cross borehole tomography are shown here schematically for the case of eight sources and eight receivers.	89
3.17	The cross borehole scanning system is shown here schematically. . .	91
3.18	A sample pattern used to detect the S_0 mode in the received experimental waveforms.	94
3.19	A simulated plate with an off center square flaw whose material has a 20% increase in velocity over the velocity of the plate (4.5 mm/ μ s.)	95
3.20	Reconstruction of the square flaw plate using the ART algorithm after a single iteration.	96
3.21	Bar chart of the RMS error in the reconstruction associated with different levels of added noise.	98
3.22	Reconstruction of the square flaw plate using the ART algorithm when noise in the range of 0-10% has been added to the time-of-flight data.	99
3.23	Reconstruction of the square flaw plate using the ART algorithm after noise in the range of 0-37% has been added to the time-of-flight data.	100
3.24	Reconstruction of the square flaw plate using the ART algorithm after noise in the range of 0-40% has been added to the time-of-flight data.	101
3.25	CBT reconstruction of the same aluminum sample with the thinned region is shown.	104
3.26	CBT reconstruction of a region of an aluminum sample with a line of five thinned regions.	107
3.27	PPT reconstruction of an aluminum plate with a 1.50cm diameter through-hole.	109
3.28	CBT reconstruction of the aluminum plate with a 1.50cm diameter through-hole.	110
3.29	PPT reconstruction of the aluminum plate with a 2.54cm diameter through-hole.	111
3.30	CBT reconstruction of the aluminum plate with a 2.54cm diameter through-hole.	112
4.1	Dispersion curves of the exact S_0 , S_1 and approximate S_0 , S_1 Lamb wave modes, and of the simple plate theory in aluminum.	117
4.2	Coordinate system for an in-plane disk in an infinite plate	118
4.3	Coordinate system for a plane S_0 Lamb wave incident upon a cylindrical inclusion in an infinite plate	121

4.4	Coordinate system for a point source S_0 Lamb wave incident upon a cylindrical inclusion in an infinite plate	136
4.5	Coordinate system for a finite source S_0 Lamb wave incident upon a cylindrical inclusion in an infinite plate	146
4.6	Right triangle joining r_1 and r_0 which allows for r_1 and θ_1 to be written in terms of r_0 , B , and θ	148
4.7	Right triangle joining r_2 and r_0 which allows for r_2 and θ_2 to be written in terms of r_0 , B , and θ	149
4.8	Geometry for the finite source well above the cylindrical inclusion in the plate.	151
4.9	Geometry for the finite source well below the cylindrical inclusion in the plate.	152
4.10	Polar plot of the magnitude of the scattered amplitude of a plane wave incident from the left upon a hole with radius $a = 0.25 \times 10^{-2}$ m.156	
4.11	Polar plot of the magnitude of the scattered amplitude of a plane wave incident from the left upon a hole with radius $a = 0.75 \times 10^{-2}$ m.157	
4.12	Polar plot of the magnitude of the scattered amplitude of a plane wave incident from the left upon a hole with radius $a = 1.27 \times 10^{-2}$ m.158	
4.13	Polar plot of the magnitude of the scattered amplitude of a point source wave incident from the left upon a hole with radius $a = 0.25 \times 10^{-2}$ m.	160
4.14	Polar plot of the magnitude of the scattered amplitude of a point source wave incident from the left upon a hole with radius $a = 0.75 \times 10^{-2}$ m.	161
4.15	Polar plot of the magnitude of the scattered amplitude of a point source wave incident from the left upon a hole with radius $a = 1.27 \times 10^{-2}$ m.	162
4.16	Polar plot of the magnitude of the scattered amplitude of a finite source wave incident from the left upon a hole with radius $a = 0.25 \times 10^{-2}$ m.	163
4.17	Polar plot of the magnitude of the scattered amplitude of a finite source wave incident from the left upon a hole with radius $a = 0.75 \times 10^{-2}$ m.	164
4.18	Polar plot of the magnitude of the scattered amplitude of a finite source wave incident from the left upon a hole with radius $a = 1.27 \times 10^{-2}$ m.	165
4.19	Polar plot of the magnitude of the scattered amplitude of a finite source wave incident from the left upon a hole with radius $a = 0.25 \times 10^{-2}$ m when the source has been shifted by +3 cm in the y direction.167	

4.20	Polar plot of the magnitude of the scattered amplitude of a finite source wave incident from the left upon a hole with radius $a = 0.75 \times 10^{-2}$ m when the source has been shifted by +3 cm in the y direction.	168
4.21	Polar plot of the magnitude of the scattered amplitude of a finite source wave incident from the left upon a hole with radius $a = 1.27 \times 10^{-2}$ m when the source has been shifted by +3 cm in the y direction.	169
4.22	Polar plot of the magnitude of the scattered amplitude of a finite source wave incident from the left upon a hole with radius $a = 0.25 \times 10^{-2}$ m when the source has been shifted by -3 cm in the y direction.	170
4.23	Polar plot of the magnitude of the scattered amplitude of a finite source wave incident from the left upon a hole with radius $a = 0.75 \times 10^{-2}$ m when the source has been shifted by -3 cm in the y direction.	171
4.24	Polar plot of the magnitude of the scattered amplitude of a finite source wave incident from the left upon a hole with radius $a = 1.27 \times 10^{-2}$ m when the source has been shifted by -3 cm in the y direction.	172
4.25	Polar plot of the magnitude of the scattered amplitude of a finite source wave incident from the left upon a hole with radius $a = 0.25 \times 10^{-2}$ m when the source has been shifted by +5 cm in the y direction.	173
4.26	Polar plot of the magnitude of the scattered amplitude of a finite source wave incident from the left upon a hole with radius $a = 0.75 \times 10^{-2}$ m when the source has been shifted by +5 cm in the y direction.	174
4.27	Polar plot of the magnitude of the scattered amplitude of a finite source wave incident from the left upon a hole with radius $a = 1.27 \times 10^{-2}$ m when the source has been shifted by +5 cm in the y direction.	175
4.28	Polar plot of the magnitude of the scattered amplitude of a finite source wave incident from the left upon a hole with radius $a = 0.25 \times 10^{-2}$ m when the source has been shifted by -5 cm in the y direction.	176
4.29	Polar plot of the magnitude of the scattered amplitude of a finite source wave incident from the left upon a hole with radius $a = 0.75 \times 10^{-2}$ m when the source has been shifted by -5 cm in the y direction.	177
4.30	Polar plot of the magnitude of the scattered amplitude of a finite source wave incident from the left upon a hole with radius $a = 1.27 \times 10^{-2}$ m when the source has been shifted by -5 cm in the y direction.	178
4.31	The line of receiver locations for a single scan in PPT is shown for the geometry of a hole in a plate.	182
4.32	Vertical displacement curve for the case of a plane wave incident from the left upon a hole with radius $a = 0.25 \times 10^{-2}$ m.	183
4.33	Vertical displacement curve for the case of a plane wave incident from the left upon a hole with radius $a = 0.75 \times 10^{-2}$ m.	184

4.34	Vertical displacement curve for the case of a plane wave incident from the left upon a hole with radius $a = 1.27 \times 10^{-2}$ m.	185
4.35	Vertical displacement curve for the case of a point source wave incident from the left upon a hole with radius $a = 0.25 \times 10^{-2}$ m. . . .	187
4.36	Vertical displacement curve for the case of a point source wave incident from the left upon a hole with radius $a = 0.75 \times 10^{-2}$ m. . . .	188
4.37	Vertical displacement curve for the case of a point source wave incident from the left upon a hole with radius $a = 1.27 \times 10^{-2}$ m. . . .	189
4.38	Vertical displacement curve for the case of a finite source wave incident from the left upon a hole with radius $a = 0.25 \times 10^{-2}$ m. . . .	191
4.39	Vertical displacement curve for the case of a finite source wave incident from the left upon a hole with radius $a = 0.75 \times 10^{-2}$ m. . . .	192
4.40	Vertical displacement curve for the case of a finite source wave incident from the left upon a hole with radius $a = 1.27 \times 10^{-2}$ m. . . .	193

Abstract

The aging world-wide aviation fleet requires methods for accurately predicting the presence of structural flaws that compromise airworthiness in aircraft structures. Nondestructive Evaluation (NDE) provides the means to assess these structures quickly, quantitatively, and noninvasively. Ultrasonic guided waves, Lamb waves, are useful for evaluating the plate and shell structures common in aerospace applications. The amplitude and time-of-flight of Lamb waves depend on the material properties and thickness of a medium, and so they can be used to detect any areas of differing thickness or material properties which indicate flaws. By scanning sending and receiving transducers over an aircraft, large sections can be evaluated after a single pass. However, while this technique enables the detection of areas of structural deterioration, it does not allow for the quantification of the extent of that deterioration. Tomographic reconstruction with Lamb waves allows for the accurate reconstruction of the variation of quantities of interest, such as thickness, throughout the investigated region, and it presents the data as a quantitative map. The location, shape, and extent of any flaw region can then be easily extracted from this tomographic image. Two Lamb wave tomography techniques using Parallel Projection tomography (PPT) and Cross Borehole tomography (CBT), are shown to accurately reconstruct flaws of interest to the aircraft industry. A comparison of the quality of reconstruction and practicality is then made between these two methods, and their limitations are discussed and shown experimentally. Higher order plate theory is used to derive analytical solutions for the scattering of the lowest order symmetric Lamb wave from a circular inclusion, and these solutions are used to explain the scattering effects seen in the tomographic reconstructions. Finally, the means by which this scattering theory can be used to develop Lamb wave tomographic algorithms that are more generally applicable in-the-field, is presented.

TOMOGRAPHY APPLIED TO LAMB WAVE CONTACT
SCANNING NONDESTRUCTIVE EVALUATION

Chapter 1

Introduction

As the world-wide aviation fleet continues to age, methods for accurately predicting the presence of structural flaws that compromise airworthiness in aircraft structures becomes increasingly necessary. Nondestructive Evaluation (NDE) provides the means to assess these structures quickly, quantitatively, and noninvasively. For example, ultrasonic guided waves, Lamb waves, are useful for evaluating the plate and shell structures common in aerospace applications.

The velocity of Lamb waves depends upon the material properties and thickness of a medium, and so can be used to detect any areas of differing thickness or material properties which indicate flaws. Since the Lamb waves are guided waves, they can travel large distances in the plate and shell structures being tested. Therefore, by scanning a pair of sending and receiving transducers over an aircraft, large sections can be evaluated after a single pass. Corrosion alters the velocity of Lamb waves as they propagate through the thinned regions. By monitoring the change in arrival time of Lamb waves traveling between sending and receiving transducers at known separation, areas of only a few percent thickness reduction can be detected even if the corrosion is hidden. However, while enabling the detection of areas of

structural deterioration, this technique does not allow for the quantification of the extent of the thinning. In addition, extracting information from the data involves complex mathematics and requires time and trained personnel. Tomographic reconstruction with Lamb waves allows for the accurate reconstruction of the variation of quantities of interest, such as thickness, throughout the investigated region, and it presents the data as a quantitative map. The location, shape, and extent of any flaw region can then be easily extracted from this tomographic image.

The use of x-ray computerized tomography for medical non-invasive diagnostics is a mature technology, employing a set of projections around the body and a convolution-type of reconstruction to image cross-sections through the body. Different tomographic techniques exist using seismic waves to image subsurface structures for development of oil and mineral deposits. The technology from these industries has been borrowed and recombined in a new technique using ultrasonic Lamb Waves as the probing energy for a cross field geometry tomographic reconstruction. This Lamb wave tomography has been applied to samples of interest to civilian and military aircraft, and has been shown to accurately reproduce hidden thinning areas in aluminum plates. In addition, the limitations of this technique have been found, and the framework has been set to make Lamb wave tomography generally applicable for practical in-the-field inspections of aircraft.

The organization of this dissertation is as follows. In Chapter 2, a complete review of the Lamb wave literature and an overview of the tomographic literature are presented. Following this, the key points for the present work are discussed. In Chapter 3, the theory for Lamb waves propagating in a free, isotropic plate is presented. Then the experimental procedure is discussed and sample data is shown for the Lamb wave contact scanning of aluminum plates. Next, the theory, experimental apparatus, and tomographic algorithms for Parallel Projection tomography

(PPT) and Cross Borehole tomography (CBT) are presented. Results are shown for each method for the reconstruction of thinned regions in aluminum plates, and a comparison of the reconstruction quality and practicality of the two methods is made. Finally the limitations of PPT and CBT are discussed and shown experimentally by scanning plates with through holes of increasing size. In Chapter 4, analytical solutions for the scattering of plane, point source, and finite source Lamb waves from a cylindrical flaw in a plate are derived, and the case of a cylindrical hole in a plate is specifically investigated. These solutions are used to explain the scattering effects seen in the tomographic reconstructions of an aluminum plate with a large hole. Finally, their application as corrections for the two tomographic techniques is discussed. In Chapter 5 the results and limitations of this work are summarized, and future directions of research are outlined.

Chapter 2

Literature Review

In this chapter a chronological review of the literature for Lamb waves and tomography is presented. The review of the Lamb wave literature is complete, while that for the tomography focuses on the development of techniques and algorithms. Following the literature review is a brief discussion of the key points.

2.1 Review of Lamb Wave Literature

Ultrasonic guided waves are a special kind of ultrasonic wave that are guided or only propagate in certain structures, such as plates, shells, surfaces, interface layers, rods and wires. They are much more complicated than simple elastic waves in that each wave consists of many modes whose individual propagation and attenuation depend upon the generation frequency and guiding material parameters. In addition, these modes are often grouped into subcategories describing their motion. For example, Lamb waves, which propagate in thin plates, are divided into groups of symmetric and asymmetric modes corresponding to the motion of the plate with respect to its center line. These modes, which are also called dilatational and flexu-

ral. are designated by the notation (S_0, S_1, S_2, \dots) and (A_0, A_1, A_2, \dots) respectively. Since ultrasonic guided waves can travel large distance in their respective guiding materials, they allow for the rapid nondestructive evaluation of large areas. Below we present a review of the development and applications of ultrasonic guided waves with an emphasis on Lamb waves.

1917-1950

In 1917, Lamb published his work on the theory of two dimensional elastic waves in plates in vacuum [1]. In it he derived the dispersion relations, or "period equations" as he called them, for the symmetric and asymmetric modes. He showed that in the limit of small wavelength, these equations matched those for Rayleigh waves, and that in the limit of large wavelength, they matched the approximate solutions used previously. Lamb examined the first few symmetric and asymmetric modes assuming incompressibility, and he outlined the procedure for examining the symmetric modes when the material has some compressibility. In 1934, Balamuth described a new means of measuring the elastic moduli of a material by affixing a cross-section of piezoelectric quartz to the material and then driving it at various frequencies by applying a variable electric current [2]. This technique was the precursor to the piezoelectric transducers used today. In 1945, Osborne and Hart theoretically examined the interaction of an underwater explosion with a steel disc [3]. In their work they followed the method of Lamb, but took into account the loading of the plate by water. Their dispersion equations for the symmetric and asymmetric modes match those of Lamb with the addition of terms correcting for the presence of water. They showed that those modes which have a wavenumber with an appreciable imaginary component rapidly leak off their energy into the water.

1951-1959

In 1951 Mindlin derived a two-dimensional theory of flexural motions in isotropic, elastic plates from the three-dimensional equations of elasticity [4]. His plate equations were extremely close to the exact values of Lamb's theory, but were much less computationally intense. In 1954 Kane used Mindlin's two-dimensional plate theory to study the reflection of a straight-crested flexural wave from the edge of a semi-infinite plate [5]. He found that a flexural wave incident to the edge at an arbitrary angle produces three reflected waves: two flexural and one shear. In 1956 Kane and Mindlin followed the procedure for the flexural waves, to derive a two-dimensional plate theory for extensional waves from the three-dimensional equations of elasticity [6]. They then solved these equations for the case of axially symmetric vibrations of a circular disc and showed how they are accurate for low and high modes of thin plates and low modes of thick plates, while the equations of generalized plane stress are only accurate for low modes of thin plates. In 1957 Kane studied the reflection of straight-crested dilatational waves at the edge of a semi-infinite plate using the two-dimensional plate theory [7]. He found that a dilatational wave incident to the edge at an arbitrary angle produces three reflected waves, two dilatational and one shear. He also showed that the plate theory was much closer to the exact Lamb theory than the generalized plane stress theory. Also in 1957 Worlton presented the first experimental data taken using Lamb waves [8]. He submerged the test materials in water and used ultrasonic transducers at certain angles to preferentially generate specific Lamb wave modes in the test material. He showed that laminar flaws and radial cracks could be detected in plates and hollow cylindrical objects. In 1959 Mindlin and Medick updated the approximate, two-dimensional equations of extensional motion of isotropic, elastic plates to include coupling with

symmetric thickness-shear modes [9]. Gazis derived the characteristic equation for free harmonic waves propagating along a hollow cylinder of infinite extent [10], and he presented numerical results for some representative cylinders [11].

1960-1969

In 1960 Gazis, Herman, and Wallis performed a theoretical study of surface waves in cubic crystals using both continuum theory and discrete particle theory [12]. They showed that as the wavelength approached the particle spacing in the crystal, the discrete particle theory predicted dispersion while the continuum theory remained dispersionless. In 1961 Worlton published a second paper on experimental results using Lamb waves [13]. In this paper he rewrote Lamb's theory in the notation most commonly used today, and he plotted the phase velocity as a function of the frequency times thickness for the first several modes in aluminum and zirconium. Next, using the experimental setup discussed in his previous paper he verified his dispersion curves with experimental data, and he demonstrated that as the plate thickness increased only the lowest order symmetric and asymmetric Lamb wave modes existed and they approached their Rayleigh wave counterparts. He also showed that the Lamb waves were sensitive to the thickness change caused by a hole being drilled into the back of the plate. In 1964 Jones studied the propagation of Rayleigh waves in a two-layered medium [14]. In 1966 Gournay discussed how part of the electromagnetic energy from an incident laser is converted to an elastic wave in the absorbing medium, and showed results for a Q-switched ruby laser incident on various absorbing liquids [15]. In 1967 Viktorov wrote a monograph on Rayleigh and Lamb waves that was to become a classic reference [16]. In this monograph he discusses Lamb wave theory for vacuum loaded plates, fluid loaded plates, and cylindrical layers, methods of Lamb wave generation and detection, and

their application to flaw detection in sheets, tubes, and other thin-walled shapes. Jones and Whittier studied the character of interface waves in a flexibly bonded interface between two dissimilar half spaces [17]. Torvik extended Mindlin's work on the reflection of wave trains from the free edge of a semi-infinite plate to incorporate an evanescent mode in the incident wave [18]. In 1969 Hu developed a spherical model for the acoustic pressure wave generated by rapid laser heating in a liquid [19], and Kim and Smith studied the thermal expansion of Lithium Tantalate and Lithium Niobate single crystals [20].

1970-1974

In 1970 Anderholm reported accurate measurements of a laser-generated stress wave in the immediate vicinity of the absorber region on a solid [21]. In 1972 O'Keefe and Skeen showed that the magnitude of a laser induced stress wave in aluminum could be significantly increased by coating the aluminum target with a thin layer of a transparent, relatively volatile material [22]. Fairand, Wilcox, Gallagher, and Williams showed that stress waves generated by a giant pulsed laser could change the in-depth microstructural and mechanical properties of 7075 aluminum [23]. Dragonette used schlieren visualization to measure the group and trace velocity of guided modes generated in aluminum plates submerged in water [24]. Short acoustic pulses at different angles of incidence were used to generate the modes, and there was good agreement between the experimental angles that produced results and those predicted by Worlton's theory for plate thicknesses greater than 0.58 times the longitudinal wavelength. For plate thicknesses below this, the agreement worsened probably due to the effects of the water loading. Smith used an ultrasonic immersion technique and simple elastic waves to measure the elastic constants of carbon fibers and their composites [25]. Rybak determined the average field for

longitudinal and flexural waves in a plate containing random inhomogeneities [26], and he studied the effects of random coupling between flexural and longitudinal vibrations of plates [27]. In 1973 Neubauer showed that for a finite beam incident on a liquid-solid interface at the Rayleigh angle, there was no separation between the specular and Rayleigh reflections as predicted, so the Rayleigh wave must have continuously radiated into the fluid [28]. Nelson and Dong studied high frequency vibrations and waves in infinite homogeneous and laminated orthotropic plates using the Ritz technique [29]. This technique uses exact expressions for the wave form along the extent of the plate but uses generalized coordinates to model the through-the-thickness behavior of the plate. Lockett outlined the motion of material particles in, the initiation of, and the effect of pulse propagation on Lamb waves, and discussed their usefulness for detecting flaws on the inner and outer surfaces of tubes [30]. Solie and Auld used a numerical implementation of a mathematical formalism to obtain dispersion relations for acoustic waves in arbitrarily anisotropic plates to present the plate wave dispersion relations for propagation in a 001-cut cubic plate [31]. Germogenova used geometrical theory to model transverse flexure waves propagating in thin shells [32]. In 1974 Fairand, Clauer, Jung, and Wilcox quantitatively assessed laser-induced stress waves by measuring the pressure environment at the back surface of the sample. Their results compared favorably with those predicted by a one-dimensional radiation hydrodynamics computer code [33]. Fox used paint and water coatings to increase the stress generated in a target by a short-pulse laser, and showed that his results were comparable to the transparent overlay method applied in a vacuum [34].

1975-1979

In 1975 Garber and Granato used a quasiharmonic-anisotropic-continuum model

to calculate the theoretical temperature dependence of second-order elastic constants in cubic materials [35]. In 1976 Pitts, Plona, and Mayer studied the theoretical similarities of Rayleigh and Lamb modes of vibration [36]. In 1977 von Gutfeld and Melcher generated 20-MHz acoustic waves from pulsed thermoelastic expansions of constrained surfaces, and used them for flaw detection [37]. Rosenberg and Thurston showed how the relationship between the lowest Lamb-like plate modes of a tube and the surface modes of the tube is quite different from the relationship between the two lowest Lamb modes of a flat plate and the Rayleigh modes at the plate surfaces [38]. Auld and Tsao used variational analysis to model the reflection of the fundamental symmetric Lamb wave at the free edge of a semi-infinite plate [39]. In 1978 Nayfeh and Nassar showed that the influence of bonding material on the dynamic behavior of laminated composites increases with the stiffness of the bonding material, and that this influence can be modeled by either the trilaminated or reduced model analysis [40]. Sachse and Pao developed a new technique to determine the dispersion relation and the propagational speeds of waves in dispersive solids using the fact that the phase spectrum of a broadband pulse is linearly related to the dispersion relation of the dispersive medium [41]. They applied their technique to measure the phase and group velocities of waves in fiber-reinforced composite materials and in thin wires. In 1979 Fiorito, Madigosky, and Uberall used resonance scattering theory to study the interaction of acoustic waves with a fluid loaded plate and showed that their theory agreed with the exact theory and allowed for easier extraction of information [42]. Von Gutfeld and Budd studied the thermoelastic generation of MHz elastic waves in a substrate covered by a metallic film in contact with a liquid, and their results showed that the magnitude of the strain wave was strongly dependent on the expansion coefficient of the liquid and the thickness of the metal film [43]. Claus and Kline used Stonely waves to examine the adhesive

bondline between two glass specimens and determined that Stoneley wave attenuation increases as a function of increasing surface roughness [44]. Habeger, Mann, and Baum modeled paper as a homogeneous orthotropic plate, used a computer to derive the dispersion relations at low frequencies, and experimentally verified portions of these dispersion curves [45]. Achenbach and Harris used elastodynamic ray theory to study the acoustic emissions produced by elementary processes of deformation and fracture at a crack edge [46].

1980-1981

In 1980 Scruby, Dewhurst, Hutchins, and Palmer built a calibrated wide-band detection system to record the acoustic waveforms thermoelastically generated by unfocused laser radiation [47]. Using the data from this system they were able to characterize the relationship between the incident radiation and the waveforms recorded at the epicenter, and to develop a simple theoretical model for the thermoelastic source. Rokhlin used a numerical implementation of the generalized Wiener-Hopf method to investigate the diffraction of Lamb waves by a finite crack in an elastic layer [48]. Schoenberg developed the theory for a linear slip condition between two elastic media and derived the plane wave reflection coefficients for plane slip interfaces [49]. Rokhlin, Hefets, and Rosen developed a model for the waveguide properties of a thin film separating two elastic half-spaces possessing a shear modulus higher than that of the film, and showed that a complex shear viscoelastic modulus of the film can be determined from experimental data of the interface wave velocity and transmission losses [50]. In 1981 Hutchins, Dewhurst, and Palmer experimentally determined the directivity patterns of laser-generated ultrasound in aluminum, and showed that thermoelastic mechanisms dominate in the absence of plasma, while momentum transfer from ablating material dominates at higher power

densities [51]. Rokhlin, Hefets, and Rosen showed how their interface-wave method could be used to predict the strength of adhesive bonds [52]. Aindow, Dewhurst, Hutchins, and Palmer studied the generation efficiency of longitudinal, shear, and Rayleigh modes laser-generated in a free metal surface without any confining layers and without any visible damage [53]. Nayfeh, Chimenti, Adler, and Crane developed a model for bounded acoustic beam reflection at the Rayleigh angle from a fluid-solid interface loaded by a thin solid layer, and obtained experimental results in agreement with the theory as long as the film thickness was small compared to the Rayleigh wavelength [54]. Parnes calculated and studied the dispersion relations of waves propagating in a rod embedded in an elastic medium [55]. Voyiadjis and Baluch presented a refined theory for flexural motions of isotropic elastic plates taking into account the influence of transverse normal strain and transverse normal stress together with rotary inertia and transverse shear [56].

1982-1983

In 1982 Bar-Cohen and Crane experimentally studied acoustic backscattering in the Rayleigh region from fiber-reinforced composites and found a significant increase in backscattering when the fibers or cracks were at normal incidence [57]. Using this information they were able to map fiber orientations and cracks within specific plies. Clark and Hart studied the reflection of shear and longitudinal waves from liquid layers of submicron thickness and found that the layers no longer acted as the predicted perfect reflectors for thicknesses at or below 3000 angstroms [58]. Chimenti, Nayfeh, and Butler developed a theoretical model of the nonspecular reflection of finite acoustic beams incident at or near the Rayleigh angle onto a fluid-solid interface loaded by an elastic layer, and supported it with experimental measurements [59]. Jackins and Gaunaud showed the usefulness of the resonance

scattering theory to model and provide physical interpretations for the scattering of radar from a set of two contiguous plane dielectric layers separating two dissimilar nonconducting media [60]. Datta, Shah, and Fortunko used a combined finite element and analytical technique to model the diffraction of shear horizontal waves by edge cracks at various orientations and showed good agreement with experimental data [61]. Knollman and Hartog used Rayleigh critical-angle reflectivity measurements to determine shear modulus gradients in adhesive interfaces [62]. Dewhurst, Hutchins, Palmer, and Scruby extended their previous work on quantitatively assessing laser-generated acoustic waves in aluminum by using a wide range of laser power densities and various metallic samples [63]. Veith and Kowatsch reported the generation of continuous surface acoustic waves using a low intensity continuous wave dye laser instead of the usual pulsed high power Q-switched lasers [64]. Shah and Datta presented a stiffness method using the continuity of displacement and traction at the interfaces of the laminated composite medium and Floquet's theory to model harmonic wave propagation in layered composites [65]. In contrast to earlier methods, theirs could be applied to anisotropic layers.

1984-1985

In 1984 Houze, Nongaillard, Gazalet, Rouvaen, and Bruneel described an ultrasonic interferometric system for the measurement of coating thicknesses as thin as 5 micrometers [66]. Royer and Dieulesaint developed a theoretical analysis for the thermal generation of Rayleigh waves in anisotropic materials, and showed that their results were in good agreement with experimental measurements from a piezoelectric crystal of lithium niobate [67]. Tam demonstrated the pulsed-laser generation of ultrashort acoustic pulses and their usefulness in measuring steel film thicknesses as thin as 12 micrometers [68]. Koshiha, Karakida, and Suzuki used a hybrid analytical

and finite element analysis to model the scattering of the fundamental symmetric Lamb wave from wedge-shaped internal and surface cracks in an elastic plate [69]. In 1985 Vasudevan and Mal modeled the response of an infinite, homogeneous elastic plate to infinitesimal surface and internal disturbances using a classical integral transform technique [70]. Pilarski examined the possibility of using ultrasonic wave velocity measurements of surface, plate, or interface waves for the evaluation of adhesive bond strength [71]. He numerically determined the dispersion curves for both layer-layer and layer-base systems with welded and smooth boundary conditions, and he experimentally determined relationships between the velocity of plate waves and bond strength. Chimenti and Nayfeh used experimental measurements of Leaky Lamb wave propagation in fiber-reinforced unidirectional composite laminates to generate dispersion curves and compared them to their theoretical predictions [72]. Sessler, Gerhard-Multhaupt, West, and von Seggern demonstrated the optoacoustic generation of subnanosecond acoustic pulses in quartz and several polymers [73]. Sontag and Tam used an interferometric technique to monitor both longitudinal and Lamb wave photoacoustic pulses generated by a weak laser pulse in silicon wafers [74]. Their technique provided a fully noncontact and nondestructive means of measuring the elastic properties and orientation of thin silicon wafers. Dong and Huang used a finite-element method to model edge vibrations in laminated composite plates [75]. Maze, Izbicki, and Ripoche experimentally verified that resonances in the normal diffusion of an ultrasonic plane wave by cylinders and plates corresponded to the natural modes of the cylinders and plates [76].

1986-1987

In 1986 Rokhlin and Marom used longitudinal waves obliquely incident on two adhesively bonded layers to show that changes of the reflected amplitude during

curing occurred simultaneously with changes of the ultrasonic velocity in the adhesive, and so the quality of adhesive bonds could be determined [77]. Crosbie, Dewhurst, and Palmer used nanosecond pulses from a Nd:YAG laser to excite clamped and partially clamped aluminum disks to resonance, and then used the generated flexural modes and longitudinal ring-around pulses to measure the depth of a flat-bottom hole on the surface of the disk [78]. Tam and Ayers used sub-nanosecond photoacoustic pulse generation to simultaneously provide information on a thick substrate and thin coating and produce an ultrasonic image of the layered medium [79]. Chimenti and Nayfeh showed that there is anomalous ultrasonic dispersion in fluid-coupled, fibrous composite plates resulting from a mixing of the two fundamental plate modes at phase velocities near the bulk composite transverse wavespeed [80]. Thomsen, Grahn, Maris, and Tauc reported experiments in which picosecond light pulses were used to generate and detect very short stress pulses in various thin films [81]. Liu studied the frequency dependence of ultrasonic wave propagation in metal-matrix composite plates and showed that at frequencies below 10MHz, the velocity dispersion is primarily controlled by the geometry of the plate with only minor contributions from the microstructure [82]. Bar-Cohen and Chimenti discussed the usefulness of Leaky Lamb wave analysis for the detection of flaws in graphite/epoxy composite plates [83]. Angel presented a numerical solution for the scattering of Love waves by a surface-breaking crack normal to the free surface [84]. In 1987 Shah, Chin, and Datta used Datta's combined analytical and finite element method [61] to study the scattering of in-plane body and surface waves by canted planar and normal surface-breaking branched cracks [85]. Dewhurst, Edwards, McKie, and Palmer used pulse laser generated and laser interferometer detected Lamb waves to estimate the thickness of thin metal sheets [86]. Lang, Kurkjian, McClellan, Morris, and Parks demonstrated a technique to esti-

mate dispersion relations from arrays of sonic logging waveforms [87]. Adler, Rose, Rokhlin, and Nagy discussed the use of Lamb waves and Leaky Lamb waves for the characterization of fiber reinforced composites [88]. Caslini, Zanotti, and O'Brien used fracture mechanics to study matrix cracking and delamination in glass/epoxy composites [89].

1988

In 1988 Zhang, Chen, and Ying experimentally studied the reflection of single Lamb wave modes from a free plate edge [90]. Nayfeh and Chimenti experimentally generated dispersion curves for guided wave propagation in fluid-coupled fiber-reinforced composites and found excellent agreement with their theoretical predictions [91]. De Billy and Molinero investigated the reflection and transmission effects for angles of excitation of Lamb waves near the longitudinal critical angle and found that at this angle the leaky-surface-wave-radiation does not occur for liquid/solid/liquid configurations [92]. Pilarski and Rose found that transverse-wave ultrasonic oblique-incidence techniques are better for interfacial weakness detection than the previous longitudinal-wave techniques [93]. Nayfeh and Chimenti presented a unified analytical treatment of the interaction of ultrasonic waves with arbitrarily oriented liquid-coupled orthotropic elastic plates, and they supported it with experimental data taken from a composite plate [94]. Mal described a matrix method for deriving the dispersion equation for guided waves in multilayered plates and half spaces which was free from numerical instability at high frequencies [95]. Datta, Shah, Bratton, and Chakraborty presented a stiffness method to numerically determine the dispersion characteristics of waves propagating in a plate with an arbitrary number of arbitrarily anisotropic laminae [96]. Nagy, Jungman, and Adler used a broadband pulse-echo technique to measure backscattered Leaky

Lamb waves from a fiber-reinforced composite plate immersed in water [97]. Dean used measurements of Lamb wave velocities to determine the elastic properties of plastics and other polymers [98]. Mal and Bar-Cohen reviewed the ultrasonic non-destructive techniques used for the detection of defects in composites at that time and focused on the leaky guided wave technique [99]. Mal and Bar-Cohen presented a matrix method to calculate the phase velocity of Rayleigh-Lamb waves traveling in fiber-reinforced composite plates made up of transversely isotropic laminae, and compared the theoretical results with leaky Lamb wave data [100].

1989

In 1989 Hutchins, Lundgren, and Palmer described laser techniques for generating and detecting transient ultrasonic Lamb waves in thin materials, and used measurements of the velocity and dispersion characteristics of the lowest order modes to estimate the thickness and elastic properties of the samples [101]. Tang and Henneke experimentally determined the dispersion curves for the lowest order symmetric and asymmetric Lamb wave modes in laminated composite plates, and showed that the lowest order asymmetric mode was sensitive to damage in composite plates such as stiffness reduction [102]. Tsukahara and Ohira calculated the reflection coefficients for a steel substrate with a polymer coating for both perfect and smooth bonding conditions, and showed that the frequency spectrum changed when the bonding became smooth [103]. McDonald modeled photoacoustic pulse generation using generalized thermoelastic equations and the hyperbolic heat conduction equation to avoid an infinite thermal propagation property [104]. Dayal and Kinra developed an exact solution for the dispersion equation of for Leaky Lamb waves in an anisotropic plate, and showed agreement between the numerical and experimental results for a graphite/epoxy composite plate [105]. Bar-Cohen

and Mal experimentally studied the leaky Lamb wave phenomenon in composite laminates using pulses rather than toneburst or continuous waveforms, and showed that when the pulses propagate obliquely to the fibers, they are strongly influenced by flaws within the laminate [106]. Kline and Doroudian demonstrated the capability of Lamb waves to detect artificial flaws and damage due to cyclic loading in adhesively bonded composite joints [107]. Nayfeh and Chimenti developed the analysis for the propagation of free waves in a general anisotropic plate, and presented numerical free-wave dispersion results for a monoclinic and higher symmetry plates [108]. Kline, Doroudian, and Hsiao developed a numerical analysis procedure to calculate the dispersion relationships for plate waves propagating along arbitrary directions in a transversely isotropic plate [109]. Dayal, Iyer, and Kinra used measurements of wavespeed and attenuation for longitudinal and leaky Lamb waves to detect microcracks and characterize damage in composite plates [110]. Noiret and Roget made theoretical calculations of the wave propagation of a steady wave in a unidirectional composite plate and successfully compared them to experimental data found in the literature [111]. Epstein, Deason, Abdallah, and Murakami presented a computational analysis for the propagation of elastic Lamb waves in an orthotropic media and used it to experimentally examine graphite/epoxy plates that had mechanical impact in the direction of the layering [112]. Tang and Henneke presented an approximate theory for the lowest Lamb modes in the low frequency, long wavelength region for a unidirectional laminate, and showed that it matched experimental results taken in the same region from laminates with and without damage [113]. Kapania and Raciti summarized the recent advances in the analysis of laminated beams and plates with an emphasis on vibrations and wave propagations [114].

1990

In 1990 Papadakis wrote monographs on the measurement of ultrasonic velocity [115] and ultrasonic attenuation [116], and Hutchins and Hayward wrote a monograph on the radiated fields of ultrasonic transducers [117]. Balasubramaniam and Rose published a review of the breakthroughs in the utilization and understanding of guided plate waves in thin composites [118]. Karim, Mal, and Bar-Cohen presented a numerical procedure for the inversion of leaky Lamb wave data to determine the material properties of a waveguide, using a modified version of the simplex algorithm [119]. Spicer, McKie, and Wagner used a numerical inversion of the Hankel-Laplace transform for the case of ultrasonic displacements in an infinite, homogeneous, isotropic plate which has been excited by a thermoelastic pulse, to determine the elastic moduli and plate thickness for thin and thick plates [120]. Xu and Datta showed that the spring model and density model approximations of the dispersion of elastic waves in a bonded plate only match the exact solution in two overlapping regions of the density and stiffness ratios [121]. McDonald used a formulation of pulsed photoacoustic generation to show how the precursor in laser-induced ultrasound waveforms arises from the interaction of the thermal and elastic modes at the illuminated surface [122]. Deaton, McKie, Spicer, and Wagner used a passively mode-locked, flashlamp-pumped Nd:YAG laser with a long cavity to study the noncontact generation of narrow-band ultrasound in an aluminum sample [123]. Chimenti and Nayfeh presented numerous experimental results on ultrasonic reflection and guided wave propagation in biaxially laminated composite plates [124]. Burger, Duffer, and Schumacher described a new procedure for ultrasonic evaluation of laminated composites using a short duration high energy laser pulse directed towards a selected location on the sample surface through an optical bundle to generate the plate waves and a noncontact fiber tip interferometer to

detect them [125]. Nayfeh and Chimenti theoretically and experimentally studied the interaction of ultrasonic waves with multilayered monoclinic plates submerged in water [126]. Rokhlin and Wang used the critical angle measurement and double transmission time-delay measurement ultrasonic methods to determine the elastic constants in thick sectioned composites, and the transmission resonance ultrasonic measurement to determine the elastic constants in thinner composites [127]. Bouden and Datta theoretically studied guided wave propagation in coated anisotropic media [128]. Jansen and Hutchins used the filtered back-projection technique to tomographically image flaws in aluminum plates using ultrasonic Lamb waves. The plates were submerged in an immersion tank, and amplitude variation and propagation delay were used to image attenuation and velocity [129].

1991

In 1991 Alleyne and Cawley presented an extension of the phase spectrum method for determining the phase velocity of dispersive waves to the case of multi-mode propagation [130]. Bratton and Datta used a hybrid technique that combined analytical and finite element techniques to model the scattering of Lamb waves from a surface breaking crack in a composite plate [131]. Datta and Shah used the same technique to model the scattering of Lamb waves from general inhomogeneities in an elastic homogeneous isotropic plate [132]. Nakano and Nagai used the interference of two high powered lasers to generate coherent asymmetric Lamb waves in thin plates [133]. Dayal and Kinra used leaky Lamb waves to detect matrix cracking in fiber-reinforced composites [134]. Alleyne and Cawley published a second paper on their two-dimensional Fourier transform method [135]. Rokhlin and Wang obtained boundary conditions that relate stresses and displacements on both sides of a thin viscoelastic interface layer between two solids as an asymptotic representation

of the three-dimensional solutions in the limit of a small wavelength to thickness ratio [136]. Vary presented an overview of the acousto-ultrasonic technique which was devised to assess diffuse flaw populations in composite materials [137]. Chimenti and Martin demonstrated the sensitivity of leaky Lamb waves to defects in graphite-epoxy composite laminates [138].

Nayfeh and Chimenti published their work on the interactions of ultrasound with multilayered media in a second paper [139]. Yamanaka, Nagata, and Koda generated single-mode acoustic waves in multimode media using a laser beam scanned at the phase velocity of the desired mode [140]. Nayfeh discussed their theory for the general problem of elastic wave propagation in multilayered anisotropic media [141]. Bobbin, Wagner, and Cammarata used the measurement of pulse laser generated and heterodyne interferometry detected Lamb waves to determine the flexural modulus of thin films [142]. Rokhlin theoretically and experimentally studied the interaction of Lamb waves with lap-shear adhesive joints [143]. Balasubramaniam and Rose theoretically studied the effect of various flaws on the plate wave dispersion curves [144]. Datta, Karunasena, and Shah used a hybrid finite element and analytic technique to study wave propagation and scattering from matrix cracks in multilayered composite plates [145]. Mal, Yin, and Bar-Cohen used a global matrix method to calculate the reflection coefficients and dispersion curves for unidirectional and angle-ply laminates immersed in water [146]. Liu, Datta, and Ju used a hybrid numerical method to investigate the scattering of transient Rayleigh-Lamb waves by a surface-breaking crack and compared their results with experiment [147]. Al-Nassar, Datta, and Shah used a combined finite-element and Lamb wave modal expansion method to study the scattering of time harmonic Lamb waves by a normal rectangular strip weldment [148].

1992

In 1992 Nayfeh and Chien extended the analysis of the interaction of elastic waves with anisotropic plates immersed in water to include linear piezoelectric effects [149], and subsequently extended this work for anisotropic substrates [150]. Laperre and Thys modeled elastic wave dispersion in a liquid bilayer, and confirmed their theory with experimental results [151]. Bobbin, Wagner, and Cammarata studied the effect of the orientation of the laser source and receiver, film thickness, and laser spot size on the waveform structure of the lowest order symmetric and asymmetric Lamb wave modes generated in thin films [152]. Karim, Awal, and Kundu studied the scattering of elastic waves in a plate by a distribution of cracks and inclusions using the hybrid finite element and analytical technique [153]. Alleyne and Cawley discussed the optimization of Lamb wave inspection for certain requirements [154]. Kautz experimentally determined dispersion curves in ceramic matrix composites and metal matrix composites using the acousto-ultrasonic technique [155]. Ditri, Rose, and Chen investigated using a mode's energy distribution across the thickness of the layer as a means of determining the optimal Lamb wave mode for a given defect inspection [156]. Komsky, Daniel, and Lee used ultrasonic shear waves to determine layer orientation in multilayer multidirectional composites [157]. Schumacher, Gien, and Burger used a laser and fiber optic based system to generate and detect transient Lamb waves in a steel plate, a unidirectional composite panel, and a section of seam welded stainless steel tubing [158]. Guo and Cawley presented numerical results predicted by finite element analysis for the propagation and interaction with defects of the S_0 Lamb wave mode in composite laminates, and showed experimental results of long range inspections using this mode [159].

Wu and Zhu showed that leaky Lamb waves can be used to measure the physical parameters of liquids bordering plates [160]. Yamanaka, Nagata, and Koda

further investigated the nature of the acoustic waves generated using their phase velocity scanning method [161]. Mal and Lih derived the theoretical solution for the response of a unidirectional composite plate to a dynamic surface load [162]. Verdict, Gien, and Burger performed a finite element study of Lamb wave interactions with flawed and unflawed rivet holes in thin plates [163]. Liu, Datta, and Shah used Datta's hybrid finite element and integral representation method to model the scattering of ultrasound by cracks in a glass plate [164]. Sun showed that low order plate waves in combination with an acoustic dampener could be used for delamination detection in aluminum plate assemblies [165]. Dewen and Cawley presented an ultrasonic scanning technique using Lamb wave modes to quantitatively determine the cohesive properties of adhesive joints [166]. Mal, Gorman, and Prosser used low-frequency experimental plate wave dispersion data to determine the elastic constants of a graphite/epoxy composite [167]. Hutchins presented an overview of the uses of pulsed lasers for quantitative ultrasonic nondestructive evaluation [168]. Fergusson and Pilkey studied the formation of frequency-dependent structural matrices [169]. Alleyne and Cawley used finite element analysis to investigate the interaction of Lamb waves with various defects simulated by notches and checked their results with experiment [170]. Jansen and Hutchins published their work using Rayleigh waves to reconstruct images of surface defects in thick metallic samples and using Lamb waves to image defects in thin metallic plates. They again immersed the samples in an ultrasound tank and used the filtered back-projection method to reconstruct tomographic images from traveltime data [171].

1993

In 1993 Pilarski, Rose, Ditri, Jiao, and Rajana discussed Lamb wave mode selection criteria for increased sensitivity to interfacial weaknesses of adhesive bonds

[172]. Chien, Sheen, and Raptis showed that time-of-flight measurements of acousto-ultrasonic waves was a better technique for measuring material anisotropy than the standard stress wave factor measurements [173]. Costley and Berthelot demonstrated how using a Fresnel lens increases the signal-to-noise ratio of laser generated Lamb waves and how the dispersion curves of these Lamb waves can be determined using laser ultrasonics [174]. Edwards, Al-Kassim, and Palmer described the use of laser ultrasound for the generation and detection of Lamb waves for the measurement of sheet thickness [175]. Komsky and Achenbach applied their self-calibrating ultrasonic technique to detect fatigue cracks in aircraft structures using Lamb waves [176]. Hutchins, Jansen, and Edwards showed that pulsed laser generated and electromagnetic acoustic transducer (EMAT) detected Lamb waves could be used to tomographically image changes in the structure of thin sheet material using the filtered-backprojection algorithm [177]. Alleyne, Pialucha, and Cawley presented a signal regeneration technique for the long-range propagation of highly dispersive Lamb wave modes [178]. Noui and Dewhurst presented a laser beam deflection technique for the non-contact quantitative detection of ultrasonic Lamb waves [179]. Rao, Sheikh, and Mukhopadhyay used the finite element method to study the large-amplitude free flexural vibration of stiffened and unstiffened plates [180]. Liu and Datta applied their hybrid finite element and boundary integral method to investigate the scattering of ultrasound from two surface-breaking cracks of different lengths and one subsurface crack [181]. Eto, Costello, Wenzel, White, and Rubinsky used a Lamb wave microsensor to measure the viscosity of dimethylsulfoxide solutions as a function of temperature [182]. Kundu and Maxfield determined Rayleigh and Lamb wave speeds in half-spaces and plates using the rate of change in the time of flight between a transmitter and receiver as the propagation distance was varied [183]. Schumacher, Burger, and Gien used their laser and

fiber optic system for Lamb wave generation and detection in plates to investigate higher order Lamb wave modes [184]. Pilarski, Ditri, and Rose presented proof for the vanishing of the normal component of the particle displacement vector on the free surfaces of an isotropic, homogeneous plate for nonzero-order symmetric Lamb waves [185].

1994

In 1994 Rose, Pilarski, Rajana, and Ditri studied the effect of a coating on the generation and detection of Lamb waves in aluminum samples [186]. Shull, Chimenti, Datta, and Ju experimentally and theoretically studied elastic plate wave inspection of bilayered plates [187]. Mal, Lih, and Bar-Cohen described the experimental setup and analytical procedure for determining the elastic constants of graphite/ epoxy composites using a pulsed leaky Lamb wave method [188]. Chien, Sheen, and Raptis extended Chien's earlier work on ultrasonic wave propagation in a piezoelectric plate to a multilayered piezoelectric medium [189]. Yapura and Kinra presented the analysis to calculate the Lamb wave dispersion branches and mode-shapes for an isotropic solid-fluid bilayer [190]. Pilarski, Ditri, Rajana, and Rose examined the benefits of using non zero-order symmetric Lamb wave modes at the first critical angle for plate inspection [191]. Dayal presented an automated leaky Lamb wave measurement system and transformed the received ultrasonic signal into the frequency domain to determine the phase velocity and group velocity [192]. Schumacher and Burger presented digital signal processing techniques to calculate the phase velocity of laser generated and detected Lamb waves [193]. Alleyne and Cawley described the use of angle piezoelectric transducers for the generation of a single Lamb wave mode in a material [194]. Ditri, Pilarski, Pavlakovic, and Rose presented a model of the generation of guided waves in an infinite, homogeneous,

linearly elastic and isotropic layer by axisymmetric normal surface loading, i.e. a contact longitudinal wave transducer [195].

Seale, Smith, Prosser, and Masters used measurements of Lamb wave velocity to monitor fatigue damage in composite samples [196]. Sun and Johnston used Lamb wave amplitude and time-of-flight measurements to detect disbonds in bonded aluminum joints [197]. Lee, Khuri-Yakub, and Saraswat used measurements of Lamb wave time-of-flight to measure the temperature of silicon wafers during rapid thermal processing [198]. Lowe and Cawley wrote a review and analysis of the plate wave techniques used for the inspection of adhesive and diffusion bonded joints [199]. Costley and Berthelot applied the two-dimensional fast fourier transform technique to laser generated waveforms to determine which modes and at what amplitudes Lamb waves had been generated in a thick plate [200]. Wang, Jen, and Cheeke presented the velocity and mass sensitivity formulae for two-layer shear horizontal plate wave sensors [201] and two-layer sagittal plane wave sensors [202]. Chimenti derived and studied the velocity dispersion of guided plate waves in a plate composed of a coherent microstructured material, and found that the dispersion was due to both Lamb wave and microstructural dispersion [203]. Jansen, Hutchins, and Mottram used a Lamb wave immersion tomography technique using a transform algorithm to image damage in advanced composite laminates [204]. Ditri and Rose theoretically studied the excitation of guided wave modes in generally anisotropic layers by finite strip sources placed on the surface of the layer [205]. Degertekin, Pei, Khuri-Yakub, and Saraswat performed in situ acoustic temperature tomography of semiconductor wafers by using measurements of Lamb wave time-of-flight to measure the temperature of the wafer along specific ray paths and then reconstructed the temperature distribution of the wafer using the simple linear equation solving approach [206]. Pierce studied the influence of structural wave dispersion on the

scattering patterns of waves incident on structures with fuzzy internals [207].

1995

In 1995 William and Mary researchers proposed using ultrasonic Lamb waves to evaluate the interface structural integrity of aircraft [208]. Alleyne and Cawley used Lamb waves for the long range detection of internal and external defects in pipes [209]. Krauss used guided waves for the detection of interior flaws in layered materials [210]. Oksanen, Stor-Pellinen, and Luukkala determined the mechanical properties of cardboard from measurements of photoacoustic Lamb waves [211]. Wright, Hutchins, Gachagan, and Hayward used a non-contact laser/air transducer system to evaluate fiber-reinforced composites [212]. Pelts and Rose theoretically studied the wave structure produced in a linearly elastic orthotropic layer by an acousto-ultrasonic source [213]. Hansch, Rajana, and Rose presented an approach for automated data evaluation of guided waves in tubing for the classification of flaws [214]. Nagata, Huang, Achenbach, and Krishnaswamy combined filtered back-projection tomography and laser-based ultrasonics to image defects in thin aluminum plates using Lamb waves [215]. Addison and McKie used a series of laser-based ultrasound line sources for the generation and detection of single mode Lamb waves in a plate [216]. Rose, Pilarski, and Rajana developed a double spring hopping probe for the Lamb wave inspection of lap splice joints in aging aircraft and tested it on a Boeing 737-222 [217].

Sun and Johnston experimentally studied the effect of rivet rows on the propagation of Lamb waves in mechanically fastened two-layer aluminum plates [218]. Johnson, Thompson, and Jamieson determined the Rayleigh and Lamb wave velocities in diamond films using an acoustic microscope [219]. Safaeinili and Chimenti presented a general method for solving Lamb wave propagation in periodically-

layered composites combining Floquet analysis and the transfer matrix approach [220]. Ditri and Rajana theoretically analyzed the wedge method of generating guided waves in isotropic plates particularly focusing on the relationship between the angularly dependent excitation amplitude of a given mode and the physical parameters of the transducer and wedge used for excitation [221]. Lowe and Cawley compared reflection coefficient minima with the dispersion curves for ultrasonic waves propagating along an embedded layer in a multilayered plate to determine if the Null Zone technique provides accurate measurements of modal properties in adhesive and diffusion bonded joints [222]. Rajana, Hongerholt, Rose, and Ditri also published the experimental results for their analysis of the wedge method for generation of guided waves [223]. Pei, Degertekin, Khuri-Yakub and Saraswat demonstrated a technique for in situ film thickness measurement using acoustic Lamb waves [224]. Huang, Brisada, and Rokhlin studied the scattering of longitudinal and shear ultrasonic waves from a multilayered fiber embedded in a matrix [225]. Karunasena, Liew, and Kitipornchai used a finite element technique to study the reflection of plate waves at the fixed edge of a composite plate [226]. Phipps studied the use of Lamb waves for the detection of disbonds in aging aircraft [227].

Yamada and Khuri-Yakub presented a new type of point contact transducer of waveguiding structure operating in the MHz frequency range that could be used for the dry coupled generation of Lamb waves in silicon wafers [228]. Rebinsky and Norris derived a general solution for the scattering of acoustic and flexural waves from a three-member junction [229]. Gachagan, Pierce, Philp, McNab, Hayward, and Culshaw presented fiber optic technology for the detection of Lamb waves in composite plates and used it to detect a variety of flaws [230]. Rogers used measurements of the phase shift over a measured path length of Rayleigh-Lamb waves in isotropic plates to determine the phase velocity of the wave and elastic

properties of the plate [231]. Tan, Guo, Wong, and Tui used the lowest order symmetric Lamb wave mode to experimentally locate and evaluate delaminations in composite plates [232], and showed that their Lamb wave technique was better at locating near-surface delaminations than the conventional pulse echo technique [233]. Bork and Challis used Lamb wave measurements and a linear network for data discrimination to nondestructively evaluate the adhesive fillet size in T-peel joints [234]. Zhu and Wu determined the dispersion equations of Lamb waves in a plate bordered with a viscous liquid layer or half-space on both sides [235]. Opie proposed using tomographic imaging for Lamb wave ultrasonic imaging systems [236].

1996

In 1996 William and Mary Researchers proposed the use of ultrasonic Lamb waves for the evaluation of multilayer structural integrity [237]. Guo and Lim studied the propagation of Lamb waves in aluminum honeycomb structures using a multilayer model [238]. Seale and Smith theoretically and experimentally studied the effect of thermal damage in composites on Lamb wave propagation [239]. Cheng and Zhang developed a general theory for the propagation of coupled Lamb waves along an arbitrary direction in an orthotropic fiber composite plate [240]. Rajana, Cho, and Rose modified their earlier mode selection criterion to simply examining the variation of the available energy at the surface along each mode, and compared their results with those from a boundary element method and from experiment [241]. Hirao, Yokota, and Fukuoka used the lowest order symmetric leaky Lamb wave mode to nondestructively evaluate the Young's modulus of VCR magnetic tapes [242]. Kundu, Karpur, Matikas, and Nicolaou studied the sensitivity of different leaky Lamb wave modes to defects in different layers of composite plates and produced

Lamb wave scanning images of these layers [243]. Ji, Sullivan, and Balasubramaniam used a model based on the Thomson-Haskell transfer matrix to analyze guided wave behavior in multi-layered inhomogeneous anisotropic plates [244]. Hirose and Yamano used a boundary element method to study the scattering of Lamb waves from a subsurface horizontal crack [245]. Chan and Cawley studied the effect of various levels of attenuation on Lamb wave dispersion curves [246]. Chang, Guo, and Mal used the global local finite element method to study the characteristics of Lamb waves propagating across a lap joint model [247]. Pei, Yousuf, Degertekin, Honein, and Khuri-Yakub used a Hertzian contact to generate Lamb waves in pipes and plates without couplant, and they presented a filtered back-projection tomographic image of an aluminum plate with a depression milled into it [248].

Spies and Kroning used a Green's function technique to determine the disturbance resulting from a point source and to investigate Rayleigh wave propagation in a transversely isotropic half-space [249]. Hinders derived exact and analytical eigenfunction solutions for the scattering of lowest order symmetric and asymmetric Lamb waves from a disk [250]. Laurent and Bastien studied the effect of transducer shape and electrical connection symmetry on the production of Lamb and shear-horizontal waves by interdigital transducers on both sides of a piezoelectric plate [251]. Alleyne and Cawley described a dry-coupled piezoelectric transducer system for the detection of corrosion in chemical plant pipework using cylindrical Lamb waves [252]. Sweet discussed the use of acoustic waves for the detection of first-time nuclear tests [253]. Desmet, Kawald, Mourad, Lauriks, and Thoen theoretically and experimentally studied the behavior of Lamb waves in stressed polymer foils [254]. Kundu, Maslov, Karpur, Matikas, and Nicolaou also produced Lamb wave images from titanium matrix composites [255]. Read and Seiler proposed the development of a Lamb wave scanning and tomographic

imaging instrument for the nondestructive evaluation of metallic and composite plate-like structures [256], [257], [258]. Young, Yuan, and Dickinson presented a three-dimensional analysis of the free vibration of very thick rectangular plates with depressions, grooves, or cut-outs [259].

Turner and Weaver studied diffuse energy propagation on heterogeneous plates using structural acoustics radiative transfer theory [260]. Xiang, Liew, and Kitipornchai presented vibration solutions for circular and annular Mindlin plates with concentric internal ring stiffeners [261]. Park, Kim, and Yoon showed the feasibility of Lamb wave ultrasonic inspection for the detection of flaws in insulated or inaccessible long steel pipes [262]. Castaings and Cawley described a finite element study of the generation of Lamb waves in plates from a finite air-coupled transducer, the interaction of these waves with defects, and their detection using an air-coupled transducer, and they compared it with experimental results [263]. Khmelevskaja-Plotnikova and Pavlov presented a nonlinear evolution equation for the study of the transversal structure of finite amplitude Lamb waves in the atmosphere near the Earth's surface [264]. Cho and Rose used the boundary element method for the study of the mode conversion of Lamb waves reflecting from an edge [265]. Cheng and Berthelot presented a model for the thermoelastic excitation of transient Lamb waves propagating along the principal directions in an orthotropic plate, and used it for a quantitative analysis of the noncontact and nondestructive detection of the elastic stiffness properties of machine-made paper using the laser-generated Lamb wave technique [266]. Balasubramanyam, Quinney, Challis, and Todd described a simple finite-difference method to simulate S_0 and A_1 Lamb wave modes in plane metal sheets and corresponded their results with experiment [267]. Secora showed that Lamb wave experiments could be used to detect flaws in laboratory specimens and a damaged aircraft panel [268]. Seale conducted a theoretical and experimental

study to determine the effect of fatigue, thermal, and thermal-mechanical damage in composites on Lamb wave velocity [269].

1997

In 1997 Pelts, Cysyk, and Rose used the boundary element method for flaw classification in wave guides [270]. Pavlakovic, Lowe, Alleyne, and Cawley presented DISPERSE, a general purpose program for creating dispersion curves using the global matrix method [271]. Singher, Segal, and Shamir performed a numerical study on the scattering of guided waves from a cylindrical flaw [272]. Cho, Hongerholt, and Rose used a hybrid boundary element technique to study the effect of defect shape on the scattering of Lamb waves in an attempt to develop a means for flaw characterization [273]. Jia presented a modal analysis to describe the excitation of Lamb waves in an elastic plate using a liquid wedge transducer [274]. Alleyne and Cawley presented on site data from their dry coupled piezoelectric transducer system for corrosion detection in chemical plant pipework [275]. Maslov and Kundu theoretically predicted the leaky Lamb modes most sensitive to various internal defects in a composite laminate and verified their results experimentally [276]. Pierce, Culshaw, Philp, Lecuyer, and Farlow performed broadband measurements of Lamb wave dispersion in aluminum, carbon, and carbon/glass fibre hybrid composite materials using a non-contacting optical technique and showed that their results agreed well with theoretical modeling [277]. Nayfeh and Nagy extended the work of Zhu and Wu to produce the exact dispersion equations for a viscous fluid loaded plate that are not limited to low frequencies and viscosities, and they used them to illustrate the effect of viscous fluid loading on the attenuation of the lowest order symmetric and asymmetric leaky Lamb wave modes [278]. Cathignol, Sapozhnikov, and Zhang showed that Lamb waves in the piezoelectric focused radiator were re-

sponsible for the discrepancy between the observed acoustic field and that predicted by O'Neil's formula [279].

Briers, Leroy, and Shkerdin developed a model to describe the Lamb and Rayleigh waves generated by a liquid wedge [280]. Kundu and Maslov investigated the propagation of Lamb waves through a two-layered glass plate with different interface conditions in order to determine the effectiveness of Lamb waves to detect interface defects in addition to the interface strength [281]. Kielczynski derived an analytical formula relating the attenuation of a Love wave propagating in a viscous surface layer deposited on a perfect elastic substrate to the viscoelastic properties of the waveguide structure [282]. Moulin, Assaad, Delebarre, Kaczmarek, and Balageas showed that Lamb waves could be effectively generated by a piezoelectric transducer embedded in a composite plate [283]. Zinin, Lefeuvre, Briggs, Zeller, Cawley, Kinloch, and Thompson showed that the behavior of the attenuation of surface acoustic waves propagating on a fast-on-slow layered system is anomalous past the shear wave velocity of the substrate cutoff point, and verified their results using acoustic microscopy [284]. Makarov and Belkova performed a numerical study of high velocity pseudosurface waves on coated LiNbO_3 [285]. Jia developed a normal-mode theory for the nonspecular effects of a finite-aperture ultrasonic beam incident onto layered elastic media, and studied the features of leaky wave fields at liquid-solid and liquid-solid-liquid interfaces [286]. Poncelet and Deschamps theoretically investigated the generation of Lamb waves in immersed plates by complex harmonic inhomogeneous plane waves which have complex frequency in contrast to leaky waves [287]. Darinskii derived approximate expressions for the leaky wave speed and the coefficients of plane wave conversion for a "supersonic" Rayleigh wave converted into a leaky wave by a thin solid layer on an anisotropic medium [288]. Kapoor and Schmidt developed an approximate analytical solution for the scatter-

ing of sound from a three-dimensional protuberance on a thin, infinite, submerged elastic plate [289].

Lobkis developed a theoretical model of the effect of surface roughness on the propagation of elastic guided waves in plates [290] and compared the results with experiment [291]. de Billy experimentally studied the scattering of antisymmetric edge modes [292]. Losin studied the long and short-wave asymptotics of the flexural vibrations of an infinite, isotropic, elastic plate [293]. Monkhouse, Wilcox, and Cawley described the development of flexible interdigital PVDF transducers for the generation and detection of Lamb waves in plates [294]. Wang and Shen used a T-matrix and boundary element hybrid method to study the scattering of elastic waves by a crack in an isotropic plate [295]. Guo, Achenbach, and Krishnaswamy presented the EMAT generation and laser interferometer detection of single Lamb wave modes in thin plates [296]. Singher studied the applicability of ultrasonic guided waves for measuring bond strength [297]. Singher, Segal, and Shamir presented a theoretical model for the diffraction of ultrasonic guided waves propagating in a nonuniform elastic adhesive layer [298]. Schindel, Forsyth, Hutchins, and Fahr investigated the feasibility of using wideband air-couple ultrasonic transducers for evaluating the integrity of bonded aluminum lap joints [299].

Hassan and Nagy studied the feasibility of fatigue crack detection in fluid-filled cylindrical holes using circumferential creeping waves [300]. Mal, Chang, and Gorman used the global local finite element method and experiments to study the interaction of Lamb waves with near-edge defects in a semi-infinite plate [301]. Pecorari presented a model to predict the Rayleigh wave velocity changes due to distributions of one-dimensional, interacting surface cracks [302]. Chimenti and Lobkis reported experimental measurements and a theoretical calculation of the effect of surface roughness on guided waves propagating in a planar fluid-loaded solid

waveguide [303]. Yang and Gung studied the influence of fluid conductivity on the propagation of acoustic waves in a piezoelectric plate immersed in a conducting fluid [304]. Evans and Cawley studied the generation of diffuse Lamb waves in uniform rectangular plates [305]. Guo, Mal, Ono, and Gorman studied the nature of Lamb waves generated by microfractures in composite plates [306]. Wilcox, Castaings, Monkhouse, Cawley, and Lowe discussed the use of interdigital PVDF transducers to generate and receive a high order Lamb wave mode in a pipe [307]. Yang, Caron, Mehl, and Steiner presented a system for laser generation and detection of Lamb waves in graphite/polymer composite laminates [308]. Rose, Barshinger, and Zaidi used ultrasonic guided waves for the inspection of titanium diffusion bonds [309].

Shin, Quarry, and Rose explored the use of non-axisymmetric ultrasonic guided waves for faster and simpler inspection and defect sizing analysis in tubes [310]. Lowe, Alleyne, and Cawley studied the mode conversion of guided waves by defects in pipes [311]. Alleyne, Cawley, Lank, and Mudge reported the first set of "blind trials" using Lamb waves to inspect an insulated chemical plant pipe for defects [312]. Rose, Jiao, and Spanner also presented their work on using ultrasonic guided waves for piping inspection [313]. El-Azab, Mal, Bar-Cohen, and Lih used plate wave dispersion data to measure the thickness and elastic properties of electroactive polymer films [314]. Kawashima, Fujii, Sato, and Okade measured the acoustoelastic coefficients of aluminum with leaky Rayleigh waves [315]. Li, Achenbach, and Cheng used a time-resolved line-focus acoustic microscopy technique to examine the reflection and transmission of leaky Rayleigh waves by a surface-breaking crack and to determine crack depth [316]. Wright, Hutchens, Jansen, and Schindel modified their earlier work on Lamb wave tomography by using air-coupled transducers instead of immersion or laser generation [317].

1998

In 1998 Mesquida, Otero, and Ramos analyzed wave propagation in layered piezoelectric structures [318]. Pierce, Culshaw, and Shan used a modulated continuous wave diode laser to generate ultrasonic Lamb waves in thin plates [319]. Darinskii extended his earlier work to show that leaky waves could also be generated in a crystal-thin solid layer by exceptional bulk waves [320]. Pecorari presented a model of Rayleigh wave dispersion due to a distribution of semi-elliptical surface-breaking cracks [321]. Wang and Zhang derived the dispersion equation of Love wave propagation in a transversely isotropic fluid-saturated porous layered half-space [322]. Zhang, Xiong, Yu, Lan, and Li investigated the energy distributions of guided waves in multilayered elastic solid media [323]. Bescond and Deschamps modeled the dynamical surface response of a semi-infinite anisotropic elastic medium to an impulsive point source or line source at any location on its free surface [324]. Moreno and Acevedo evaluated the feasibility of using Lamb waves for thickness measurement in composite materials [325]. Kundu, Maji, Ghosh, and Maslov used leaky Lamb waves for the detection of kissing bonds [326]. Rose, Zhu, and Zaidi demonstrated how Lamb waves can be used to evaluate the diffusion bonding states in diffusion bonded titanium plates [327].

2.2 Review of Tomography Literature

Tomography is the reconstruction of a two-dimensional cross section of a three-dimensional object in terms of some physical property of that object. This is accomplished by measuring values along a ray passing through the plane of the object, and relating those values to the physical property of interest. The majority of tomography research has been done in the medical and seismic fields. In the

medical field where it is possible to scan an object from all angles. speed is critical. while in seismology where only a limited number of views is possible. accuracy with limited data is critical. Therefore two groups of tomographic reconstruction algorithms. transform methods and series expansion methods. have been developed. Beyond this. other algorithms have been created to overcome the limitations of these two groups of methods. A review of the development and applications of these algorithms is presented below.

1917-1967

In 1917, Radon [328] developed the mathematics necessary to relate the values measured along a ray passing through a two-dimensional object to a physical property of that object. Although this work forms the basis for all of the tomographic techniques. it was overlooked for decades. and several other researchers later duplicated his work. The first tomography which involved reconstructing a two-dimensional map of some physical property of an object by measuring some parameter along several rays through the object. was done in the field of radio astronomy fifty years after Radon's paper [329].

1968-1973

With the advent of computers. it was possible to automate the required calculations. This not only minimized the error in the calculations. but the time required as well. and this made medical imaging of cross-sections of the human body practical. Most of the earliest codes to reconstruct tomographic images used the Radon transform to calculate the physical properties from the measured data; but in 1970. Gordon, Bender, and Herman proposed a new direct method. the Algebraic Reconstruction Technique (ART) [330]. This iterative technique was superior to the

transform method in that it could reconstruct completely asymmetric objects, little storage was required so small computers could be used, it was directly applicable to X-ray photography, and it required fewer rays to reconstruct so less radiation was necessary. However, in 1971 Ramachandran and Lakshminarayanan developed a new reconstruction technique using convolutions [331]. This convolution method was faster than both the transform method and the ART method, but it required the object to be rotated between a parallel beam of radiation. The authors also mentioned that three-dimensional images could be obtained by combining the two-dimensional radiographs or electron micrographs. However, the idea of using parallel radiation was new and the existing devices only used divergent beam radiation.

1974-1975

In 1974, three key papers were published in the IEEE Transactions on Nuclear Science. Gordon [332] published a tutorial on ART in which he discussed the original ART algorithm and some revisions that had been undertaken to try and improve convergence and speed. Budinger and Gullberg [333] examined several techniques for the reconstruction of 3-D isotope distributions in the head, heart or liver. And Shepp and Logan [334] generalized the convolution method of Ramachandran and Lakshminarayanan and studied its effectiveness in reconstructing a phantom section. Their work confirmed that the convolution method provided equivalent reconstructions in a shorter time, but the problem of the existing medical apparatus setup remained. In 1975 Lakshminarayanan [335] wrote a technical report in which he defined a convolution method to reconstruct images from divergent ray or fan beam data. Also in 1975, Tanaka and Iinuma [336] examined various correction functions for minimizing the numerical noise present in the images obtained using the convolution method.

1976-1978

In 1976, Herman and Lent [337] did a comparison of several iterative techniques and the convolution method. They found that the accuracy of the ART and convolution methods was comparable and that the Simultaneous Iterative Reconstruction Technique (SIRT) method was inferior. However, in cases of missing rays and different measuring models, the ART method was superior. Also in 1976, Dreike and Boyd, who were apparently unaware of Lakshminarayanan's technical report, published a paper in which they define a method for using the parallel beam convolution method with fan beam data [338]. In 1977, Peters and Lewitt [339] also published a method for using the parallel convolution method which they called filtered back projection, with fan beam data. Their method depended upon the high symmetry possible when scanning around a patient, and they claimed that it was better than the divergent ray convolution method because hardware implementation was impractical for the current data taking times. Herman and Naparstek [340] presented another method of reconstructing an image from divergent ray data which was as accurate as the parallel beam convolution method. This paper was important because the authors acknowledged that Radon's formula for projections [328] was the basis for the tomographic techniques, and they modified it for their own technique. Wang [341] also published a paper using the parallel convolution method with fan beam data. However, Wernecke and D'Addario [342] published a paper in which they used a maximum entropy factor to obtain reconstructions from noisy or limited data. This iterative method was slower than the direct methods, but was shown to be useful in radio astronomy applications.

1979

In 1979 Dines and Lytle [343] published the first paper using computerized tomography to reconstruct seismic data. Although others had used the Radon formula to obtain data from a single ray, Dines and Lytle were the first to create a two dimensional map of the properties of a cross section of earth between two boreholes. In their paper they examined the ART and SIRT methods and presented reconstructions using SIRT. Kenue and Greenleaf [344] published a paper in which they presented three methods of increasing the speed of convolution for the filtered back-projection or convolution method. These methods were: extending the convolution kernel into Fourier space, generating a binary approximation for the kernel, and doing recursive convolution.

1980-1982

In 1980 Lytle and Dines [345] published a second paper in which they took into account the ray bending effects that seismic and electromagnetic rays can experience when traveling in rock strata. They used an iterated sequence of numerical ray tracing and linear system inversion similar to that of their earlier paper. In 1981 Thompson and Peters [346] published an article describing some specialized hardware to improve the speed of back-projection. This paper showed how important speed was for medical applications. This was why the convolution methods implemented into hardware were chosen for the commercial computed tomography systems.

1983

In 1983 three important papers were published in the Proceedings of the IEEE. Censor [347] published a paper discussing all of the finite series-expansion techniques. Lewitt [348] published a paper discussing all of the transform methods of

reconstruction, and Bates, Garden, and Peters [349] published a paper discussing the future developments that the tomographic methods would be likely to undergo. Also in 1983, Wong, Hurley, and West [350] (who seem to have been unaware of the work by Dines and Lytle) published a paper using the simple Fourier back-projection technique to image crosshole data in crystalline rocks. However, McMechan [351] who was aware of the earlier seismic tomography papers, published his work on comparing the reconstructions of simulated seismic data using ART for crosshole, hole to surface, and combined configurations, where the combined geometry gave the best results. Ichida, Sato, and Linzer [352] published a paper in which they used the Fourier transform method to image the nonlinear ultrasonic parameter of a medium which describes the dependence of ultrasonic velocity on pressure. Munk and Wunsch [353] introduced modal tomography for obtaining reconstructions from regions in the ocean where ray theory is not valid, such as when several rays arrive together and are indistinguishable.

1984-1985

In 1984 Menke [354] published a paper in which he examined the effect of the number and spacing of transducers in the boreholes, while Devaney [355] presented a filtered backpropagation method using the Born or Rytov approximations for geophysical diffraction tomography. In 1985 Peterson, Paulsson, and McEvelly [356] examined various ART techniques applied to real crosshole seismic data and found that while all of the algorithms produced accurate reconstructions, those with weighting functions were slightly better. Ivansson [357] examined the effectiveness of several techniques to reconstruct synthetic seismic data. He confirmed that methods using many cells and some kind of damping gave the best results, and that taking into account ray bending could improve results. Hartz, Bristow, and Mullani [358] de-

veloped some hardware which they called a slice-backproject engine, to facilitate real-time time-of-flight positron emission tomography or TOFPET, while Llacer and Meng [359] showed that with better computers simple matrix inversion tomography for PET was becoming practical, and they suggested the possibility of parallel processing to compete with other methods.

1986

In 1986 Testardi, Norton, and Hsieh [360] proposed acoustic dimensional resonance tomography where they used resonance frequencies to map out one dimensional systems. This paper was noteworthy because the authors claimed the method could be used to nondestructively evaluate aluminum rods. Ivansson [361] compared the ART, SIRT, and convolution-gradient (CG) methods as applied to seismic borehole tomography. He found that CG converged faster than ART which converged faster than SIRT, but the CG method required much more computer storage space. Gustavsson, Ivansson, Moren, and Pihl [362] presented tomographic reconstructions using a fully in-the-field system that they had designed. Chang and McMechan [363] used an excitation-time imaging condition to image vertical seismic profiling (VSP) data. In this method, ray tracing was used to define the paths from the source to the receivers, then a finite-difference code was used to extrapolate the motion of the recorded wave field backward in time to the source. At each step in the finite-difference code, the amplitude values at all points in the mesh intersected by the wave front were recorded. When the finite-difference code finished, an amplitude map of the region had been generated. Jones, Georges, and Riley [364] extended the earlier work of Munk and Wunsch with modal tomography to account for asymmetric velocity profiles. Nakagawa, Hou, Cai, Arnold, Wade, Yoneyama, and Nakagawa [365] presented a new method of nonlinear parameter imaging using

second-harmonic waves.

1987

In 1987 Blackledge, Burge, Hopcraft, and Wombell [366] presented a method of quantitative diffraction tomography using the Born approximation for pulsed elastic waves. This method allowed the elastic parameters of a material to be reconstructed, and so could be applied to nondestructive evaluation. Scales [367] presented another comparison between CG and ART, and he also found that the CG method converged faster than the ART method. Bording, Gersztenkorn, Lines, Scales, and Treitel [368] presented reconstructions for both reflection and transmission seismic tomography. For the reflection case Iterative Migration Tomography (IMT), which uses Scales' CG algorithm combined with Kirchoff migration, was used, while the Singular Value Decomposition algorithm (SVD) was used for the synthetic transmission case. Chiu, Lynch, and Johannessen [369] used the direct matrix inversion technique to map out mesoscale eddies in the marginal ice zone. They found that resolution of different layers was poor unless additional information was provided by satellites or moored points. Um and Thurber [370] presented a new approximate algorithm for two-point seismic ray tracing which accurately calculated the ray paths in far less time than the 3-D ray tracing programs.

1988

In 1988 Pratt and Worthington [371] applied the diffraction tomography method of Devaney to the reconstruction of cross-hole seismic data. Dyer and Worthington [372] discussed two common sources of distortion in seismic tomographic images, namely inaccurate source and receiver locations and ray bending effects. The authors presented a method for iteratively improving the source/receiver locations and

showed that ray bending is not nearly as important as ray coverage. East, Worthington, and Gouly [373] showed that for crosshole seismic data, the convolution backprojection algorithm was faster and less susceptible to noise than the SIRT algorithm. Lo, Toksoz, Xu, and Wu [374] presented the results of an ultrasonic laboratory study in which they compared the filtered backpropagation algorithm to SIRT. They found that for cases where the scattered field could be obtained, the diffraction tomography gave the best result; however, SIRT did not place any restrictions on the properties of the object to be measured and only the first arrivals had to be measured. Lines and LaFehr [375] used ART to obtain a velocity profile for various models and then generated models using kinked-ray modeling and finite-difference acoustical modeling to check the accuracy. In all cases, the models were in agreement, but the authors noted that they were nonunique. The accuracy of the velocity model was improved by adding VSP or uphole data. Jones, Byars, and Casey [376] developed a VLSI architecture to perform multiple iterations per second for the expectation maximization (EM) algorithm for PET. Also Kak and Slaney [377] published a tutorial overview of tomography that has become the classic reference for later works.

1989-1990

In 1989 Lines and LaFehr [378] published a second paper, and Bregman, Bailey, and Chapman [379] showed that their two-dimensional iterative ray tracing and damped least-squares inversion algorithm could be successfully applied to crosshole seismic data. In 1990 Chen, Zimmerman, and Tugnait [380] compared surface seismic imaging, reverse vertical seismic profiling (RVSP), and SIRT and found that RVSP and SIRT were better than surface imaging and were capable of resolving complex structures. Pratt and Worthington [381] presented a new method

of imaging crosshole data that was similar to diffraction tomography except that the method of finite-differences was applied directly to the frequency-domain wave equation. In this paper the acoustic wave equation was used and it was shown that diffraction tomography was only better in cases where the weak-scatter approximation was valid. Pratt then presented similar work using the elastic wave equation both in a full paper [382] and a short note [383]. For these methods, as in diffraction tomography, it was necessary to use the full waveform instead of just first arrival times. Jansen and Hutchins [129] used the filtered back-projection technique to image flaws in aluminum plates using ultrasonic Lamb waves. The plates were submerged in an immersion tank, and amplitude variation and propagation delay were used to image attenuation and velocity. Chen, Lee, and Cho [384] published their work on a parallel implementation of the convolution backprojection method, and Barresi, Bollini, and Del Guerra [385] published their work on using parallel processing for direct 3-D image reconstruction in 3-D PET.

1991-1992

In 1991 Pratt and Goultly [386] presented images of simulated crosshole data obtained by combining ray tracing and SIRT with wave-equation imaging in the frequency-domain. Atkins, Murray, and Harrop [387] discussed the benefits of parallelizing their 3-D PET algorithm, and Chen, Lee, and Cho [388] published their work on parallelizing the EM algorithm for 3-D PET. Moser [389] presented another method of ray tracing which calculated the shortest path traveltime through a network that represented the earth. In 1992 Jansen and Hutchins [171] published their work using Rayleigh waves to reconstruct images of surface defects in thick metallic samples and using Lamb waves to image defects in thin metallic plates. They again immersed the samples in an ultrasound tank and used the filtered back-

projection method to reconstruct the images from traveltimes data. Snieder and Malcolm [390] presented the use of ray perturbation theory to calculate the traveltimes and ray paths in 3-D heterogeneous media. Huang, Xie, Salkeld, Plakowski, Thorn, Williams, Hunt, and Beck [391] used a transputer and non-intrusive capacitance sensor system for the process tomography of an oil/water flow in a 75 mm diameter pipe in real-time.

1993

In 1993 Hutchins, Jansen, and Edwards [177] published another paper using Lamb wave data to produce tomographic images. However, in this work they used a laser to generate the Lamb waves and EMATs for detection, and they measured peak amplitude, time-of-flight, integrated energy of the spectral peak, and centroid of the spectrum location. Rajan, Frisk, Doust, and Sellers [392] used the iterative ray tracing and linear system inversion technique of Lytle and Dines [345] to image speed profiles in sea ice. Pade and Mandelis [393] published a new computational thermal-wave diffraction tomography method and applied it to simulated data. Agi, Hurst, and Current [394] presented a VLSI digital signal processor that could be used with both transform and iterative methods applied to fan-beam or parallel-beam data. Vasco and Majer [395], Schuster and Quintus-Bosz [396], and Ammon and Vidale [397] all presented papers using wavepath eikonal tomography in which a finite-difference code was used to solve the elastic wave equation and backproject the wave front position with time. All of these authors seem to have been unaware of the earlier work by Pratt using the elastic wave equation. Farra [398] published a review of ray tracing methods in complex three-dimensional media. Asakawa and Kawanaka [399] presented a new ray tracing method called linear traveltimes interpolation which was shown to be faster and more accurate than the finite difference methods, and

Fischer and Lees [400] presented a technique for improving the efficiency of shortest path ray tracing. Goncharov and Voronovich [401] studied modal tomography, and Jones, Shang, and Georges [402] extended the nonperturbative modal tomography of Munk and Wunsch to a range-dependent environment. Isaksen and Nordtvedt [403] presented a new reconstruction algorithm for the process tomography of oil/gas pipe flows and compared their results to those obtained using the linear back projection algorithm.

1994

In 1994 Ratcliff and Weber [404] presented a new method for producing seismic images of subsurface salt regions called 3D prestack depth migration or PSDM. For this method the authors first used time migration techniques to develop an accurate velocity model which was then improved by their depth migration technique. PSDM provided much more accurate images, but it required large amounts of data and computational time. Zhang and Gong [405] published their work on computer simulation of acoustic nonlinear parameter tomography in which they used the filtered back-projection algorithm with various filters. Zhu and Chun [406] published their work on ray tracing in elastic and anelastic inhomogeneous media using complex rays. Jansen, Hutchins, and Mottram [204] extended their earlier work on Lamb wave tomography to composite plates. French [407] discussed the improvements that massively parallel processing computers were providing for in-the-field seismic imaging. Jones and Georges [408] applied their nonperturbative ray tomography method to simulated data from a range independent model, and Jones, Howe, Mercer, Spindel, and Georges [409] applied it to actual experimental data. Wang and Kline [410] developed an iterative ray tracing technique for isotropic and anisotropic materials based on Fermat's principle and implemented it with a

traditional ART algorithm. Degertekin, Pei, Khuri-Yakub, and Saraswat [206] performed in situ acoustic temperature tomography of semiconductor wafers by using measurements of Lamb wave time-of-flight to measure the temperature of the wafer along specific ray paths and then reconstructed the temperature distribution of the wafer using the simple linear equation solving approach.

1995

In 1995 Shang, Wang, Jones, and Georges [411] applied their nonperturbative modal tomography technique to numerically simulated range-independent and range-dependent cases. Nagata, Huang, Achenbach, and Krishnaswamy [215] used the filtered back-projection algorithm to produce tomographic images from Lamb wave attenuation data. A laser was used for generation and a dual point interferometer was used to measure the attenuation. Jalinoos, Olson, Aouad, and Balch [412] nondestructively evaluated concrete for flaws by applying the CG and SIRT algorithms with curved rays to acoustic travelttime data. Zhang and Gong [413] extended their earlier examination of filter influence on nonlinearity parameter imaging by considering four filters in the filtered convolution method. Jalinoos, Olson, and Aouad [414] published their same work in another conference proceedings. Daily and Ramirez [415] discussed the potential of seismic tomography and electrical resistance tomography for environmental process tomography. Green, Horbury, Rahim, Dickins, Naylor, and Pridmore [416] used optical fibre sensors for the process tomography of low concentrations of conveyed particles in a flow. Hoyle [417] studied the limitations of ultrasonic process tomography applied to dynamic flowing mixture processes.

1996

In 1996 Jalinoos and Olson [418] extended their previous work of examining concrete members with two-sided access to examining large concrete sections between PVC access pipes in dams and bridges. In this work which was simply crosshole tomography applied to dams and bridges, they used the SIRT algorithm. Sullivan, Kline, Mignogna, and Delsanto [419] modified the iterative ray tracing and linear system inversion algorithm of Lytle and Dines [345] to be used on a massively parallel architecture. Zhang, Gong, and Ye [420] applied their acoustic nonlinearity parameter tomography to experimental data from real biological samples. Ingesson and Pickalov [421] presented an iterative projection space reconstruction algorithm for systems with irregular coverage. Their algorithm involved iterating between projection space and real space and applying *a priori* information and smoothing. Beck and Williams [422] reviewed the recent developments in the design and application of tomographic sensors for measurements in industrial processes. Hoyle [423] reviewed ultrasound and ultrasonic transducers and discussed their potential for process tomography applications. Zhu, Duvauchelle, Pelx, and Babot [424] used X-ray Compton backscattering techniques for the nondestructive evaluation of materials with applications to process tomography. Dyakowski [425] described the application of existing tomographic techniques to the process tomography of multi-phase flows. Gibbs and Hall [426] showed that magnetic resonance imaging could be used in process tomography to perform fundamental studies of transport phenomena in heterogeneous, multiphase systems. Schlberg and Hoyle [427] described the development of an ultrasonic reflection tomography system for the real-time imaging of two-component flows. Pei, Yousuf, Degertekin, Honein, and Khuri-Yakub [248] used a Hertzian contact to generate Lamb waves in pipes and plates without couplant, and they presented a filtered back-projection tomographic image of an aluminum plate with a depression milled into it.

1997

In 1997 Dickens and Winbow [428] examined the resolution capability for the filtered back-propagation diffraction tomography algorithm with various source/receiver and target geometries. Wright, Hutchens, Jansen, and Schindel [317] modified their earlier work on Lamb wave tomography by using air-coupled transducers instead of immersion or laser generation. Xu and Xu [429] used a filtered backprojection algorithm to image fan-beam and parallel-beam data from a bubbly gas/liquid two phase flow. Subbarao, Munshi, and Muralidhar [430] compared three additive ART, three multiplicative ART, SIRT, Maximum Entropy, and Minimum Energy algorithms on phantom data and found that the MART3 algorithm worked best on perfect projection data. They then proceeded to look at the effect of noisy data on the MART3 reconstructions. Interestingly, they cited Censor's 1983 paper [347] but appear to have ignored his comment on MART. He stated that the behavior of the MART algorithms in realistic situations where the equations are inconsistent is not well understood while the behavior of the ART algorithm is. Since Subbarao, Munshi, and Muralidhar only compared the algorithms using perfect simulated data, their conclusion that MART is better than ART is not necessarily true in realistic situations. Mensah and Lefebvre [431] presented the results of their enhanced compressibility tomography on biological phantoms in which they used ultrasonic diffraction tomography and reconstructed their quantitative images in terms of compressibility. Ko and Meyyappan [432] showed that for a computer simulated solid specimen, shear-wave scanning tomographic acoustic microscopy (STAM) had better resolution than longitudinal wave STAM. In their work they measured the shear wave energy and longitudinal wave energy at various insonification angles and used the back-and-forth propagation algorithm to reconstruct

the images. Wells, Smith, and Suparta [433] showed how the bow-tie or hexagonal sampling pattern of Rattey and Lindgren provides a more efficient means of data taking for Convolution-Backprojection tomography than the standard square sampling. However, this technique required a more elaborate apparatus and control software. Vengrinovich, Denkevich, Tillack and Nockemann [434] presented a multi step reconstruction method for 3D X-ray tomography with a limited number of projections and views. Greenawald, Levenberry, Poranski, Everett, Simmonds, Batra, and Hu [435] showed that x-ray backscatter tomography can be used to monitor porosity distribution in gasar-processed metal plates. Reibold and Kwiek [436] estimated the uncertainty of ultrasonic field maps produced using light diffraction tomography.

Schlaberg, Yang, Hoyle, Beck, and Lenn [437] described the design of wide-angle transducers for a real-time ultrasonic process tomography system that produces reflection mode tomographs of objects in a liquid. Hebbler, Oldenburg, Farnocombe, and Celler [438] presented a means for estimating the dynamic parameters of Single Photon Emission Computerized Tomography (SPECT) reconstruction directly from the projections. Beyer, Kinahan, and Townsend [439] investigated the optimization of transmission and emission scan duration in 3D whole body PET. Yuasa, Akiba, Takeda, Kazama, Hoshino, Watanabe, Hyodo, and Dilmajian [440] described a new system of incoherent scatter computed tomography using monochromatic synchrotron X rays and discussed its potential to be used in in vivo medical imaging. Schiepers, Nuyts, Wu, and Verma [441] showed that the maximum likelihood expectation maximization (MLEM) iterative reconstruction method provided images of superior quality to the filtered back projection method at the expense of ten times the reconstruction duration when applied to PET data. Kinahan, Fessler, and Karp [442] presented improved PET images by combining

volume imaging with the penalized weighted least squares statistical reconstruction method. Hawkins [443] used Fourier transform resampling of a nonstandard experimental geometry to obtain a data set in a standard geometry. Celler, Sitek, and Harrop [444] demonstrated that a series of collimated line sources parallel to the axis of rotation of the detector camera can be used in SPECT to generate sufficient data for the reconstruction of the attenuation map. Pan and Metz [445] studied the noise characteristics of non-iterative methods in 2D SPECT image reconstruction. Khosla and Singh [446] showed that the maximum-entropy method could be used for Magnetoencephalographic source imaging.

Heanue, Brown, Tang, and Hasegawa [447] showed that the effect of radionuclide scatter in emission-transmission CT is small compared to the effect of attenuation and collimator blur, but scatter correction is still preferable to scatter rejection. Noo, Clack, and Defrise [448] examined the effectiveness of three Radon rebinning algorithms for cone-beam reconstruction from general discrete vertex sets. Johnson, Seidel, Carson, Gandler, Sofer, Green, and Daube-Witherspoon [449] evaluated the effect of six reconstruction algorithms on the image quality of a small animal PET camera, and determined that 3D expectation maximization (EM) and 3D ordered subset expectation maximization (OSEM) gave the best results. Chen, Miyanga, Yamanaka, Nakai, Yamanaka, and Nakai [450] used an X-ray emission computed tomography technique to produce three-dimensional images of laser-imploded targets. Nagarkar, Gordon, Gupta, Vasile, Gothoskar, Squillante, and Entine [451] demonstrated the benefits of a CCD-based high resolution digital radiography system over the standard polycrystalline phosphor system for nondestructive evaluation applications. Glick, and Xia [452] presented a reconstruction approach which first processes the projection data to compensate for photon attenuation and the limited nonstationary spatial resolution of the detector and then performs filtered backpro-

jection to obtain better SPECT reconstructions. Zeng, Weng, and Gullberg [453] showed a MLEM iterative technique for SPECT reconstruction from cone-beam projections acquired via nonplanar orbits. Yuasa, Akiba, Takeda, Kazama, Hoshino, Watanabe, Hyodo, Dimanian, Akatsuka, and Itai [454] described an attenuation correction method for fluorescent X-ray computed tomography using a least-squares method with singular value decomposition. Maguire, Missimer, Emert, Townsend, Dollinger, and Leenders [455] used a multiring PET instrument to perform PET on large rock samples in order to measure relative changes in porosity. Li and Hoyle [456] showed that the real-time performance of ultrasonic process tomography could be maximized by using multiple active sensors and a spectral analysis strategy.

1998

In 1998 Rust and Weigelt [457] used the ART and MLEM algorithms with X-ray fluorescent computer tomography to quantitatively calculate the distribution of a nonradioactive element within a cross section of a specimen.

2.3 Discussion

From the Lamb wave literature, it can be seen that guided waves offer a rapid and quite sensitive means for examining interfaces, rods, pipes, wires, surfaces, and multilayer or solid plates. Specifically, Lamb waves can be used to rapidly inspect or characterize plate-like materials. Since the skin of an aircraft is made of plate-like materials, Lamb wave scanning offers a rapid, nondestructive means for the evaluation of flaws in the aircraft structure. However, in order to interpret the complicated Lamb wave signals, a highly trained individual is necessary. Therefore, we have

combined Lamb wave contact scanning with tomography to produce an instrument capable of in-the-field inspection of aircraft, which produces an image that can easily be interpreted by a technician. In contrast to the other researchers who have performed Lamb wave tomography using the parallel projection techniques commonly used in earlier medical applications [129], [171], [177], [206], [204], [215], [317], we have performed a review of tomography literature to determine the tomographic technique best suited for our application.

Based upon this literature, the algebraic reconstruction technique (ART) has been chosen as the most appropriate algorithm to be applied to Lamb wave tomography. ART is superior to the transform, convolution, CG, and diffraction methods because it places no restrictions upon the objects to be reconstructed or upon the scanning geometry, it requires less computer storage space, and it can produce accurate reconstructions with fewer or missing rays. The ART algorithm also converges faster than other iterative techniques such as SIRT. The limitations of ART are its assumptions of straight rays and of a linear relationship between the difference in calculated and measured traveltimes and the required change in physical properties. We will address these problems later in the dissertation.

Chapter 3

Theory and Experimental Results

In this chapter background theory and experimental results are presented. Ultrasonic Lamb wave contact scanning is first discussed, as are novel implementations for tomographic imaging with Lamb waves in Parallel Projection and Cross Borehole configurations. For both techniques, the experimental geometry and apparatus are presented. The tomographic reconstruction algorithms used for each method of tomography are discussed, and a comparison is made between the results of these two methods. Finally, the limitations of these tomographic methods are shown.

3.1 Lamb Wave Scanning

In order to perform quantitative tomographic reconstruction with Lamb waves, it is necessary to develop a theoretical framework which accurately describes the dynamical behavior of an elastic plate.

Consider [458] the conservation of mass,

$$\frac{\partial \rho}{\partial t} + \frac{\partial(\rho v_i)}{\partial x_i} = 0. \quad (3.1)$$

the conservation of momentum.

$$\frac{\partial \sigma_{ij}}{\partial x_j} + X_i = \rho \alpha_i. \quad (3.2)$$

and the stress-strain relation for a homogeneous, elastic solid.

$$\sigma_{ij} = C_{ijkl} e_{kl}. \quad (3.3)$$

In these equations, $u_i(x_1, x_2, x_3, t)$ is the displacement of a particle located at x_1, x_2, x_3 at time t from its position in the zero stress state, the particle velocity is given by the material derivative of the particle displacement,

$$v_i = \frac{\partial u_i}{\partial t} + v_j \frac{\partial u_i}{\partial x_j}. \quad (3.4)$$

the particle acceleration is given by the material derivative of the particle velocity,

$$\alpha_i = \frac{\partial v_i}{\partial t} + v_j \frac{\partial v_i}{\partial x_j}. \quad (3.5)$$

and e_{ij} is the strain tensor given by

$$e_{ij} = \frac{1}{2} \left[\frac{\partial u_j}{\partial x_i} + \frac{\partial u_i}{\partial x_j} + \frac{\partial u_k}{\partial x_i} \frac{\partial u_k}{\partial x_j} \right]. \quad (3.6)$$

Here σ_{ij} is the stress tensor, C_{ijkl} is a tensor of elastic constants which are independent of stress or strain, ρ is the mass density of the material per unit volume, X_i is the body force per unit volume, and the indices range over 1,2,3. If we assume that the particle displacements and velocities are infinitesimal, then the nonlinear terms in Equations 3.4 - 3.6 can be neglected [458] and we have for a linear, homogeneous, elastic solid,

$$v_i = \frac{\partial u_i}{\partial t} \quad \alpha_i = \frac{\partial v_i}{\partial t} \quad e_{ij} = \frac{1}{2} \left(\frac{\partial u_i}{\partial x_j} + \frac{\partial u_j}{\partial x_i} \right). \quad (3.7)$$

Finally if we assume that the solid is isotropic in addition to being linear, homogeneous, and elastic, then there are only two independent elastic constants, λ and μ .

which are called the Lamé parameters. These assumptions allow us a sufficiently accurate description of the Lamb wave ultrasonic measurements in this work. Now the stress-strain relation for a linearly elastic, homogeneous, isotropic solid can be written as

$$\sigma_{ij} = \lambda \epsilon_{\alpha\alpha} \delta_{ij} + 2\mu \epsilon_{ij} \quad (3.8)$$

where

$$\delta_{ij} = \begin{cases} 1 & \text{if } i = j \\ 0 & \text{if } i \neq j \end{cases}. \quad (3.9)$$

and $\alpha = 1, 2, 3$ [458].

Plugging the linearized expression for strain into Equation 3.8 we have [459].

$$\sigma_{ij} = \lambda \frac{\partial u_\alpha}{\partial x_\alpha} \delta_{ij} + \mu \left(\frac{\partial u_i}{\partial x_j} + \frac{\partial u_j}{\partial x_i} \right). \quad (3.10)$$

and substituting this into Equation 3.2, we have

$$\frac{\partial}{\partial x_j} \left(\lambda \frac{\partial u_\alpha}{\partial x_\alpha} \delta_{ij} + \mu \left(\frac{\partial u_i}{\partial x_j} + \frac{\partial u_j}{\partial x_i} \right) \right) + X_i = \rho \alpha_i. \quad (3.11)$$

Simplifying this and noting that $\frac{\partial u_\alpha}{\partial x_\alpha} = \frac{\partial u_j}{\partial x_j}$, we have

$$\mu \frac{\partial^2 u_i}{\partial x_j^2} + (\lambda + \mu) \frac{\partial^2 u_j}{\partial x_i \partial x_j} + X_i = \rho \frac{\partial^2 u_i}{\partial t^2}. \quad (3.12)$$

which is Navier's equation in index notation for the motion of a linearly elastic, homogeneous, isotropic solid [458] [459]. Since there are no body forces that affect the Lamb waves we set $X_i = 0$, and we can rewrite Navier's equation in vector notation as

$$\mu \nabla^2 \vec{u} + (\lambda + \mu) \nabla \nabla \cdot \vec{u} = \rho \frac{\partial^2 \vec{u}}{\partial t^2} \quad (3.13)$$

since

$$u_i \rightarrow \vec{u} \quad \frac{\partial u_i}{\partial x_j} \rightarrow \nabla \vec{u} \quad \frac{\partial u_j}{\partial x_j} \rightarrow \nabla \cdot \vec{u} \quad \nabla \cdot \nabla = \nabla^2. \quad (3.14)$$

According to Helmholtz's theorem, the displacement vector, $\vec{u} = (u_1, u_2, u_3)$, can be written in terms of two potentials as $\vec{u} = \nabla\phi + \nabla \times \vec{\psi}$. For Lamb waves we need only consider plane strain motion in the (x_1, x_2) -plane, and we have $u_3 = 0$ with no dependence on x_3 for the other displacement components. So the potentials ϕ and ψ satisfy the following scalar wave equations.

$$(\nabla^2 + \omega^2/c_L^2)\phi = 0 \quad (\nabla^2 + \omega^2/c_T^2)\psi = 0 \quad (3.15)$$

where $\nabla^2 = \frac{\partial^2}{\partial x_1^2} + \frac{\partial^2}{\partial x_2^2}$ and $c_L = \left(\frac{\lambda+2\mu}{\rho}\right)^{\frac{1}{2}}$, $c_T = \left(\frac{\mu}{\rho}\right)^{\frac{1}{2}}$ are the longitudinal and transverse bulk wave speeds respectively. For the material discussed in this work (aluminum), $c_L = 6568$ m/s and $c_T = 3149$ m/s. The nonzero displacement components are given by

$$u_1 = \frac{\partial\phi}{\partial x_1} + \frac{\partial\psi}{\partial x_2} \quad u_2 = \frac{\partial\phi}{\partial x_2} - \frac{\partial\psi}{\partial x_1} \quad (3.16)$$

where $\psi = \hat{x}_3 \cdot \vec{\psi}$, and the relevant components of the stress tensor are then

$$\sigma_{12} = \mu \left(2 \frac{\partial^2\phi}{\partial x_1\partial x_2} - \frac{\partial^2\psi}{\partial x_1^2} + \frac{\partial^2\psi}{\partial x_2^2} \right)$$

$$\sigma_{22} = \lambda \left(\frac{\partial^2\phi}{\partial x_1^2} + \frac{\partial^2\phi}{\partial x_2^2} \right) + 2\mu \left(\frac{\partial^2\phi}{\partial x_2^2} - \frac{\partial^2\psi}{\partial x_1\partial x_2} \right). \quad (3.17)$$

To investigate Lamb wave motion in an elastic layer (Figure 3.1) we consider solutions of the form

$$\phi = \Phi(x_2)e^{i(kx_1 - \omega t)} \quad \psi = \Psi(x_2)e^{i(kx_1 - \omega t)} \quad (3.18)$$

which give

$$\Phi(x_2) = A_1 \sin(px_2) + A_2 \cos(px_2)$$

$$\Psi(x_2) = A_1 \sin(qx_2) + A_2 \cos(qx_2) \quad (3.19)$$

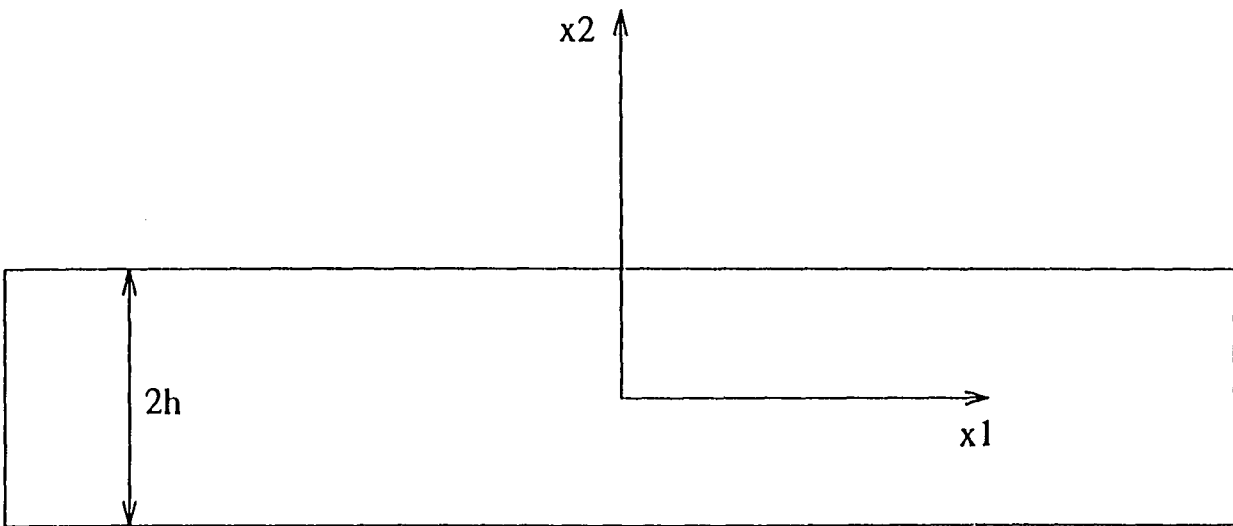


Figure 3.1: Coordinate system for Lamb wave propagation in an elastic layer. The plate is of thickness $2h$, with the top and bottom of the plate given by $x_2 = \pm h$. Since the plate is infinite in extent, propagation in the x_1 direction can be assumed without loss of generality.

where

$$p^2 = \omega^2/c_L^2 - k^2 \qquad q^2 = \omega^2/c_T^2 - k^2. \quad (3.20)$$

We can suppress the $e^{i(kx_1 - \omega t)}$ factor since it is a multiplier in all terms. Displacements and stresses are then given by

$$u_1 = ik\Phi + \frac{d\Psi}{dx_2} \qquad u_2 = \frac{d\Phi}{dx_2} - ik\Psi \quad (3.21)$$

and

$$\begin{aligned} \sigma_{12} &= \mu \left(2ik \frac{d\Psi}{dx_2} + k^2\Psi + \frac{d^2\Psi}{dx_2^2} \right) \\ \sigma_{22} &= \lambda \left(\frac{d\Phi}{dx_2} - k^2\Phi \right) + 2\mu \left(\frac{d^2\Psi}{dx_2^2} - ik \frac{d\Psi}{dx_2} \right). \end{aligned} \quad (3.22)$$

Note from Figure 3.2 that for the displacement in the x_1 -direction the motion is symmetric (asymmetric) with regard to $x_2 = 0$ if u_1 contains cosines (sines), while the displacement in the x_2 -direction is symmetric (asymmetric) if u_2 contains sines (cosines).

Thus we can separate symmetric:

$$\Phi = A_2 \cos(px_2) \qquad \Psi = B_1 \sin(qx_2)$$

$$u_1 = ikA_2 \cos(px_2) + qB_1 \cos(qx_2)$$

$$u_2 = -pA_2 \sin(px_2) - ikB_1 \sin(qx_2)$$

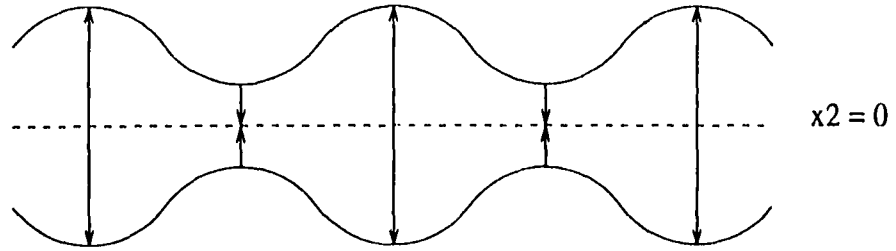
$$\sigma_{12} = \mu \left[-2ikpA_2 \sin(px_2) + (k^2 - q^2)B_1 \sin(qx_2) \right]$$

$$\sigma_{22} = -\lambda(k^2 + p^2)A_2 \cos(px_2) - 2\mu \left[p^2 A_2 \cos(px_2) + ikqB_1 \cos(qx_2) \right] \quad (3.23)$$

and asymmetric modes:

$$\Phi = A_1 \sin(px_2) \qquad \Psi = B_2 \cos(qx_2)$$

Symmetric Motion



Asymmetric Motion

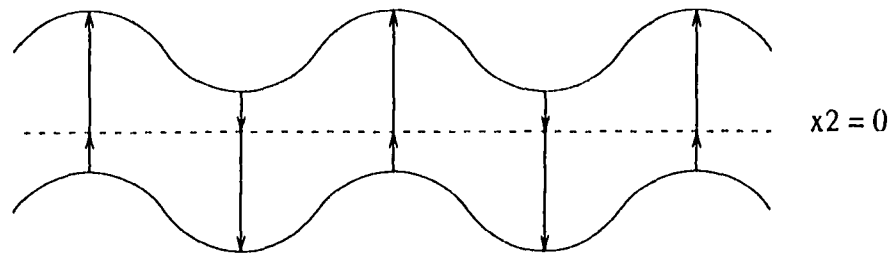


Figure 3.2: Symmetric and Asymmetric motion of a plate for S_0 and A_0 Lamb wave propagation respectively.

$$\begin{aligned}
u_1 &= ikA_1 \sin(px_2) - qB_2 \sin(qx_2) \\
u_2 &= -pA_1 \cos(px_2) - ikB_2 \cos(qx_2) \\
\sigma_{12} &= \mu [2ikpA_1 \cos(px_2) + (k^2 - q^2)B_2 \cos(qx_2)] \\
\sigma_{22} &= -\lambda(k^2 + p^2)A_1 \sin(px_2) - 2\mu [p^2 A_1 \sin(px_2) + ikqB_2 \sin(qx_2)].
\end{aligned} \tag{3.24}$$

If the boundaries are free at $x_2 = \pm h$ then the stress components, σ_{12} and σ_{22} , vanish there. In matrix form with $x_2 = h$, we have for the symmetric case,

$$\begin{pmatrix} -2\mu ikp \sin(ph) & \mu(k^2 - q^2) \sin(qh) \\ -(\lambda k^2 + (\lambda + 2\mu)p^2) \cos(ph) & -2\mu ikq \cos(qh) \end{pmatrix} \begin{pmatrix} A_2 \\ B_1 \end{pmatrix} = \begin{pmatrix} 0 \\ 0 \end{pmatrix}. \tag{3.25}$$

and for the asymmetric case

$$\begin{pmatrix} 2\mu ikp \cos(ph) & \mu(k^2 - q^2) \cos(qh) \\ -(\lambda k^2 + (\lambda + 2\mu)p^2) \sin(ph) & -2\mu ikq \sin(qh) \end{pmatrix} \begin{pmatrix} A_1 \\ B_2 \end{pmatrix} = \begin{pmatrix} 0 \\ 0 \end{pmatrix}. \tag{3.26}$$

For each case, the homogeneous system of boundary conditions has non-trivial solutions when the determinant of the coefficient matrix vanishes, or when

$$\begin{vmatrix} -2\mu ikp \sin(ph) & \mu(k^2 - q^2) \sin(qh) \\ -(\lambda k^2 + (\lambda + 2\mu)p^2) \cos(ph) & -2\mu ikq \cos(qh) \end{vmatrix} = 0 \tag{3.27}$$

for the symmetric case, and

$$\begin{vmatrix} 2\mu ikp \cos(ph) & \mu(k^2 - q^2) \cos(qh) \\ -(\lambda k^2 + (\lambda + 2\mu)p^2) \sin(ph) & -2\mu ikq \sin(qh) \end{vmatrix} = 0 \tag{3.28}$$

for the asymmetric case. These equations give us the dispersion relations for the Lamb waves. For the symmetric modes we get the dispersion relation

$$\frac{\tan(qh)}{\tan(ph)} = -\frac{4k^2 pq}{(q^2 - k^2)^2} \tag{3.29}$$

and for the asymmetric modes we get

$$\frac{\tan(qh)}{\tan(ph)} = -\frac{(q^2 - k^2)^2}{4k^2 pq}. \quad (3.30)$$

These transcendental equations have an infinite number of solutions each corresponding to a particular Lamb wave mode. The symmetric and asymmetric modes are numbered independently and according to increasing cutoff frequency. So we have S_0, S_1, S_2, \dots for the symmetric modes and A_0, A_1, A_2, \dots for the asymmetric modes. Figure 3.3 shows the dispersion curves for the four lowest modes (A_0, S_0, A_1, S_1) in an aluminum plate plotted as phase velocity in $\text{mm}/\mu\text{s}$ versus frequency-thickness in $\text{MHZ}\cdot\text{mm}$. For the frequency-thickness range shown, all modes higher than S_1 are cut off, and this is why only the first four modes are visible. Notice that for low frequency-thicknesses, only the S_0 and A_0 modes exist, and they have quite distinct phase velocities. This is in contrast to the case of higher frequency-thicknesses where there are many modes which approach the same phase velocity value of $3.149 \text{ mm}/\mu\text{s}$, which is the bulk shear wave velocity in aluminum.

Specific Lamb wave modes are more sensitive to certain types of flaws, and techniques using oblique insonification in an ultrasound tank or angle block transducers have been developed for the excitation of specific modes. While these techniques work well in a laboratory environment where extreme care can be taken in maintaining the correct angle of insonification for a specific mode, they are not practical for automated scans of aircraft in-the-field. The first requires pieces of the aircraft to be placed in a tank, and the second requires the angle to be precisely maintained during the automated scan. In addition, if the material is not flat, then the angle will have to be carefully altered as the scan progresses. Again while this is possible in a laboratory, it is impractical to implement for in-the-field scanning.

Another problem with generating Lamb waves is the coupling between the

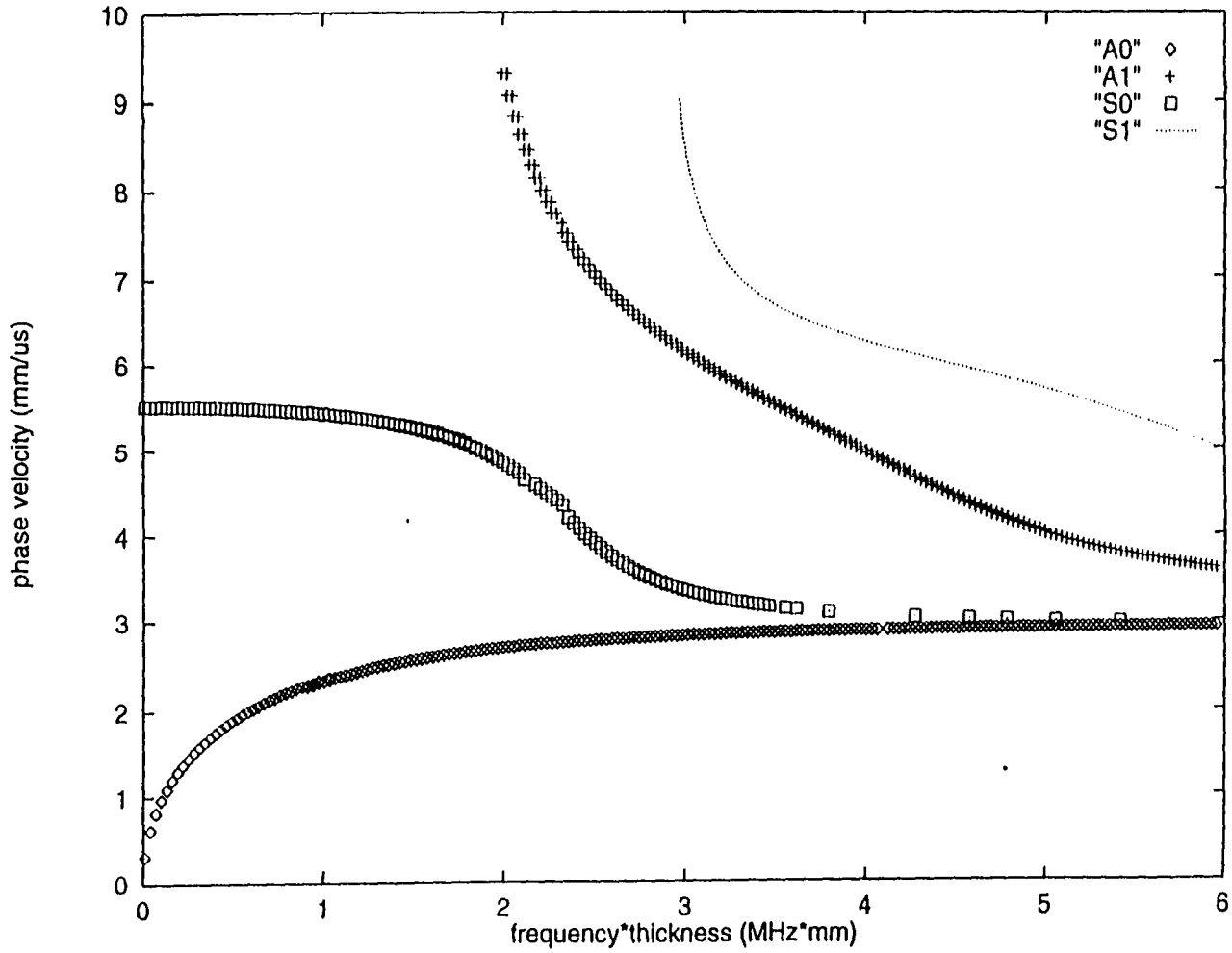


Figure 3.3: Dispersion curves of the A0, S0, A1, and S1 Lamb wave modes in aluminum. For lower fd values, only the S0 and A0 modes propagate appreciably, and the S0 mode is significantly faster than the A0 mode. For higher fd values, the modes all approach the phase velocity value of $3.149 \frac{mm}{us}$ which is the bulk shear velocity.

transducer and the test medium, since at MHz frequencies, the sound wave cannot propagate across the small air gap between the sample and the contact transducers. Experiments performed in a tank avoid this problem because the entire sample and transducer are immersed in water through which MHz frequency sound waves can propagate. However, as was stated above, tank experiments are not practical for in-the-field experiments. For contact transducers, there must always be a layer of water between the transducer and the sample to ensure good coupling of the sound waves into the medium. One way to do this involves using 'squirters' which are special transducers that have a water source attachment. Water continually flows into the region between the transducer and the sample to provide coupling. However, while this works well, it requires that a water source and delivery system be included with the scanning system. This adds expense and complexity to the scanner. In addition, experiments performed in the field will not always be performed on flat samples. Aircraft have curved sides, and so experiments will be performed where the transducers are almost upside down. This can make it difficult for the squirters to provide equal coupling at all orientations.

In this work normal incidence shear or longitudinal contact transducers are used. The transducers are spring loaded to the sample, and water is applied at the start of a scan. Since the transducers are spring loaded, they hold the water in position and carry it with them at each step in the scan. To generate the Lamb waves, the contact transducers are excited by a toneburst, and the Lamb wave modes are then allowed to develop as the ultrasonic energy propagates. Here toneburst refers to a Gaussian envelope containing a specified number of cycles at a specified frequency. The toneburst has a repetition rate such that the echoes from a previous toneburst die down before the next toneburst is generated. For this generation technique, the number of Lamb wave modes produced is only limited by

the frequency chosen for generation. This is in contrast to the oblique incidence methods which only generate a single mode. In order to minimize the number of modes produced and so the complexity of the received signal, the frequency is chosen so that the frequency-thickness corresponds to the region where only the S_0 and A_0 modes propagate appreciably. From Figure 3.3, it can be seen that this range corresponds to $fd < 2.6$ MHz-mm for aluminum. The A_1 mode does not propagate appreciably because the attenuation of any mode near its cutoff point is very large. Since the phase velocity of the S_0 mode is faster than that of the A_0 mode in this range in a pitch-catch setup, the S_0 mode will arrive first and will be distinct from the A_0 mode in the received waveform. Figures 3.4 and 3.5 show two sample waveforms obtained from an aluminum plate of thickness 2.42 mm, using two contact transducers in a pitch-catch arrangement excited by a three-cycle toneburst with a repetition rate given by

$$\text{Generation Frequency}/6300. \quad (3.31)$$

In the first waveform, which was obtained at a lower frequency ($fd = 1.51$ MHz-mm), the S_0 and A_0 modes are clearly distinguishable. In the second waveform where the frequency has been increased ($fd = 2.42$ MHz-mm), the S_0 mode is still the first arrival, but the A_0 mode is mixed in with noise and reflections from the plate edge.

The frequency level generating the first waveform works well when changes in amplitude of the S_0 and A_0 modes are used for flaw detection. However, even though amplitude measurements are often more sensitive to the presence of flaws, the received signals tend to be strongly affected by the variations in coupling inherent in automated scanning. Therefore, time-of-flight measurements are used here because the aim of this work is to develop automated scanning methods that

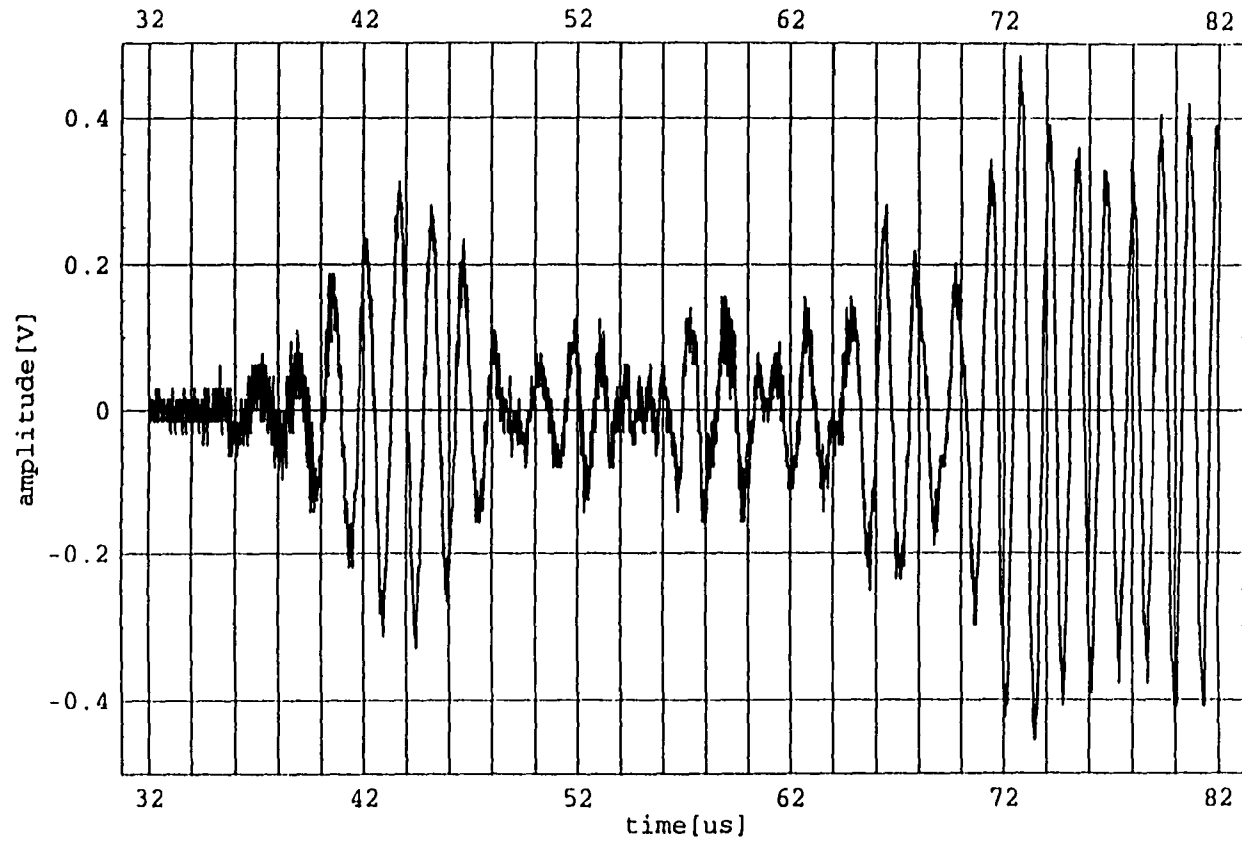


Figure 3.4: Typical Lamb wave waveform obtained at a fd value of 1.51 MHz-mm. Note that the S_0 and A_0 modes are both distinguishable in this waveform with the S_0 mode as the first arrival.

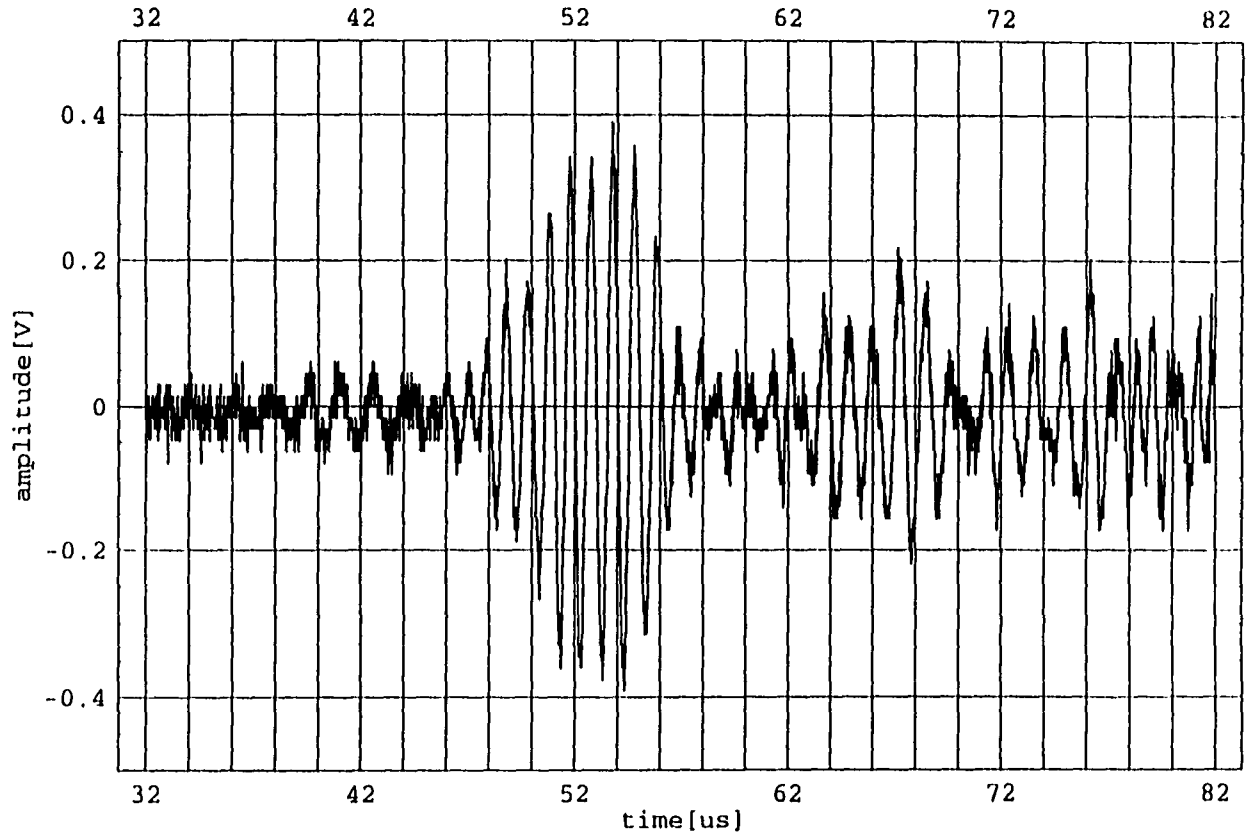


Figure 3.5: Typical Lamb wave waveform obtained at a fd value of 2.42 MHz-mm. Note that the S_0 mode is still distinguishable as the first arrival, but the A_0 mode is mixed into the complicated signal.

don't require an expert operator and that minimize human intervention as much as possible.

In order to detect flaws by changes in time-of-flight, the frequency-thickness must be chosen so that the measurements are performed where the dispersion curves have a high enough slope. Then a small change in thickness will cause a large enough change in the velocity and the time-of-flight can be detected with the available electronics. In Figure 3.6 the frequency-thickness range has been chosen so that only the region where the S_0 and A_0 modes propagate appreciably is shown. From this figure, the regions of high slope for the A_0 and S_0 modes are $(fd < 0.8)$ MHz-mm and $(2.0 \text{ MHz-mm} \leq fd \leq 2.6 \text{ MHz-mm})$ respectively. It is convenient to monitor the S_0 mode because no matter how complicated the waveform gets, it is always at the front of the waveform. The waveform shown in Figure 3.5 was obtained in the region of high slope for the S_0 mode. As was stated above, the A_0 mode is mixed into the complicated signal, but the S_0 mode is easily detectable as the first arrival.

For the measurements, a pair of normal incidence shear contact transducers in pitch-catch arrangement is automatically scanned in the direction perpendicular to the Lamb wave propagation. At each location of the transducer pair, the phase shift of the S_0 mode is acquired through pulse-phase-lock-loop (P2L2) circuitry [460]. This instrument compares the phase of its pulsed output signal, which is sent to the transmitting transducer, with that of the amplified and low-pass filtered returned signal from the receiving transducer. A frequency counter is connected to the output of the P2L2, which gives information on the phase difference of the two signals in terms of frequency. The value of this reference frequency can be used to calculate both the time of flight and, because the distance between the two transducers is fixed, the integrated velocity of the Lamb waves.

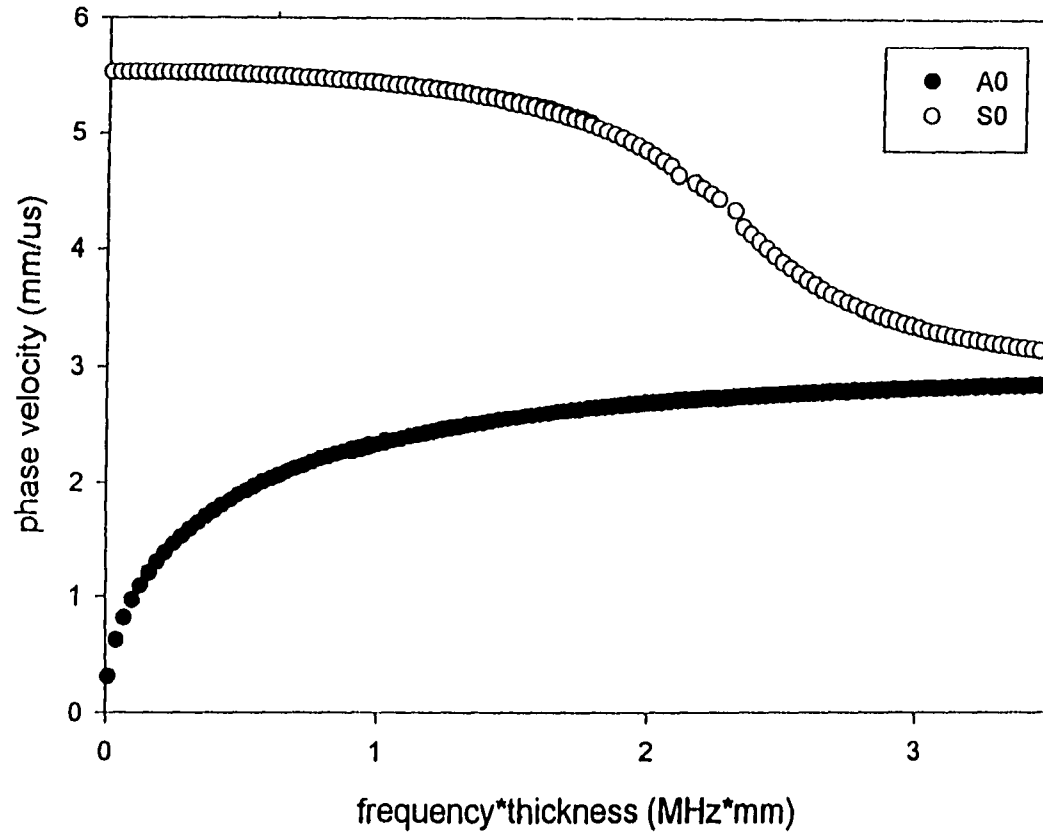


Figure 3.6: Dispersion curves of the Lamb wave modes in aluminum are shown over the frequency-thickness range where only the S_0 and A_0 modes propagate appreciably. For measurements performed at $fd \approx 2$ MHz-mm, only the S_0 and A_0 modes propagate appreciably. The A_1 mode does not propagate appreciably because the attenuation of any mode near its cutoff point is very large. Note that the region of high slope for the A_0 mode is $fd < 0.8$ MHz-mm, while that for the S_0 mode is $2.0\text{MHz-mm} \leq fd \leq 2.6\text{MHz-mm}$.

Figure 3.7 shows the measured frequency data from an aluminum sample with a 2.54 cm diameter 50% thickness reduction flat-bottom hole simulating corrosion. A definite increase in the frequency, which corresponds to an increase in the velocity, is seen for the measurements over the thinned region. From the figure, the flaw can be located between positions 39 and 65 with a length of approximately 26 mm along the scanning direction. By rotating the plate 90° and repeating the scan (Figure 3.8), the flaw can be located between positions 41 and 63 with a length of approximately 22 mm along that scan direction. This indicates that the flaw is contained in a rectangular region of 26 mm × 22 mm. An image of this flaw region can be produced by manually processing the data and then multiplying the processed 0° and 90° data to produce a two-dimensional map [461]. In order for this to work, any data outside of the defined flaw region must be zero, so that erroneous flaw areas are not produced by the multiplication of the two data sets. For plates with isolated flaws this is approximately the case. Figures 3.9 and 3.10 show the data sets after the zeroing and normalization have taken place. A two dimensional array of these values can be obtained by multiplying the elements of the processed 0° data by those of the processed 90° data, that is

$$C_{ij} = c_{0i} \times c_{90j} \quad (3.32)$$

where C_{ij} is the two-dimensional array, c_{0i} is the processed 0° data array, c_{90j} is the processed 90° data array, and i, j are summed to the number of data points in a scan. Figure 3.11 shows the image corresponding to this two-dimensional array. The flaw location is clearly visible, but there is no quantitative information about the magnitude or shape of the flaw. By taking scans along various orientations, we can continue to improve the mapping of the flaw shape and position. However, this method only provides a qualitative image of the flaw's location and relative

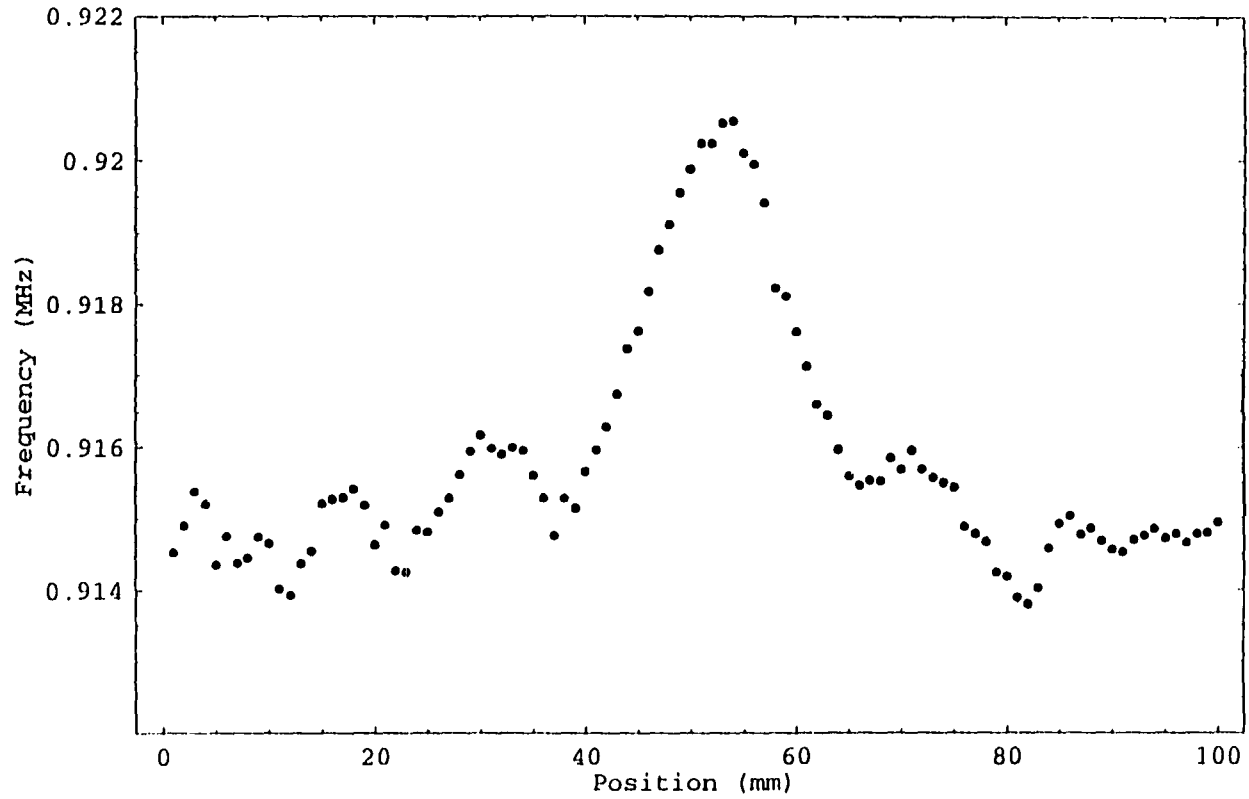


Figure 3.7: Experimental frequency data obtained from a single scan on an aluminum plate with a 2.54cm diameter 50% thinning region. There is a definite increase seen in the frequency values when the Lamb waves pass through the thinning region. From this plot we can determine the length of the flaw to be 26mm in this scan direction.

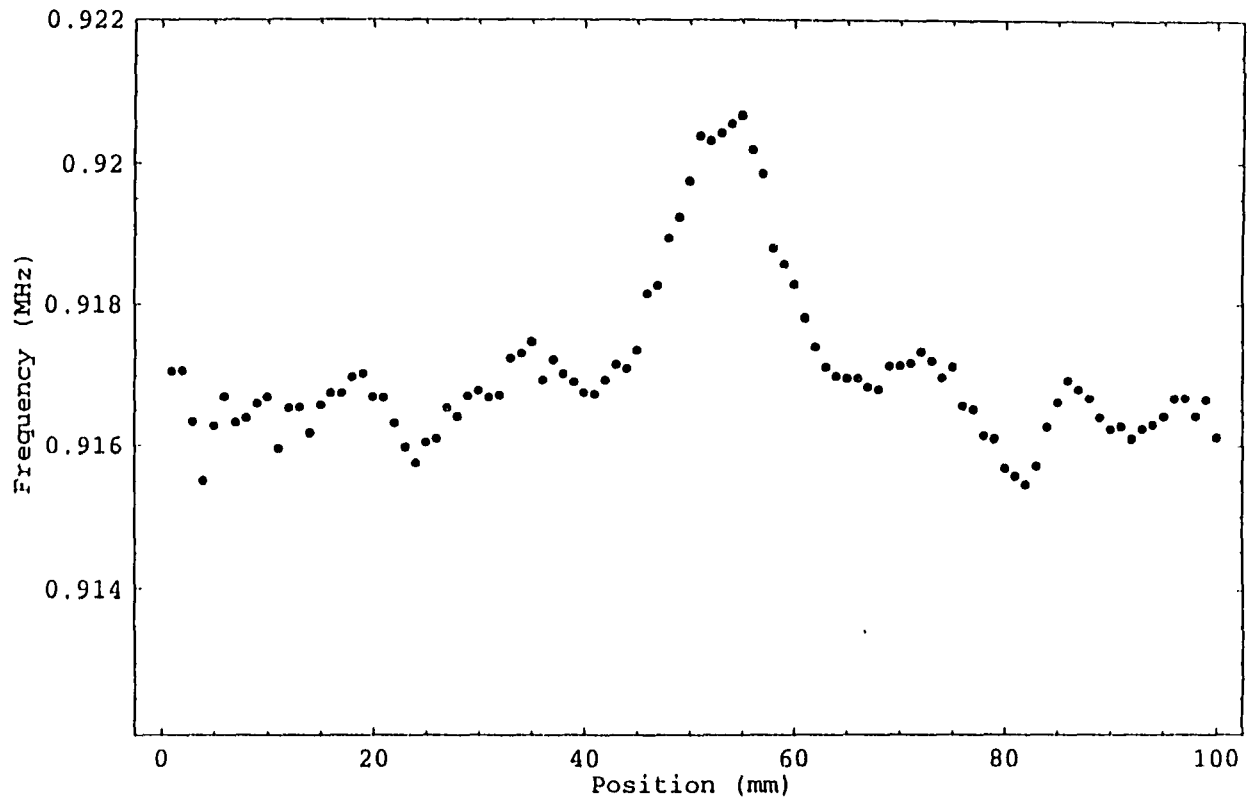


Figure 3.8: Experimental frequency data obtained from a single scan on an aluminum plate with a 2.54cm diameter 50% thinning region after the plate has been rotated by 90° . Again we see a definite increase in the frequency in the flaw area, and we can calculate the flaw length along this scanning direction to be 22 mm.

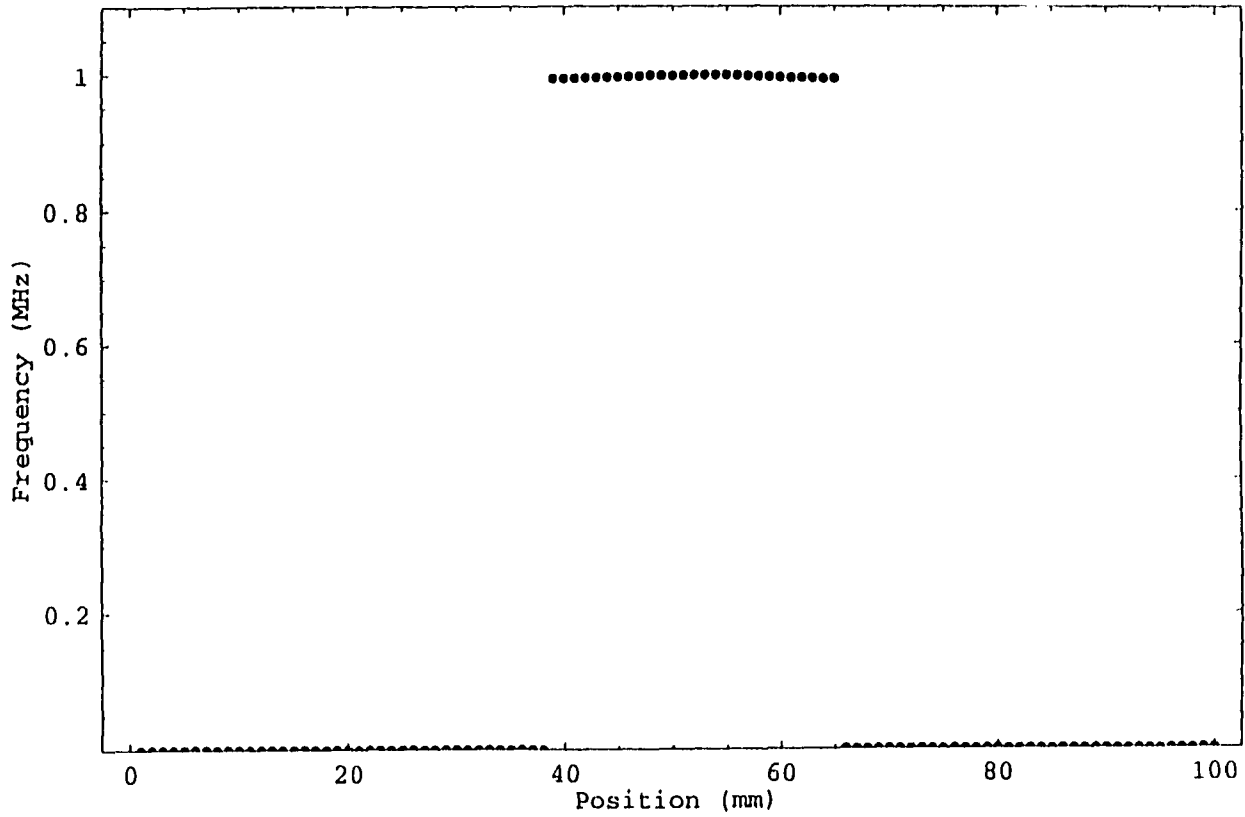


Figure 3.9: Normalized experimental frequency data obtained from a single scan along the 0° orientation on a 2.286 mm thick aluminum plate with a 2.54cm diameter 50% thinning region after all values outside of the defined flaw region have been set to zero.

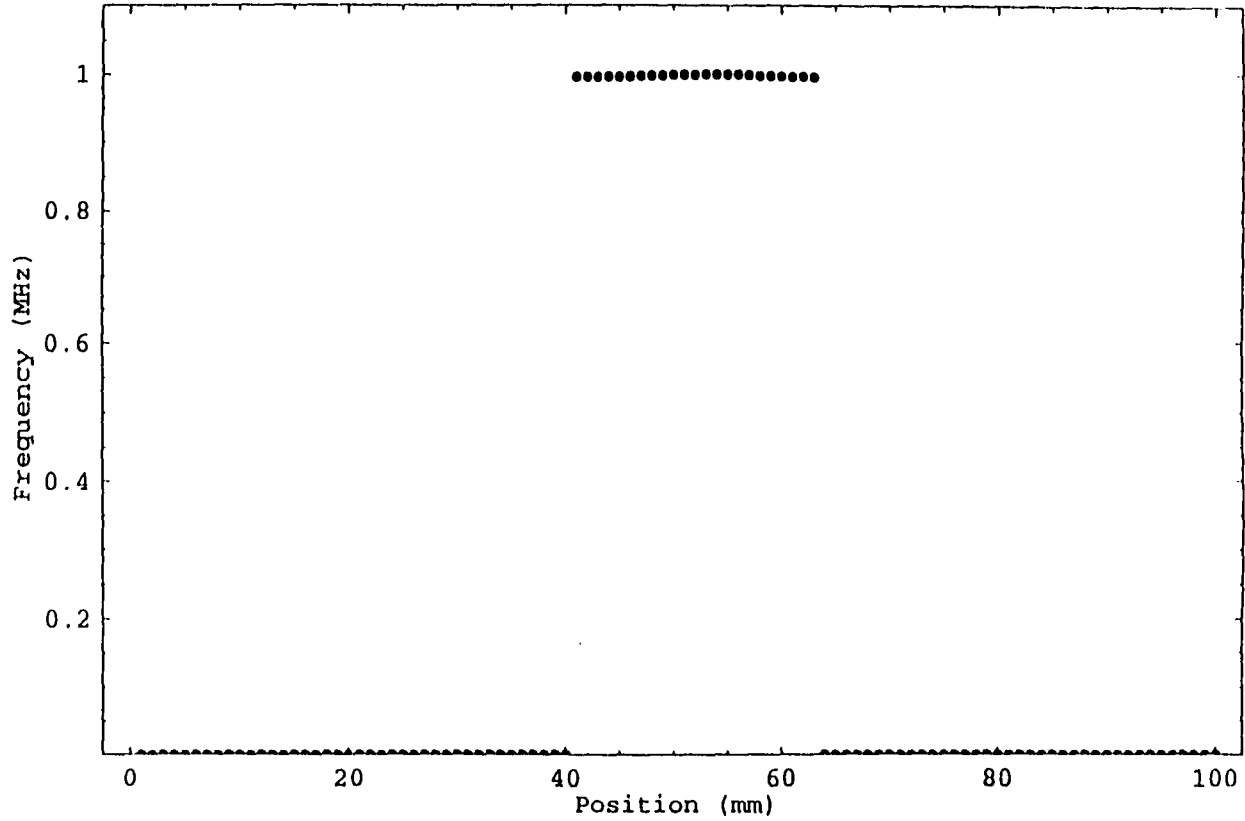


Figure 3.10: Normalized experimental frequency data obtained from a single scan along the 90° orientation on a 2.286 mm thick aluminum plate with a 2.54cm diameter 50% thinning region after all values outside of the defined flaw region have been set to zero.

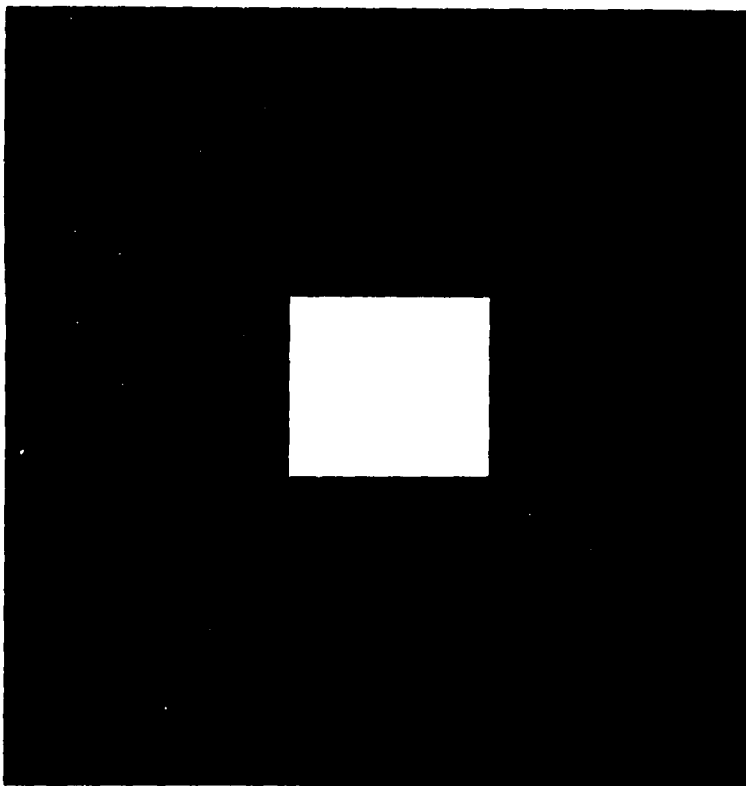


Figure 3.11: Image corresponding to the two-dimensional array produced by multiplying the processed 0° and 90° data sets. A rectangular flaw region is clearly visible, but no information about the actual shape and magnitude of the flaw is available.

size. It does not provide any information about the magnitude of the flaw, and any information contained in the experimental data outside of the defined flaw area, is thrown away. Thus smaller secondary flaws can be overlooked. In order to use the full unprocessed experimental data and obtain a quantitative map revealing the location, size, and magnitude of any flaws, it is necessary to use tomographic reconstruction methods.

3.2 Parallel Projection Tomography

Parallel Projection Tomography (PPT) is the method that was used in the first generation of medical imaging CAT scanners. It provides a quick means of producing accurate two-dimensional reconstruction images of cross-sections of a three-dimensional object as long as measurements can be taken from all angles. In addition, the reconstructions are greatly improved for cases of symmetric flaws. This same technique can be used to image the two-dimensional plate-like structures commonly found on aircraft via Lamb wave ultrasonics.

Geometry and Apparatus

Figure 3.12 shows schematically the geometry for Lamb wave PPT. The transducers are scanned along parallel lines with the Lamb waves propagating between them. At each position in the scan a measurement of some property of the Lamb waves, which are assumed to propagate along the straight rays shown, is recorded. Once the measurement has been done along each of the rays for that orientation, the sample is rotated by a fixed amount and the measurement is repeated. Projections consisting of seven parallel rays (transducer-pair positions) for four orientations (0, 45, 90 and 135 degrees) are shown. The ray density for PPT is

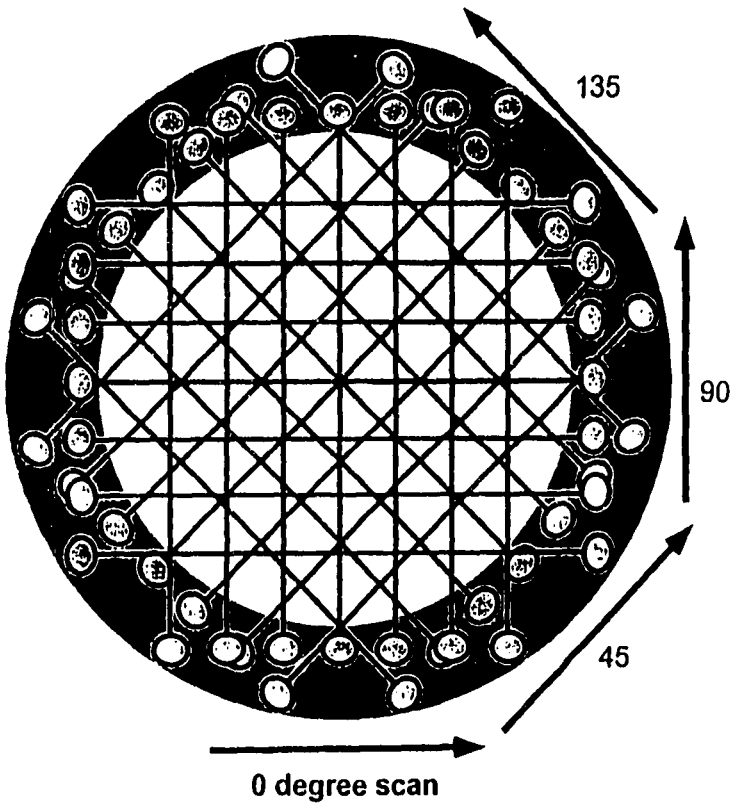


Figure 3.12: The geometry for parallel-projection tomography is shown here schematically for the case of seven parallel rays at four orientations. Note that the ray density is uniform, and a fairly large obstruction free ring (shaded area) is necessary for contact scanning.

uniform and the rays cover all angles since projections must be evenly spaced over 180 degrees, both of which are critical to the quality of reconstruction. However, this can be a disadvantage for contact scanning. As scans are taken along many orientations, a fairly large ring surrounding the region of interest (shown shaded in Figure 3.12) must be free of obstructions. This is necessary so that the scanner can freely rotate to the starting position of each scan without changing its center point, and so that the transducers will have uniform contact with the material for Lamb wave generation and detection. If there are obstructions in the ring region, then fewer orientations must be used to avoid them, and the scanner may have to be repositioned manually between scans. This is detrimental to the reconstruction quality.

In this research an ultrasonic system has been built that allows Lamb wave scans to be made in the parallel projection geometry. A schematic of the parallel projection scanner is shown in Figure 3.13. Broadbanded contact piezoelectric transducers generate and receive the Lamb waves in a pitch-catch arrangement, and a small amount of water is used to ensure consistent coupling. During the scan, the two transducers are scanned as a pair and their orientation to each other remains fixed. That is, the transducers are a fixed distance apart and are simply shifted together along the scan direction without changing the direction in which they point. Because of this, shear contact transducers can be used which produce directional beam patterns that have a preferential amplitude along a certain direction. By aligning two shear contact transducers in pitch-catch mode, the signal along the 0° direction will be preferentially received by the receiving transducer. Thus, signals due to reflections which are received along different angles are minimized. So for the parallel projection configuration, shear contact transducers which are automatically scanned in the direction perpendicular to the Lamb wave propagation

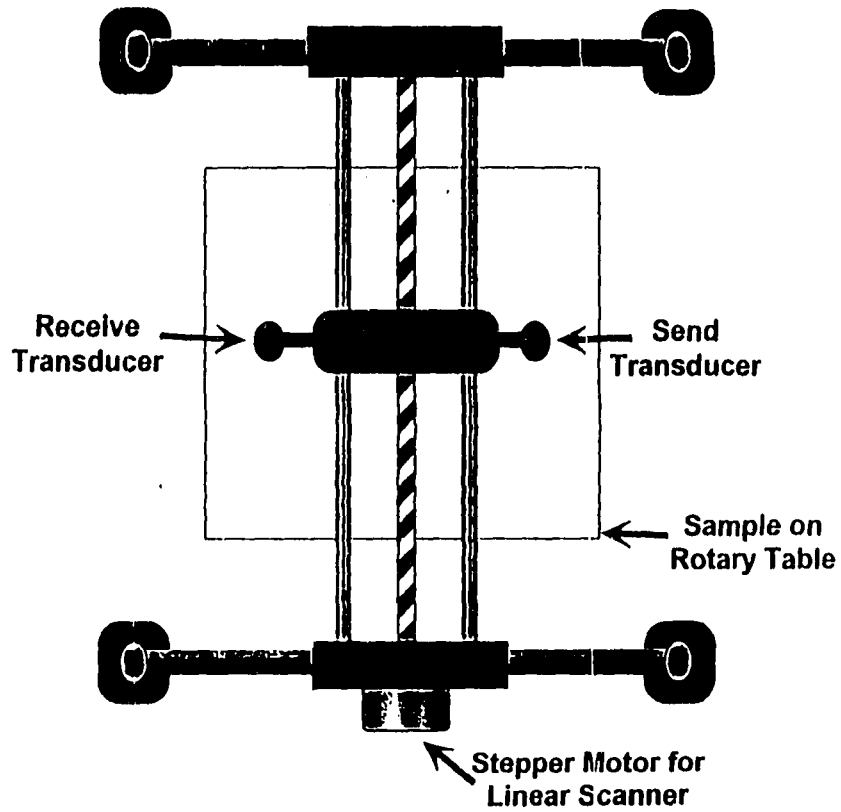


Figure 3.13: The parallel projection scanning system is shown here schematically. A pair of shear contact transducers in pitch-catch arrangement are scanned perpendicular to the direction of Lamb wave propagation. Measurements are taken at each point in the scan, and the sample is rotated by a computer controlled rotary table at the end of each scan in order to obtain data from the different orientations.

are used. Two predominant signals, the lowest-order symmetric (S_0 mode is first arrival) and asymmetric (A_0 is second arrival) can be observed at a frequency in the range 0.7 – 1.5 MHz for aluminum plates about 90 mil thick. At each location of the transducer pair, the frequency value corresponding to the phase shift in the signal is recorded using the P2L2 as described above. In the laboratory setup the sample is automatically rotated by a fixed amount between each scan by a computer-controlled rotary table in order to obtain data from the different orientations necessary for tomographic measurements. The frequency values for each projection are then the input for the tomographic algorithm that produces the reconstructed image.

Algorithm

For completeness, some of the standard development [377] for recovering the image of a cross section of an object from parallel projection data is included here. We define the projection at some angle θ along some line $x \cos \theta + y \sin \theta = t$ as

$$P_{\theta}(t) = \int_{-\infty}^{\infty} f(t, s) ds \quad (3.33)$$

where (t, s) is the coordinate system at an angle θ to the (x, y) system (Figure 3.14). Here $f(t, s)$ is called the object function. For example, if $f(t, s)$ is the two-dimensional distribution of slowness in the plate, then $P_{\theta}(t)$ is the time-of-flight projection for the angle θ . The Fourier transform of $P_{\theta}(t)$ is:

$$S_{\theta}(w) = \int_{-\infty}^{\infty} P_{\theta}(t) e^{-2\pi i w t} dt \quad (3.34)$$

and substituting in our above definition for the projection gives

$$S_{\theta}(w) = \int_{-\infty}^{\infty} \int_{-\infty}^{\infty} [f(t, s) ds] e^{-2\pi i w t} dt. \quad (3.35)$$

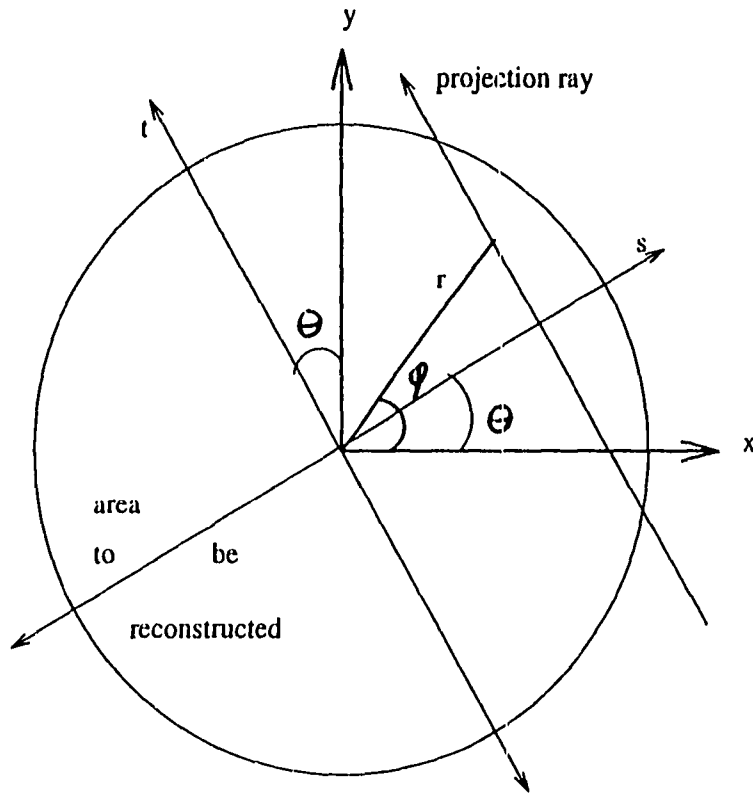


Figure 3.14: The projection at some angle θ along some line $x \cos \theta + y \sin \theta = t$ passing through an object function $f(t, s)$ is shown.

If we transform this back into the (x, y) coordinate system, we have

$$S_{\theta}(w) = \int_{-\infty}^{\infty} \int_{-\infty}^{\infty} f(x, y) e^{-2\pi i w(x \cos \theta + y \sin \theta)} dx dy \quad (3.36)$$

and we see that the right-hand side is the two-dimensional Fourier transform of $f(x, y)$ at a spatial frequency of $(u = w \cos \theta, v = w \sin \theta)$, or

$$S_{\theta}(w) = F(w, \theta) = F(w \cos \theta, w \sin \theta) = F(u, v). \quad (3.37)$$

This equation indicates that by taking projections of an object function at many angles, $\theta_1, \dots, \theta_k$, and Fourier transforming each of these, we can determine the corresponding value for $F(u, v)$. Then the object function, $f(x, y)$, can be recovered by using the inverse transform:

$$f(x, y) = \int_{-\infty}^{\infty} \int_{-\infty}^{\infty} F(u, v) e^{2\pi i(ux+vy)} du dv. \quad (3.38)$$

Using polar coordinates we can write this as

$$f(x, y) = \int_0^{2\pi} \int_0^{\infty} F(w, \theta) e^{2\pi i w(x \cos \theta + y \sin \theta)} w dw d\theta \quad (3.39)$$

and splitting the θ -integration into two parts and noting that $F(w, \theta + \pi) = F(-w, \theta)$ we have

$$f(x, y) = \int_0^{\pi} \int_{-\infty}^{\infty} F(w, \theta) |w| e^{2\pi i w t} dw d\theta \quad (3.40)$$

where we have used $t = x \cos \theta + y \sin \theta$ for convenience. Finally, introducing

$$Q_{\theta}(t) = \int_{-\infty}^{\infty} S_{\theta}(w) |w| e^{2\pi i w t} dw \quad (3.41)$$

we write

$$f(x, y) = \int_0^{\pi} Q_{\theta}(x \cos \theta + y \sin \theta) d\theta \quad (3.42)$$

which gives the object function in terms of x , y , and the projection angle, θ_i . However since we cannot take an infinite number of projections, these integrals need to be replaced with the appropriate summations. For example

$$Q_i(k/2w) \approx \frac{2w}{N} \sum_{m=-N/2}^{N/2} S_j(m2w/N) \left[\frac{2w}{N} \right] e^{2\pi i(mk/N)}$$

$$f(x, y) \approx \frac{\pi}{K} \sum_{i=1}^K Q_{\theta_i}(x \cos \theta_i + y \sin \theta_i). \quad (3.43)$$

Thus, the scan is made for K angles θ_i and for N points along each of those scans. In Figure 3.12 the scan is shown for 4 projection angles of 7 points each, while in the experiment 18 projection angles of 100 points each have been used. Also in the experiments, a Convolution-Backprojection algorithm was used where instead of just taking the inverse transform of $F(w, \theta)$ as in Equation 3.39, the convolution of $F(w, \theta)$ and some filter function, $h(w, \theta)$, is calculated. Therefore, Equation 3.39 is replaced by

$$f(x, y) = \int_0^{2\pi} \int_0^{\infty} F(x - w, y - \theta) h(w, \theta) e^{2\pi i w(x \cos \theta + y \sin \theta)} w dw d\theta. \quad (3.44)$$

Results

Figure 3.15 shows a parallel projection tomographic reconstruction contour plot of Lamb wave contact scanning data taken on a 2.45 mm thick aluminum plate with a 20 cm² region of 50% thickness reduction. The image covers 100 × 100 mm and was reconstructed from 18 projections of 100 rays each. The thinned region is shown clearly as the white region in the center of the image. So PPT can be used to convert the data obtained using the mathematically complex Lamb waves into a quantitative map of the recorded frequency values for the inspected region.

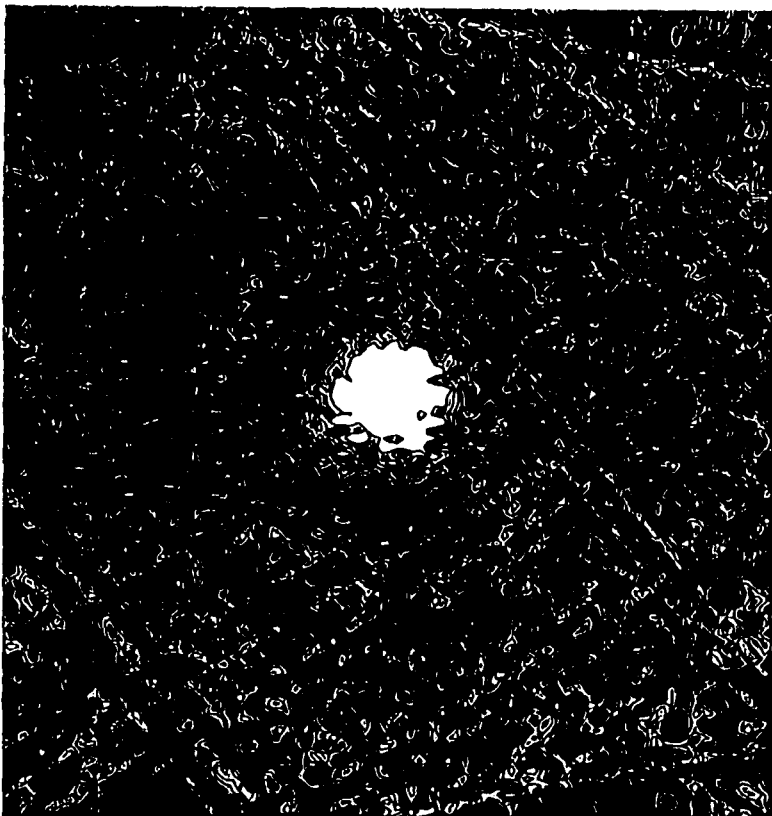


Figure 3.15: Parallel projection tomographic reconstruction contour plot of Lamb wave contact scanning data taken on a 2.45 mm thick aluminum plate with a 20 cm^2 region of 50% thickness reduction is shown here. The image covers $100 \times 100 \text{ mm}$ and was reconstructed from 18 projections of 100 rays each. The thinned region is shown clearly as the white region in the center of the image.

These frequency values can then be converted to velocity or thickness values using the dispersion relations presented earlier. The location, size and magnitude of any flaw regions can easily be distinguished from this map, which can be displayed as an image or further processed by a specialized algorithm for automated flaw detection. For example, the total volume of corrosion can easily be calculated by simple algorithm, and a threshold value can be used to make airworthiness decisions.

While PPT has been shown to give quite accurate results for symmetric flaws, such as the circular thinning, with 18 scans taken in 10° increments, many more orientations will be necessary for accurate reconstructions of less symmetric flaws and contact scanning is time intensive. In addition, while it is easy in a laboratory setting to rotate small samples for all of the necessary orientations, this becomes problematic for in-the-field applications. For example, an aircraft being inspected cannot be rotated, and a rotating plus scanning apparatus would be mechanically complex because its center point must remain exactly stationary, and the coupling of the transducers is a major concern. In addition, as more orientations are needed, a fairly large ring region must be obstruction free as was discussed earlier. This makes scanning riveted lap joints or doublers, which are of great importance in aircraft assessment, impossible. Finally, the desired end result of the aircraft inspection is to produce a map of the full aircraft composed from the individual scans. PPT tomography produces maps of circular regions, so either information will be missing between the individual maps or consecutive maps will have to overlap significantly. In the image above a square region inside of the actual circular data region is shown. These methods for producing the composite map are as inefficient and time consuming as point measurements (C-scans). Therefore, in order to develop a Lamb wave tomography method that can be practically applied in-the-field, a different method of tomography was developed.

3.3 Cross Borehole Tomography

Geometry and Apparatus

Cross Borehole Tomography (CBT) is a technique commonly used in seismological imaging where the detection of subsurface pockets of oil or natural gas, or the mapping of the properties of the Earth's crust are of interest. For these tests it is impossible to obtain measurements from all sides of the region of interest. Instead, two vertical holes are bored into the ground, and the two-dimensional area between them is reconstructed in terms of a physical parameter such as time-of-flight. In one hole, a seismic wave is generated at successive depths using an explosion or hydrophone, and the time-of-flight to each of the multiple receivers in the second hole is recorded. In contrast to the parallel rays in PPT, this results in sound waves traveling in criss-cross patterns across the region between the boreholes. Thus we have the name cross borehole. A line of receivers can also be placed along the surface for improved reconstruction, but there is never access to the fourth side.

This method has been applied to the reconstruction of two-dimensional plate-like structures by having the senders and receivers in two parallel lines on the surface of the plate. The plate region between them can then be tomographically reconstructed. Figure 3.16 shows the scanning geometry and ray paths for CBT tomography for eight combinations of sources and receivers. Note how the ray density varies and that the rays do not pass through the region of interest from all orientations. These drawbacks in the reconstruction quality are offset by the increased practicality of the measurement. Namely, only two narrow strips (shown shaded in Figure 3.16) need to be free of obstructions for contact scanning. These strips indicate the space necessary for the senders and receivers to freely move to all of the locations necessary for the tomographic reconstruction. This space is

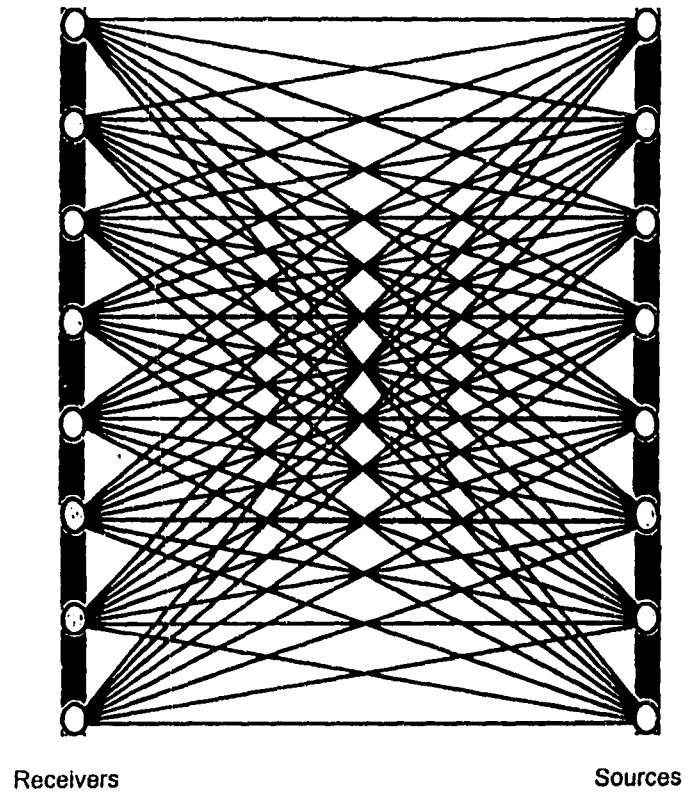


Figure 3.16: The scanning geometry and raypaths for cross borehole tomography are shown here schematically for the case of eight sources and eight receivers. Note that the sixty-four raypaths produced do not provide a uniform ray density, but only two narrow obstruction free strips (shaded) are necessary for contact scanning.

much smaller than that required for PPT, and since the scanning apparatus does not have to rotate, inspecting lines of rivets is not a problem. The sending and receiving positions can simply be located on either side of the line of rivets. Also, since access is only required from two sides, the reconstructions are rectangular. Now when a map of the full aircraft is composed from the individual tomographic maps, the images can simply be lined up next to one another. There are no gaps between the individual maps, and no data needs to be thrown away. Therefore, CBT provides a far more practical means for producing a composite flaw map of a full aircraft than PPT.

An ultrasonic system has also been assembled that allows Lamb wave scans to be made in the cross borehole geometry. A schematic of the CBT scanner is shown in Figure 3.17. Broadbanded contact transducers in a pitch-catch arrangement are again used to generate and receive the Lamb waves. However, they are scanned independently so that measurements are recorded at all of the necessary sender/receiver positions. Since the relative orientation of the transducers is constantly changing during the scan, the highly directional shear transducers can not be used even though they usually give a better signal in contact scanning. Instead, longitudinal contact transducers are used because their beam pattern is isotropic and signals can be received from any angle. Also, since the path length between the sender/receiver pairs varies during the scan, the P2L2 cannot be used for measurements. The large changes in path length cause it to jump lock, and so its recorded values are meaningless. Instead, the received signal is sent to an oscilloscope, which digitizes the waveform and sends it to a personal computer for further analysis.

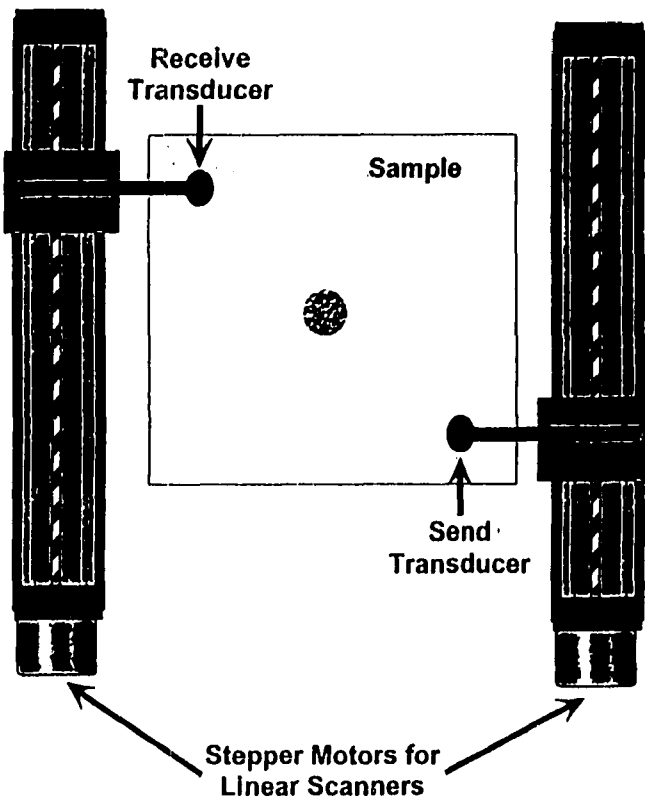


Figure 3.17: The cross borehole scanning system is shown here schematically. Two longitudinal contact transducers are scanned independently to the various sender/receiver positions by two computer controlled linear scanners. At each sender/receiver position, the received waveform is digitized and saved on a personal computer for later analysis.

Expert System

In order to make use of the recorded Lamb wave data, it is necessary to extract the time-of-flight of the S_0 mode from each sender/receiver pair waveform. While experts can pick out the correct part of the waveform by eye, they cannot determine the time value with high enough accuracy. In addition, the number of waveforms required for tomographic reconstruction can reach well into the thousands which is far too many for a human to process. Therefore, a rudimentary expert system has been developed to automatically extract the time-of-flight value from each waveform.

In these experiments, the transducers are excited by a toneburst containing a specified number of cycles at a specified frequency. Each mode in the received waveform contains the same number of cycles at that same frequency. However, the waveform is complicated by noise, overlapping reflections, dispersion, and multiple modes. The human eye is able to pick the first pattern of specified cycles out of the noise and other complexity of the signal, but as was stated above, the number of waveforms and accuracy required make human interpretation impractical.

Instead a computer program has been written which finds the best match to a specified normalized pattern. This pattern consists of a number of cycles at the operating and sampling frequencies used in the experiment. The computer program first calculates the estimated time-of-flight for a given raypath in the material without flaws and converts this value to a point location in the waveform. It then compares the specified pattern to a normalized portion of the waveform containing the same number of points as the pattern. For the results shown here, it begins with the point 500 ahead of the time-of-flight estimate and shifts the normalized portion point by point until the portion starting on the point 500 after the time-

of-flight estimate has been tested. For each portion, the error between the pattern and the normalized portion is calculated, and the S_0 time-of-flight value is taken as the starting point of the normalized portion with the least error. This is done for each waveform to generate the file of arrival times needed as input for the CBT algorithm.

As an example consider the waveform shown in Figure 3.5. Simply looking at the plot of the waveform, an expert can detect the S_0 mode at a time of approximately $48 \mu\text{s}$. The pattern shown in Figure 3.18 consists of 3 cycles at a generating frequency of 1.05 MHz and a sampling frequency of 100 MHz, where the amplitudes of the cycles are 0.6, 0.8, and 1.0 respectively. Using this pattern, the computer program determines the time-of-flight value to be $49.65 \mu\text{s}$. The percent difference between this and the value estimated visually is 3.4%. However, this was for a relatively clear signal over an unflawed region of the aluminum plate. When the signal passes through flawed regions, its amplitude can drop below the noise level, and picking out the S_0 mode can be very difficult.

In order to determine how much of an effect the accuracy of the time-of-flight values has on the reconstruction quality, a simulated sample is considered. Figure 3.19 shows a plate region with a square flaw placed offcenter. The velocity value of the flaw is 20% greater than that of the plate which is chosen as $4.5 \text{ mm}/\mu\text{s}$. The S_0 time-of-flights can be calculated by mapping out the raypath for each sender/receiver pair and using the velocity values of the regions through which a given ray passes to calculate the time-of-flight for that raypath. From Figure 3.20, it can be seen that these time-of-flight values allow for a quite accurate reconstruction after only a single iteration. If however, we add noise to the time-of-flight values to simulate error in the determination of the time-of-flight, the reconstruction quality decreases.

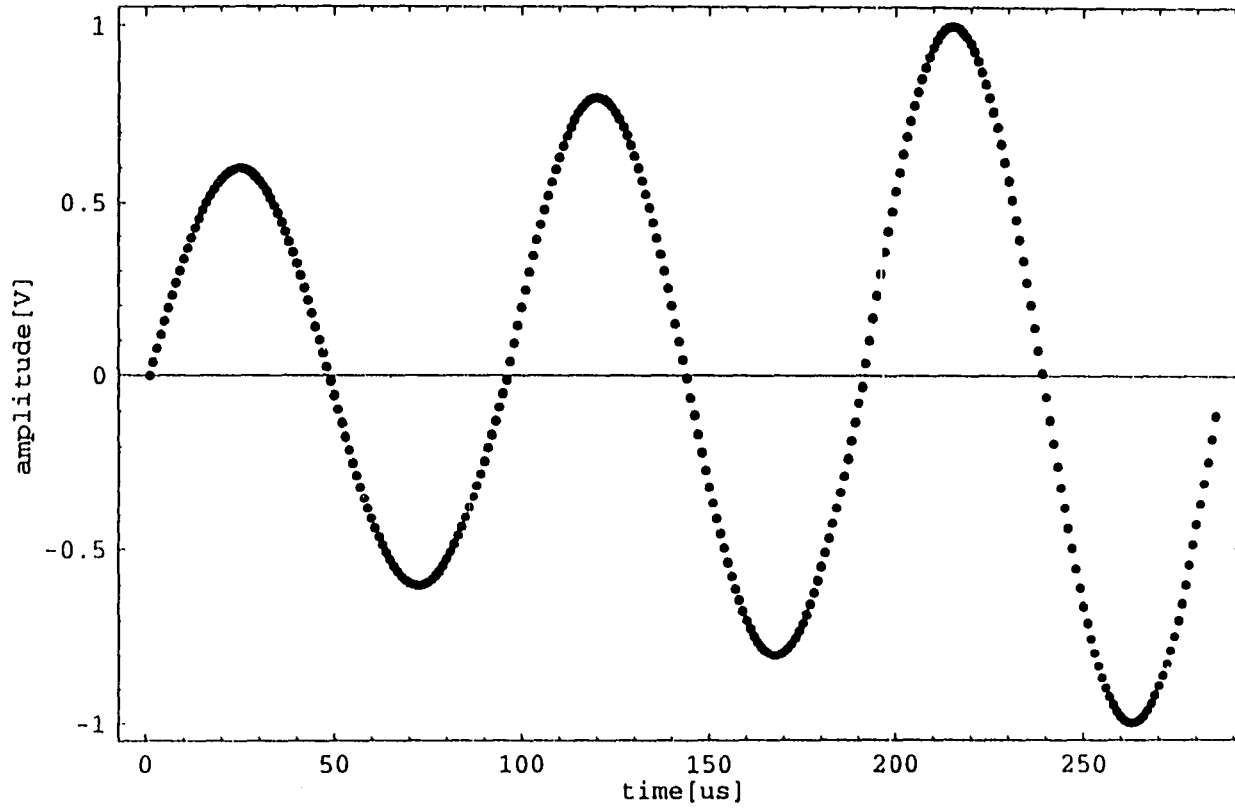


Figure 3.18: A sample pattern used to detect the $S0$ mode in the received experimental waveforms. This pattern consists of 3 cycles at a generating frequency of 1.05 MHz and a sampling frequency of 100 MHz, where the amplitudes of the cycles are 0.6, 0.8, and 1.0 respectively.

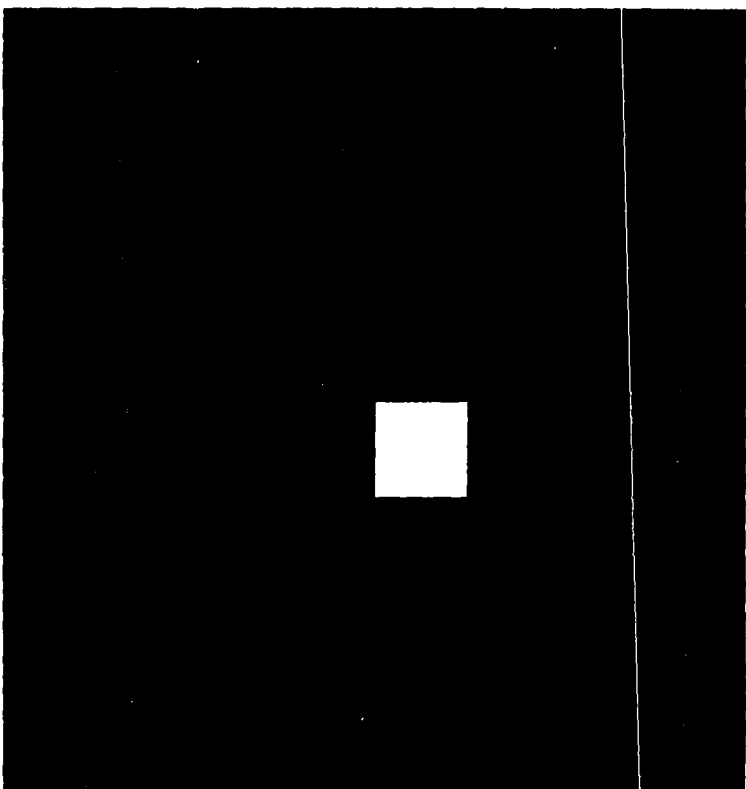


Figure 3.19: A simulated plate with an off center square flaw whose material has a 20% increase in velocity over the velocity of the plate (4.5 mm/ μ s.)

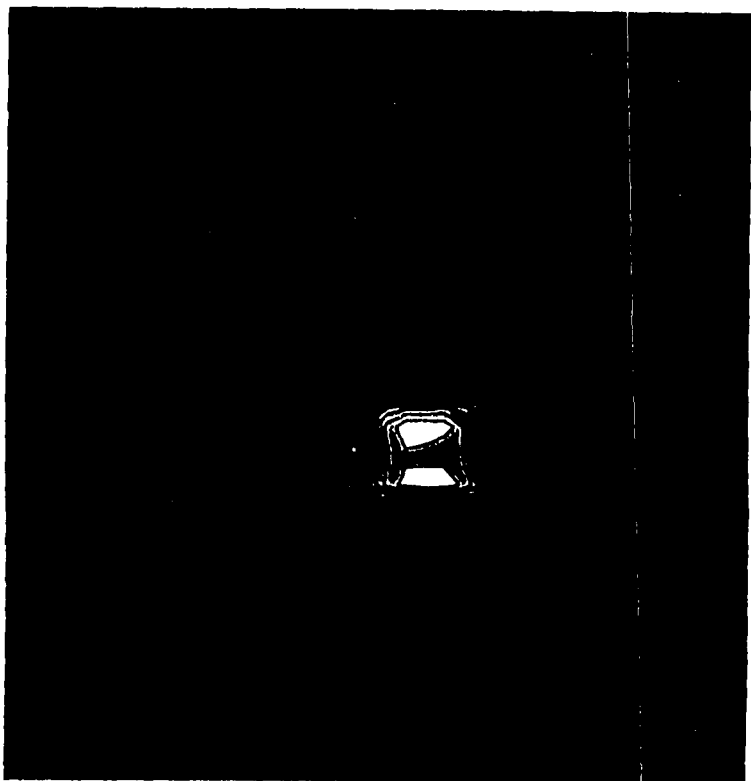


Figure 3.20: Reconstruction of the square flaw plate using the ART algorithm after a single iteration. Notice that with the accurate time-of-flight values possible in the simulation, the reconstruction is quite accurate after only one iteration.

A study was performed on the effect of adding various levels of random noise to the time-of-flight values on the quality of reconstruction after a single iteration. The noise was added by first determining the maximum percentage of noise to add, N , and then adding a random value between 0 and $N \times t_0$ to each of the t_j values, where t_j is the array of the time-of-flight values. Figure 3.21 shows a bar chart of the root mean square error between the simulated plate image and the reconstruction made with N noise for values of N ranging from 0 to 40. The vertical scale of 50 has been chosen so that the smaller RMS values are distinguishable. In fact, for $N = 10$ the RMS error has already increased by an order of magnitude, while for $N = 37$ and $N = 40$ it has actually increased by 6 orders of magnitude and 15 orders of magnitude respectively. Figures 3.22, 3.23, and 3.24 show the reconstructions for $N = 10$, $N = 37$, and $N = 40$ respectively. In the first case, a blob in the area of the flaw is partially visible behind a speckled pattern, while for the second and third cases, only a diagonal line is visible. A diagonal line is always obtained using the ART algorithm when there is either not enough data or the data is too inaccurate to converge. In addition, if enough iterations are done for any real data case, the solution always converges to the diagonal. However, for more accurate data, this can take hundreds of iterations, and only a few are usually used. In addition, although a flaw is somewhat visible for the $N = 10$ case, the position and shape of the flaw are known. In general, such a reconstruction would not convincingly reveal a flaw. Also, while the $N = 10$ value calls for a maximum of 10% noise to be added, the majority of the noise would be less than this. Therefore, even a few percent inaccuracy in the time-of-flight values can cause the reconstructions to be unrevealing. This is why the development of an expert system to determine the time-of-flight values from the experimental waveforms has been so important to the results of this dissertation.

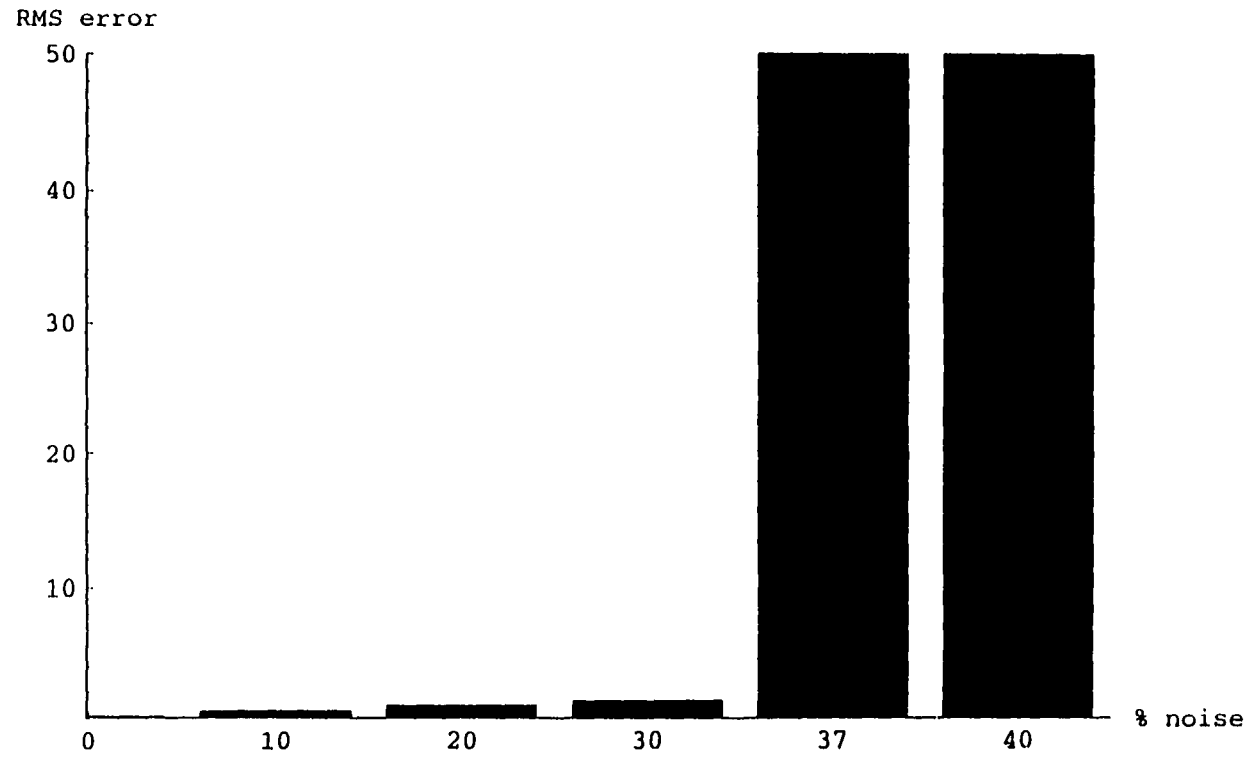


Figure 3.21: Bar chart of the RMS error in the reconstruction associated with different levels of added noise.

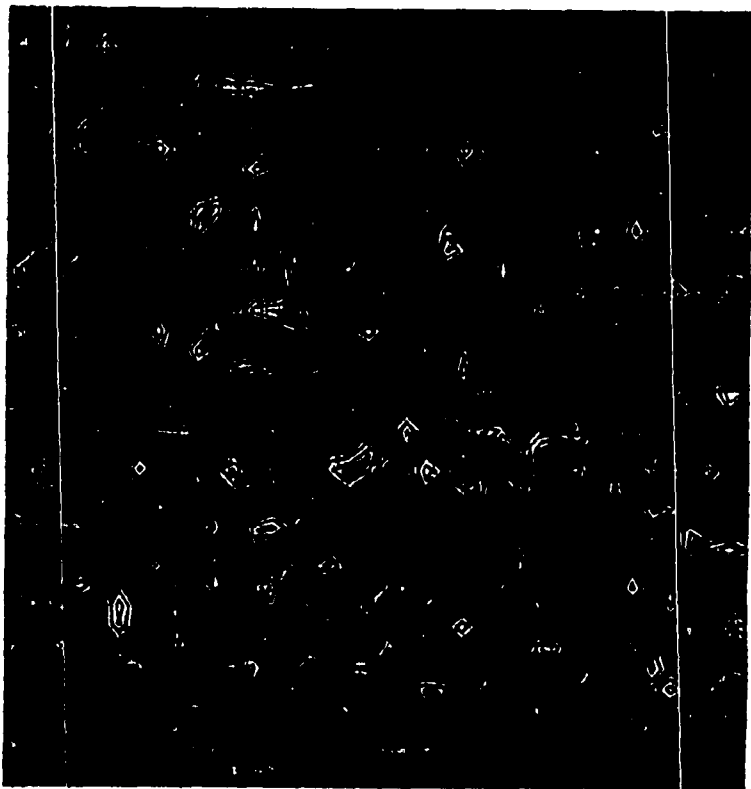


Figure 3.22: Reconstruction of the square flaw plate using the ART algorithm when noise in the range of 0-10% has been added to the time-of-flight data. After a single iteration, the flaw is barely visible since its location is known. The RMS error has increased by an order of magnitude.

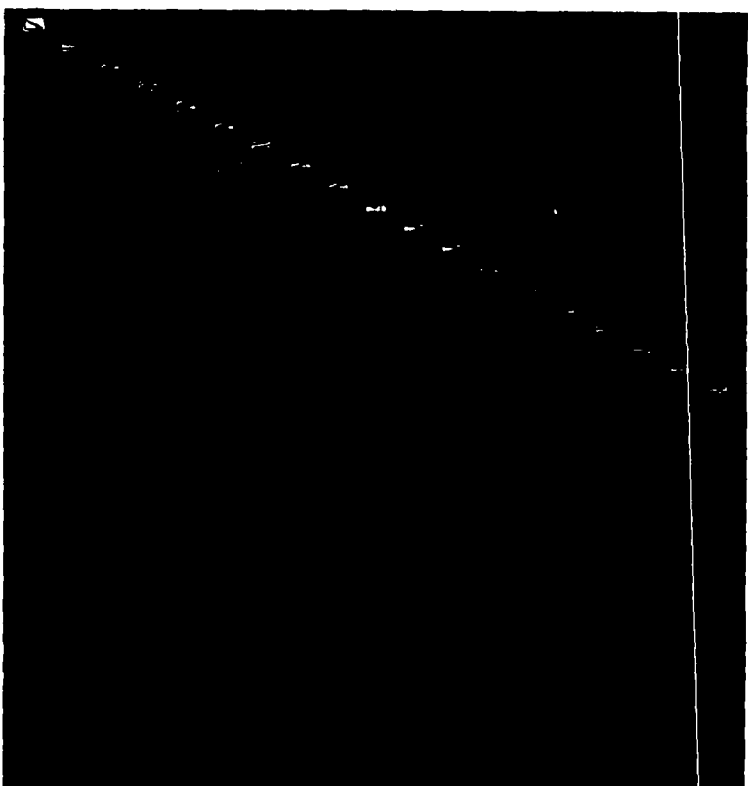


Figure 3.23: Reconstruction of the square flow plate using the ART algorithm after noise in the range of 0-37% has been added to the time-of-flight data. After a single iteration, the reconstruction only shows a diagonal line. This diagonal line indicates that the data is too inaccurate to converge properly, and the RMS error has increased by 6 orders of magnitude.

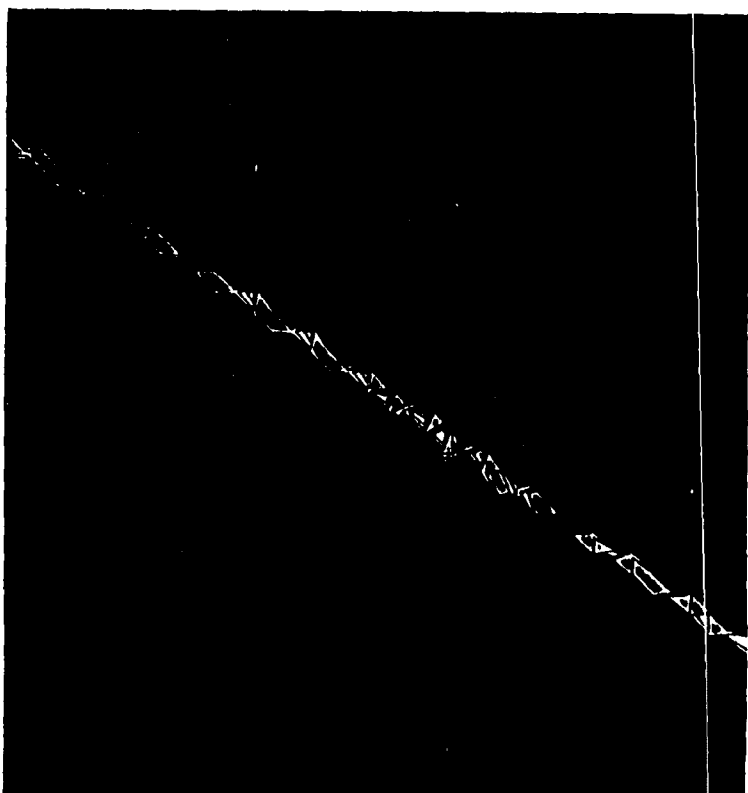


Figure 3.24: Reconstruction of the square flaw plate using the ART algorithm after noise in the range of 0-40% has been added to the time-of-flight data. After a single iteration, the reconstruction again only shows a diagonal line. However, the RMS error has now increased by 15 orders of magnitude.

Algorithm

In this section the calculation for geophysical cross borehole tomography is outlined for completeness. The geometry consists of a series of source and detector locations, and a ray projection exists for every combination. The intervening space is discretized as a rectangular grid space with a number of rays passing through each element in this space. The reconstruction of the value at each element, e.g. wave speed, involves solving a large set of equations. An Algebraic Reconstruction Technique (ART) has been chosen for this purpose [343].

In the Lamb wave measurements, I_{tot} is the number of source locations and J_{tot} is the number of columns between the sources and receivers. This means that the area between the source and receiver line is divided up into a rectangular area with ij number of cells. A ray connects every combination of source and receiver, and the corresponding line which goes through the cells is defined as

$$i = \left(\frac{i_d - i_s}{J_{tot}} \right) j + i_s \quad (3.45)$$

where the source location is i_s and the detector location is i_d . To construct the data vector, we write

$$g_k = f_{ij} \Delta s_{ijk} \quad (3.46)$$

where the summation over i and j is implied. Δs_{ijk} is the segment of the k -th ray passing through the cell ij , and f_{ij} corresponds to the value of the physical parameter of interest, e.g. wave speed, in the cell ij .

In order to determine the values of f_{ij} for the discretized space, we first calculate the Δs_{ijk} , estimate the f_{ij} components, and calculate g_k

$$g_k = f_{ij}^q \Delta s_{ijk} \quad (3.47)$$

Next, for each ray we use the difference between the g_k value and the corresponding data value, Δg_k , to calculate the update for the f_{ij}^q values for that ray.

$$\Delta f_{ijk}^q = \frac{(\Delta g_k - g_k)}{L_k} \quad (3.48)$$

where L_k is the length of the k -th ray

$$L_k = \sqrt{(i_k - i_n)^2 + (J_{z:zr})^2}. \quad (3.49)$$

Then we add the update to the current f_{ij}^q values for that ray

$$f_{ij}^{q+1} = f_{ij}^q + \Delta f_{ijk}^q \quad (3.50)$$

to obtain the next set of f_{ij} values, f_{ij}^{q+1} . A single iteration involves repeating this process for all of the rays, and iterations are repeated until a specified number has been reached or until the residual has approached some small number

$$r = \sum_k [g_k - \Delta g_k]^2. \quad (3.51)$$

In Figure 3.16 there are 8 sources and 8 receivers so a single iteration would involve 64 rays, while for the experiment 20 sources and 20 receivers giving 400 rays and 10 iterations have been used.

Results

Figure 3.25 shows a CBT reconstruction of the same 100×100 mm region of the aluminum sample used in the PPT reconstruction. This image was produced using the ART algorithm and 400 rays. Note that although the much lower ray density in the flaw region decreases the accuracy of the reconstruction, the location and size of the thinned region are accurately reproduced. The CBT image is inherently lower resolution because the number of pixels corresponds to a much coarser computational grid.

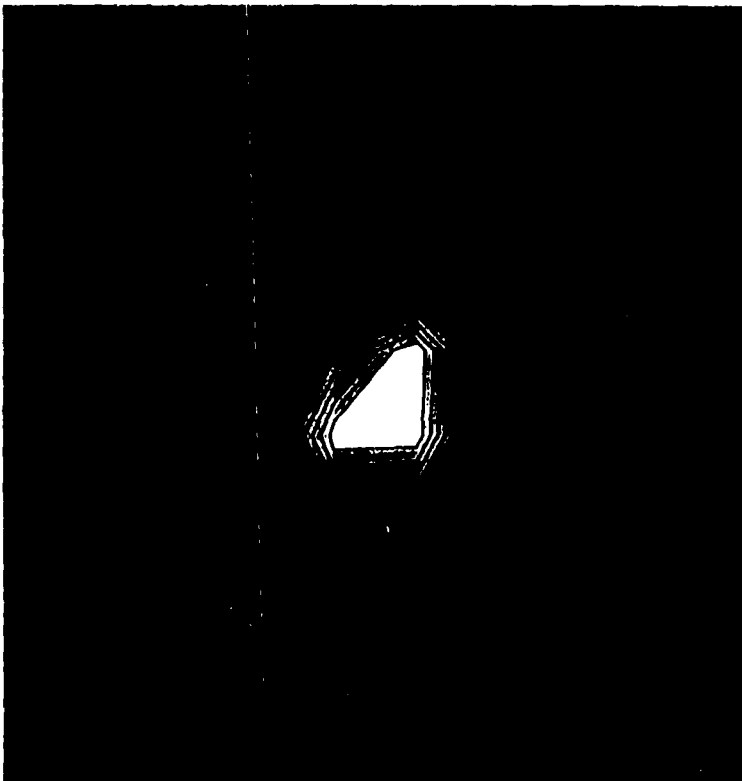


Figure 3.25: Cross borehole tomographic reconstruction of the same 100×100 mm region of the aluminum sample is shown. This image was produced using the ART algorithm and 400 rays. Note that although the much lower ray density in the flaw region decreases the accuracy of the reconstruction, both the location and size of the thinned region are accurately reproduced. The CBT image is inherently lower resolution because the number of pixels corresponds to a much coarser computational grid.

In general, the quality of the reconstruction improves with the number of rays and the number of iterations. However, the value of 400 rays was chosen in order to minimize the time required for the reconstruction, while still producing quality results (see the design study in Appendix A). In addition, the storage space required on a computer hard drive for thousands of rays is exceedingly large, with even modern hard drives filling up after a few scans. For example, the Pentium Pro 200 MHz computer with 196 MB of RAM and a 2 GB drive used in this experiment, was unable to process data sets with more than 4000 rays, and for data sets of 1600 rays, the hard drive filled up after only 10 scans. The benefit of saving the waveform for each ray is that multiple features can be extracted for reconstruction purposes, although in this work, only the time-of-flight of the S0 Lamb wave mode has been used. Therefore, in addition to producing quality reconstructions in less time, the choice of 400 rays enabled the data from many tomographic scans to be stored on the computer, and so provided the best results for the hardware used for this study. As computers continue to improve, tomographic data sets of thousands of rays will easily be stored and processed in very little time. Therefore, the quality of the CBT images will be improved. It should be noted that for aircraft applications, the reconstruction *time* is not a concern. The reconstruction shown here took 5 seconds, and including the time to process the experimental data and extract the time-of-flight values, this value only increases to about 5 minutes.

As was stated earlier, one of the disadvantages of the PPT technique is that it requires measurements to be made from all sides of the region of interest. This is clearly impractical in any number of materials testing situations, and the CBT technique, which requires access to only two sides of the region, has been chosen for the development of a practical scanning technique. As an example of a practical situation where PPT is not possible, we consider a line of rivets along a plate

structure. In the aircraft industry, the integrity of the rivets bonding the aircraft skin together and to the frame is extremely important. Scanning or rotating transducers across a lap joint is problematic in terms of coupling and possible damage to the transducers. In addition, uniform contact with the plate is necessary for the generation and reception of the Lamb waves and this is not possible when the transducers are placed on the line of rivets.

The CBT technique offers an ideal solution since the sending and receiving positions can be lined up parallel to the line of rivets but on opposite sides. Then Lamb waves can be generated and received from uniform sections of the plate while fully investigating the line of rivets. Figure 3.26 shows the results of a CBT scan on a 2.52 mm thick aluminum plate with a line of five 2.54 cm diameter thinned regions along the full length of the sample. Although it is not a line of rivets, the line of flaws still provides a situation where PPT is not possible. The scanned region, 160×130 mm, only covers four of the thinned regions, and due to the ray density of CBT reconstructions and the hardware limitations on the number of rays possible, only the center thinned region has been fully reconstructed with a second flaw region partially reconstructed just below. However, an image of a flaw region has been produced using CBT in a situation where PPT is not possible. As the use of more rays becomes possible, the reconstruction quality will improve.

3.4 Discussion

The most serious limitation in the tomographic reconstruction algorithms that have been presented in this chapter is that they neglect diffraction and ray bending effects. It was assumed that the thinning only caused the Lamb wave velocity to change, but that there was no scattering of the Lamb waves. For slight

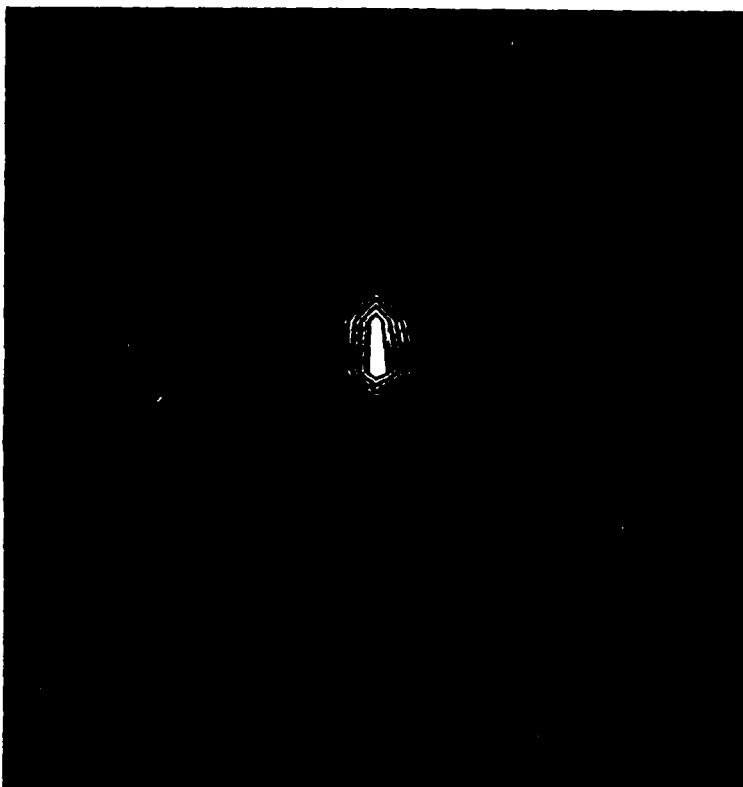


Figure 3.26: CBT reconstruction of a region of an aluminum sample with a line of five thinned regions. Only the center flaw is fully reconstructed, but we are able to obtain an image from this sample with the CBT method, when we are unable to do so with the PPT method.

changes in thickness this is a reasonable assumption, but for many flaws there will be significant scattering. In order to determine the importance of scattering effects, two through-hole samples have been examined with the tomographic techniques.

The first sample is a 2.42 mm thick aluminum plate with a 1.5 cm diameter hole milled through it. The 100×100 mm PPT reconstruction is shown in Figure 3.27, while that for the CBT is shown in Figure 3.28. In both images, the hole is shown in the correct location and with about the correct size, but the higher resolution PPT image shows slight scalloping around the edges of the hole. Scalloping is indicative of diffraction, but the effects are quite small for this case. This is probably because this hole is only slightly larger than the element size of the transducer. Therefore, enough of the beam may be skirting the hole to minimize the diffraction effects.

The second sample is a 2.32 mm thick aluminum plate with an irregular 2.54 cm diameter hole milled through it. This is about twice as large as the transducer diameter. For this sample the 100×100 mm PPT reconstruction is shown in Figure 3.29, while the CBT reconstruction is shown in Figure 3.30. This time definite scalloping and a starburst streaking effect are seen in the PPT image, and the hole in the CBT image has been reconstructed in the wrong position. Clearly scattering effects are important for this case and the diffraction effects can no longer be ignored. In order for Lamb wave tomography to be fully applicable in-the-field, scattering needs to be accounted for in the tomographic algorithms. As a first step in this process, a theoretical understanding of the Lamb wave scattering needs to be developed. In the next chapter, the scattering theory necessary to model these effects is presented.

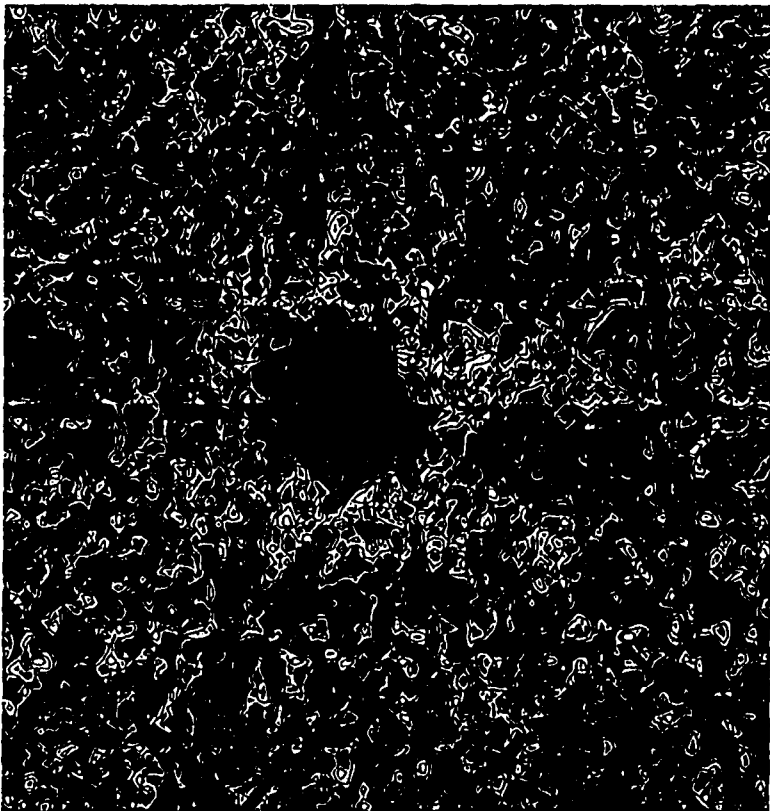


Figure 3.27: PPT reconstruction of an aluminum plate with a 1.50cm diameter through-hole. Note that although the hole is reconstructed in the correct position and with the correct shape, it has some slight scalloping at the edges. This indicates slight diffraction effects.

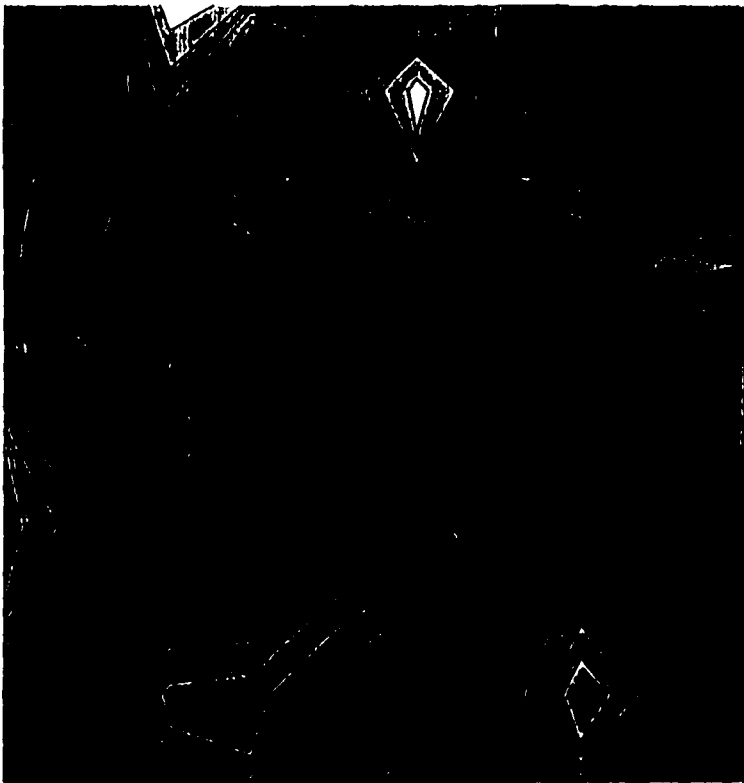


Figure 3.28: CBT reconstruction of the aluminum plate with a 1.50cm diameter through-hole. Again there is lower resolution due to the fewer rays, but the location and size are fairly accurately reproduced.

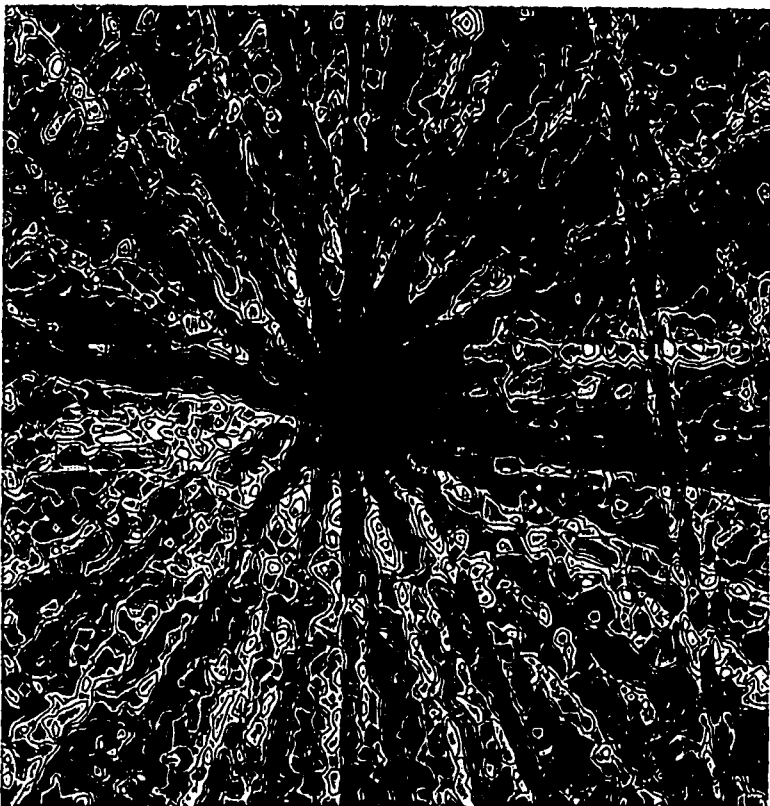


Figure 3.29: PPT reconstruction of the aluminum plate with a 2.54cm diameter through-hole. The hole position and size are still accurately reproduced, but the scalloping is more pronounced and a starburst streaking pattern is visible. These indicate significant diffraction effects.

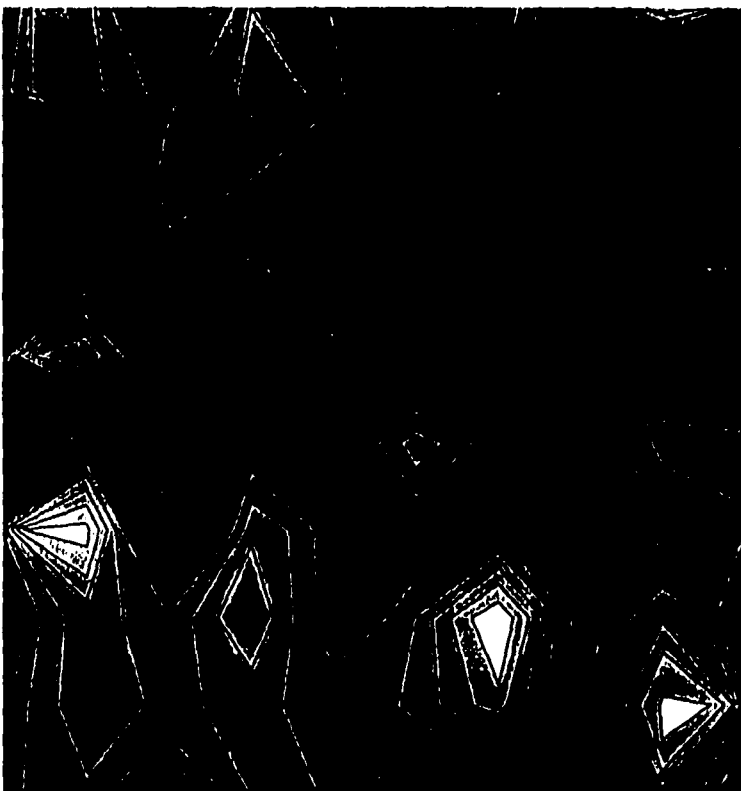


Figure 3.30: CBT reconstruction of the aluminum plate with a 2.54cm diameter through-hole. The hole has been reconstructed in the wrong position. This also shows significant scattering effects for this flaw.

Chapter 4

Scattering Theory

While the simplest plate theories are often used to model the behavior of the lowest order asymmetric Lamb waves, they only describe the dispersionless region of the S_0 curve [250]. Since we are using the dispersion of the S_0 wave to determine the changes in time-of-flight, a theory that accurately models the behavior of the S_0 Lamb wave is necessary. In this chapter, the higher order plate theory of Kane and Mindlin [7] for modeling lower order symmetric Lamb waves is presented, and we show that this approximate theory is valid over the frequency range of interest in our experiments. Next, using this theory, analytical expressions for the scattering of S_0 Lamb waves from a cylindrical inclusion in a plate are derived for an incident plane wave, a point source and a finite source. The expressions are explicitly evaluated for the case of a hole in a plate, and plots of the scattering behavior are used to explain the scattering effects seen in the images at the end of chapter 3.

4.1 Theory of Kane and Mindlin

Consider a homogeneous, isotropic, and linearly elastic plate lying in the xy -plane bounded by air at the planes $z = \pm h$ (Figure 3.1). Because the thickness is small, the components of displacement for dilatational plate waves can be approximated by

$$u_x = v_x(x, y, t) \quad u_y = v_y(x, y, t) \quad u_z = \frac{z}{h} v_z(x, y, t) \quad (4.1)$$

where v_x, v_y, v_z are not functions of z . For the study of free vibrations (of circular frequency ω), these plate displacement components can be expressed in terms of three independent scalar potentials, $\phi_1(x, y), \phi_2(x, y), \Psi$ as

$$v_x = \left(\frac{\partial \phi_1}{\partial x} + \frac{\partial \phi_2}{\partial x} + \frac{\partial \Psi}{\partial y} \right) e^{-i\omega t}$$

$$v_y = \left(\frac{\partial \phi_1}{\partial y} + \frac{\partial \phi_2}{\partial y} - \frac{\partial \Psi}{\partial x} \right) e^{-i\omega t}$$

$$v_z = (\sigma_1 \phi_1 + \sigma_2 \phi_2) e^{-i\omega t}. \quad (4.2)$$

These potentials are chosen to satisfy the scalar Helmholtz equations

$$(\nabla^2 + k_1^2)\phi_1 = 0 \quad (\nabla^2 + k_2^2)\phi_2 = 0 \quad (\nabla^2 + K^2)\Psi = 0 \quad (4.3)$$

where ∇^2 is the 2-D Laplacian, and the effective wavenumbers are given by

$$k_i^2 = \frac{3\kappa^2}{2\beta h} \left[(\alpha + \beta) \frac{\omega^2}{\omega_0^2} - 1 - (-1)^i \psi \right] \quad (i = 1, 2) \quad K^2 = \frac{\omega^2}{c_T^2}. \quad (4.4)$$

In the above equations,

$$\sigma_i = \frac{h(\lambda + 2\mu)}{\kappa\lambda} \left(k_i^2 - \frac{\omega^2}{c_L^2} \right), \quad (i = 1, 2) \quad (4.5)$$

$$\psi = \left[\left((\alpha + \beta) \frac{\omega^2}{\omega_0^2} - 1 \right)^2 + 4\alpha\beta \frac{\omega^2}{\omega_0^2} \left(1 - \frac{\omega^2}{\omega_0^2} \right) \right]^{\frac{1}{2}} \quad (4.6)$$

$$\alpha = \frac{c_L^2}{c_P^2} \quad \beta = \frac{c_T^2}{c_P^2} \quad \omega_0^2 = \frac{\pi^2(\lambda + 2\mu)}{4h^2\rho} \quad (4.7)$$

$$c_L^2 = \frac{\lambda + 2\mu}{\rho} \quad c_T^2 = \frac{\mu}{\rho} \quad c_P^2 = \frac{4\mu(\lambda + \mu)}{\rho(\lambda + 2\mu)} \quad (4.8)$$

where ρ is the mass density of the plate material. λ and μ are the Lamé parameters, and c_L , c_T and c_P are the compressional, shear, and plate wave speeds in isotropic media. Also ω_0 is the frequency corresponding to the first mode of pure thickness vibration of an infinite plate, and the parameter $\kappa^2 = \frac{\pi^2}{12}$ is inserted ad hoc to improve the results [7].

Now we consider specifically straight crested or plane waves. If any one of the functions ϕ_1 , ϕ_2 , or Ψ is taken to be proportional to $e^{i\gamma x}$ while the remaining two are set equal to zero, there results a plane wave propagating in the x -direction and having a wavelength and velocity equal to $\frac{2\pi}{\gamma}$ and $\frac{c}{\gamma}$ respectively. In order to satisfy the above conditions,

$$\gamma = k_1, k_2, K \quad (4.9)$$

depending on which potential is nonzero.

In order to compare this plate theory with the exact theory, the phase velocity, c , is considered. For $\phi_i \neq 0$, $i = 1, 2$, $\Psi = 0$,

$$c = \left(2\alpha c_T^2 \frac{\omega^2}{\omega_0^2} \left[(\alpha + \beta) \frac{\omega^2}{\omega_0^2} - 1 - (-1)^i \psi \right]^{-1} \right)^{\frac{1}{2}} \quad (4.10)$$

and for $\phi_i = 0$, $i = 1, 2$, $\Psi \neq 0$,

$$c = c_T. \quad (4.11)$$

Equation 4.11 obviously shows that the $\Psi \neq 0$ wave matches the shear horizontal wave of exact theory; however, in order to verify these expressions for the $S0$ ($i = 1$) and $S1$ ($i = 2$) Lamb waves, plots of these expressions for phase velocity versus fd can be examined. Figure 4.1 shows the $S0$ and $S1$ dispersion curves for the exact, simple plate, and higher order plate theories. Notice that the higher order plate theory is in qualitative agreement with the exact theory over the full range of fd shown. Most importantly, the dispersion behavior of the $S0$ and $S1$ modes has been captured by the higher order plate theory. The simple plate theory does not model the dispersion behavior of these modes, and the full three-dimensional theory is too complicated to use for scattering calculations. Therefore, these two-dimensional higher-order plate theory expressions for the $S0$ and $S1$ Lamb wave modes contain enough of the mathematical complexity of the Lamb waves to model their behavior, but are not too complicated to prevent their use in scattering calculations.

4.2 Scattering From Cylindrical Inclusions

In this section the theory of Kane and Mindlin is used to study the scattering of plane, point source, and finite source $S0$ Lamb waves from a cylindrical inclusion in a plate. Since we are considering a cylindrical flaw, these calculations are done in cylindrical coordinates.

As in the previous section we consider an infinite plate that is homogeneous, isotropic and linearly elastic. We assume that the plate is bounded by air at the planes $z = \pm h$ and that there is an in-plane disk of radius $r = a$ and thickness h' ,

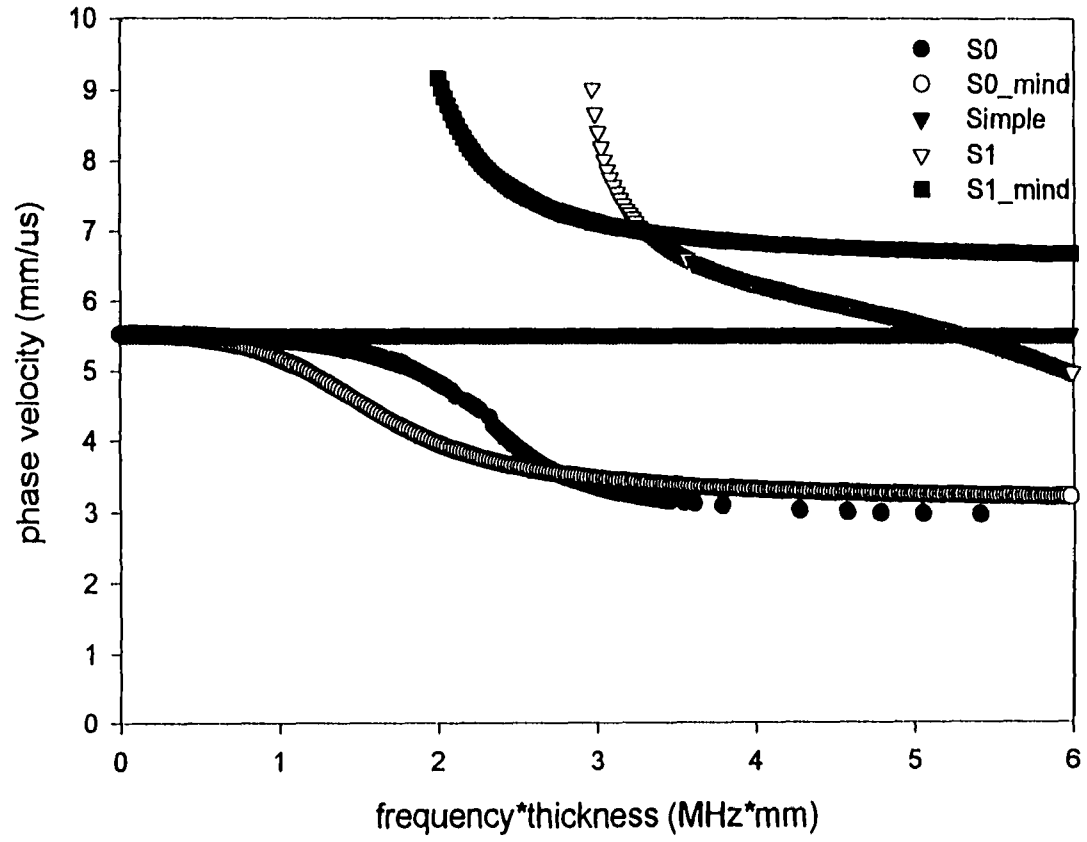


Figure 4.1: Dispersion curves of the exact S_0 , S_1 and approximate S_0 , S_1 Lamb wave modes, and of simple plate theory in aluminum. Note that the approximate theory is in qualitative agreement with the exact theory over the full range shown.

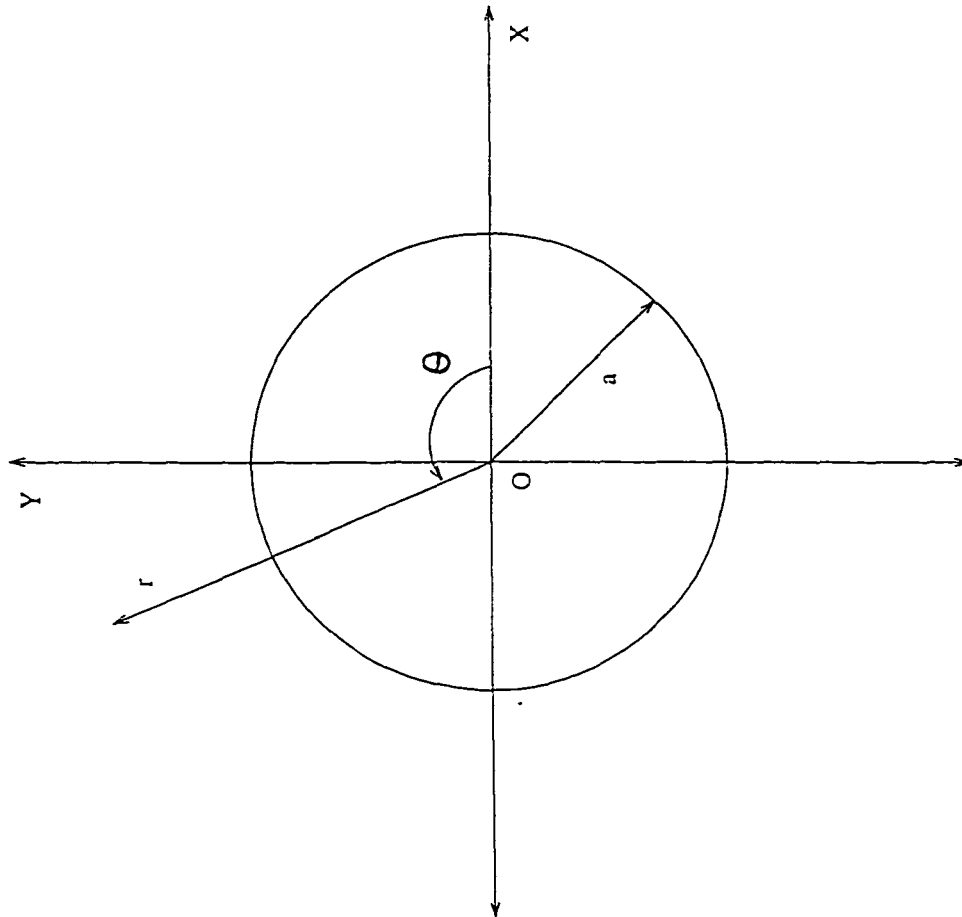


Figure 4.2: Coordinate system for an in-plane disk in an infinite plate

at the origin of a cylindrical coordinate system (Figure 4.2). The disk has material parameters (ρ', λ', μ') that are arbitrarily different from those of the plate (ρ, λ, μ) .

For thin plates we assume that the components of displacement in cylindrical coordinates are approximated sufficiently well by

$$u_r(r, \theta, t) = v_r(r, \theta, t) \quad u_\theta(r, \theta, t) = v_\theta(r, \theta, t) \quad u_z(r, \theta, t) = \frac{z}{h} v_z(r, \theta, t) \quad (4.12)$$

We then introduce three independent displacement potentials $\phi_1(r, \theta)$, $\phi_2(r, \theta)$, $\Psi(r, \theta)$ allowing us to write the displacement components as

$$v_r = \left(\frac{\partial \phi_1}{\partial r} + \frac{\partial \phi_2}{\partial r} + \frac{1}{r} \frac{\partial \Psi}{\partial \theta} \right) e^{-i\omega t}$$

$$v_\theta = \left(\frac{1}{r} \frac{\partial \phi_1}{\partial \theta} + \frac{1}{r} \frac{\partial \phi_2}{\partial \theta} - \frac{\partial \Psi}{\partial r} \right) e^{-i\omega t}$$

$$v_z = \sigma_1 \phi_1 + \sigma_2 \phi_2 e^{-i\omega t}. \quad (4.13)$$

These displacement potentials each satisfy a scalar Helmholtz equation:

$$(\nabla^2 + k_1^2) \phi_1 = 0 \quad (\nabla^2 + k_2^2) \phi_2 = 0 \quad (\nabla^2 + K^2) \Psi = 0. \quad (4.14)$$

In these equations k_i , K , σ_i , ψ , α , β , ω_0 , and κ are the same as in the previous section.

In cylindrical coordinates, the plate stresses defined in terms of three-dimensional stress theory are given by

$$(N_{rr}, N_{\theta\theta}, N_{zz}, N_{r\theta}) = \int_{-h}^h (\sigma_{rr}, \sigma_{\theta\theta}, \sigma_{zz}, \sigma_{r\theta}) dz$$

$$(R_{rz}, R_{\theta z}) = \int_{-h}^h (\sigma_{rz}, \sigma_{\theta z}) z dz. \quad (4.15)$$

For the geometry of this problem we will only be concerned with N_{rr} , $N_{r\theta}$, and N_{rz} . Suppressing the $e^{-i\omega t}$ time variation, the necessary stress components are given by

$$\begin{aligned} \sigma_{rr} &= (\lambda + 2\mu) \frac{\partial v_r}{\partial r} + \lambda \left(\frac{1}{r} \frac{\partial v_\theta}{\partial \theta} + \frac{v_r}{r} + \frac{v_z}{h} \right) \\ \sigma_{r\theta} &= \mu \left(\frac{1}{r} \frac{\partial v_r}{\partial \theta} + \frac{\partial v_\theta}{\partial r} - \frac{v_\theta}{r} \right) \\ \sigma_{rz} &= \mu \left(\frac{z}{h} \frac{\partial v_z}{\partial r} \right) \end{aligned} \quad (4.16)$$

and the useful plate stresses can be written as

$$\begin{aligned} N_{rr} &= 2h \left[(\lambda + 2\mu) \frac{\partial v_r}{\partial r} + \lambda \left(\frac{1}{r} \frac{\partial v_\theta}{\partial \theta} + \frac{v_r}{r} + \frac{v_z}{h} \right) \right] \\ N_{r\theta} &= 2h\mu \left(\frac{1}{r} \frac{\partial v_r}{\partial \theta} + \frac{\partial v_\theta}{\partial r} - \frac{v_\theta}{r} \right) \\ N_{rz} &= \frac{2\mu h^2}{3} \frac{\partial v_z}{\partial r}. \end{aligned} \quad (4.17)$$

Plane Waves

Now we consider the case of an incident plane S0 wave (Figure 4.3) described by, suppressing $e^{-i\omega t}$,

$$\phi_1^{INC} = e^{ik_1 x} \quad \phi_2^{INC} = \Psi^{INC} = 0. \quad (4.18)$$

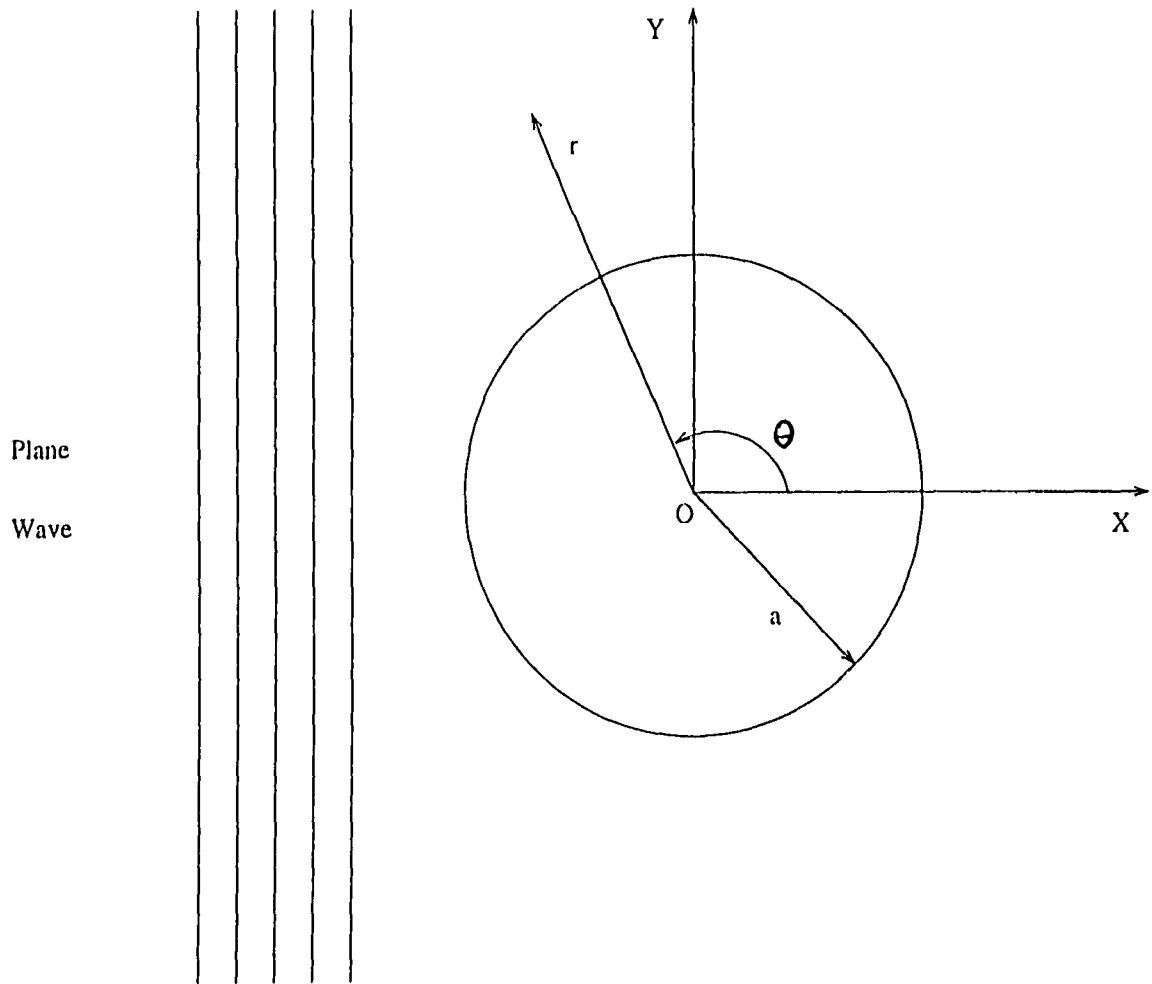


Figure 4.3: Coordinate system for a plane S_0 Lamb wave incident upon a cylindrical inclusion in an infinite plate

For a cylindrical scatterer at the origin of a cylindrical coordinate system, the general solutions of the scattered and transmitted waves are expanded as

$$\begin{aligned}
 \phi_1^{SCAT} &= \sum_{n=-\infty}^{\infty} A_n H_n(k_1 r) e^{in\theta} \\
 \phi_2^{SCAT} &= \sum_{n=-\infty}^{\infty} B_n H_n(k_2 r) e^{in\theta} \\
 \Psi^{SCAT} &= \sum_{n=-\infty}^{\infty} C_n H_n(Kr) e^{in\theta} \\
 \phi_1^{TRANS} &= \sum_{n=-\infty}^{\infty} A'_n J_n(k'_1 r) e^{in\theta} \\
 \phi_2^{TRANS} &= \sum_{n=-\infty}^{\infty} B'_n J_n(k'_2 r) e^{in\theta} \\
 \Psi^{TRANS} &= \sum_{n=-\infty}^{\infty} C'_n J_n(K'r) e^{in\theta} \tag{4.19}
 \end{aligned}$$

where A_n, \dots, C'_n are unknown modal coefficients to be determined from the boundary conditions, J_n are Bessel functions, and H_n are Hankel functions of the first kind. The Bessel and Hankel functions have been chosen so that the waves approaching zero and those approaching infinity are finite.

In cylindrical coordinates, the plane wave is represented by

$$\phi_1^{INC} = e^{ik_1 r \cos \theta}, \tag{4.20}$$

and using the generating function for $J_n(x)$,

$$e^{x(t-1/t)/2} = \sum_{n=-\infty}^{\infty} J_n(x) t^n, \tag{4.21}$$

we can expand the incident plane wave potential as

$$\phi_1^{INC} = \sum_{n=-\infty}^{\infty} i^n J_n(k_1 r) e^{in\theta}. \quad (4.22)$$

Because of the form of the incident wave, we rewrite the scattered and transmitted waves as

$$\begin{aligned} \phi_1^{SCAT} &= \sum_{n=-\infty}^{\infty} A_n i^n H_n(k_1 r) e^{in\theta} \\ \phi_2^{SCAT} &= \sum_{n=-\infty}^{\infty} B_n i^n H_n(k_2 r) e^{in\theta} \\ \Psi^{SCAT} &= \sum_{n=-\infty}^{\infty} C_n i^n H_n(K r) e^{in\theta} \\ \phi_1^{TRANS} &= \sum_{n=-\infty}^{\infty} A'_n i^n J_n(k'_1 r) e^{in\theta} \\ \phi_2^{TRANS} &= \sum_{n=-\infty}^{\infty} B'_n i^n J_n(k'_2 r) e^{in\theta} \\ \Psi^{TRANS} &= \sum_{n=-\infty}^{\infty} C'_n i^n J_n(K' r) e^{in\theta} \end{aligned} \quad (4.23)$$

where we have simply pulled a factor of i^n out of each modal coefficient for later convenience.

For this problem, we need to consider continuity of displacements at $r = a$

$$v_r^{INC} + v_r^{SCAT} = v_r^{TRANS}$$

$$v_\theta^{INC} + v_\theta^{SCAT} = v_\theta^{TRANS}$$

$$v_z^{INC} + v_z^{SCAT} = v_z^{TRANS} \quad (4.24)$$

and continuity of plate stresses at $r = a$

$$N_{rr}^{INC} + N_{rr}^{SCAT} = N_{rr}^{TRANS}$$

$$N_{r\theta}^{INC} + N_{r\theta}^{SCAT} = N_{r\theta}^{TRANS}$$

$$R_{rz}^{INC} + R_{rz}^{SCAT} = R_{rz}^{TRANS}. \quad (4.25)$$

So we have six equations and six unknowns. After using Equations 4.13 and 4.17, dropping the summations, and rewriting, these boundary condition equations become

$$\begin{aligned} & A_n[(k_1 a)H'_n(k_1 a)] + B_n[(k_2 a)H'_n(k_2 a)] + C_n[(in)H_n(Ka)] \\ + & A'_n[-(k'_1 a)J'_n(k'_1 a)] + B'_n[-(k'_2 a)J'_n(k'_2 a)] + C'_n[-(in)J_n(K'a)] \\ = & [-(k_1 a)J'_n(k_1 a)] \end{aligned} \quad (4.26)$$

$$\begin{aligned} & A_n[(in)H_n(k_1 a)] + B_n[(in)H_n(k_2 a)] + C_n[-(Ka)H'_n(Ka)] \\ + & A'_n[-(in)J_n(k'_1 a)] + B'_n[-(in)J_n(k'_2 a)] + C'_n[(K'a)J'_n(K'a)] \\ = & [-(in)J_n(k_1 a)] \end{aligned} \quad (4.27)$$

$$\begin{aligned}
& A_n \left[\left(\frac{\sigma_1 a^2}{h} \right) H_n(k_1 a) \right] + B_n \left[\left(\frac{\sigma_2 a^2}{h} \right) H_n(k_2 a) \right] \\
+ & A'_n \left[- \left(\frac{h' \sigma'_1 a^2}{h h'} \right) J_n(k'_1 a) \right] + B'_n \left[- \left(\frac{h' \sigma'_2 a^2}{h h'} \right) J_n(k'_2 a) \right] \\
= & \left[- \left(\frac{\sigma_1 a^2}{h} \right) J_n(k_1 a) \right] \tag{4.28}
\end{aligned}$$

$$\begin{aligned}
& A_n [\alpha_1 H_n(k_1 a) - (k_1 a) H'_n(k_1 a)] \\
+ & B_n [\alpha_2 H_n(k_2 a) - (k_2 a) H'_n(k_2 a)] \\
+ & C_n [(inK a) H'_n(K a) - (in) H_n(K a)] \\
- & A'_n \left(\frac{\mu'}{\mu} \right) \left(\frac{h'}{h} \right) [\alpha'_1 J_n(k'_1 a) - (k'_1 a) J'_n(k'_1 a)] \\
- & B'_n \left(\frac{\mu'}{\mu} \right) \left(\frac{h'}{h} \right) [\alpha'_2 J_n(k'_2 a) - (k'_2 a) J'_n(k'_2 a)] \\
- & C'_n \left(\frac{\mu'}{\mu} \right) \left(\frac{h'}{h} \right) [(inK' a) J'_n(K' a) - (in) J_n(K' a)] \\
= & -[\alpha_1 J_n(k_1 a) - (k_1 a) J'_n(k_1 a)] \tag{4.29}
\end{aligned}$$

$$\begin{aligned}
& A_n [(2ink_1 a) H'_n(k_1 a) - (2in) H_n(k_1 a)] \\
+ & B_n [(2ink_2 a) H'_n(k_2 a) - (2in) H_n(k_2 a)] \\
+ & C_n [((K a)^2 - 2n^2) H_n(K a) + (2K a) H'_n(K a)] \\
- & A'_n \left(\frac{\mu'}{\mu} \right) \left(\frac{h'}{h} \right) [(2ink'_1 a) J'_n(k'_1 a) - (2in) J_n(k'_1 a)] \\
- & B'_n \left(\frac{\mu'}{\mu} \right) \left(\frac{h'}{h} \right) [(2ink'_2 a) J'_n(k'_2 a) - (2in) J_n(k'_2 a)] \\
- & C'_n \left(\frac{\mu'}{\mu} \right) \left(\frac{h'}{h} \right) [((K' a)^2 - 2n^2) J_n(K' a) + (2K' a) J'_n(K' a)] \\
= & -[(2ink_1 a) J'_n(k_1 a) - (2in) J_n(k_1 a)] \tag{4.30}
\end{aligned}$$

$$\begin{aligned}
& A_n \left[\left(\frac{\sigma_1 a^2}{h} \right) (k_1 a) H'_n(k_1 a) \right] \\
& + B_n \left[\left(\frac{\sigma_2 a^2}{h} \right) (k_2 a) H'_n(k_2 a) \right] \\
& - A'_n \left(\frac{\mu'}{\mu} \right) \left(\frac{h'}{h} \right)^3 \left[\left(\frac{\sigma'_1 a^2}{h'} \right) (k'_1 a) J'_n(k'_1 a) \right] \\
& - B'_n \left(\frac{\mu'}{\mu} \right) \left(\frac{h'}{h} \right)^3 \left[\left(\frac{\sigma'_2 a^2}{h'} \right) (k'_2 a) J'_n(k'_2 a) \right] \\
& = - \left[\left(\frac{\sigma_1 a^2}{h} \right) (k_1 a) J'_n(k_1 a) \right]
\end{aligned} \tag{4.31}$$

where

$$\begin{aligned}
\alpha_{1,2} &= \frac{1}{2} \frac{c_L^2}{c_T^2} \left(\frac{\sigma_{1,2} a^2}{h} - (k_{1,2} a)^2 \right) + n^2 - \frac{\sigma_{1,2} a^2}{h} \\
\alpha'_{1,2} &= \frac{1}{2} \frac{c_L'^2}{c_T'^2} \left(\frac{\sigma'_{1,2} a^2}{h'} - (k'_{1,2} a)^2 \right) + n^2 - \frac{\sigma'_{1,2} a^2}{h'}
\end{aligned} \tag{4.32}$$

and the prime on the Bessel and Hankel functions denotes $\frac{\partial}{\partial(\gamma r)}$ where gamma is the same as in Equation 4.9. Note that for this work we have used the fact that

$$\frac{\partial}{\partial r} = \frac{\partial}{\partial(\gamma r)} \frac{\partial(\gamma r)}{\partial r} = \gamma \frac{\partial}{\partial(\gamma r)}. \tag{4.33}$$

We can rewrite the six boundary condition equations in matrix form as

$$\left(\begin{array}{cccc}
(k_1 a) H'_n(k_1 a) & (k_2 a) H'_n(k_2 a) & (in) H_n(K a) & -(k'_1 a) J'_n(k'_1 a) \\
(in) H_n(k_1 a) & (in) H_n(k_2 a) & -(K a) H'_n(K a) & -(in) J_n(k'_1 a) \\
\left(\frac{\sigma_1 a^2}{h} \right) H_n(k_1 a) & \left(\frac{\sigma_2 a^2}{h} \right) H_n(k_2 a) & 0 & -\left(\frac{h'}{h} \frac{\sigma'_1 a^2}{h'} \right) J_n(k'_1 a) \\
B_{41} & B_{42} & B_{43} & B_{44} \\
B_{51} & B_{52} & B_{53} & B_{54} \\
B_{61} & B_{62} & 0 & B_{64}
\end{array} \right)$$

$$\begin{pmatrix} -(k'_2 a) J'_n(k'_2 a) & -(in) J_n(K' a) \\ -(in) J_n(k'_2 a) & (K' a) J'_n(K' a) \\ -(\frac{h'}{h} \frac{\sigma'_2 a^2}{h'}) J_n(k'_2 a) & 0 \\ B_{45} & B_{46} \\ B_{55} & B_{56} \\ B_{65} & 0 \end{pmatrix} \begin{pmatrix} A_n \\ B_n \\ C_n \\ A'_n \\ B'_n \\ C'_n \end{pmatrix} = \begin{pmatrix} -(k_1 a) J'_n(k_1 a) \\ -(in) J_n(k_1 a) \\ -(\frac{\sigma_1 a^2}{h}) J_n(k_1 a) \\ C_{41} \\ C_{51} \\ C_{61} \end{pmatrix} \quad (4.34)$$

where

$$\begin{aligned} B_{41} &= [\alpha_1 H_n(k_1 a) - (k_1 a) H'_n(k_1 a)] \\ B_{42} &= [\alpha_2 H_n(k_2 a) - (k_2 a) H'_n(k_2 a)] \\ B_{43} &= [(in K a) H'_n(K a) - (in) H_n(K a)] \\ B_{44} &= -\left(\frac{\mu'}{\mu}\right) \left(\frac{h'}{h}\right) [\alpha'_1 J_n(k'_1 a) - (k'_1 a) J'_n(k'_1 a)] \\ B_{45} &= -\left(\frac{\mu'}{\mu}\right) \left(\frac{h'}{h}\right) [\alpha'_2 J_n(k'_2 a) - (k'_2 a) J'_n(k'_2 a)] \\ B_{46} &= -\left(\frac{\mu'}{\mu}\right) \left(\frac{h'}{h}\right) [(in K' a) J'_n(K' a) - (in) J_n(K' a)] \end{aligned} \quad (4.35)$$

$$\begin{aligned} B_{51} &= [(2ink_1 a) H'_n(k_1 a) - (2in) H_n(k_1 a)] \\ B_{52} &= [(2ink_2 a) H'_n(k_2 a) - (2in) H_n(k_2 a)] \\ B_{53} &= [((K a)^2 - 2n^2) H_n(K a) - (2K a) H'_n(K a)] \\ B_{54} &= -\left(\frac{\mu'}{\mu}\right) \left(\frac{h'}{h}\right) [(2ink'_1 a) J'_n(k'_1 a) - (2in) J_n(k'_1 a)] \\ B_{55} &= -\left(\frac{\mu'}{\mu}\right) \left(\frac{h'}{h}\right) [(2ink'_2 a) J'_n(k'_2 a) - (2in) J_n(k'_2 a)] \\ B_{56} &= -\left(\frac{\mu'}{\mu}\right) \left(\frac{h'}{h}\right) [((K' a)^2 - 2n^2) J_n(K' a) + (2K' a) J'_n(K' a)] \end{aligned} \quad (4.36)$$

$$\begin{aligned}
B_{61} &= \left[\left(\frac{\sigma_1 a^2}{h} \right) (k_1 a) H'_n(k_1 a) \right] \\
B_{62} &= \left[\left(\frac{\sigma_2 a^2}{h} \right) (k_2 a) H'_n(k_2 a) \right] \\
B_{64} &= - \left(\frac{\mu'}{\mu} \right) \left(\frac{h'}{h} \right)^3 \left[\left(\frac{\sigma'_1 a^2}{h'} \right) (k'_1 a) J'_n(k'_1 a) \right] \\
B_{65} &= - \left(\frac{\mu'}{\mu} \right) \left(\frac{h'}{h} \right)^3 \left[\left(\frac{\sigma'_2 a^2}{h'} \right) (k'_2 a) J'_n(k'_2 a) \right]
\end{aligned} \tag{4.37}$$

$$\begin{aligned}
C_{41} &= -[\alpha_1 J_n(k_1 a) - (k_1 a) J'_n(k_1 a)] \\
C_{51} &= -[(2in k_1 a) J'_n(k_1 a) - (2in) J_n(k_1 a)] \\
C_{61} &= - \left[\left(\frac{\sigma_1 a^2}{h} \right) (k_1 a) J'_n(k_1 a) \right].
\end{aligned} \tag{4.38}$$

Then using Cramer's rule, we can solve this matrix equation for the unknown modal coefficients and write them as

$$\begin{aligned}
A_n &= \frac{\Delta_1}{\Delta_0} & B_n &= \frac{\Delta_2}{\Delta_0} & C_n &= \frac{\Delta_3}{\Delta_0} \\
A'_n &= \frac{\Delta_4}{\Delta_0} & B'_n &= \frac{\Delta_5}{\Delta_0} & C'_n &= \frac{\Delta_6}{\Delta_0}
\end{aligned} \tag{4.39}$$

where

$$\Delta_0 = \begin{vmatrix}
(k_1 a) H'_n(k_1 a) & (k_2 a) H'_n(k_2 a) & (in) H_n(K a) & -(k'_1 a) J'_n(k'_1 a) \\
(in) H_n(k_1 a) & (in) H_n(k_2 a) & -(K a) H'_n(K a) & -(in) J_n(k'_1 a) \\
\left(\frac{\sigma_1 a^2}{h} \right) H_n(k_1 a) & \left(\frac{\sigma_2 a^2}{h} \right) H_n(k_2 a) & 0 & -\left(\frac{h'}{h} \frac{\sigma'_1 a^2}{h'} \right) J_n(k'_1 a) \\
B_{41} & B_{42} & B_{43} & B_{44} \\
B_{51} & B_{52} & B_{53} & B_{54} \\
B_{61} & B_{62} & 0 & B_{64}
\end{vmatrix}$$

$$\begin{array}{cc|c}
 -(k'_2 a) J'_n(k'_2 a) & -(in) J_n(K' a) & \\
 -(in) J_n(k'_2 a) & (K' a) J'_n(K' a) & \\
 -(\frac{\hbar'}{\hbar} \frac{\sigma'_2 a^2}{\hbar'}) J_n(k'_2 a) & 0 & \\
 B_{45} & B_{46} & \\
 B_{55} & B_{56} & \\
 B_{65} & 0 &
 \end{array} \quad (4.40)$$

$$\Delta_1 = \begin{array}{cccc|c}
 -(k_1 a) J'_n(k_1 a) & (k_2 a) H'_n(k_2 a) & (in) H_n(K a) & -(k'_1 a) J'_n(k'_1 a) & \\
 -(in) J_n(k_1 a) & (in) H_n(k_2 a) & -(K a) H'_n(K a) & -(in) J_n(k'_1 a) & \\
 -(\frac{\sigma_1 a^2}{\hbar}) J_n(k_1 a) & (\frac{\sigma_2 a^2}{\hbar}) H_n(k_2 a) & 0 & -(\frac{\hbar'}{\hbar} \frac{\sigma'_1 a^2}{\hbar'}) J_n(k'_1 a) & \\
 C_{41} & B_{42} & B_{43} & B_{44} & \\
 C_{51} & B_{52} & B_{53} & B_{54} & \\
 C_{61} & B_{62} & 0 & B_{64} &
 \end{array}$$

$$\begin{array}{cc|c}
 -(k'_2 a) J'_n(k'_2 a) & -(in) J_n(K' a) & \\
 -(in) J_n(k'_2 a) & (K' a) J'_n(K' a) & \\
 -(\frac{\hbar'}{\hbar} \frac{\sigma'_2 a^2}{\hbar'}) J_n(k'_2 a) & 0 & \\
 B_{45} & B_{46} & \\
 B_{55} & B_{56} & \\
 B_{65} & 0 &
 \end{array} \quad (4.41)$$

$$\Delta_2 = \begin{vmatrix} (k_1 a)H'_n(k_1 a) & -(k_1 a)J'_n(k_1 a) & (in)H_n(Ka) & -(k'_1 a)J'_n(k'_1 a) \\ (in)H_n(k_1 a) & -(in)J_n(k_1 a) & -(Ka)H'_n(Ka) & -(in)J_n(k'_1 a) \\ (\frac{\sigma_1 a^2}{h})H_n(k_1 a) & -(\frac{\sigma_1 a^2}{h})J_n(k_1 a) & 0 & -(\frac{h'}{h} \frac{\sigma'_1 a^2}{h'})J_n(k'_1 a) \\ B_{41} & C_{41} & B_{43} & B_{44} \\ B_{51} & C_{51} & B_{53} & B_{54} \\ B_{61} & C_{61} & 0 & B_{64} \end{vmatrix}$$

$$\begin{vmatrix} -(k'_2 a)J'_n(k'_2 a) & -(in)J_n(K'a) \\ -(in)J_n(k'_2 a) & (K'a)J'_n(K'a) \\ -(\frac{h'}{h} \frac{\sigma'_2 a^2}{h'})J_n(k'_2 a) & 0 \\ B_{45} & B_{46} \\ B_{55} & B_{56} \\ B_{65} & 0 \end{vmatrix} \quad (4.42)$$

$$\Delta_3 = \begin{vmatrix} (k_1 a)H'_n(k_1 a) & (k_2 a)H'_n(k_2 a) & -(k_1 a)J'_n(k_1 a) & -(k'_1 a)J'_n(k'_1 a) \\ (in)H_n(k_1 a) & (in)H_n(k_2 a) & -(in)J_n(k_1 a) & -(in)J_n(k'_1 a) \\ (\frac{\sigma_1 a^2}{h})H_n(k_1 a) & (\frac{\sigma_2 a^2}{h})H_n(k_2 a) & -(\frac{\sigma_1 a^2}{h})J_n(k_1 a) & -(\frac{h'}{h} \frac{\sigma'_1 a^2}{h'})J_n(k'_1 a) \\ B_{41} & B_{42} & C_{41} & B_{44} \\ B_{51} & B_{52} & C_{51} & B_{54} \\ B_{61} & B_{62} & C_{61} & B_{64} \end{vmatrix}$$

$$\begin{array}{cc|c}
 -(k'_2 a) J'_n(k'_2 a) & -(in) J_n(K' a) & \\
 -(in) J_n(k'_2 a) & (K' a) J'_n(K' a) & \\
 -\left(\frac{h'}{h} \frac{\sigma'_2 a^2}{h'}\right) J_n(k'_2 a) & 0 & \\
 B_{45} & B_{46} & \\
 B_{55} & B_{56} & \\
 B_{65} & 0 &
 \end{array} \quad (4.43)$$

$$\Delta_4 = \begin{array}{cccc|c}
 (k_1 a) H'_n(k_1 a) & (k_2 a) H'_n(k_2 a) & (in) H_n(K a) & -(k_1 a) J'_n(k_1 a) & \\
 (in) H_n(k_1 a) & (in) H_n(k_2 a) & -(K a) H'_n(K a) & -(in) J_n(k_1 a) & \\
 \left(\frac{\sigma_1 a^2}{h}\right) H_n(k_1 a) & \left(\frac{\sigma_2 a^2}{h}\right) H_n(k_2 a) & 0 & -\left(\frac{\sigma_1 a^2}{h}\right) J_n(k_1 a) & \\
 B_{41} & B_{42} & B_{43} & C_{41} & \\
 B_{51} & B_{52} & B_{53} & C_{51} & \\
 B_{61} & B_{62} & 0 & C_{61} &
 \end{array}$$

$$\begin{array}{cc|c}
 -(k'_2 a) J'_n(k'_2 a) & -(in) J_n(K' a) & \\
 -(in) J_n(k'_2 a) & (K' a) J'_n(K' a) & \\
 -\left(\frac{h'}{h} \frac{\sigma'_2 a^2}{h'}\right) J_n(k'_2 a) & 0 & \\
 B_{45} & B_{46} & \\
 B_{55} & B_{56} & \\
 B_{65} & 0 &
 \end{array} \quad (4.44)$$

$$\begin{aligned}
 \Delta_5 = & \left| \begin{array}{cccc}
 (k_1 a)H'_n(k_1 a) & (k_2 a)H'_n(k_2 a) & (in)H_n(Ka) & -(k'_1 a)J'_n(k'_1 a) \\
 (in)H_n(k_1 a) & (in)H_n(k_2 a) & -(Ka)H'_n(Ka) & -(in)J_n(k'_1 a) \\
 (\frac{\sigma_1 a^2}{h})H_n(k_1 a) & (\frac{\sigma_2 a^2}{h})H_n(k_2 a) & 0 & -(\frac{h'}{h} \frac{\sigma'_1 a^2}{h'})J_n(k'_1 a) \\
 B_{41} & B_{42} & B_{43} & B_{44} \\
 B_{51} & B_{52} & B_{53} & B_{54} \\
 B_{61} & B_{62} & 0 & B_{64}
 \end{array} \right. \\
 & \left. \begin{array}{cc}
 -(k_1 a)J'_n(k_1 a) & -(in)J_n(K'a) \\
 -(in)J_n(k_1 a) & (K'a)J'_n(K'a) \\
 -(\frac{\sigma_1 a^2}{h})J_n(k_1 a) & 0 \\
 C_{41} & B_{46} \\
 C_{51} & B_{56} \\
 C_{61} & 0
 \end{array} \right| \quad (4.45)
 \end{aligned}$$

$$\Delta_6 = \left| \begin{array}{cccc}
 (k_1 a)H'_n(k_1 a) & (k_2 a)H'_n(k_2 a) & (in)H_n(Ka) & -(k'_1 a)J'_n(k'_1 a) \\
 (in)H_n(k_1 a) & (in)H_n(k_2 a) & -(Ka)H'_n(Ka) & -(in)J_n(k'_1 a) \\
 (\frac{\sigma_1 a^2}{h})H_n(k_1 a) & (\frac{\sigma_2 a^2}{h})H_n(k_2 a) & 0 & -(\frac{h'}{h} \frac{\sigma'_1 a^2}{h'})J_n(k'_1 a) \\
 B_{41} & B_{42} & B_{43} & B_{44} \\
 B_{51} & B_{52} & B_{53} & B_{54} \\
 B_{61} & B_{62} & 0 & B_{64}
 \end{array} \right|$$

$$\begin{array}{cc}
 -(k'_2 a) J'_n(k'_2 a) & -(k_1 a) J'_n(k_1 a) \\
 -(in) J_n(k'_2 a) & -(in) J_n(k_1 a) \\
 -\left(\frac{h'}{h} \frac{\sigma'_2 a^2}{h'}\right) J_n(k'_2 a) & -\left(\frac{\sigma_1 a^2}{h}\right) J_n(k_1 a) \\
 B_{45} & C_{41} \\
 B_{55} & C_{51} \\
 B_{65} & C_{61}
 \end{array} \Bigg| \quad (4.46)$$

Now we have expressions for the modal coefficients for the case of a plane wave incident upon a general cylindrical scatterer. However, in order to explain the scattering effects seen in Figures 3.29 and 3.30, the specific case of the cylindrical scatterer being a hole must be considered. In this case, the normal tractions at the boundary must equal zero, and we set $A'_n \equiv B'_n \equiv C'_n \equiv 0$. Now we have three unknown modal coefficients (A_n, B_n, C_n). Therefore, we only consider the three plate stress boundary conditions of Equation 4.25. For this case, the matrix equation becomes

$$\begin{pmatrix} B_{41} & B_{42} & B_{43} \\ B_{51} & B_{52} & B_{53} \\ B_{61} & B_{62} & 0 \end{pmatrix} \begin{pmatrix} A_n \\ B_n \\ C_n \end{pmatrix} = \begin{pmatrix} C_{41} \\ C_{51} \\ C_{61} \end{pmatrix} \quad (4.47)$$

where the B_{ij} 's and C_{ij} 's are as defined in Equations 4.35 - 4.38. Again applying Cramer's Rule we have

$$A_n = \frac{\Delta_1}{\Delta_0}, \quad B_n = \frac{\Delta_2}{\Delta_0}, \quad C_n = \frac{\Delta_3}{\Delta_0} \quad (4.48)$$

where the Δ 's are now

$$\Delta_0 = \begin{vmatrix} B_{41} & B_{42} & B_{43} \\ B_{51} & B_{52} & B_{53} \\ B_{61} & B_{62} & 0 \end{vmatrix} \quad \Delta_1 = \begin{vmatrix} C_{41} & B_{42} & B_{43} \\ C_{51} & B_{52} & B_{53} \\ C_{61} & B_{62} & 0 \end{vmatrix} \quad (4.49)$$

$$\Delta_2 = \begin{vmatrix} B_{41} & C_{41} & B_{43} \\ B_{51} & C_{51} & B_{53} \\ B_{61} & C_{61} & 0 \end{vmatrix} \quad \Delta_3 = \begin{vmatrix} B_{41} & B_{42} & C_{41} \\ B_{51} & B_{52} & C_{51} \\ B_{61} & B_{62} & C_{61} \end{vmatrix}. \quad (4.50)$$

Expanding these determinants then gives

$$\begin{aligned} \Delta_0 &= \left(\frac{\sigma_1 a^2}{h}\right) (k_1 a) (\alpha_2 (K a)^2 + 2n^2 (1 - \alpha_2)) H'_n(k_1 a) H_n(k_2 a) H_n(K a) \\ &+ 2 \left(\frac{\sigma_1 a^2}{h}\right) (k_1 a) (K a) (\alpha_2 - n^2) H'_n(k_1 a) H_n(k_2 a) H'_n(K a) \\ &+ (k_1 a) (k_2 a) (K a)^2 \left(\frac{\sigma_2 a^2}{h} - \frac{\sigma_1 a^2}{h}\right) H'_n(k_1 a) H'_n(k_2 a) H_n(K a) \\ &- 2(k_1 a) (k_2 a) (K a) (n^2 - 1) \left(\frac{\sigma_2 a^2}{h} - \frac{\sigma_1 a^2}{h}\right) H'_n(k_1 a) H'_n(k_2 a) H'_n(K a) \\ &- \left(\frac{\sigma_2 a^2}{h}\right) (k_2 a) (\alpha_1 (K a)^2 + 2n^2 (1 - \alpha_1)) H_n(k_1 a) H'_n(k_2 a) H_n(K a) \\ &- 2 \left(\frac{\sigma_2 a^2}{h}\right) (k_2 a) (K a) (\alpha_1 - n^2) H_n(k_1 a) H'_n(k_2 a) H'_n(K a) \end{aligned} \quad (4.51)$$

$$\begin{aligned}
\Delta_1 = & -\left(\frac{\sigma_1 a^2}{h}\right) (k_1 a)(\alpha_2(Ka)^2 + 2n^2(1 - \alpha_2))J'_n(k_1 a)H_n(k_2 a)H_n(Ka) \\
& - 2\left(\frac{\sigma_1 a^2}{h}\right) (k_1 a)(Ka)(\alpha_2 - n^2)J'_n(k_1 a)H_n(k_2 a)H'_n(Ka) \\
& - (k_1 a)(k_2 a)(Ka)^2\left(\frac{\sigma_2 a^2}{h} - \frac{\sigma_1 a^2}{h}\right)J'_n(k_1 a)H'_n(k_2 a)H_n(Ka) \\
& + 2(k_1 a)(k_2 a)(Ka)(n^2 - 1)\left(\frac{\sigma_2 a^2}{h} - \frac{\sigma_1 a^2}{h}\right)J'_n(k_1 a)H'_n(k_2 a)H'_n(Ka) \\
& + \left(\frac{\sigma_2 a^2}{h}\right) (k_2 a)(\alpha_1(Ka)^2 + 2n^2(1 - \alpha_1))J_n(k_1 a)H'_n(k_2 a)H_n(Ka) \\
& + 2\left(\frac{\sigma_2 a^2}{h}\right) (k_2 a)(Ka)(\alpha_1 - n^2)J_n(k_1 a)H'_n(k_2 a)H'_n(Ka) \tag{4.52}
\end{aligned}$$

$$\Delta_2 = -\frac{2i}{\pi}\left(\frac{\sigma_1 a^2}{h}\right)[(\alpha_1(Ka)^2 + 2n^2(1 - \alpha_1))H_n(Ka) + 2(Ka)(\alpha_1 - n^2)H'_n(Ka)] \tag{4.53}$$

$$\Delta_3 = \frac{4n}{\pi}\left[(k_2 a)\left(\frac{\sigma_2 a^2}{h} - \frac{\sigma_1 a^2}{h}\right)(\alpha_1 - 1)H'_n(k_2 a) - \left(\frac{\sigma_1 a^2}{h}\right)(\alpha_2 - \alpha_1)H_n(k_2 a)\right]. \tag{4.54}$$

The behavior of the S_0 Lamb wave field for the case of a plane wave incident upon a hole can now be examined using the equations for ϕ_1^{INC} , ϕ_1^{SCAT} , and A_n . These equations are far too complicated to give any intuitive understanding, so instead plots of the magnitude of the scattered amplitude of the S_0 wave and of the vertical displacement of the top surface of the plate due to the combined incident and scattered S_0 wave at the point of measurement in the experiments are shown.

Point Source

We next consider the case of the incident S_0 Lamb wave being generated by a point source. The geometry for this case is shown in Figure 4.4. Following the

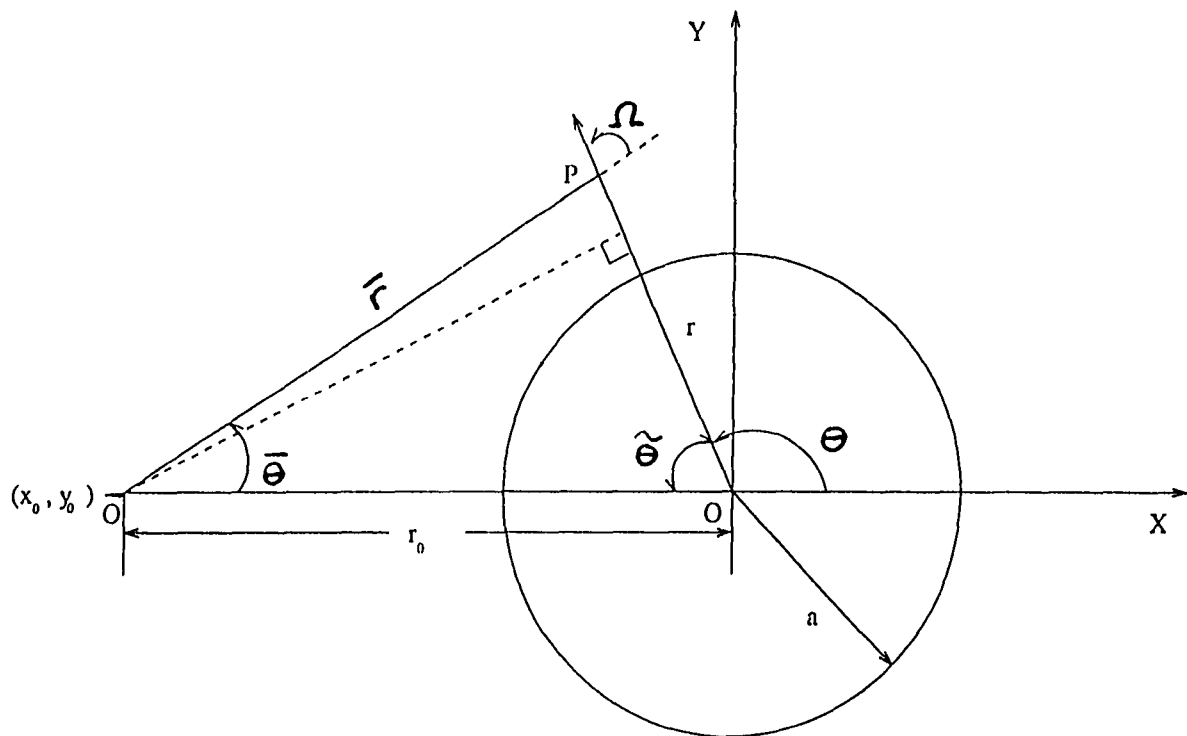


Figure 4.4: Coordinate system for a point source S_0 Lamb wave incident upon a cylindrical inclusion in an infinite plate

discussion of Pao and Mow [462], the incident wave potential from a point source in two dimensions can be expanded in cylindrical functions as, suppressing $e^{-i\omega t}$,

$$\phi_1^{INC} = \sum_{n=-\infty}^{\infty} H_0(k_1 \bar{r}). \quad (4.55)$$

This represents a cylindrical wave propagating outward from the source at $\bar{0}$ in the $(\bar{r}, \bar{\theta})$ coordinate system. Because of the axial symmetry of the source, only the zeroth order Hankel function is necessary. The scattered and transmitted fields are again given by Equation 4.19, in which the waves are propagating outward from the axis 0 in the (r, θ) coordinate system. Therefore, we need to transform the incident wave from the $(\bar{r}, \bar{\theta})$ to the (r, θ) coordinates.

From Figure 4.4. we can see that

$$\begin{aligned} \bar{r} \sin \Omega &= r_0 \sin \bar{\theta} \\ \bar{r} \cos \Omega &= \bar{r} \cos (\bar{\theta} - \theta) = r - r_0 \cos \bar{\theta}, \end{aligned} \quad (4.56)$$

and we can represent $H_m(k_1 \bar{r})e^{im\bar{\theta}}$ as

$$\frac{1}{\pi} \int_{C_1} e^{ik_1 \bar{r} \cos \phi + im(\phi + \bar{\theta} - \frac{\pi}{2})} d\phi \quad (4.57)$$

where C_1 is the contour path going from $m = -\frac{\pi}{2}$ to $m = \frac{\pi}{2}$ [462]. Because of the periodic properties of the integrand, we can write this integral expression as

$$\frac{1}{\pi} \int_{C_1} e^{ik_1 \bar{r} \cos(\phi + \Omega) + im(\phi + \bar{\theta} + \Omega - \frac{\pi}{2})} d\phi. \quad (4.58)$$

Then using Equation 4.56 and the fact that $\Omega = \theta - \bar{\theta}$, we have

$$\frac{1}{\pi} \int_{C_1} e^{ik_1 r \cos \phi + ik_1 r_0 \cos(\theta + \phi) + im(\phi + \theta - \frac{\pi}{2})} d\phi. \quad (4.59)$$

Using Equation 4.21, we can write

$$e^{ik_1 r_0 \cos(\theta + \phi)} = \sum_{n=-\infty}^{\infty} (-1)^n e^{-in\frac{\pi}{2}} J_n(k_1 r_0) e^{in(\theta + \phi)} \quad (4.60)$$

since

$$e^{-in\frac{\pi}{2}} = (e^{-i\frac{\pi}{2}})^n = (\cos\frac{\pi}{2} - i\sin\frac{\pi}{2})^n = (-i)^n. \quad (4.61)$$

Plugging this into our integral gives

$$\frac{1}{\pi} \int_{C_1} e^{ik_1 r \cos\phi + im(\phi + \theta - \frac{\pi}{2})} \sum_{n=-\infty}^{\infty} (-1)^n e^{-in\frac{\pi}{2}} J_n(k_1 r_0) e^{in(\theta + \phi)} d\phi. \quad (4.62)$$

and reversing the order of summation and integration we have [462]

$$\frac{1}{\pi} \sum_{n=-\infty}^{\infty} (-1)^n J_n(k_1 r_0) \int_{C_1} e^{ik_1 r \cos\phi + im(\phi + \theta - \frac{\pi}{2}) + in(\theta + \phi - \frac{\pi}{2})} d\phi \quad (4.63)$$

or

$$\sum_{n=-\infty}^{\infty} (-1)^n J_n(k_1 r_0) e^{i(n+m)\theta} \frac{1}{\pi} \int_{C_1} e^{ik_1 r \cos\phi + i(n+m)(\phi - \frac{\pi}{2})} d\phi. \quad (4.64)$$

So we see that

$$H_m(k_1 \bar{r}) e^{im\bar{\theta}} = \sum_{n=-\infty}^{\infty} (-1)^n J_n(k_1 r_0) H_{n+m}(k_1 r) e^{i(n+m)\theta} \quad (4.65)$$

[462]. However since our source is given by $H_0(k_1 \bar{r})$ which implies that $m = 0$, we can write

$$H_0(k_1 \bar{r}) = \sum_{n=-\infty}^{\infty} (-1)^n J_n(k_1 r_0) H_n(k_1 r) e^{in\theta}. \quad (4.66)$$

This equation is appropriate for $r \geq r_0$ since the Hankel function, which is dependent on r , is finite at infinity. However, if $r \leq r_0$, then that Hankel function will cause the expression to diverge as $r \rightarrow 0$. For this case it is necessary to replace the above equation by [462]

$$H_0(k_1 \bar{r}) = \sum_{n=-\infty}^{\infty} (-1)^n H_n(k_1 r_0) J_n(k_1 r) e^{in\theta} \quad (4.67)$$

where the r dependence is in the Bessel function which is finite at $r = 0$.

Since we are concerned with an incident wave starting at a distance r_0 and propagating towards $r = 0$, we are interested in the range where $r \leq r_0$, and so must use the second equation for the point source. Therefore, the incident potential is written as

$$\phi_1^{INC} = \sum_{n=-\infty}^{\infty} (-1)^n H_n(k_1 r_0) J_n(k_1 r) e^{in\theta}. \quad (4.68)$$

Because of the form of the incident wave, we rewrite the scattered and transmitted waves as

$$\phi_1^{SCAT} = \sum_{n=-\infty}^{\infty} A_n (-1)^n H_n(k_1 r) e^{in\theta}$$

$$\phi_2^{SCAT} = \sum_{n=-\infty}^{\infty} B_n (-1)^n H_n(k_2 r) e^{in\theta}$$

$$\Psi^{SCAT} = \sum_{n=-\infty}^{\infty} C_n (-1)^n H_n(K r) e^{in\theta}$$

$$\phi_1^{TRANS} = \sum_{n=-\infty}^{\infty} A'_n (-1)^n J_n(k'_1 r) e^{in\theta}$$

$$\phi_2^{TRANS} = \sum_{n=-\infty}^{\infty} B'_n (-1)^n J_n(k'_2 r) e^{in\theta}$$

$$\Psi^{TRANS} = \sum_{n=-\infty}^{\infty} C'_n (-1)^n J_n(K' r) e^{in\theta} \quad (4.69)$$

where we have now pulled a factor of $(-1)^n$ out of each modal coefficient for later convenience.

The boundary conditions for this problem are again given by Equations 4.24 and 4.25, providing six equations for the six unknowns. After using Equations 4.13

and 4.17, dropping the summations, and rewriting, the boundary condition equations for the point source case become

$$\begin{aligned}
& A_n[(k_1 a)H'_n(k_1 a)] + B_n[(k_2 a)H'_n(k_2 a)] + C_n[(in)H_n(Ka)] \\
+ & A'_n[-(k'_1 a)J'_n(k'_1 a)] + B'_n[-(k'_2 a)J'_n(k'_2 a)] + C'_n[-(in)J_n(K'a)] \\
= & [-(k_1 a)H_n(k_1 r_0)J'_n(k_1 a)] \tag{4.70}
\end{aligned}$$

$$\begin{aligned}
& A_n[(in)H_n(k_1 a)] + B_n[(in)H_n(k_2 a)] + C_n[-(Ka)H'_n(Ka)] \\
+ & A'_n[-(in)J_n(k'_1 a)] + B'_n[-(in)J_n(k'_2 a)] + C'_n[(K'a)J'_n(K'a)] \\
= & [-(in)H_n(k_1 r_0)J_n(k_1 a)] \tag{4.71}
\end{aligned}$$

$$\begin{aligned}
& A_n \left[\left(\frac{\sigma_1 a^2}{h} \right) H_n(k_1 a) \right] + B_n \left[\left(\frac{\sigma_2 a^2}{h} \right) H_n(k_2 a) \right] \\
+ & A'_n \left[- \left(\frac{h' \sigma'_1 a^2}{h h'} \right) J_n(k'_1 a) \right] + B'_n \left[- \left(\frac{h' \sigma'_2 a^2}{h h'} \right) J_n(k'_2 a) \right] \\
= & \left[- \left(\frac{\sigma_1 a^2}{h} \right) H_n(k_1 r_0) J_n(k_1 a) \right] \tag{4.72}
\end{aligned}$$

$$\begin{aligned}
& A_n[\alpha_1 H_n(k_1 a) - (k_1 a)H'_n(k_1 a)] \\
+ & B_n[\alpha_2 H_n(k_2 a) - (k_2 a)H'_n(k_2 a)] \\
+ & C_n[(inKa)H'_n(Ka) - (in)H_n(Ka)] \\
- & A'_n \left(\frac{\mu'}{\mu} \right) \left(\frac{h'}{h} \right) [\alpha'_1 J_n(k'_1 a) - (k'_1 a)J'_n(k'_1 a)] \\
- & B'_n \left(\frac{\mu'}{\mu} \right) \left(\frac{h'}{h} \right) [\alpha'_2 J_n(k'_2 a) - (k'_2 a)J'_n(k'_2 a)] \\
- & C'_n \left(\frac{\mu'}{\mu} \right) \left(\frac{h'}{h} \right) [(inK'a)J'_n(K'a) - (in)J_n(K'a)] \\
= & -[\alpha_1 H_n(k_1 r_0)J_n(k_1 a) - (k_1 a)H_n(k_1 r_0)J'_n(k_1 a)] \tag{4.73}
\end{aligned}$$

$$\begin{aligned}
& A_n[(2ink_1a)H'_n(k_1a) - (2in)H_n(k_1a)] \\
& + B_n[(2ink_2a)H'_n(k_2a) - (2in)H_n(k_2a)] \\
& + C_n[((Ka)^2 - 2n^2)H_n(Ka) + (2Ka)H'_n(Ka)] \\
& - A'_n\left(\frac{\mu'}{\mu}\right)\left(\frac{h'}{h}\right)[(2ink'_1a)J'_n(k'_1a) - (2in)J_n(k'_1a)] \\
& - B'_n\left(\frac{\mu'}{\mu}\right)\left(\frac{h'}{h}\right)[(2ink'_2a)J'_n(k'_2a) - (2in)J_n(k'_2a)] \\
& - C'_n\left(\frac{\mu'}{\mu}\right)\left(\frac{h'}{h}\right)[((K'a)^2 - 2n^2)J_n(K'a) + (2K'a)J'_n(K'a)] \\
& = -[(2ink_1a)H_n(k_1r_0)J'_n(k_1a) - (2in)H_n(k_1r_0)J_n(k_1a)] \tag{4.74}
\end{aligned}$$

$$\begin{aligned}
& A_n\left[\left(\frac{\sigma_1 a^2}{h}\right)(k_1a)H'_n(k_1a)\right] \\
& + B_n\left[\left(\frac{\sigma_2 a^2}{h}\right)(k_2a)H'_n(k_2a)\right] \\
& - A'_n\left(\frac{\mu'}{\mu}\right)\left(\frac{h'}{h}\right)^3\left[\left(\frac{\sigma'_1 a^2}{h'}\right)(k'_1a)J'_n(k'_1a)\right] \\
& - B'_n\left(\frac{\mu'}{\mu}\right)\left(\frac{h'}{h}\right)^3\left[\left(\frac{\sigma'_2 a^2}{h'}\right)(k'_2a)J'_n(k'_2a)\right] \\
& = -\left[\left(\frac{\sigma_1 a^2}{h}\right)(k_1a)H_n(k_1r_0)J'_n(k_1a)\right] \tag{4.75}
\end{aligned}$$

where the prime on the Bessel and Hankel functions, $\alpha_{1,2}$, and $\alpha'_{1,2}$ are as defined above.

Writing the six boundary condition equations in matrix form we have,

$$\begin{pmatrix}
(k_1 a)H'_n(k_1 a) & (k_2 a)H'_n(k_2 a) & (in)H_n(Ka) & -(k'_1 a)J'_n(k'_1 a) \\
(in)H_n(k_1 a) & (in)H_n(k_2 a) & -(Ka)H'_n(Ka) & -(in)J_n(k'_1 a) \\
\left(\frac{\sigma_1 a^2}{h}\right)H_n(k_1 a) & \left(\frac{\sigma_2 a^2}{h}\right)H_n(k_2 a) & 0 & -\left(\frac{h' \sigma'_1 a^2}{h}\right)J_n(k'_1 a) \\
B_{41} & B_{42} & B_{43} & B_{44} \\
B_{51} & B_{52} & B_{53} & B_{54} \\
B_{61} & B_{62} & 0 & B_{64}
\end{pmatrix}
\begin{pmatrix}
-(k'_2 a)J'_n(k'_2 a) & -(in)J_n(K'a) \\
-(in)J_n(k'_2 a) & (K'a)J'_n(K'a) \\
-\left(\frac{h' \sigma'_2 a^2}{h}\right)J_n(k'_2 a) & 0 \\
B_{45} & B_{46} \\
B_{55} & B_{56} \\
B_{65} & 0
\end{pmatrix}
\begin{pmatrix}
A_n \\
B_n \\
C_n \\
A'_n \\
B'_n \\
C'_n
\end{pmatrix}
=
\begin{pmatrix}
C_{11}^{ps} \\
C_{21}^{ps} \\
C_{31}^{ps} \\
C_{41}^{ps} \\
C_{51}^{ps} \\
C_{61}^{ps}
\end{pmatrix} \quad (4.76)$$

where the B_{ij} 's are as given in Equations 4.35 - 4.37 and

$$\begin{aligned}
C_{11}^{ps} &= -(k_1 a)H_n(k_1 r_0)J'_n(k_1 a) \\
C_{21}^{ps} &= -(in)H_n(k_1 r_0)J_n(k_1 a) \\
C_{31}^{ps} &= -\left(\frac{\sigma_1 a^2}{h}\right)H_n(k_1 r_0)J_n(k_1 a) \\
C_{41}^{ps} &= -[\alpha_1 H_n(k_1 r_0)J_n(k_1 a) - (k_1 a)H_n(k_1 r_0)J'_n(k_1 a)] \\
C_{51}^{ps} &= -[(2ink_1 a)H_n(k_1 r_0)J'_n(k_1 a) - (2in)H_n(k_1 r_0)J_n(k_1 a)] \\
C_{61}^{ps} &= -\left[\left(\frac{\sigma_1 a^2}{h}\right)(k_1 a)H_n(k_1 r_0)J'_n(k_1 a)\right]. \quad (4.77)
\end{aligned}$$

Rewriting the matrix equation gives

$$\begin{pmatrix}
 (k_1 a)H'_n(k_1 a) & (k_2 a)H'_n(k_2 a) & (in)H_n(K'a) & -(k'_1 a)J'_n(k'_1 a) \\
 (in)H_n(k_1 a) & (in)H_n(k_2 a) & -(K'a)H'_n(K'a) & -(in)J_n(k'_1 a) \\
 (\frac{\sigma_1 a^2}{h})H_n(k_1 a) & (\frac{\sigma_2 a^2}{h})H_n(k_2 a) & 0 & -(\frac{h'}{h} \frac{\sigma'_1 a^2}{h'})J_n(k'_1 a) \\
 B_{41} & B_{42} & B_{43} & B_{44} \\
 B_{51} & B_{52} & B_{53} & B_{54} \\
 B_{61} & B_{62} & 0 & B_{64}
 \end{pmatrix}
 \begin{pmatrix}
 -(k'_2 a)J'_n(k'_2 a) & -(in)J_n(K'a) \\
 -(in)J_n(k'_2 a) & (K'a)J'_n(K'a) \\
 -(\frac{h'}{h} \frac{\sigma'_2 a^2}{h'})J_n(k'_2 a) & 0 \\
 B_{45} & B_{46} \\
 B_{55} & B_{56} \\
 B_{65} & 0
 \end{pmatrix}
 \begin{pmatrix}
 \frac{1}{H_n(k_1 r_0)} A_n \\
 \frac{1}{H_n(k_1 r_0)} B_n \\
 \frac{1}{H_n(k_1 r_0)} C_n \\
 \frac{1}{H_n(k_1 r_0)} A'_n \\
 \frac{1}{H_n(k_1 r_0)} B'_n \\
 \frac{1}{H_n(k_1 r_0)} C'_n
 \end{pmatrix}
 =
 \begin{pmatrix}
 -(k_1 a)J'_n(k_1 a) \\
 -(in)J_n(k_1 a) \\
 -(\frac{\sigma_1 a^2}{h})J_n(k_1 a) \\
 C_{41} \\
 C_{51} \\
 C_{61}
 \end{pmatrix}
 \tag{4.78}$$

and by Cramer's Rule the coefficients are

$$A_n = H_n(k_1 r_0) \left(\frac{\Delta_1}{\Delta_0} \right) \quad B_n = H_n(k_1 r_0) \left(\frac{\Delta_2}{\Delta_0} \right) \quad C_n = H_n(k_1 r_0) \left(\frac{\Delta_3}{\Delta_0} \right)$$

$$A'_n = H_n(k_1 r_0) \left(\frac{\Delta_4}{\Delta_0} \right) \quad B'_n = H_n(k_1 r_0) \left(\frac{\Delta_5}{\Delta_0} \right) \quad C'_n = H_n(k_1 r_0) \left(\frac{\Delta_6}{\Delta_0} \right) \quad (4.79)$$

where the Δ 's are the same as in the case of a plane wave incident on a general cylindrical scatterer so that algebra does not have to be redone.

Since we are specifically interested in the case of the scatterer being a cylindrical hole where the normal tractions at the boundary must equal zero, we again set $A'_n \equiv B'_n \equiv C'_n \equiv 0$. This leaves three unknown modal coefficients (A_n, B_n, C_n), and only the three plate stress boundary conditions in Equation 4.25 are considered. For the case of a point source $S0$ Lamb wave incident on a cylindrical hole, the matrix equation thus becomes

$$\begin{pmatrix} B_{41} & B_{42} & B_{43} \\ B_{51} & B_{52} & B_{53} \\ B_{61} & B_{62} & 0 \end{pmatrix} \begin{pmatrix} \frac{1}{H_n(k_1 r_0)} A_n \\ \frac{1}{H_n(k_1 r_0)} B_n \\ \frac{1}{H_n(k_1 r_0)} C_n \end{pmatrix} = \begin{pmatrix} C_{41} \\ C_{51} \\ C_{61} \end{pmatrix} \quad (4.80)$$

where the B_{ij} 's and C_{ij} 's are as defined in Equations 4.35 - 4.38. Again applying Cramer's Rule we have

$$A_n = H_n(k_1 r_0) \left(\frac{\Delta_1}{\Delta_0} \right) \quad B_n = H_n(k_1 r_0) \left(\frac{\Delta_2}{\Delta_0} \right) \quad C_n = H_n(k_1 r_0) \left(\frac{\Delta_3}{\Delta_0} \right) \quad (4.81)$$

where the Δ 's are the same as for the case of a plane wave incident upon a cylindrical hole (Equations 4.51 - 4.54).

The behavior of the $S0$ Lamb wave field for the case of a point source can now be examined using the equations for ϕ_1^{INC} , ϕ_1^{SCAT} , and A_n . Since these expressions are far too complicated for an intuitive understanding of the behavior, plots of the

magnitude of the scattered amplitude of the S_0 wave and of the vertical displacement of the top surface of the plate due to the combined incident and scattered S_0 wave at the point of measurement in the experiments are examined.

Finite Source

In the laboratory experiments we use piezoelectric transducers to generate the Lamb waves in the plate. Piezoelectric transducers work by converting electrical signals into mechanical vibrations. These vibrations then generate the elastic waves in the test material. The transducers are, of course, finite sources, so the plane wave and point source incident waves do not accurately describe the Lamb wave propagation in the experiments. However, by Huygen's principle, we can model any finite source by a combination of point sources.

While the longitudinal contact transducers radiate uniformly over the full range of angles, the shear contact transducers used in the PPT experiments, generate a directional Lamb wave field. This field for the shear contact transducers used in the experiments, has been measured to be 100% at $\pm 0^\circ$, 50% at $\pm 20^\circ$, and 26% at $\pm 30^\circ$ [463]. A good approximation to this beam pattern has been found to be a line of five point sources at a distance r_0 from the center of the coordinate system as shown in Figure 4.5. For the experimental value of r_0 equal to 8.75 cm, the point separation to generate the expected beam pattern is $2B = 0.635$ cm, and the necessary amplitudes of the point sources are

$$C_j = 1.0 \quad (j = 1, 2, 3, 5) \quad C_4 = 3.0. \quad (4.82)$$

For each point source we have incident and reflected S_0 Lamb waves given

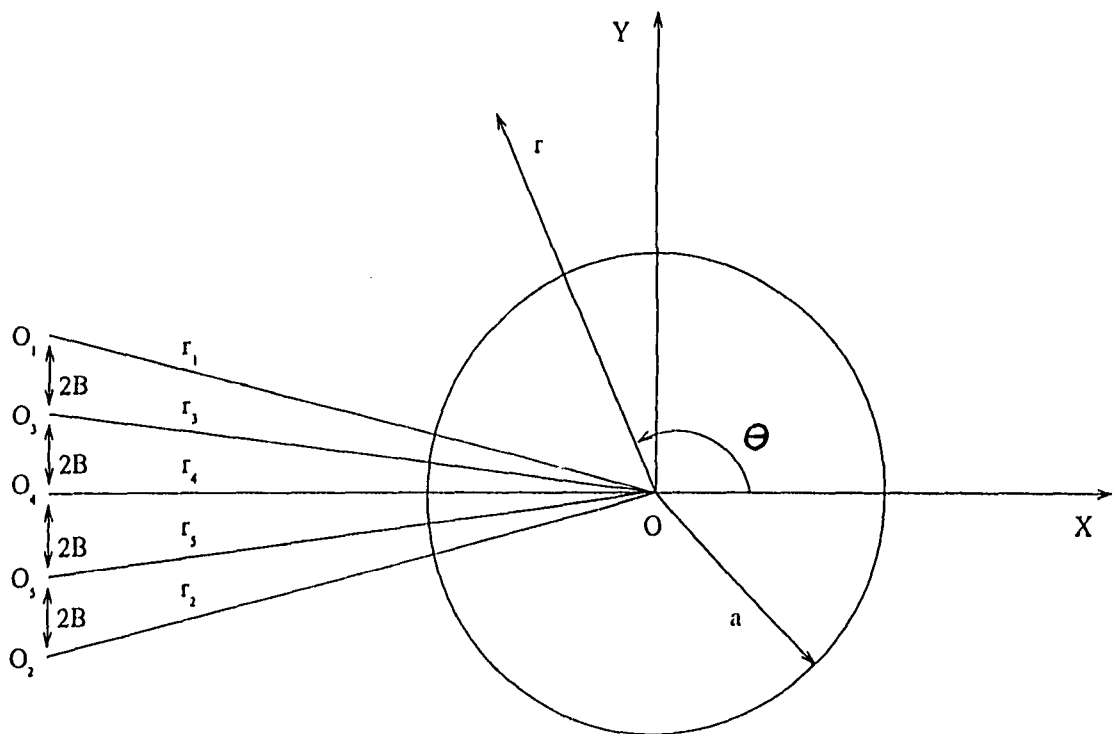


Figure 4.5: Coordinate system for a finite source S_0 Lamb wave incident upon a cylindrical inclusion in an infinite plate

by

$$\begin{aligned}\phi_1^{INC(j)} &= \sum_{n=-\infty}^{\infty} C_j (-1)^n H_n(k_1 r_j) J_n(k_1 r) e^{in\theta}, \\ \phi_1^{SCAT(j)} &= \sum_{n=-\infty}^{\infty} C_j A_n^j (-1)^n H_n(k_1 r) e^{in\theta},\end{aligned}\quad (4.83)$$

where

$$A_n^j = H_n(k_1 r_j) \left(\frac{\Delta_1}{\Delta_0} \right) \quad (4.84)$$

and $j = 1, 2, 3, 4, 5$.

In the same way that the finite source incident wave can be generated by summing the contributions of the individual point sources.

$$\phi_1^{INC(js)} = \sum_{j=1}^5 \phi_1^{INC(j)}, \quad (4.85)$$

the S_0 scattered field for the finite source can be determined by first calculating the S_0 scattered field for each point source and then summing them.

$$\phi_1^{SCAT(js)} = \sum_{j=1}^5 \phi_1^{SCAT(j)}. \quad (4.86)$$

In order to facilitate this process, the r_j 's and θ_j 's are defined in terms of r_0 , B , and θ . This is possible because a right triangle can be drawn connecting each r_j to r_0 (e.g. Figures 4.6 and 4.7). For the geometry shown in Figure 4.5, we have

$$\begin{aligned}r_1 &= ((r_0)^2 + (4B)^2)^{\frac{1}{2}} \\ r_2 &= ((r_0)^2 + (-4B)^2)^{\frac{1}{2}} \\ r_3 &= ((r_0)^2 + (2B)^2)^{\frac{1}{2}} \\ r_4 &= r_0 \\ r_5 &= ((r_0)^2 + (-2B)^2)^{\frac{1}{2}}\end{aligned}\quad (4.87)$$

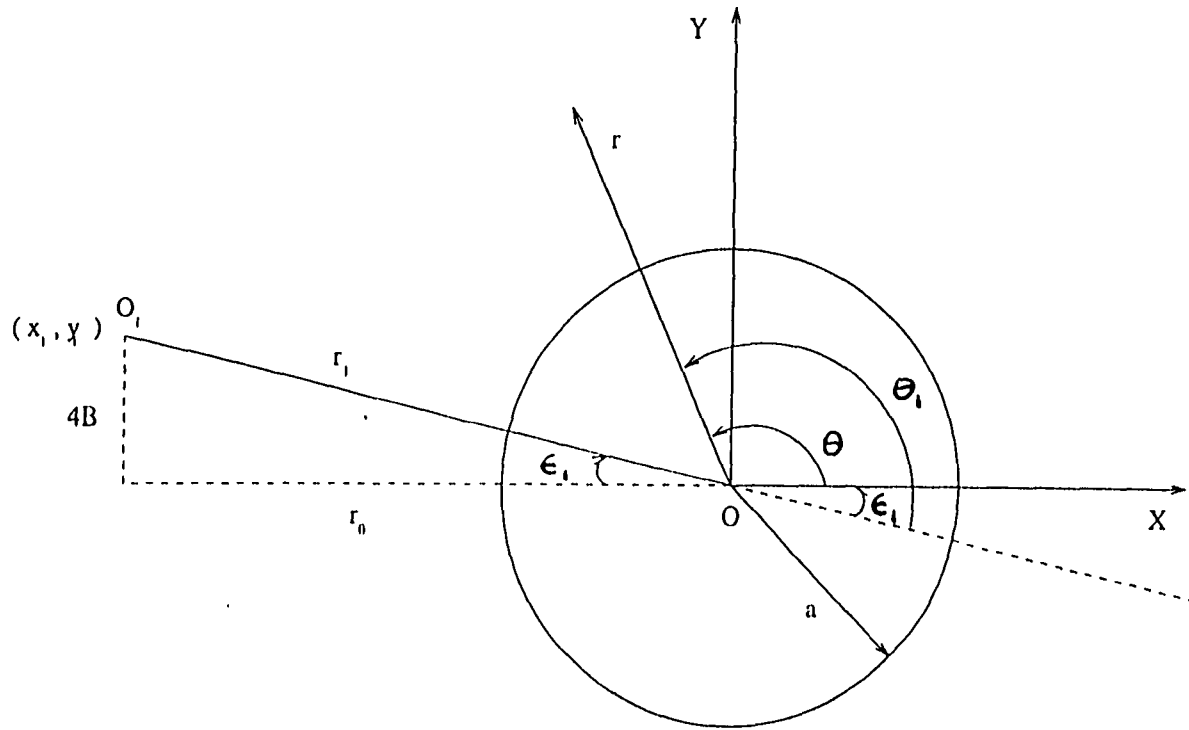


Figure 4.6: Right triangle joining r_1 and r_0 which allows for r_1 and θ_1 to be written in terms of r_0 , B , and θ . Notice that for this case where the y -coordinate of the source point is greater than zero, $\theta_1 = \theta + \epsilon_1$.

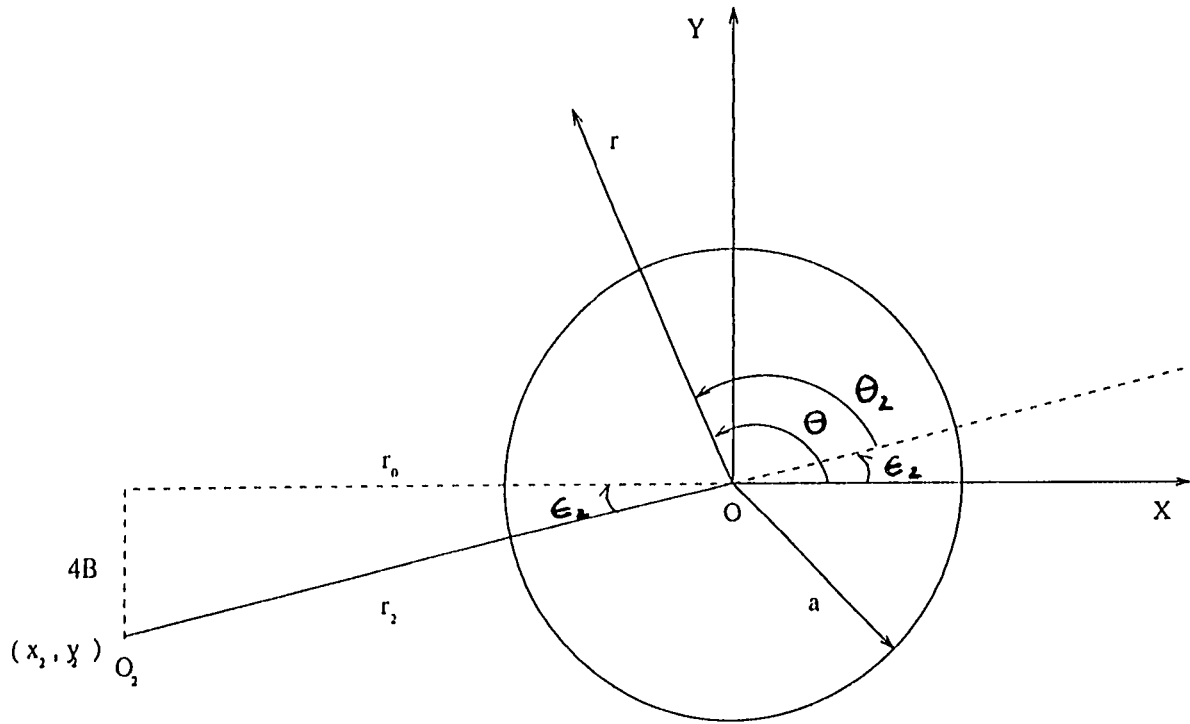


Figure 4.7: Right triangle joining r_2 and r_0 which allows for r_2 and θ_2 to be written in terms of r_0 , B , and θ . Notice that for this case where the y -coordinate of the source point is less than zero, $\theta_2 = \theta - \epsilon_2$.

and using

$$\epsilon = \arctan\left(\frac{y}{x}\right) \quad (4.88)$$

we can define the angles

$$\begin{aligned} \epsilon_1 &= \arctan\left|\frac{4B}{r_0}\right| \\ \epsilon_2 &= \arctan\left|\frac{-4B}{r_0}\right| \\ \epsilon_3 &= \arctan\left|\frac{2B}{r_0}\right| \\ \epsilon_4 &= 0 \\ \epsilon_5 &= \arctan\left|\frac{-2B}{r_0}\right|. \end{aligned} \quad (4.89)$$

Then since $y_{1,3,4} \geq 0$ (Figure 4.6), we have

$$\theta_{1,3,4} = \theta + \epsilon_{1,3,4}, \quad (4.90)$$

while for $y_{2,5} < 0$ (Figure 4.7), we have

$$\theta_{2,5} = \theta - \epsilon_{2,5}. \quad (4.91)$$

However, the point sources making up the finite source will not always be in the geometry shown in Figure 4.5. In the experiments, the transducer starts at a position well above the flaw and scans down past the flaw to a position well below the flaw. This means that in addition to the case of the finite source being centered on the flaw, we will also have cases where all of the point sources have $y_j > 0$ (Figure 4.8) or $y_j < 0$ (Figure 4.9). Therefore, it is necessary to generalize the above expressions for the r_j 's and θ_j 's. This is done using a variable called *SHIFT* which defines the y -coordinate of the center point source (Figures 4.8, 4.9). Using this variable, we now have,

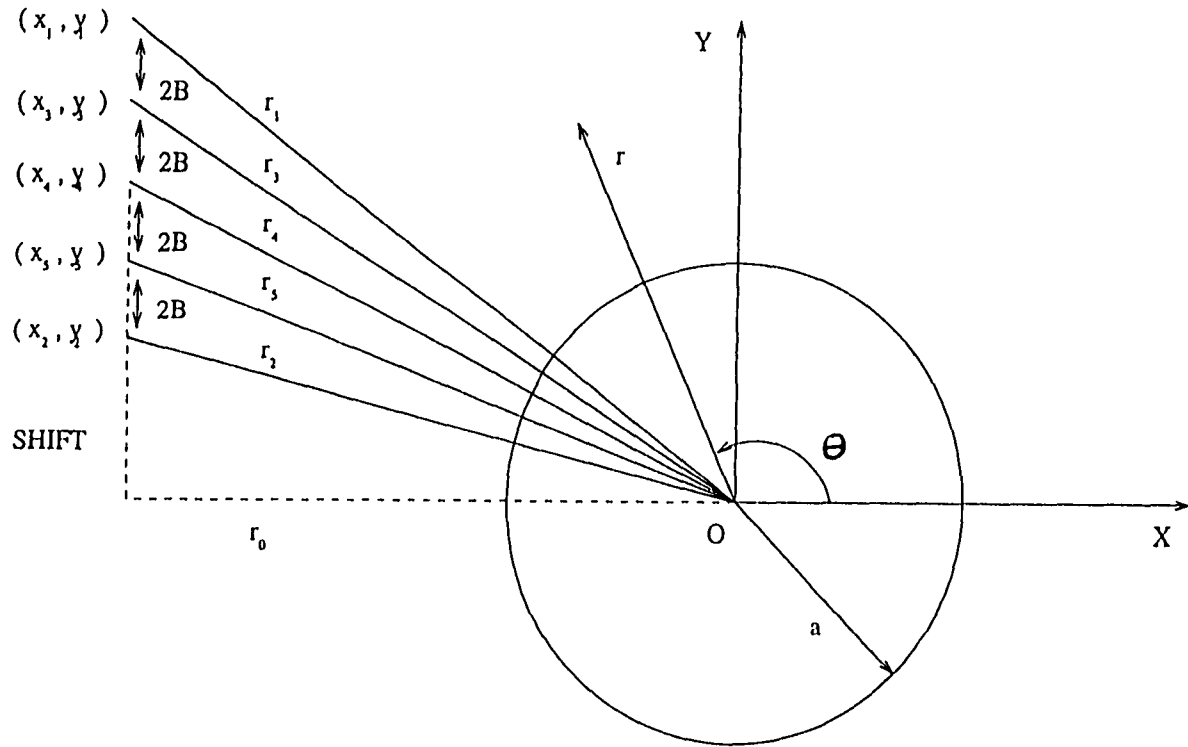


Figure 4.8: Geometry for the finite source well above the cylindrical inclusion in the plate. Note that the y -coordinate of the center point source is defined in terms of the variable $SHIFT$ and the spacing of the point sources remains the same.

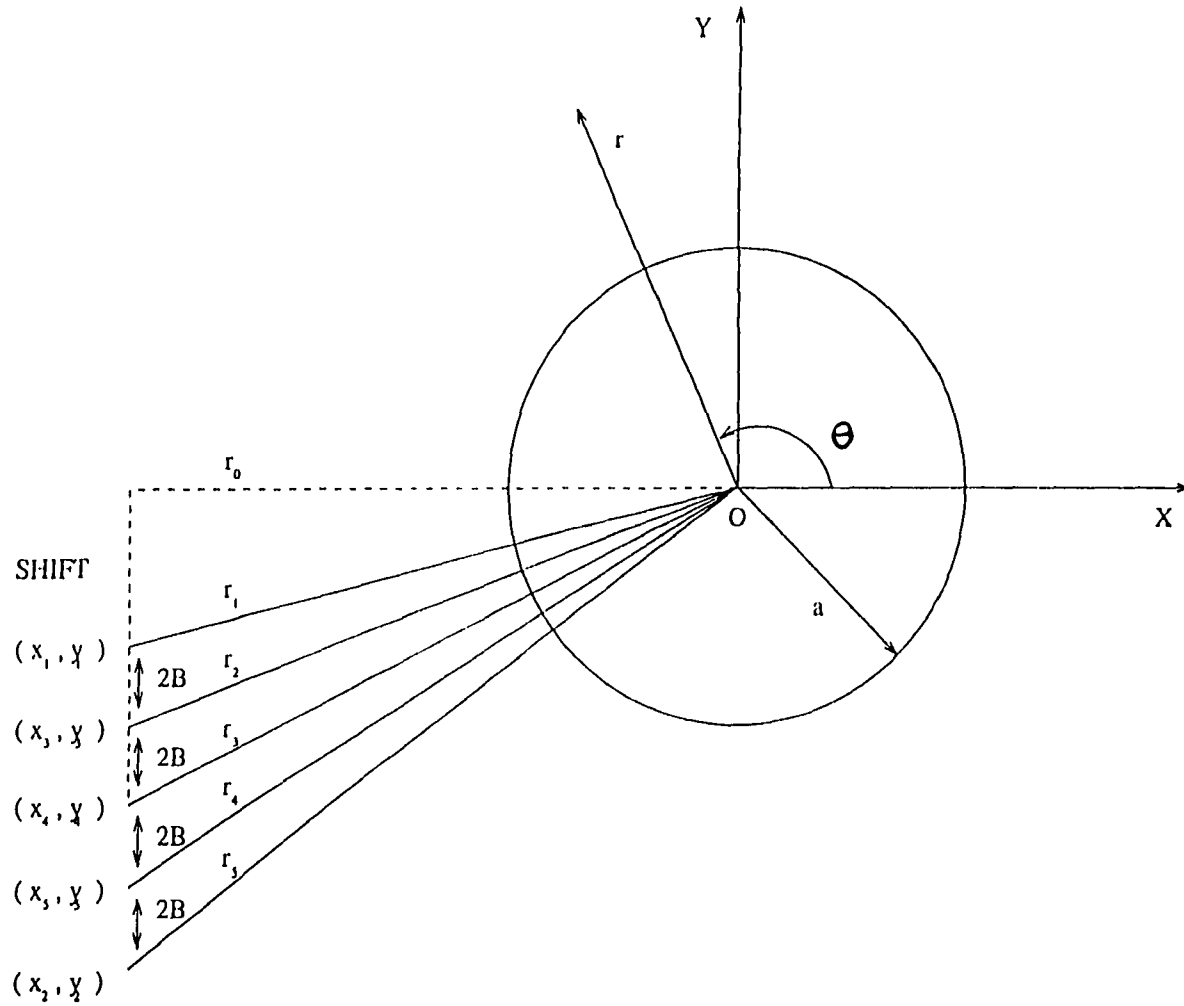


Figure 4.9: Geometry for the finite source well below the cylindrical inclusion in the plate. Note that the y -coordinate of the center point source is defined in terms of the variable *SHIFT* and the spacing of the point sources remains the same.

$$\begin{aligned}
r_1 &= ((r_0)^2 + (4B + SHIFT)^2)^{\frac{1}{2}} \\
r_2 &= ((r_0)^2 + (-4B + SHIFT)^2)^{\frac{1}{2}} \\
r_3 &= ((r_0)^2 + (2B + SHIFT)^2)^{\frac{1}{2}} \\
r_4 &= ((r_0)^2 + (SHIFT)^2)^{\frac{1}{2}} \\
r_5 &= ((r_0)^2 + (-2B + SHIFT)^2)^{\frac{1}{2}}
\end{aligned} \tag{4.92}$$

and

$$\begin{aligned}
\epsilon_1 &= \arctan \left| \frac{4B + SHIFT}{r_0} \right| \\
\epsilon_2 &= \arctan \left| \frac{-4B + SHIFT}{r_0} \right| \\
\epsilon_3 &= \arctan \left| \frac{2B + SHIFT}{r_0} \right| \\
\epsilon_4 &= \arctan \left| \frac{SHIFT}{r_0} \right| \\
\epsilon_5 &= \arctan \left| \frac{-2B + SHIFT}{r_0} \right|.
\end{aligned} \tag{4.93}$$

Then if $y_j \geq 0$, we have

$$\theta_j = \theta + \epsilon_j, \tag{4.94}$$

while for $y_j < 0$, we have

$$\theta_j = \theta - \epsilon_j. \tag{4.95}$$

Now we have expressions for each point source in terms of the known parameters r_0 , B , and θ , and we can sum the individual contributions of the point sources to obtain the scattered field for the finite source. These equations are again far too complicated for an intuitive understanding of the behavior of the S_0 Lamb wave. Therefore, plots of the magnitude of the scattered amplitude of the S_0 wave

and of the vertical displacement of the top surface of the plate due to the combined incident and scattered S_0 wave at the point of measurement in the experiments are examined.

4.3 Results of the Scattering Theory

Now that exact and analytic closed-form expressions for the scattering of plane, point source, and finite source S_0 Lamb waves from a cylindrical hole in a plate have been derived, the results predicted by the theory can be used to explain the scattering effects seen in the images at the end of Chapter 3. The standard way to display scattering results predicted by theory is to show polar plots of the magnitude of the amplitude of the scattered wave as a function of θ . Thus, for the incident plane wave where ϕ_1^{SCAT} is defined by Equation 4.23, we have a scattered amplitude given by

$$A_n i^n e^{in\theta}. \quad (4.96)$$

The magnitude of this scattered amplitude is given by

$$|A_n i^n e^{in\theta}| \quad (4.97)$$

with

$$A_n = \frac{\Delta_1}{\Delta_0} \quad (4.98)$$

and

$$|| = ((REAL)^2 + (IMAG)^2)^{\frac{1}{2}}. \quad (4.99)$$

Similarly for the point source case where ϕ_1^{SCAT} is defined by equation 4.69, the magnitude of the scattered amplitude is given by

$$|A_n (-1)^n e^{in\theta}| \quad (4.100)$$

with

$$A_n = H_n(k_1 r_0) \left(\frac{\Delta_1}{\Delta_0} \right). \quad (4.101)$$

Finally for the finite source case we have for each point source a scattered field defined by Equation 4.83, and so the scattered amplitudes are of the form

$$C_j A_n^j (-1)^n e^{in\theta_j}, \quad (j = 1, 2, 3, 4, 5) \quad (4.102)$$

where the C_j 's, A_n^j 's, and θ_j 's are as given in Equations 4.82, 4.84, 4.94, and 4.95. Since the scattered field for the finite source is given by the sum of the scattered fields for the individual point sources, the scattered amplitude for the finite source case is given by the sum of the individual scattered amplitudes,

$$\sum_{j=1}^5 C_j A_n^j (-1)^n e^{in\theta_j}. \quad (4.103)$$

The magnitude of the scattered amplitude for the finite source case is then

$$\left| \sum_{j=1}^5 C_j A_n^j (-1)^n e^{in\theta_j} \right|. \quad (4.104)$$

Figures 4.10 - 4.12 show the magnitude of the plane wave scattered amplitude for holes of radius $a = 0.25 \times 10^{-2}$ m, $a = 0.75 \times 10^{-2}$ m, and $a = 1.27 \times 10^{-2}$ m respectively. In order to match the experiments, the values $\lambda = 6.293 \times 10^{10}$ kg/ms², $\mu = 2.677 \times 10^{10}$ kg/ms², $\rho = 2700$ kg/m³, $\omega = 2\pi(1.1) \times 10^6$ Hz, and $h = 1.143 \times 10^{-3}$ m have been chosen. For the smallest hole (Figure 4.10), the largest lobe is in the 180° direction and the other lobes are of approximately the same amplitude and are about evenly spaced over the remaining range of angles. For the middle hole (Figure 4.11), the largest lobes are near 90° and 270°, there is only a small forward scattered component, and the remaining lobes are all in the backscattered direction. Finally for the largest hole (Figure 4.12), the largest lobes

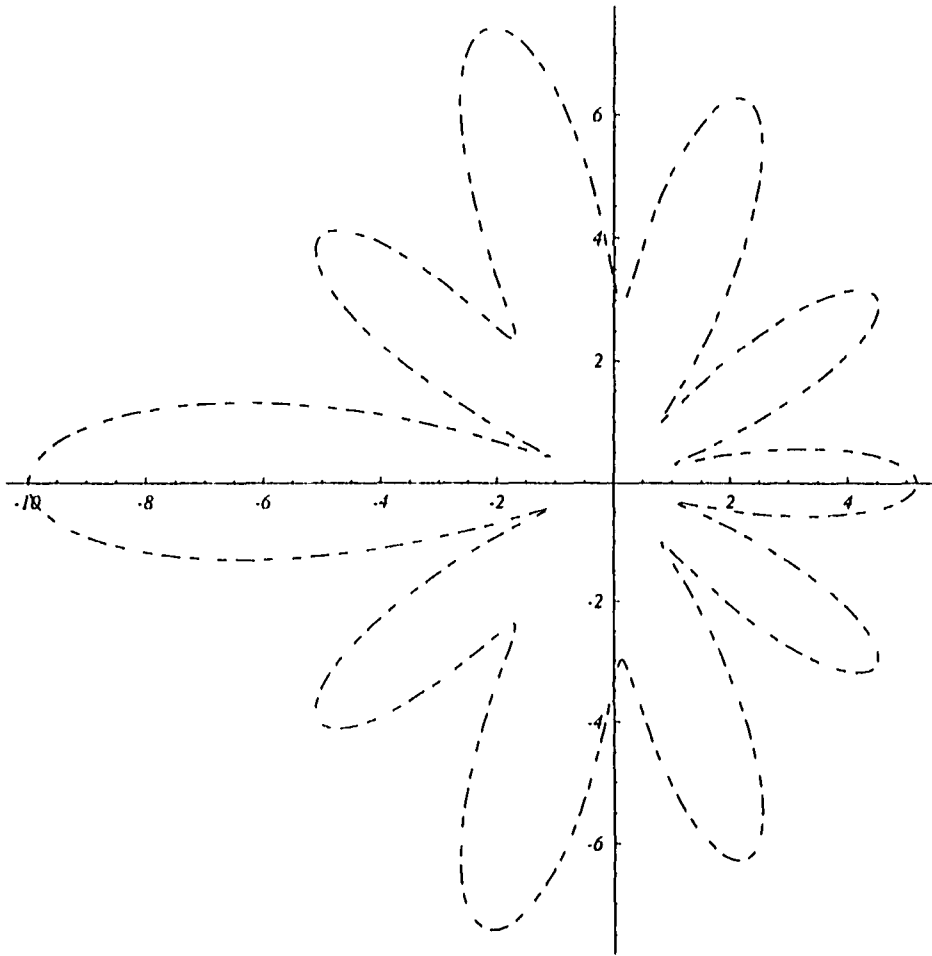


Figure 4.10: Polar plot of the magnitude of the scattered amplitude of a plane wave incident from the left upon a hole with radius $a = 0.25 \times 10^{-2}$ m. Notice that the lobes are about evenly spaced over the range of angles with the largest lobe in the 180° direction.

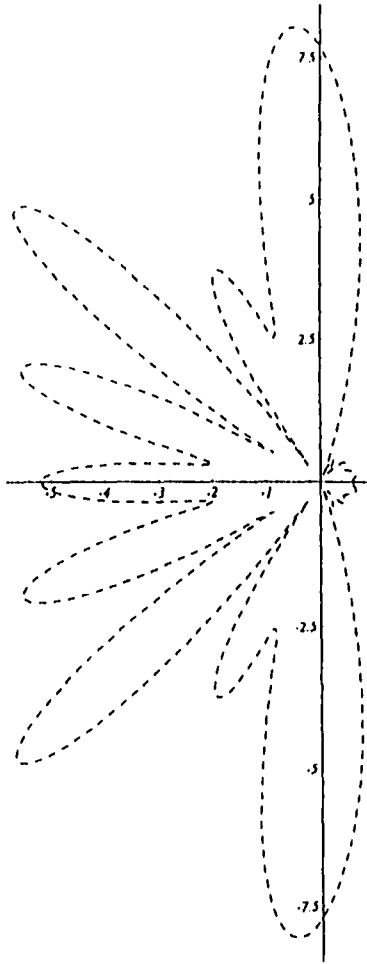


Figure 4.11: Polar plot of the magnitude of the scattered amplitude of a plane wave incident from the left upon a hole with radius $a = 0.75 \times 10^{-2}$ m. Notice that the lobes are now almost entirely in the backscattered direction with the largest lobes in the 90° and 270° directions, and only a small forward scattered component.

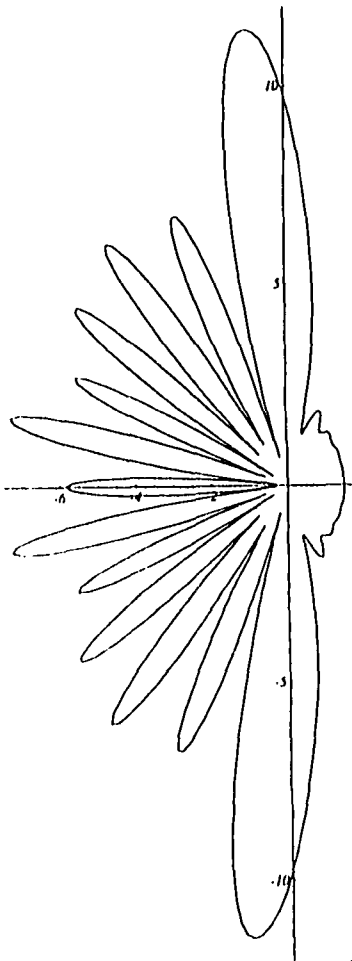


Figure 4.12: Polar plot of the magnitude of the scattered amplitude of a plane wave incident from the left upon a hole with radius $a = 1.27 \times 10^{-2}$ m. Again the lobes are almost entirely in the backscattered direction with the largest lobes in the 90° and 270° directions. The overall magnitude is slightly larger for this case.

are still near the 90° and 270° directions, there are more lobes in the backscattered direction, and there is still a small forward scattered component. Also notice that the overall magnitude is slightly larger for this case. For the incident plane wave, the scattering does get more complicated as the size of the hole increases, but the forward scattered components are probably due to the infinite size of the plane wave, rather than any other scattering effects.

Figures 4.13 - 4.15 show the magnitude of the point source scattered amplitude for holes of radius $a = 0.25 \times 10^{-2}$ m, $a = 0.75 \times 10^{-2}$ m, and $a = 1.27 \times 10^{-2}$ m respectively. The values of λ , μ , ρ , ω , and h are the same as above, and the point source has been located at a distance $r_0 = 8.75 \times 10^{-2}$ m to the left of the holes. Comparing these plots to the plane wave results, we see that although the overall magnitude is much smaller, the distribution of the lobes in the point source results is almost identical to that in the plane wave results. This is probably due to the fact that the incident point source wave, while being cylindrical, still extends far past the hole in either direction, and so is similar to the plane wave. The forward scattering is again probably due to this rather than any other scattering effects.

Figures 4.16 - 4.18 show the magnitude of the finite source scattered amplitude for holes of radii $a = 0.25 \times 10^{-2}$ m, $a = 0.75 \times 10^{-2}$ m, and $a = 1.27 \times 10^{-2}$ m respectively. The values of λ , μ , ρ , ω , and h are the same as above, and the center point source in the finite source has been located at a distance $r_1 = 8.75 \times 10^{-2}$ m to the left of the holes. The plots for the small and medium holes (Figures 4.16, 4.17) are again almost the same as those for the plane wave and point source cases aside from the actual magnitude values. However, the plot for the largest hole (Figure 4.18), while still similar, does show some differences from the earlier plots. Except for just past the second backscattered lobe on either side of the x -axis where the magnitude drops to zero, there is a backscattered region that matches

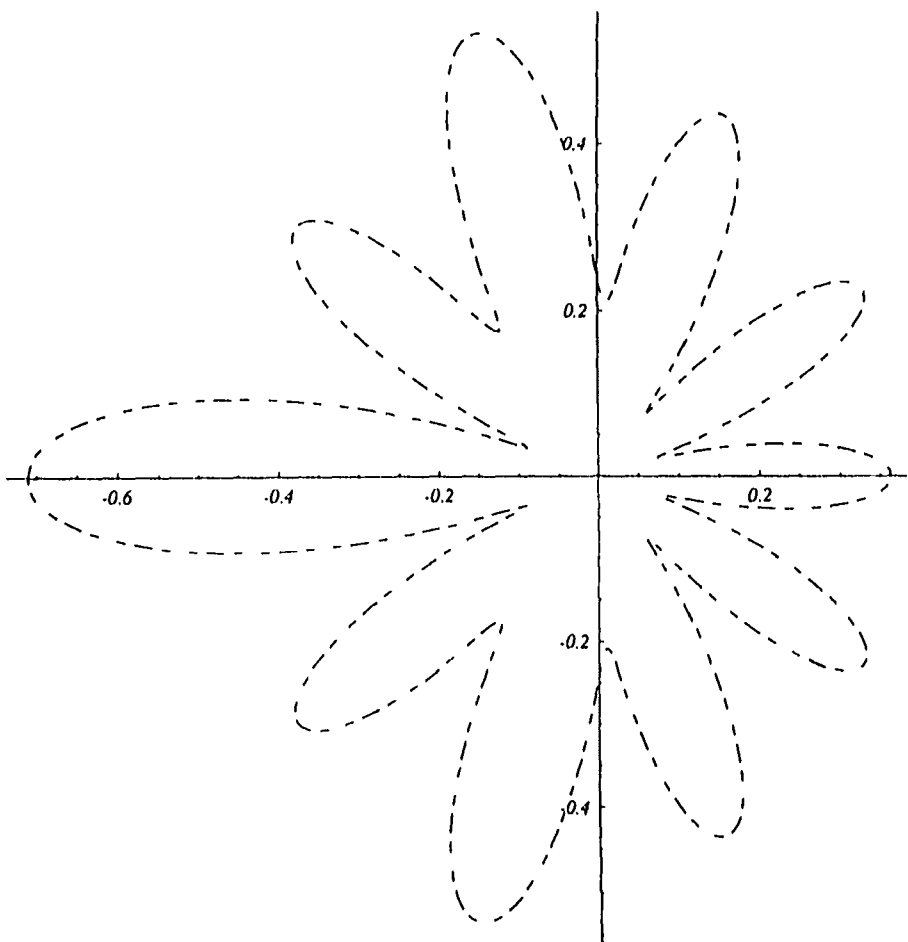


Figure 4.13: Polar plot of the magnitude of the scattered amplitude of a point source wave incident from the left upon a hole with radius $a = 0.25 \times 10^{-2}$ m. Notice that even though this wave is cylindrical, the orientation and shape of the scattering pattern matches that of the plane wave case.

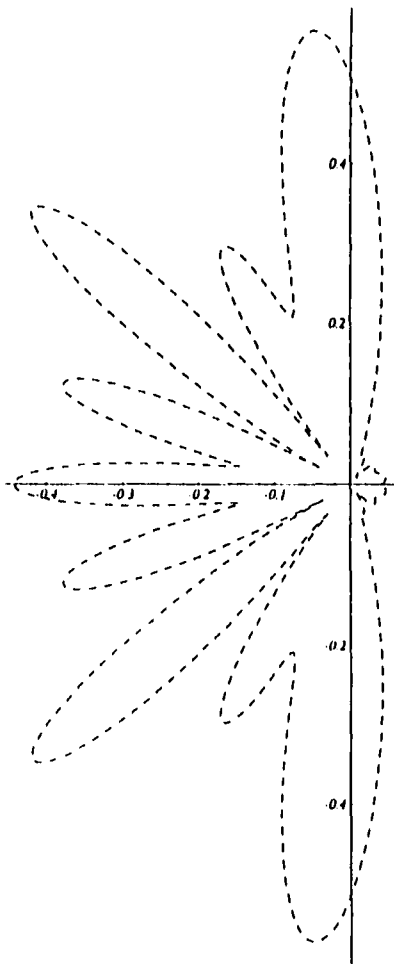


Figure 4.14: Polar plot of the magnitude of the scattered amplitude of a point source wave incident from the left upon a hole with radius $a = 0.75 \times 10^{-2}$ m. Again this plot for the point source wave is very similar to the results of the plane wave case aside from the actual magnitude values.

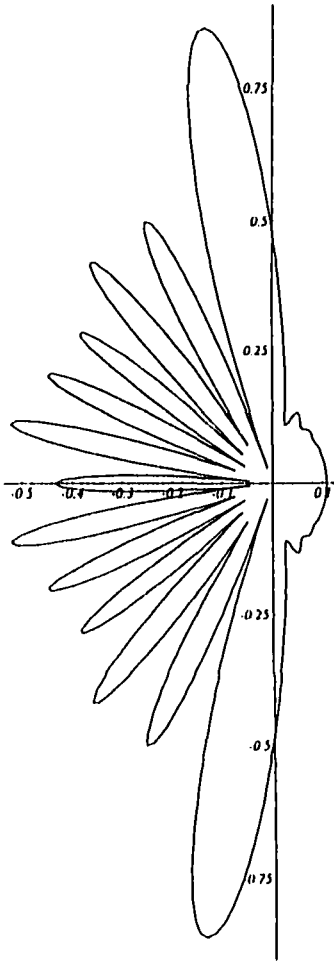


Figure 4.15: Polar plot of the magnitude of the scattered amplitude of a point source wave incident from the left upon a hole with radius $a = 1.27 \times 10^{-2}$ m. This plot is also very similar in shape and orientation to that of the corresponding plane wave case.

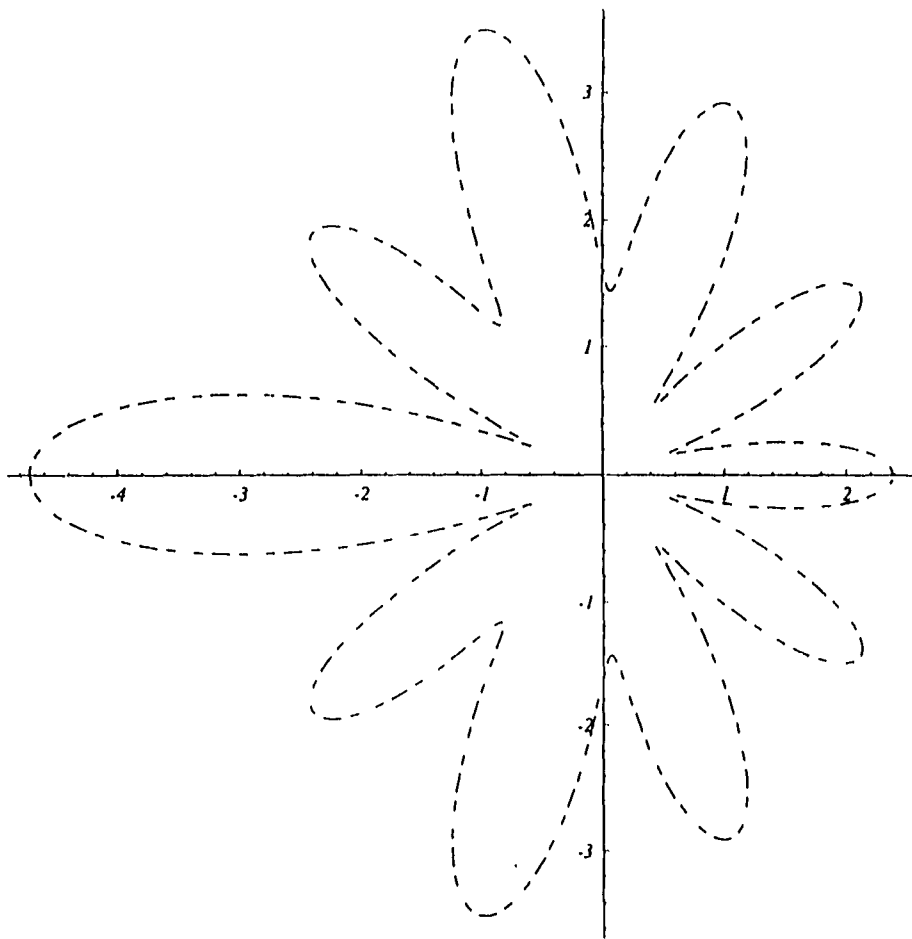


Figure 4.16: Polar plot of the magnitude of the scattered amplitude of a finite source wave incident from the left upon a hole with radius $a = 0.25 \times 10^{-2}$ m. Notice that the results seen here are almost identical to those seen in the corresponding plane and point source cases. This is because the hole is smaller than the beam width.

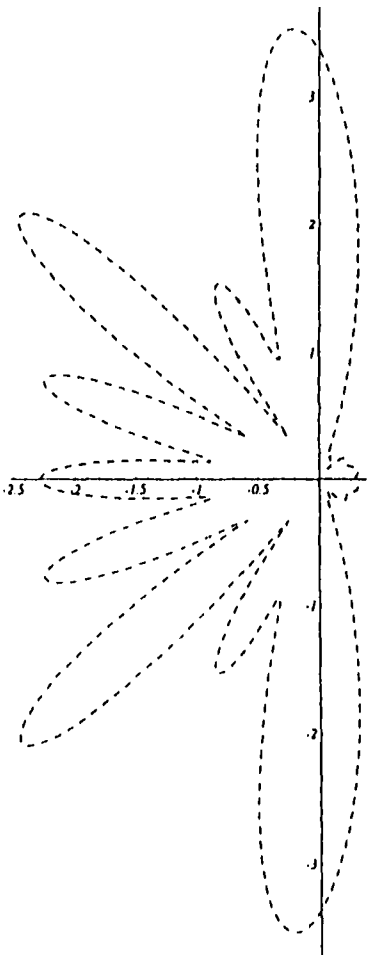


Figure 4.17: Polar plot of the magnitude of the scattered amplitude of a finite source wave incident from the left upon a hole with radius $a = 0.75 \times 10^{-2}$ m. Again the results seen here are almost identical to those seen in the corresponding plane and point source cases. This is because the hole while close in size to the beam width, still allows for some of the beam to wrap around it.

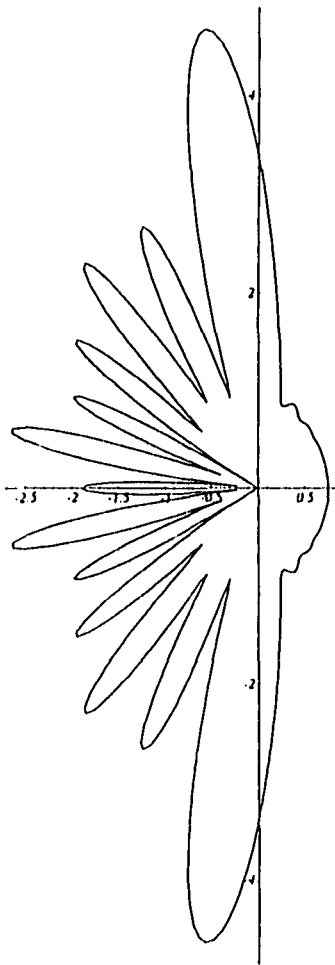


Figure 4.18: Polar plot of the magnitude of the scattered amplitude of a finite source wave incident from the left upon a hole with radius $a = 1.27 \times 10^{-2}$ m. The results seen here although similar to those seen in the corresponding plane and point source cases, do show some differences. There is a backscattered region corresponding to the front scattered one, and just past the second peak on either side of the x -axis, the magnitude goes to zero. Also, the forward scattered region is slightly different in shape from that seen in the earlier plots. For this case, the hole is slightly larger than the beam width, and so different effects are seen.

the forward scattered component. In addition, the shape of the forward scattered portion is slightly altered from the earlier plots. However, while the finite source should have a forward component due to scattering rather than the large width of the incident wave, the differences noted here are not significant enough to correlate with the scattering effects seen in the tomographic images.

Next we consider the scattering results when the finite source has been shifted along the y -axis. Figures 4.19 - 4.21 and 4.22 - 4.24 show the magnitude of the scattered amplitude when the finite source has been shifted by $+3.0 \times 10^{-2}$ m and -3.0×10^{-2} m respectively. Notice that the -3 cm shift cases are the same as the +3 cm shift cases inverted about the x -axis, and that there has been an overall decrease in magnitude. For the small hole (Figures 4.19, 4.22), the scattering pattern looks quite different from the centered source cases. The largest lobes are still in the backscattered area, but they have been shifted to match the new position of the source. Also, instead of many separate lobes, combined lobes are seen. The results for the middle hole (Figures 4.20, 4.23) basically look like a rotated version of those seen for the centered source cases. There is still the small forward scattered component, but it is joined by a small lobe. Also, combined lobes are again seen in the backscattered region. For the largest hole (Figures 4.21, 4.24), the results are essentially just a rotated version of those seen in the centered source case with the addition of a large combined lobe and slight variations in the magnitudes of the lobes.

Figures 4.25 - 4.27 and 4.28 - 4.30 show the magnitude of the scattered amplitude when the finite source has been shifted by $+5.0 \times 10^{-2}$ m and -5.0×10^{-2} m respectively. Again the -5 cm shift cases are the same as the +5 cm shift cases inverted about the x -axis, and there is an overall decrease in magnitude from the centered source case. For the small hole (Figures 4.25, 4.28), the scattering pattern

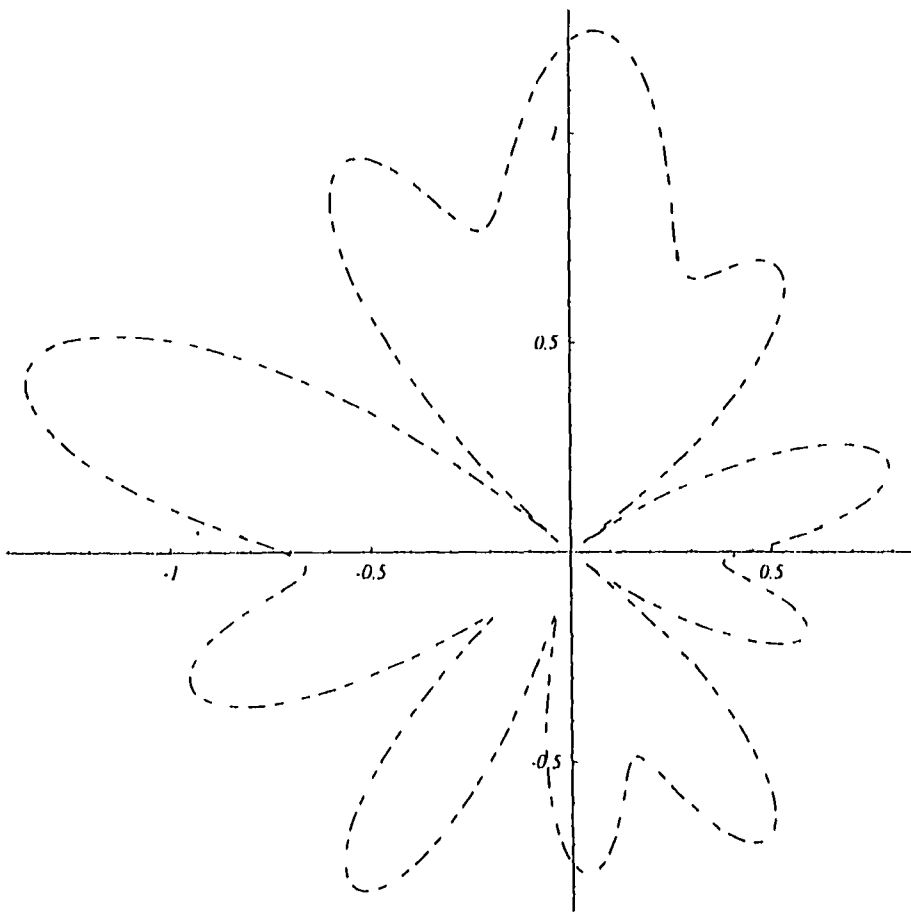


Figure 4.19: Polar plot of the magnitude of the scattered amplitude of a finite source wave incident from the left upon a hole with radius $a = 0.25 \times 10^{-2}$ m when the source has been shifted by +3 cm in the y direction. This plot is rotated and shows a different lobe structure than the previous small hole cases.

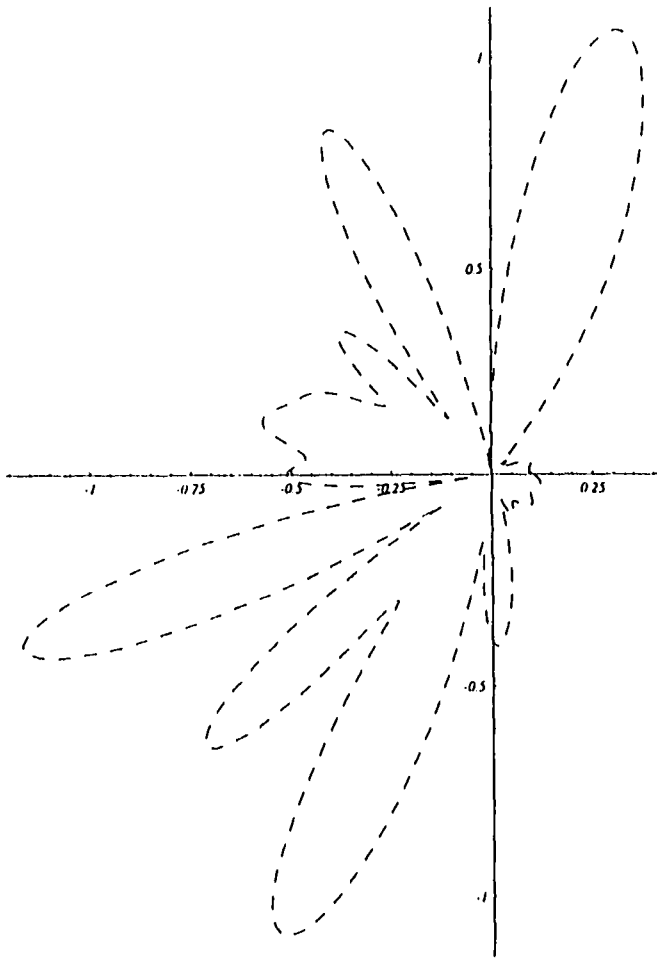


Figure 4.20: Polar plot of the magnitude of the scattered amplitude of a finite source wave incident from the left upon a hole with radius $a = 0.75 \times 10^{-2}$ m when the source has been shifted by +3 cm in the y direction. This plot is essentially a rotated version of the corresponding centered source case.

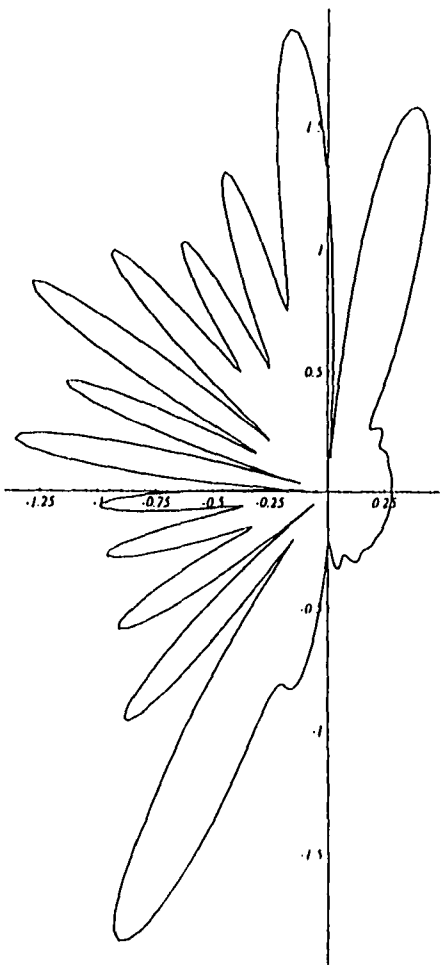


Figure 4.21: Polar plot of the magnitude of the scattered amplitude of a finite source wave incident from the left upon a hole with radius $a = 1.27 \times 10^{-2}$ m when the source has been shifted by +3 cm in the y direction. This plot is essentially a rotated version of the corresponding centered source case.

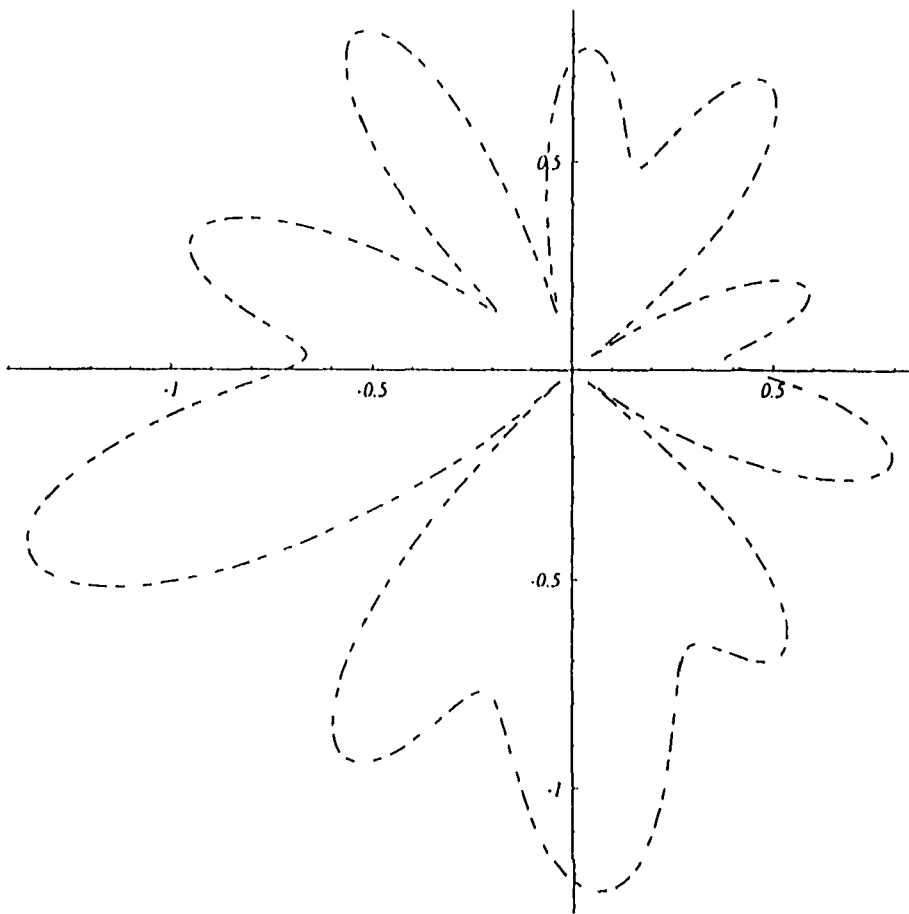


Figure 4.22: Polar plot of the magnitude of the scattered amplitude of a finite source wave incident from the left upon a hole with radius $a = 0.25 \times 10^{-2}$ m when the source has been shifted by -3 cm in the y direction. This plot is the inverse about the x -axis of the corresponding $+3$ cm shift case.

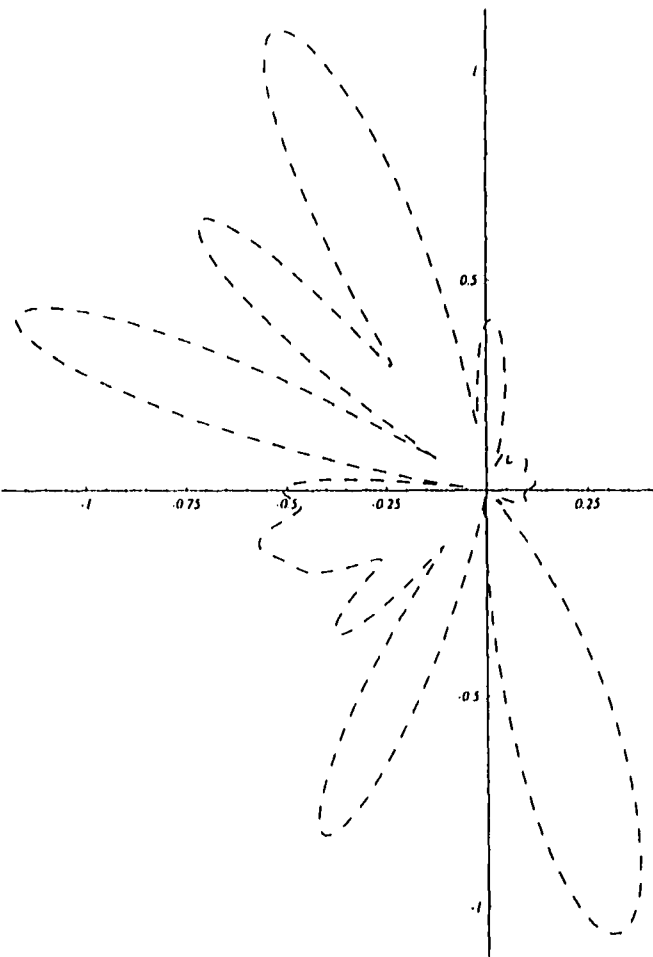


Figure 4.23: Polar plot of the magnitude of the scattered amplitude of a finite source wave incident from the left upon a hole with radius $a = 0.75 \times 10^{-2}$ m when the source has been shifted by -3 cm in the y direction. This plot is the inverse about the x -axis of the corresponding $+3$ cm shift case.

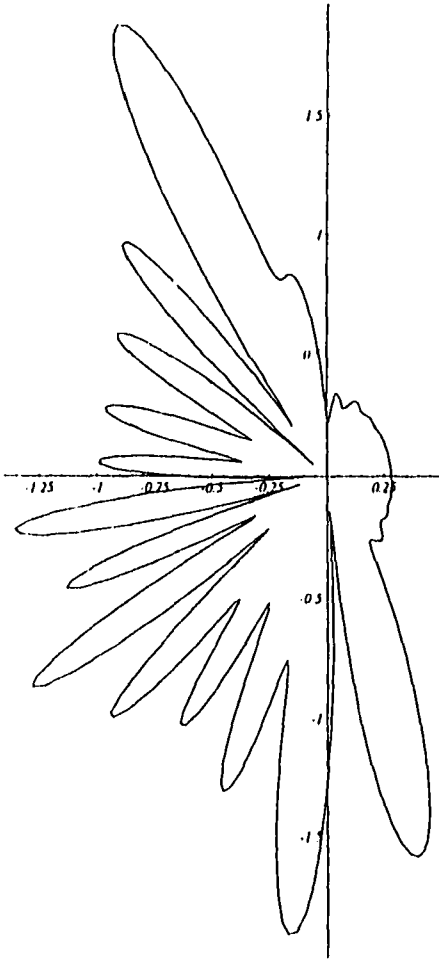


Figure 4.24: Polar plot of the magnitude of the scattered amplitude of a finite source wave incident from the left upon a hole with radius $a = 1.27 \times 10^{-2}$ m when the source has been shifted by -3 cm in the y direction. This plot is the inverse about the x -axis of the corresponding +3 cm shift case.

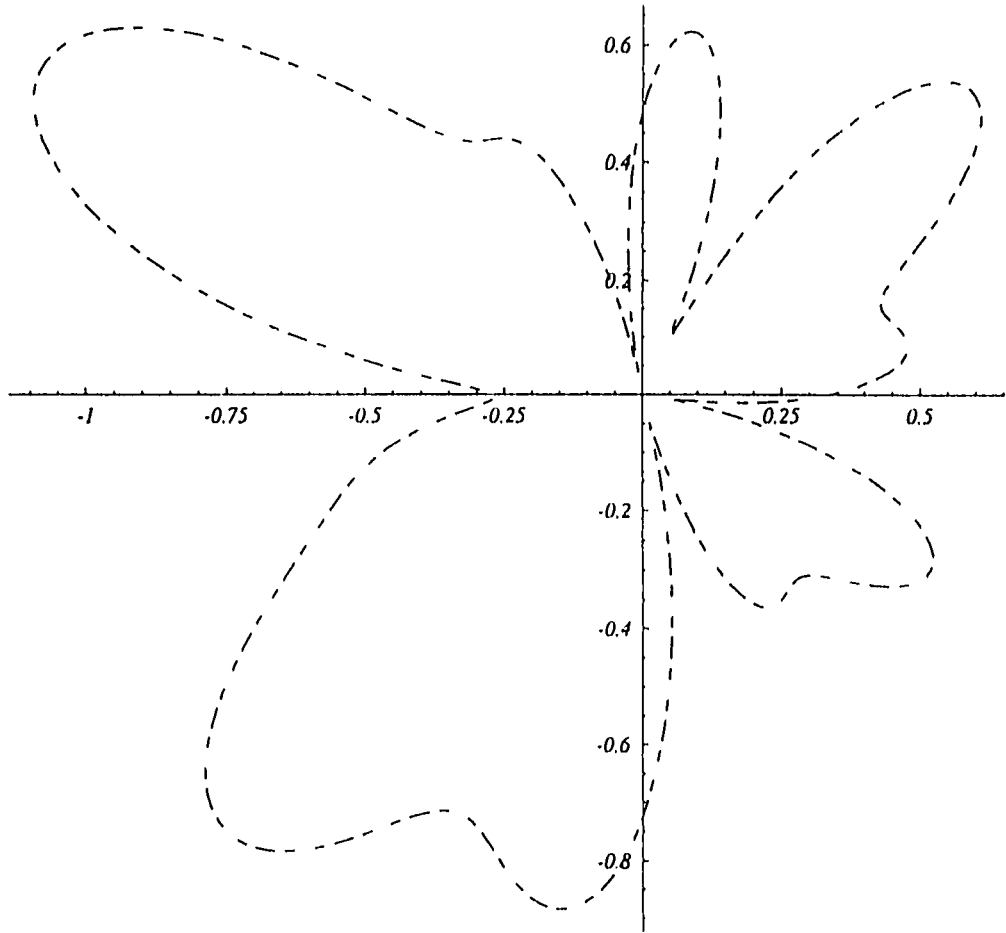


Figure 4.25: Polar plot of the magnitude of the scattered amplitude of a finite source wave incident from the left upon a hole with radius $a = 0.25 \times 10^{-2}$ m when the source has been shifted by +5 cm in the y direction. This plot is rotated and shows a different lobe structure than the previous small hole cases.

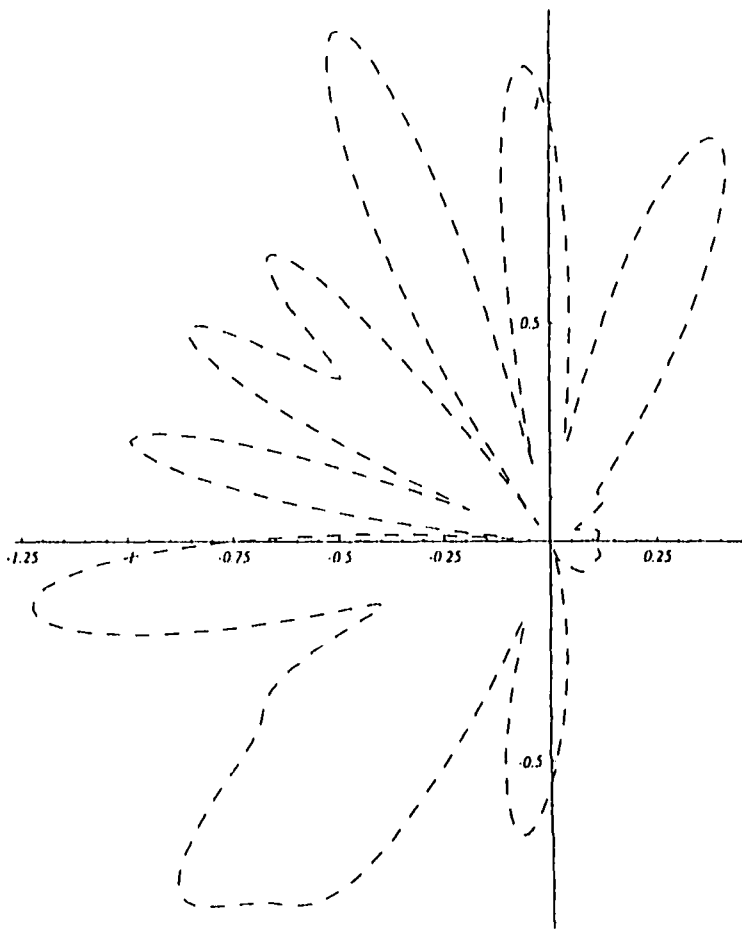


Figure 4.26: Polar plot of the magnitude of the scattered amplitude of a finite source wave incident from the left upon a hole with radius $a = 0.75 \times 10^{-2}$ m when the source has been shifted by +5 cm in the y direction. This plot is essentially a rotated version of the corresponding centered source case.

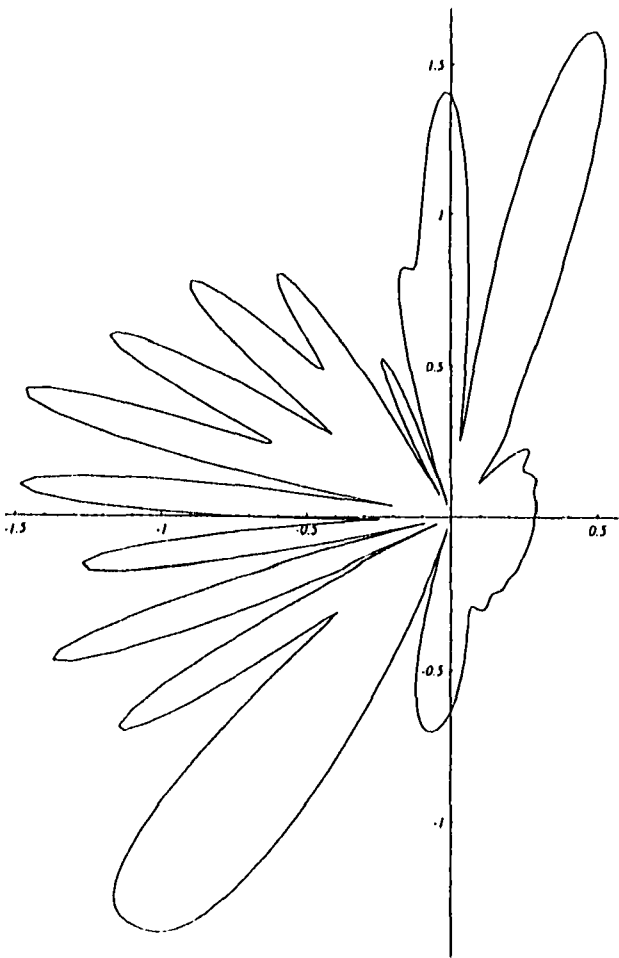


Figure 4.27: Polar plot of the magnitude of the scattered amplitude of a finite source wave incident from the left upon a hole with radius $a = 1.27 \times 10^{-2}$ m when the source has been shifted by +5 cm in the y direction. This plot is essentially a rotated version of the corresponding centered source case.

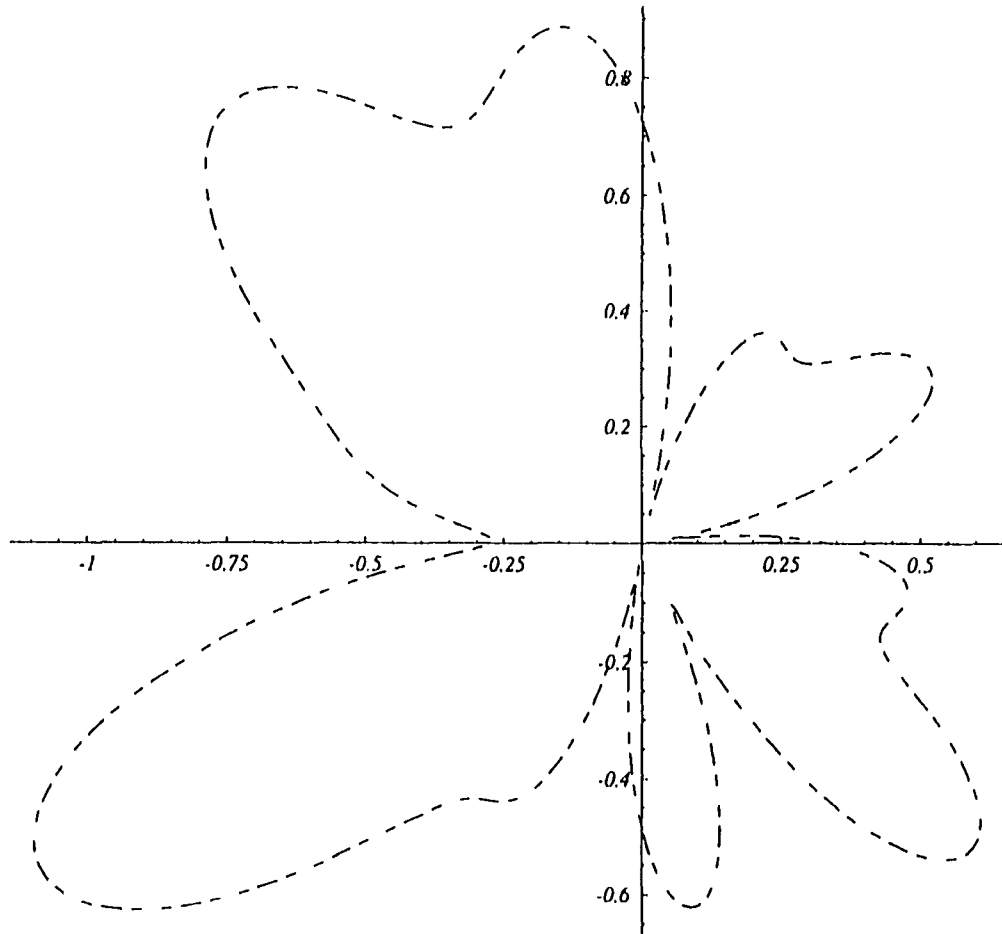


Figure 4.28: Polar plot of the magnitude of the scattered amplitude of a finite source wave incident from the left upon a hole with radius $a = 0.25 \times 10^{-2}$ m when the source has been shifted by -5 cm in the y direction. This plot is the inverse about the x -axis of the corresponding +5 cm shift case.

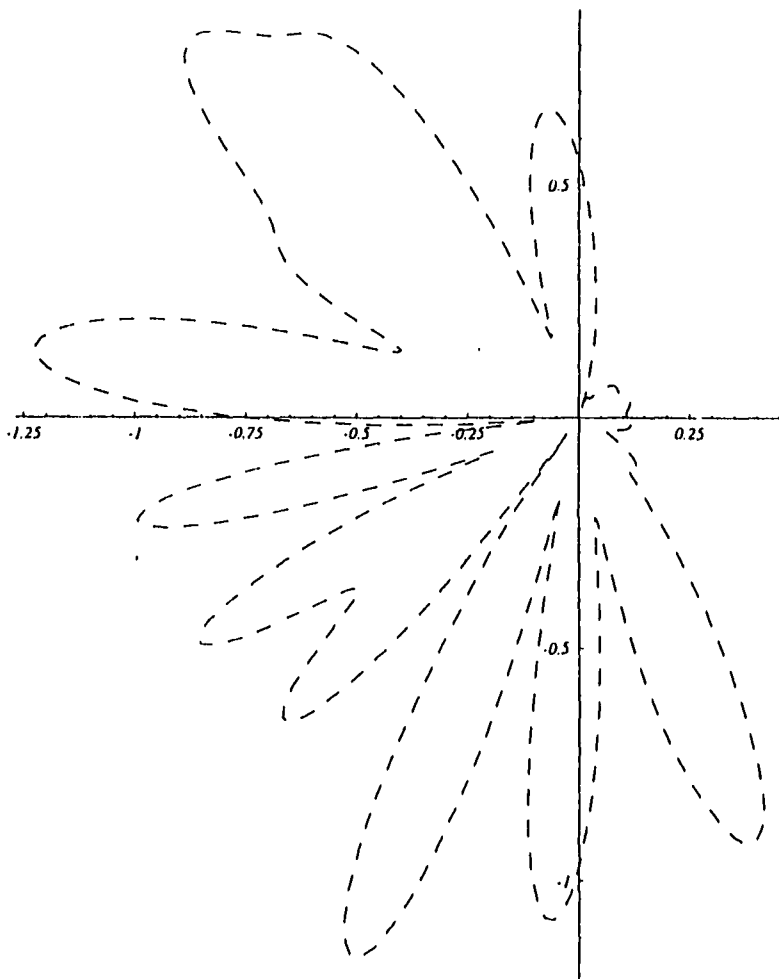


Figure 4.29: Polar plot of the magnitude of the scattered amplitude of a finite source wave incident from the left upon a hole with radius $a = 0.75 \times 10^{-2}$ m when the source has been shifted by -5 cm in the y direction. This plot is the inverse about the x -axis of the corresponding +5 cm shift case.

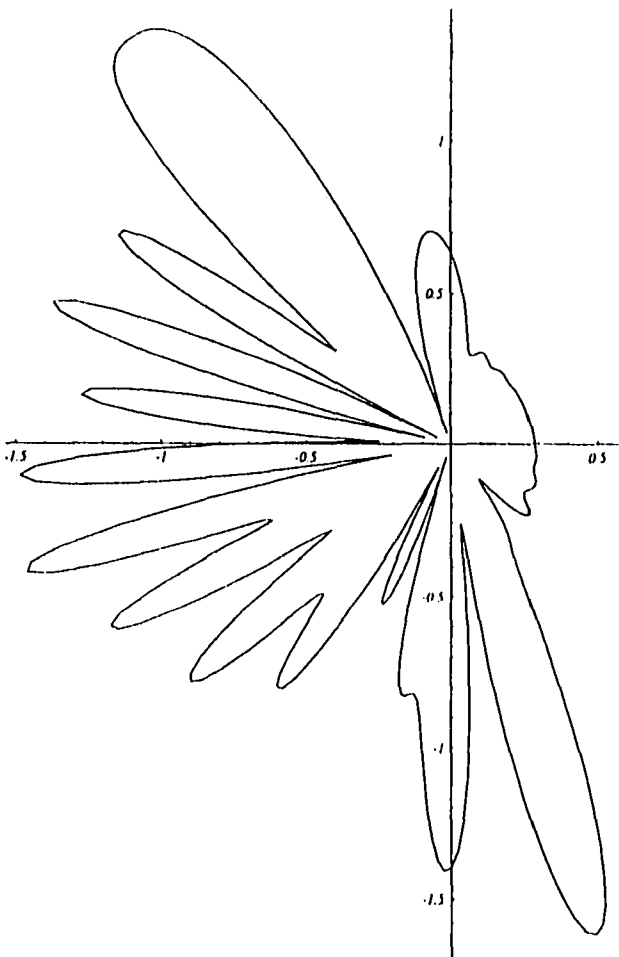


Figure 4.30: Polar plot of the magnitude of the scattered amplitude of a finite source wave incident from the left upon a hole with radius $a = 1.27 \times 10^{-2}$ m when the source has been shifted by -5 cm in the y direction. This plot is the inverse about the x -axis of the corresponding +5 cm shift case.

looks quite different from the centered source and ± 3 shift cases. Only two large lobes are seen in the backscattered direction, and three smaller lobes are seen in the forward direction. For the middle hole (Figures 4.26, 4.29), the results are again a rotated version of those seen previously. However, the magnitude of the backscattered lobes has increased, while that of the other lobes has decreased. Also note that the extra lobe in the forward direction has increased in magnitude. For the large hole (Figures 4.27, 4.30), the pattern is again rotated. The magnitude of the backscattered lobes has increased slightly from the ± 3 shift cases while that of the others has decreased slightly. There are some additional combined lobes, one of the backscattered lobes has gotten much smaller, and an additional forward scattered lobe has appeared.

Although, some differences in the scattering patterns have been noted for the finite source case as the hole size increases, such as the existence of the forward scattering components and changes in the lobe structure, these differences are not clear enough to obviously represent the scattering effects seen in the tomographic images of the large hole. Therefore plotting the magnitude of the scattered amplitude as a function of θ is not the optimum way to present the results. It assumes far-field and neglects physics that may be important here. Instead we will plot the values actually registered by the receiving transducers in the experiments.

In our experiments we use a piezoelectric transducer to receive the Lamb waves. The vibrations of the surface of the plate cause the piezoelectric element to vibrate, and this generates the received electric signal corresponding to the Lamb waves. Therefore, instead of just the scattered amplitude as defined above, we need to examine the full motion of the top surface of the plate. In addition, the transducer is receiving the incident wave as well as the scattered wave, so we need to consider both of these contributions in our calculations.

Recall that the vertical motion of the plate is described by

$$u_z(r, \theta, t) = \frac{\tilde{z}}{h} v_z(r, \theta, t), \quad (4.105)$$

where v_z is as defined in Equation 4.13. At the top surface of the plate, $z = h$, so $u_z = v_z$. Therefore we can write the incident and scattered vertical displacement fields as

$$\begin{aligned} u_z^{INC} &= \sigma_1 \phi_1^{INC} e^{-i\omega t} \\ u_z^{SCAT} &= \sigma_1 \phi_1^{SCAT} + \sigma_2 \phi_2^{SCAT} e^{-i\omega t}. \end{aligned} \quad (4.106)$$

However, since we are only measuring the $S0$ contribution, we use

$$\begin{aligned} u_z^{INC} &= \sigma_1 \phi_1^{INC} e^{-i\omega t} \\ u_z^{SCAT} &= \sigma_1 \phi_1^{SCAT} e^{-i\omega t} \end{aligned} \quad (4.107)$$

to determine the full $S0$ field,

$$u_z^{FULL} = u_z^{INC} + u_z^{SCAT}. \quad (4.108)$$

received by the transducer.

Using Equations 4.22 and 4.23, we can write u_z^{FULL} for the plane wave case as

$$u_z^{FULL} = \sigma_1 i^n e^{in\theta} (J_n(k_1 r) + A_n H_n(k_1 r)) \quad (4.109)$$

where A_n is defined in Equation 4.48. For the point source case we have, using Equations 4.68 and 4.69,

$$u_z^{FULL} = \sigma_1 (-1)^n e^{in\theta} (H_n(k_1 r_0) J_n(k_1 r) + A_n H_n(k_1 r)) \quad (4.110)$$

where A_n is defined in Equation 4.81. Finally for the finite source case we have using Equation 4.83, a general expression for each point source given by

$$u_z^{FULL(j)} = C_j \sigma_1 (-1)^n e^{in\theta_j} (H_n(k_1 r_j) J_n(k_1 r) + A_n^j H_n(k_1 r)) \quad (4.111)$$

where the A_n 's, C_j 's, r_j 's, and θ_j 's are given by Equations 4.84, 4.82, 4.92, 4.94, and 4.95. Then the vertical displacement for the finite source case is given by

$$u_z^{FULL} = \sum_{j=1}^5 u_z^{FULL(j)}. \quad (4.112)$$

In the experiments, the Lamb waves are generated at one location and received at a separate location. For PPT, the transducers are moved together as a pair, and for a given scan, the generating and receiving locations can be represented by $(-x, y)$ and (x, y) respectively. As the scan progresses, the x -coordinate of the receiver location remains fixed, while the y -coordinate varies. Thus, we obtain data along a line parallel to the y -axis (Figure 4.31).

Since

$$\begin{aligned} r &= ((x)^2 + (y)^2)^{\frac{1}{2}} \\ \theta &= \arctan\left(\frac{y}{x}\right), \end{aligned} \quad (4.113)$$

the vertical displacement of the combined incident and scattered $S0$ waves, u_z^{FULL} , can be calculated at each receiver location. Also, since the transducer is only sensitive to the real motion of the plate, only the real part of the vertical displacement is used. These calculated vertical displacement values can then be plotted as a function of y to form vertical displacement curves. These curves represent the vertical displacement of the top surface of the plate along a specified line, $x = \text{constant}$.

Figures 4.32 - 4.34 show the vertical displacement curves for the case of a plane $S0$ wave incident upon a hole of radius $a = 0.25 \times 10^{-2}$ m, $a = 0.75 \times 10^{-2}$ m, and $a = 1.27 \times 10^{-2}$ m respectively. In order to match the experiments, the values $\lambda = 6.293 \times 10^{10}$ kg/ms², $\mu = 2.677 \times 10^{10}$ kg/ms², $\rho = 2700$ kg/m³, $\omega = 2\pi(1.1) \times 10^6$ Hz, and $h = 1.143 \times 10^{-3}$ m have been chosen, and the x -coordinate of the receiver line is set as 8.75×10^{-2} m. In the absence of scattering, we would simply expect to

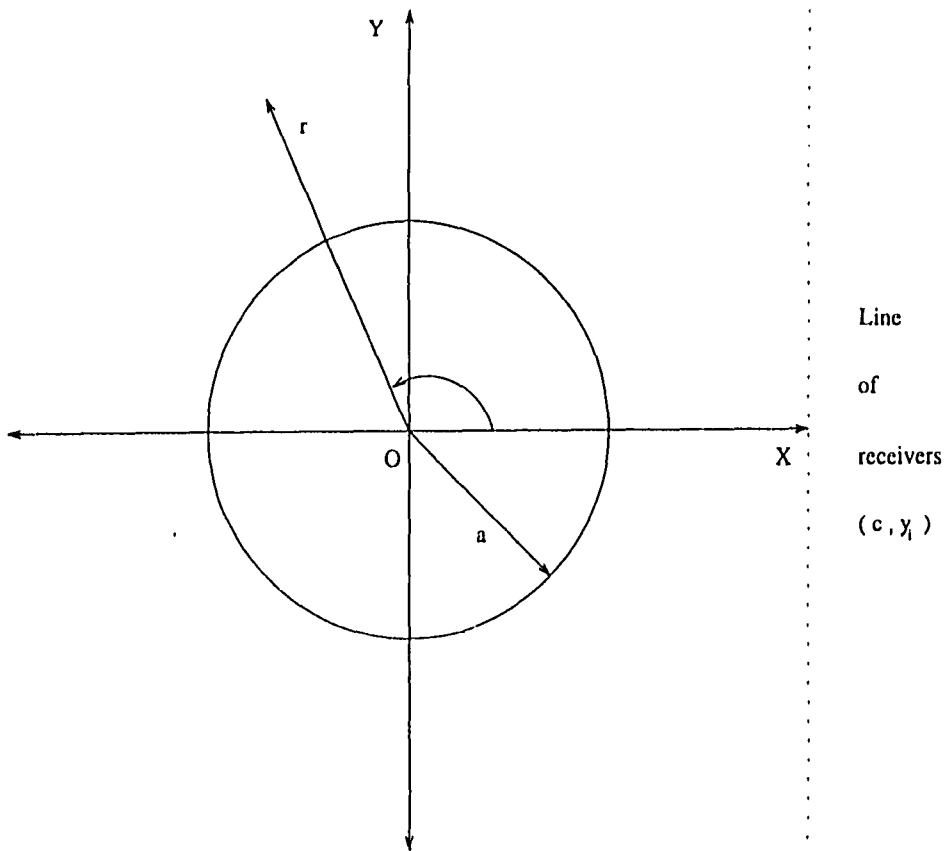


Figure 4.31: The line of receiver locations for a single scan in PPT is shown for the geometry of a hole in a plate. Notice that since all of the points have the same x -coordinate, the line is parallel to the y -axis.

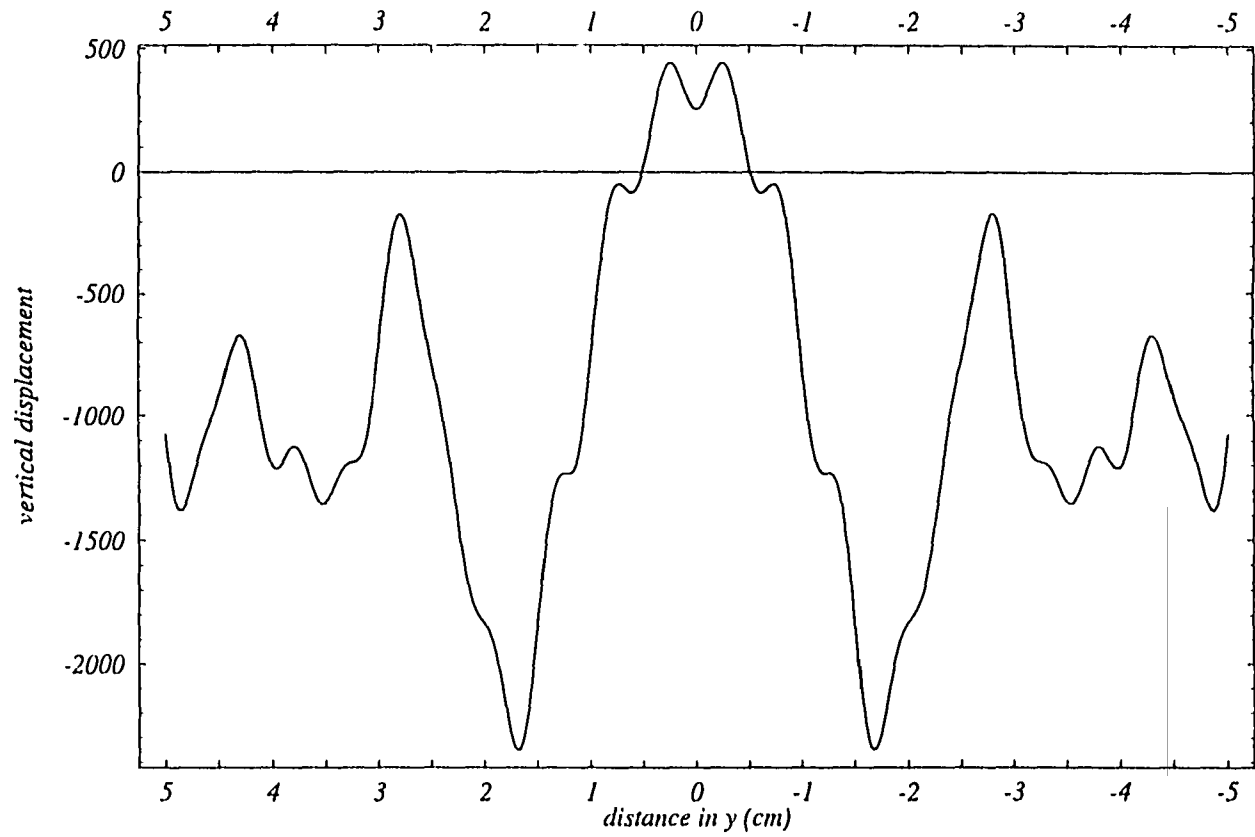


Figure 4.32: Vertical displacement curve for the case of a plane wave incident from the left upon a hole with radius $a = 0.25 \times 10^{-2}$ m. Note that the magnitude of the vertical displacement is not uniform outside of the flaw area indicating scattering effects. Also, notice that the vertical displacement is negative except in the flaw region where it is positive.

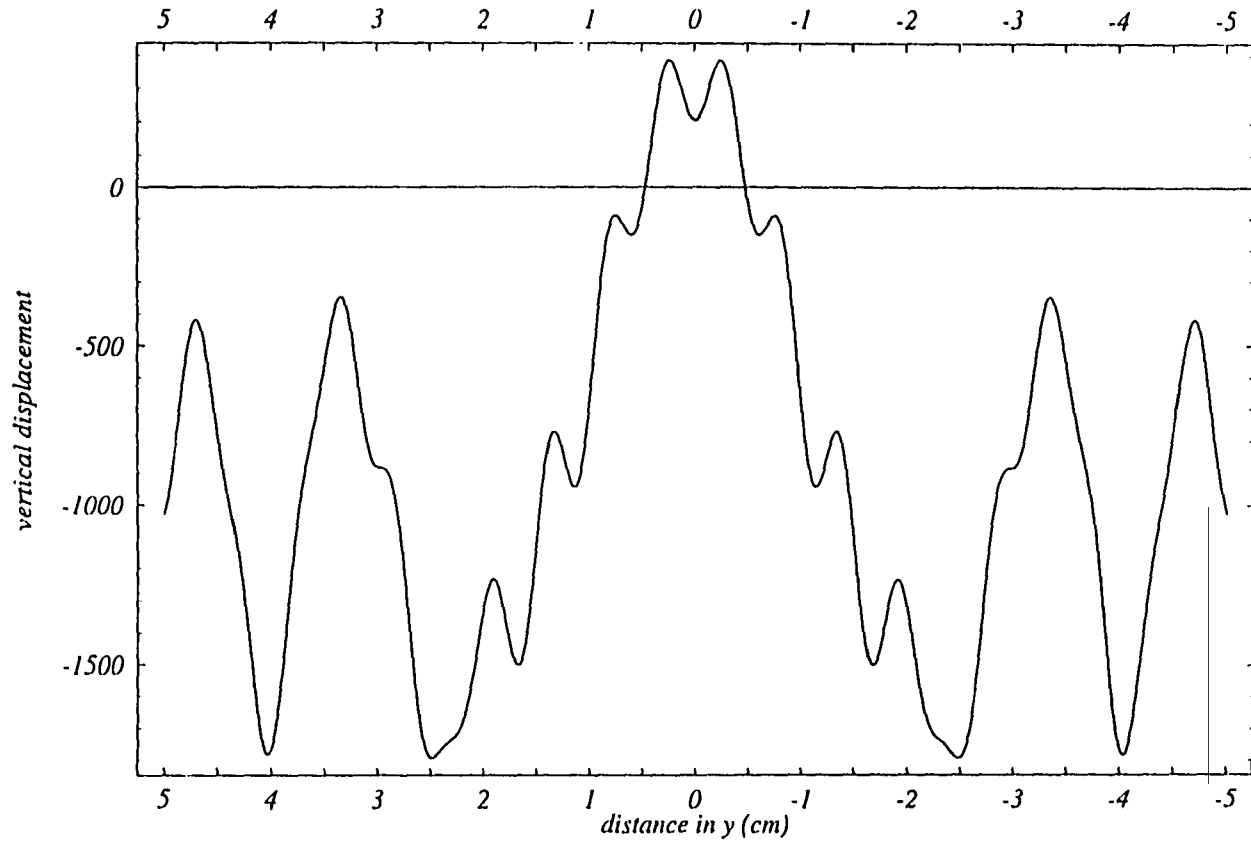


Figure 4.33: Vertical displacement curve for the case of a plane wave incident from the left upon a hole with radius $a = 0.75 \times 10^{-2}$ m. This curve shows the same features as that for the small hole case. The only difference being that the positive vertical displacement region is larger corresponding to the larger flaw size.

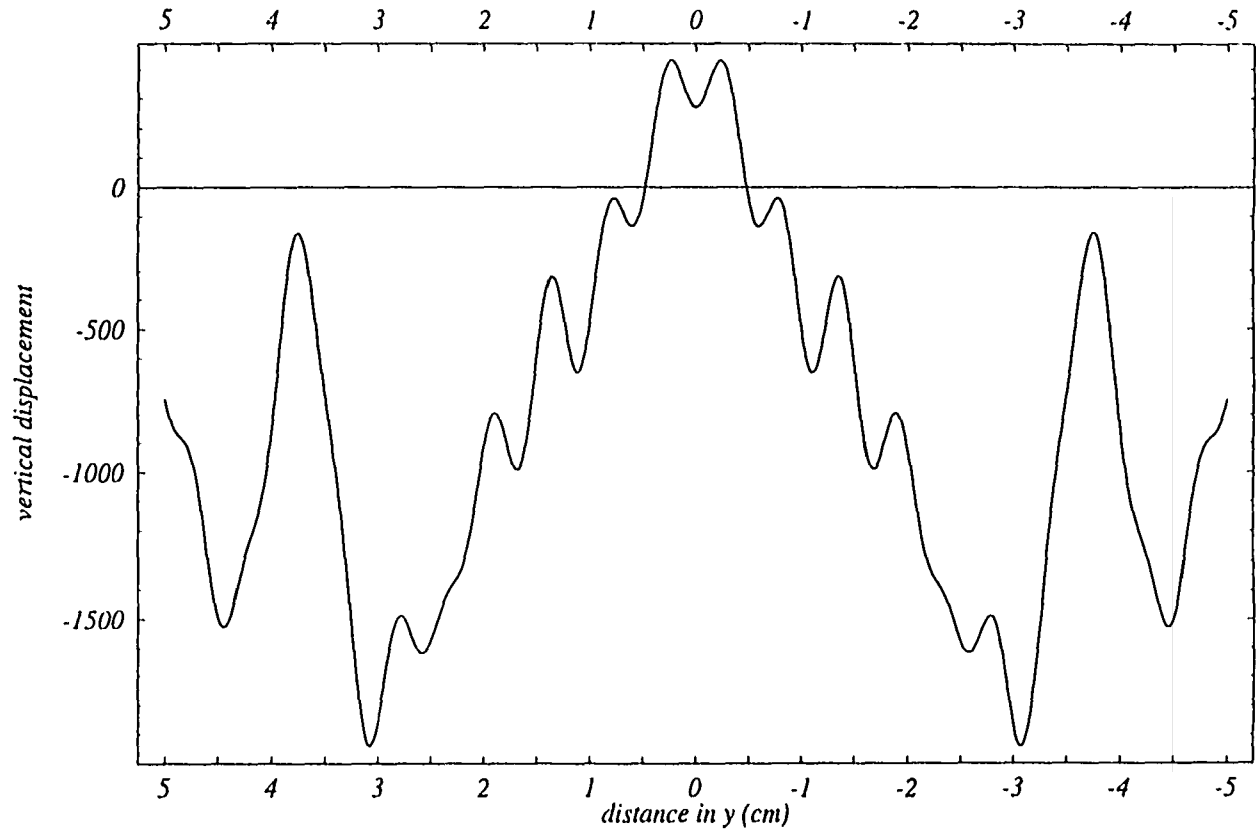


Figure 4.34: Vertical displacement curve for the case of a plane wave incident from the left upon a hole with radius $a = 1.27 \times 10^{-2}$ m. This curve also shows an increase in the positive vertical displacement region corresponding to the larger flaw size, and it exhibits the same general characteristics as the small hole case.

see a uniform value for the vertical displacement except in the flaw area where we would expect a shadow region since the $S0$ Lamb wave cannot propagate through the hole. Instead, we see fluctuations in the magnitude of the vertical displacement throughout the curve. These variations are due to the scattering of the plane wave from the hole. Comparing the three figures, we see that the majority of the curve is negative implying motion of the plate below $z = h$ (Figure 3.2). However, in the flaw region about $y = 0$, the vertical displacement is positive implying motion above $z = h$ (Figure 3.2). The main difference between the curves as the hole size increases is that the maximum negative peaks move farther away from $y = 0$ and their magnitude decreases. However, there are no sharp changes in the curves for the largest hole, and so nothing to indicate the scattering effects seen in the tomographic images.

Figures 4.35 - 4.37 show the vertical displacement curves for the case of a point source $S0$ wave incident upon a hole of radius $a = 0.25 \times 10^{-2}$ m, $a = 0.75 \times 10^{-2}$ m, and $a = 1.27 \times 10^{-2}$ m respectively. The values of λ , μ , ρ , ω , h , and of the x -coordinate of the receiver line are the same as above. In addition, the x -coordinate of the point source is set as -8.75×10^{-2} m. Since the incident wave is cylindrical, the vertical displacement values along a line will not show if the magnitude of the vertical displacement is uniform. Instead we focus on the flaw region. For the small hole (Figure 4.35), the vertical displacement is negative in the flaw region until $y = \pm 1$ where it switches to a positive value until $y = \pm 2$. Over this region, the magnitude of the vertical displacement is decreasing. For the middle hole (Figure 4.36), the vertical displacement remains negative out past $y = \pm 2$ and the magnitude is relatively constant other than small oscillations. Finally for the large hole (Figure 4.37), the vertical displacement is positive out to about $y = \pm 1.3$ where it becomes negative. The magnitude in this region gradually

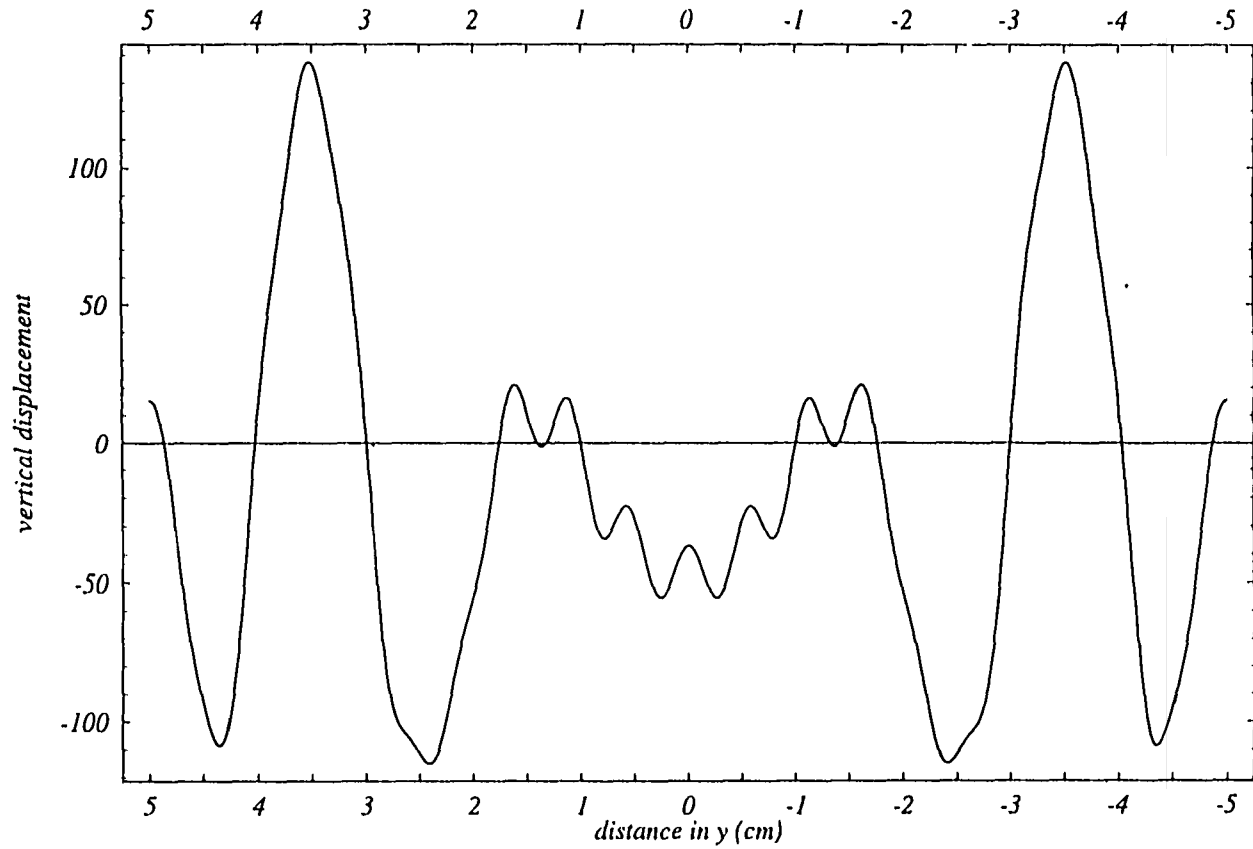


Figure 4.35: Vertical displacement curve for the case of a point source wave incident from the left upon a hole with radius $a = 0.25 \times 10^{-2}$ m. Note that the vertical displacement is negative out until $y = \pm 1$, where it briefly switches to positive vertical displacement.

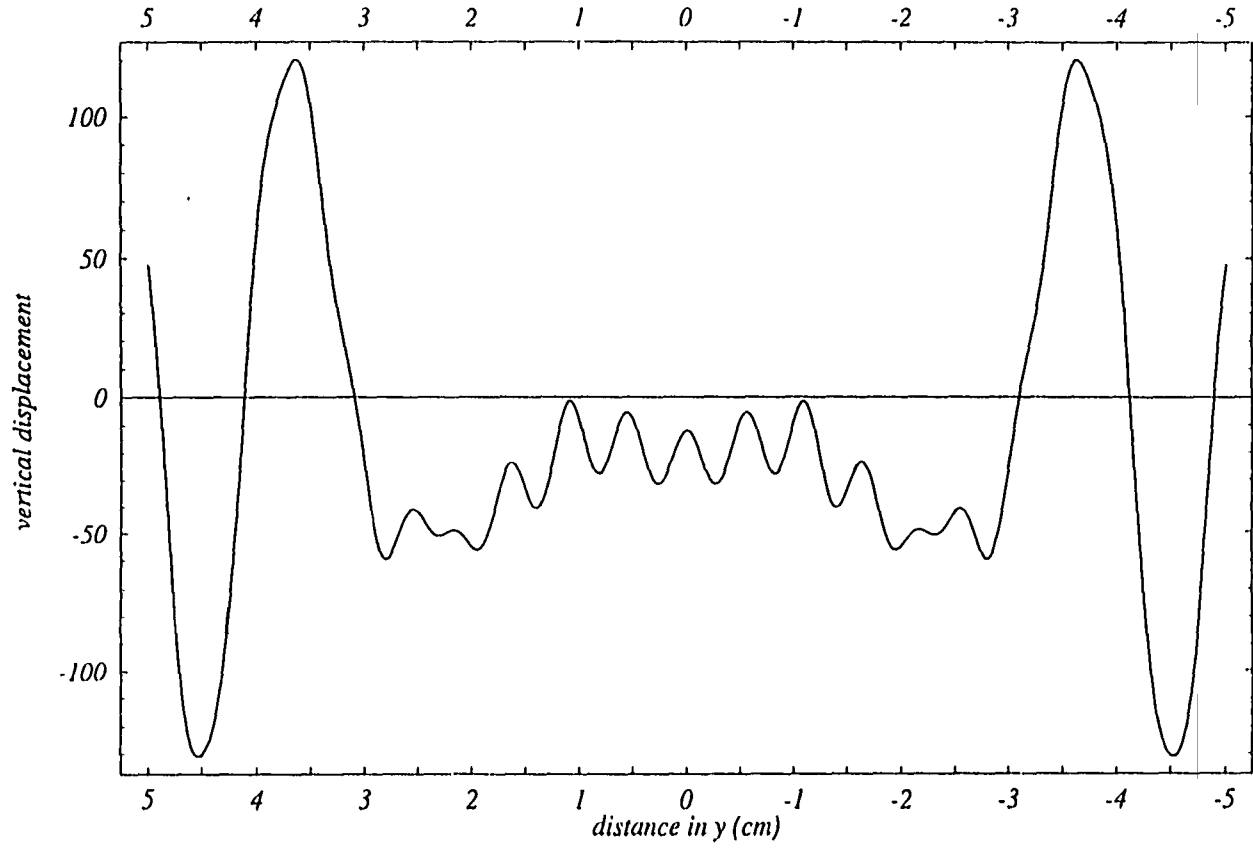


Figure 4.36: Vertical displacement curve for the case of a point source wave incident from the left upon a hole with radius $a = 0.75 \times 10^{-2}$ m. Note that the vertical displacement is negative past $y = \pm 2$, and it has a relatively uniform character.

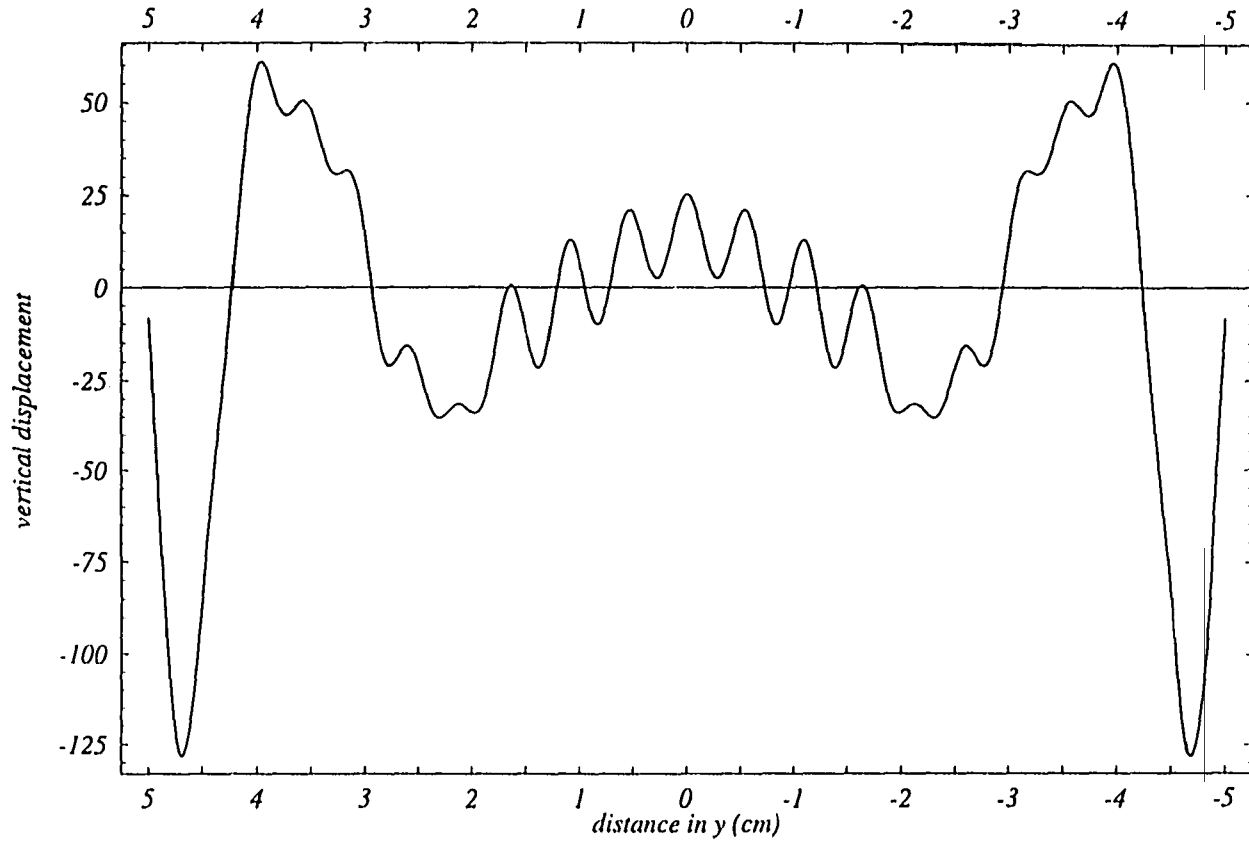


Figure 4.37: Vertical displacement curve for the case of a point source wave incident from the left upon a hole with radius $a = 1.27 \times 10^{-2}$ m. Note that the vertical displacement is now positive out until $y = \pm 1$, where it switches to negative vertical displacement. This phase change in the motion of the plate in the flaw region represents a distinct change from the behavior seen for the two smaller holes.

decreases until $y = \pm 1.3$ when it starts increasing again. This change in phase of the vertical displacement in the flaw region as the hole size increases could indicate the scattering effects seen in the tomographic images. It predicts a change in the motion of the plate, not just a change in the amplitude of the motion. However, the phase change is gradual for the point source case in which the incident wave still extends far past the flaw region.

Figures 4.38 - 4.40 show the vertical displacement curves for the case of a finite source $S0$ wave incident upon a hole of radius $a = 0.25 \times 10^{-2}$ m, $a = 0.75 \times 10^{-2}$ m, and $a = 1.27 \times 10^{-2}$ m respectively. The values of λ , μ , ρ , ω , h , and of the x -coordinate of the receiver line are the same as above. In addition, the x -coordinate of the point sources in the finite source is set as -8.75×10^{-2} m. In all three plots, we see that the magnitude is basically the same until we approach the edge of the hole. At this point the magnitude dramatically increases due to the large contribution of the scattered field with the incident field at the receiver location, and we have a large positive vertical displacement. Next, we consider the flaw region. For the small and medium holes (Figures 4.38, 4.39), the magnitude drops to almost zero at the edge of the hole, where the vertical displacement becomes negative, and then increases until $y = 0$. For the large hole (Figure 4.40), the magnitude again decreases until the very edge of the hole, where the curve starts to oscillate between positive and negative vertical displacement values until $y = 0.25$ where the magnitude increases and the vertical displacement remains positive until $y = 0$. While the large magnitudes near the edges of the holes indicate scattering effects, the rapid oscillations and positive vertical displacement values in the flaw region of the large hole indicate some additional effects. In contrast to the motion for the two smaller holes, the motion of the plate with the large hole rapidly oscillates between positive and negative values at the edge and just inside the flaw region.

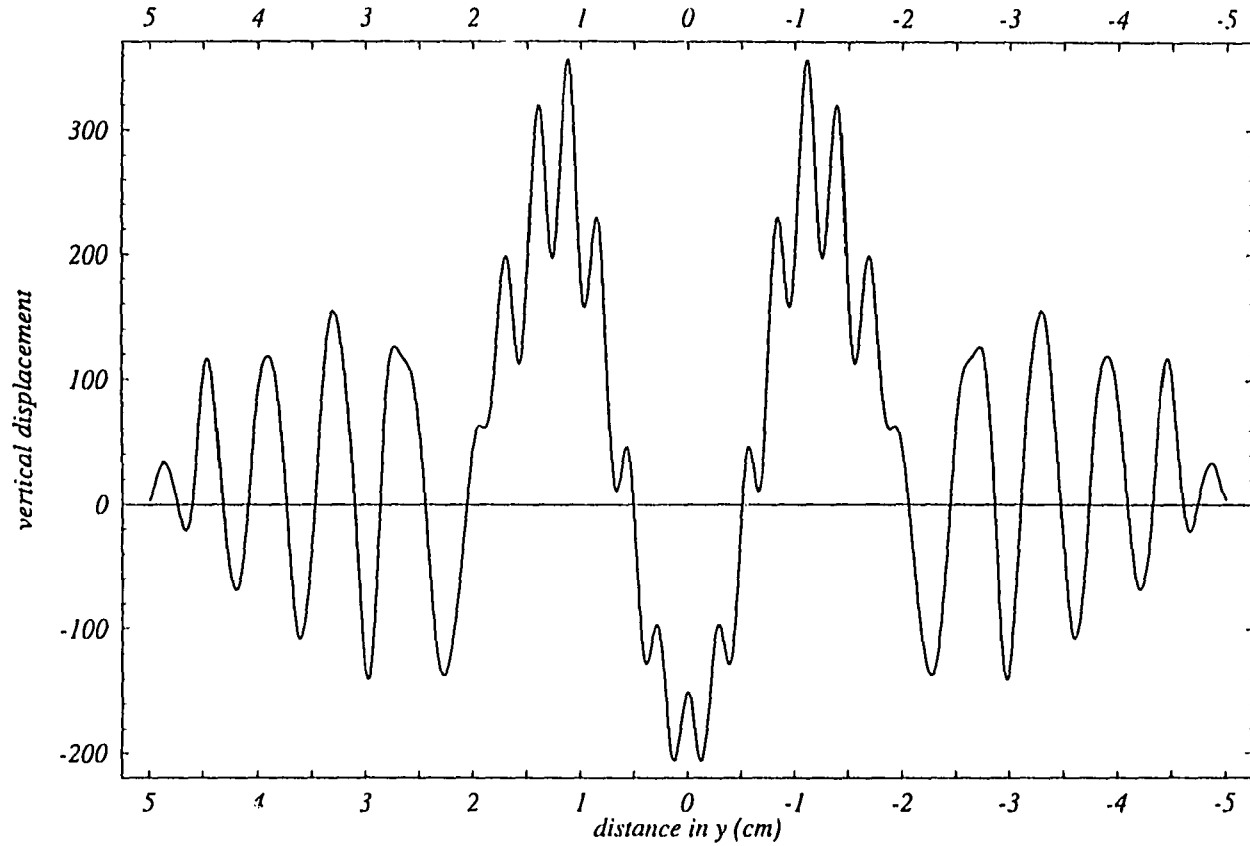


Figure 4.38: Vertical displacement curve for the case of a finite source wave incident from the left upon a hole with radius $a = 0.25 \times 10^{-2}$ m. Note the large vertical displacement values recorded near the edges of the flaw. These are due to the large scattered contributions. Also note that the magnitude drops to zero at the flaw edge where the vertical displacement becomes negative, and then gradually increases until the center of the flaw region.

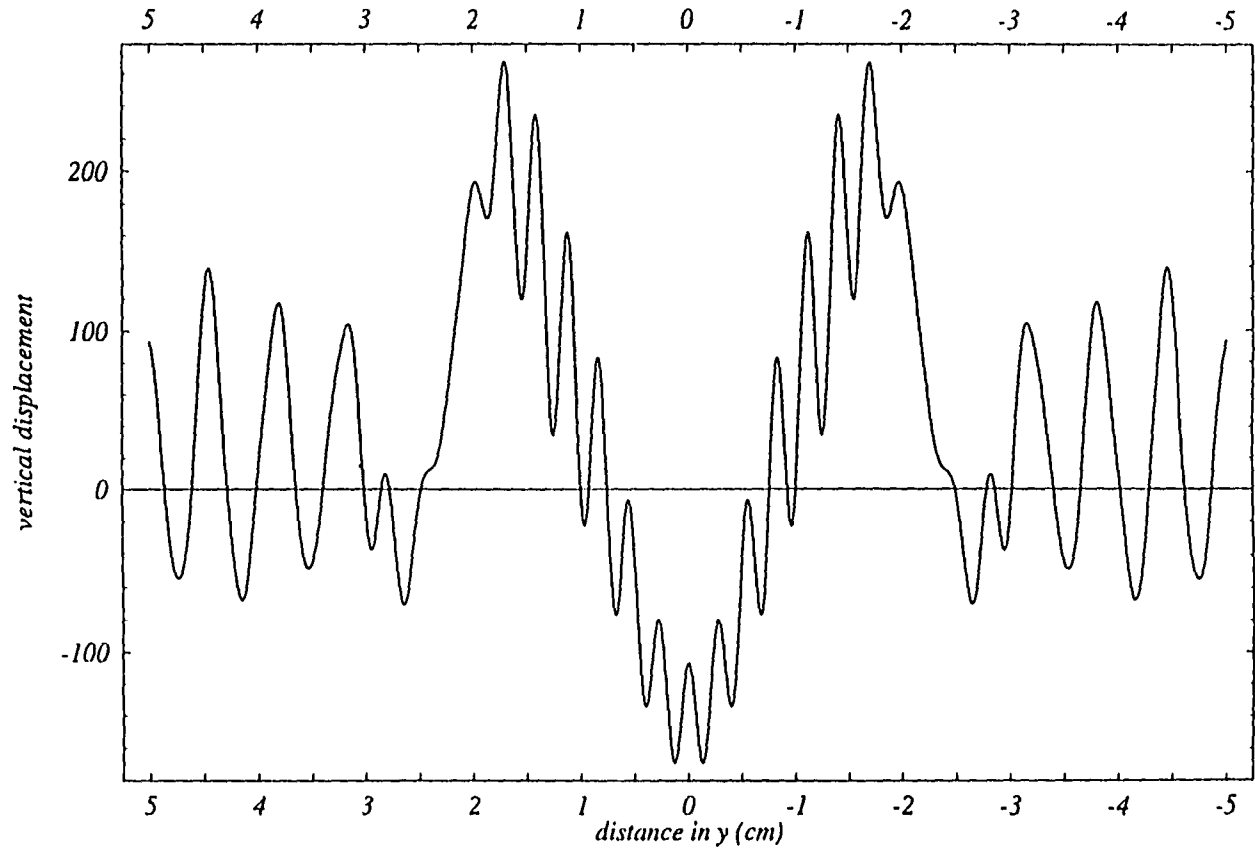


Figure 4.39: Vertical displacement curve for the case of a finite source wave incident from the left upon a hole with radius $a = 0.75 \times 10^{-2}$ m. Note the large vertical displacement values recorded near the edges of the flaw. These are due to the large scattered contributions. Again the magnitude drops to zero at the flaw edge where the vertical displacement becomes negative, and then gradually increases until the center of the flaw region.

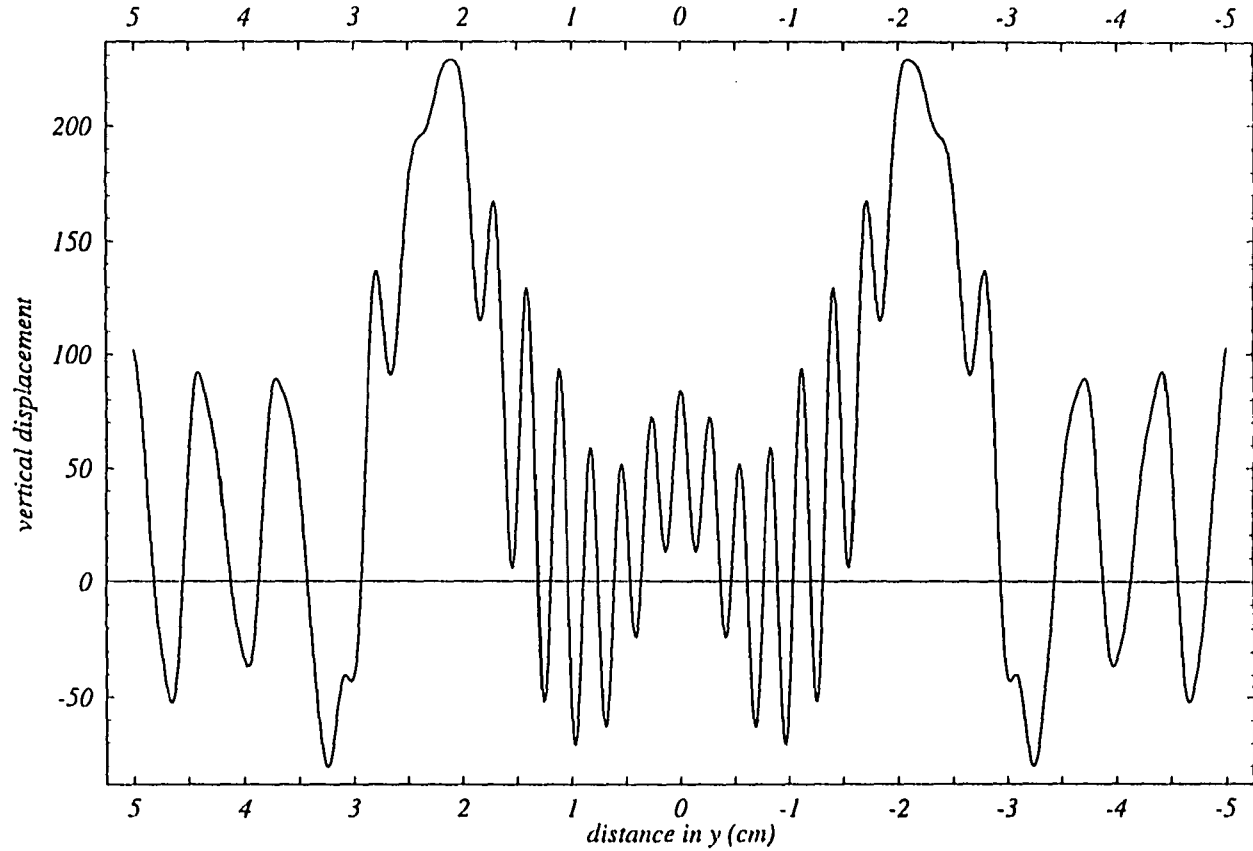


Figure 4.40: Vertical displacement curve for the case of a finite source wave incident from the left upon a hole with radius $a = 1.27 \times 10^{-2}$ m. Note the large vertical displacement values recorded near the edges of the flaw. These are due to the large scattered contributions. Also note that the magnitude decreases but does not drop to zero at the flaw edge where the vertical displacement rapidly oscillates between positive and negative values. At the center of the flaw region, the vertical displacement becomes positive and the magnitude increases. The rapid oscillations of the vertical displacement and the positive value at the center of the flaw in contrast to the results of the smaller holes, reveal distinct scattering effects for this case.

Then the plate settles into a positive vertical displacement at the center of the flaw region in contrast to the negative vertical displacement seen for the two smaller holes. The rapid oscillations which are over an area smaller than the transducer element size, could be responsible for the streaking effects seen in the tomographic images, while the phase change at the center of the flaw region may be responsible for the scalloping or other effects.

The scattering theory developed in this chapter has been shown to predict distinct behavior of the plate vertical displacement for the case of a finite source incident upon a hole of radius $a = 1.27 \times 10^{-2}$ m. This correlates with the experimental results in which the starburst streaking pattern and scalloping were seen in the PPT image for the large hole in the aluminum plate. The vertical displacement curves shown above are for the PPT transducer arrangement of a transducer pair being scanned along the sample. Vertical displacement curves have not been calculated for the CBT transducer arrangement because the resolution of the CBT images was not high enough to show definite scattering effects. However, curves which represent the vertical displacement at all of the receiver locations for each sender location in the CBT geometry, can also easily be obtained.

Chapter 5

Discussion and Future Work

Lamb waves have been shown to provide a viable means for nondestructively evaluating large sections of plate-like structures such as those found in our nation's aging aircraft. Because Lamb waves are guided waves, they can propagate large distances in these plate-like structures, while their dispersive nature allows them to be sensitive to changes in thickness. This allows for defects such as corrosion to be rapidly detected. For example, when the experiment is performed in the frequency-thickness range of $2.0 \text{ MHz-mm} \leq fd \leq 2.6 \text{ MHz-mm}$ for aluminum, a decrease in thickness corresponds to an increase in the velocity of the S_0 mode. Therefore, for the same distance, an S_0 Lamb wave passing through a region containing corrosion will have a faster time-of-flight than one passing through a flawless region. By scanning a pair of transducers along a plate structure, and recording the time-of-flight at each point in the scan, a one-dimensional map of any flaws can be obtained. For the actual scans however, a Pulse Phase Lock Loop (P2L2) can be used. The P2L2 circuitry determines the phase shift associated with the change in the time-of-flight, and uses this value to alter the frequency of the signal [460]. A plot of these frequency values corresponds to a plot of the velocity at each point along the scan

since the dispersion relation can be used to convert the frequency values to velocity values. Lamb wave scans on aluminum plates have been shown to be sensitive to thinning (simulated corrosion) and holes in aluminum plates. By performing a second scan at 90° to the first, the location of any flaws can be determined along the second coordinate direction. By combining these two scans, a flaw region can be pinpointed in the two in-plane dimensions of the plate.

Performing scans along several directions over the same region of interest allows for tomographic algorithms to be used to reconstruct a *quantitative* map of the S_0 mode velocities. Using the Lamb wave dispersion relations, these velocity values can be converted to thickness values. Therefore, a map of the region of interest which not only gives an accurate location for the flaw, but provides a quantitative measure of changes in thickness, can be obtained. Parallel Projection Tomography (PPT) using the Convolution-Backprojection algorithm is a straightforward extension of the Lamb wave scanning. For PPT, a pair of transducers is scanned spanning a certain region of interest. The plate is then rotated, and another scan is performed along the next direction. This process is repeated until scans have been performed along several equally spaced orientations. For symmetric flaws, such as the circular thinning or small hole in a plate cases, PPT has been shown to give quite accurate results with 18 scans taken in 10° increments. However, for less symmetric flaws, many more orientations will be necessary for an accurate reconstruction. This is time intensive. In addition, while it is easy in a laboratory setting to rotate small samples for all of the necessary orientations, this becomes problematic for in-the-field applications. For example, an aircraft being inspected cannot be rotated, and rotating the scanning apparatus is difficult because its center point must remain exactly stationary and the coupling of the transducers is a major concern. In addition, as more orientations are needed, a fairly large ring region must be obstruction free,

so that the apparatus can scan in all orientations. This makes scanning lines of rivets, lap joints, or doublers impossible. Finally, the desired end result of the aircraft inspection is to produce a map of the full aircraft composed from the individual scans. PPT tomography produces maps of circular regions, so either information will be missing between the individual maps, or adjacent maps will have to overlap significantly. This is inefficient and time consuming.

Cross Borehole tomography (CBT) using the Algebraic Reconstruction Technique (ART) algorithm provides a solution to these problems. In CBT, the transducers are independently scanned along two parallel lines. Because of the large changes in the distance between senders and receivers, the P2L2 can no longer be used since it jumps lock and the recorded values are inaccurate. Instead, the entire waveform for each sender/receiver pair is digitized and saved. A rudimentary expert system has been developed to extract the S_0 time-of-flight from each waveform. The expert system uses a pattern matching technique to locate the S_0 wave part of the waveform, and then records the starting point of that signal. This starting point is the time-of-flight, and the procedure is repeated for each sender/receiver pair. The ART algorithm then uses this data to produce a map of the region under inspection. Because of its origins in seismological studies, CBT does not require symmetry in the flaws, and it only requires access from two sides. The ray density is nonuniform. there are fewer rays, and the rays intersect the flaw from fewer angles. All of these reduce the quality of the tomographic reconstruction. However, since the scanning apparatus does not have to rotate, inspecting lines of rivets is not a problem, and since access is only required from two sides along the surface, the reconstructions are rectangular. Therefore a composite tomographic flaw map of a full aircraft is much easier to construct. This method is far more practical for the development of an in-the-field testing apparatus for aircraft. The CBT method has been shown

to accurately reconstruct the location and size of the thinning and small hole cases in the aluminum plates. Due to the smaller number of rays and fewer ray orientations, the reconstructed images are coarser and do not accurately reproduce the exact shape of the flaw. However, the flaws are detectable and the potential for in-the-field inspections far outweighs the better reconstructions possible with the PPT method.

Both PPT and CBT assume straight rays and no diffraction. While accurate for the thinning levels which motivated this work, these assumptions are not true in general. In order to study the limitations of these assumptions, aluminum plates with 0.75 cm and 1.27 cm radius through-holes have been studied. For the 0.75 cm radius hole, both the PPT and CBT reconstructed the hole in the correct position and with about the correct size. However, for the 1.27 cm radius hole, PPT produced a reconstruction with a starburst streaking effect and scalloping around the edges of the hole which was smaller than the actual size. CBT reconstructed the 1.27 cm hole in the wrong position and with inaccurate size and shape. Clearly, the straight ray and no diffraction assumptions are invalid for the large hole flaw.

In order to understand why the small hole is accurately reconstructed while the large hole so strongly affected the reconstructions, theoretical calculations of the scattering of the S_0 waves from through-holes in aluminum plates have been calculated. Using the higher-order plate theory of Kane and Mindlin, the scattering of plane, point source, and finite source S_0 waves from 0.25 cm, 0.75 cm and 1.27 cm holes in aluminum plates were simulated. First, polar plots of the magnitude of the scattered S_0 amplitude as a function of angle were examined. These plots did not show any special behavior for the large hole versus that of the small holes for plane, point source, or finite source incidence. Next, vertical displacement curves which plot the displacement of the top surface of the plate along a specified line

were examined. These vertical displacement values more accurately represent the experimental measurements, since the motion of the top surface of the plate provides the vibrations that produce the received signal. The plane wave and point source results did not show any distinctive behavior for the large hole. However, the finite source case which most accurately describes the experiment, did show rapid oscillations in the vertical displacement of the top surface of the plate near the edge of the hole and a difference in phase of the vertical displacement at the center of the hole from that seen in the smaller hole results. Therefore, the theoretical results have shown that for a finite source $S0$ Lamb wave scattering from a hole in a plate, as the hole reaches a size comparable to or larger than the beam width, distinct scattering effects occur. These effects are outside of the assumptions of the PPT and CBT and cause the effects seen in the tomographic reconstructions.

Lamb wave scanning has been shown to be a rapid nondestructive means by which large sections of aircraft can be inspected. Applying tomographic algorithms to the Lamb wave data has allowed for quantitative maps of the plate regions studied to be produced. Two tomographic methods, PPT and CBT, have been shown to accurately detect flaws such as thinning, in plate structures. However, while PPT provides more accurate reconstructions, CBT is more practical for in-the-field testing of aircraft. Furthermore, the limitations of these two methods have been found experimentally and have been correlated with theoretical calculations. Future work will involve converting the laboratory apparatus to practical in-the-field testing apparatus, developing the expert system to be able to extract multiple parameters for multiple modes from the received waveforms, and using the scattering theory to develop new tomographic algorithms to take into account the diffraction and ray bending effects.

For, the solution for the scattering of the $S0$ Lamb wave from a circular

region can be used to develop a diffraction tomography algorithm (Appendix B). In addition, the theory of Kane and Mindlin can also be used to model the scattering and transmission of the S_0 wave at the interface between adjacent plates (Appendix C). In CBT, when we discretize the region between the sending and receiving rows, the S_0 wave passes through adjacent cells. Therefore, this theory can be used to calculate the angle of the transmitted wave at each cell boundary, and ray bending effects can be accounted for.

Lamb wave tomography can provide a rapid and nondestructive way to inspect entire aircraft in-the-field. The tomographic reconstructions produced will not only allow for the accurate detection of flaw location and size by simply viewing an image of the aircraft, but will also provide a quantitative map of any variations in thickness or other parameters corresponding to the flaws, since the mathematical complexity of the Lamb waves has been incorporated in the algorithms. Therefore, flaw location, size, and magnitude can rapidly be determined in-the-field.

Appendix A

Characterization of the ART Algorithm

Appendix A suppressed for proprietary reasons.

NOTE TO USERS

Copyrighted materials in this document have not been filmed at the request of the author. They are available for consultation at the author's university library.

202-233

This reproduction is the best copy available.

UMI

Appendix B

Diffraction Tomography

The results of this work have shown that the straight-ray approximation is invalid for many cases. This appendix outlines an extension of Lamb wave tomography that accounts for scattering effects using the analysis of chapter 4.

For inhomogeneous media, we can write the wave equation as

$$(\nabla^2 + k(\vec{r})^2)u(\vec{r}) = 0. \quad (\text{B.1})$$

Then, assuming that we can ignore the first and higher order derivatives of the acoustic parameters of the media, we can write this equation as

$$(\nabla^2 + k_0^2)u(\vec{r}) = -k_0^2[n^2(\vec{r}) - 1]u(\vec{r}) \quad (\text{B.2})$$

where k_0 is the average wavenumber of the medium and n is the complex refractive index at position \vec{r} given by

$$n(\vec{r}) = \frac{c_0}{c(\vec{r})} \quad (\text{B.3})$$

where c_0 is the propagation velocity in the medium in which the object is located, and $c(\vec{r})$ is the propagation velocity at position \vec{r} in the object. Finally, defining

the object function,

$$o(\vec{r}) = k_0^2[n^2(\vec{r}) - 1]. \quad (\text{B.4})$$

we write

$$(\nabla^2 + k_0^2)u(\vec{r}) = -o(\vec{r})u(\vec{r}). \quad (\text{B.5})$$

Now we consider the field, $u(\vec{r})$, to be composed of an incident field, $u_0(\vec{r})$, and a scattered field, $u_s(\vec{r})$, as

$$u(\vec{r}) = u_0(\vec{r}) + u_s(\vec{r}). \quad (\text{B.6})$$

The incident field which is the field present without any inhomogeneities, is a solution to the equation

$$(\nabla^2 + k_0^2)u_0(\vec{r}) = 0. \quad (\text{B.7})$$

while the scattered field which represents that part of the field due only to the inhomogeneities, is what we are trying to find. Using Equations B.6 and B.7, we get the following wave equation for just the scattered component:

$$(\nabla^2 + k_0^2)u_s(\vec{r}) = -o(\vec{r})u(\vec{r}). \quad (\text{B.8})$$

While this scalar Helmholtz equation can't be solved directly for $u_s(\vec{r})$, a solution can be written in terms of the Green's function which is a solution of the differential equation

$$(\nabla^2 + k_0^2)g(\vec{r}|\vec{r}') = -\delta(\vec{r} - \vec{r}'). \quad (\text{B.9})$$

The Green's function is written in three dimensions as

$$g(\vec{r}|\vec{r}') = \frac{e^{jk_0R}}{4\pi R} \quad (\text{B.10})$$

and in two dimensions as

$$g(\vec{r}|\vec{r}') = \frac{j}{4} H_0^{(1)}(k_0 R) \quad (\text{B.11})$$

where $H_0^{(1)}(k_0 R)$ is the 0th order Hankel function of the first kind, and $R = |\vec{r} - \vec{r}'|$. Since the Green's function, $g(\vec{r}|\vec{r}')$, is only a function of $\vec{r} - \vec{r}'$, we will write it as $g(\vec{r} - \vec{r}')$. In Equation B.9, the object function represents a point inhomogeneity, and so the Green's function can be considered to represent the field from a single point scatterer. It is possible to represent the forcing function of the inhomogeneous wave equation (Equation B.8) as a summation of impulses weighted by $o(\vec{r})u(\vec{r})$ and shifted by \vec{r} .

$$o(\vec{r})u(\vec{r}) = \int o(\vec{r}')u(\vec{r}')\delta(\vec{r} - \vec{r}')d\vec{r}'. \quad (\text{B.12})$$

Since the left hand side of the inhomogeneous wave equation (Equation B.8) is linear, the scattered field from the whole object can be written as the sum of the scattered fields due to each point scatterer. Recalling that the Green's function represents the scattered field from a point scatterer, the total field due to the impulse $o(\vec{r}')u(\vec{r}')\delta(\vec{r} - \vec{r}')$ is written as a summation of scaled and shifted versions of the impulse response, $g(\vec{r})$, and we have

$$u_s(\vec{r}) = \int g(\vec{r} - \vec{r}')o(\vec{r}')u(\vec{r}')d\vec{r}'. \quad (\text{B.13})$$

Now we have an integral equation for $u_s(\vec{r})$, but it is in terms of $u = u_0 + u_s$. There are two approximations which allow the integral equation (Equation B.13) to be solved for the scattered field. If the scattered field, $u_s(\vec{r})$, is small compared to the incident field, $u_0(\vec{r})$, we can use the first Born approximation to write the i th order Born scattered field as [377]

$$u_B^{i+1}(\vec{r}) = \int g(\vec{r} - \vec{r}')o(\vec{r}')[u_0(\vec{r}') + u_B^i(\vec{r}')]d\vec{r}'. \quad (\text{B.14})$$

If instead the change in the scattered phase over the wavelength is small, then we can use the Rytov approximation to write the scattered field as [377]

$$u_B(\vec{r}) = u_0(\vec{r}) \ln\left[\frac{u_s}{u_0} + 1\right]. \quad (\text{B.15})$$

Note that for the Born approximation, $u_B(\vec{r})$ represents the complex amplitude of the field, while for the Rytov approximation, it represents the incident field times the complex scattered phase.

Now we will derive the Fourier Diffraction Theorem which relates the Fourier transform of the measured forward scattered data to the Fourier transform of the object. Note that this theorem is only valid when the inhomogeneities in the object are weakly scattering.

The integral equation for the scattered field,

$$u_B(\vec{r}) = \int g(\vec{r} - \vec{r}') o(\vec{r}') u(\vec{r}') d\vec{r}'. \quad (\text{B.16})$$

can be considered as a convolution of the Green's function and the product of the object function and incident field. Let the incident field be a single plane wave in two dimensions propagating along the y -axis,

$$u_0(\vec{r}) = e^{jk_0 y}. \quad (\text{B.17})$$

The two-dimensional Green's function given by Equation B.11, can be decomposed into plane waves as

$$g(\vec{r} - \vec{r}') = \frac{j}{4\pi} \int_{-\infty}^{\infty} \frac{1}{\beta} e^{j[\alpha(x-x') + \beta|y-y'|]} d\alpha \quad (\text{B.18})$$

where

$$\vec{r} = (x, y) \quad \vec{r}' = (x', y') \quad \beta = (k_0^2 - \alpha^2)^{\frac{1}{2}}. \quad (\text{B.19})$$

Since the scattered fields will be measured along a line, $y = l_0$, where l_0 is greater than any y -coordinate in the object, the $|y - y'|$ term can be replaced by $l_0 - y'$. Using this fact and our expressions for the incident field and Green's function, we can rewrite Equation B.16 as

$$u_B(x, y = l_0) = \frac{j}{4\pi} \int o(\vec{r}') e^{jk_0 y'} \int_{-\infty}^{\infty} \frac{1}{\beta} e^{j[\alpha(x-x') + \beta(l_0 - y')]} d\alpha d\vec{r}' \quad (\text{B.20})$$

or

$$u_B(x, y = l_0) = \frac{j}{4\pi} \int_{-\infty}^{\infty} d\alpha \int \frac{o(\vec{r}')}{\beta} e^{j[\alpha(x-x') + \beta(l_0 - y')]} e^{jk_0 y'} d\vec{r}'. \quad (\text{B.21})$$

Then since

$$\int o(\vec{r}') e^{-j[\alpha x' + (\beta - k_0)y']} d\vec{r}' = O(\alpha, \beta - k_0) \quad (\text{B.22})$$

where $O(\alpha, \beta - k_0)$ is the two-dimensional Fourier transform of the object function evaluated at a frequency of $(\alpha, \beta - k_0)$, we have

$$u_B(x, y = l_0) = \frac{j}{4\pi} \int_{-\infty}^{\infty} \frac{1}{\beta} e^{j(\alpha x + \beta l_0)} O(\alpha, \beta - k_0) d\alpha. \quad (\text{B.23})$$

Next, we define the Fourier transform of the one-dimensional scattered field, $u_B(x, l_0)$, as

$$U_B(\omega, l_0) = \int_{-\infty}^{\infty} u_B(x, l_0) e^{-j\omega x} dx, \quad (\text{B.24})$$

and substituting Equation B.23 into this expression we have

$$U_B(\omega, l_0) = \int_{-\infty}^{\infty} \left(\frac{j}{4\pi} \int_{-\infty}^{\infty} \frac{1}{\beta} e^{j(\alpha x + \beta l_0)} O(\alpha, \beta - k_0) d\alpha \right) e^{-j\omega x} dx. \quad (\text{B.25})$$

Then since

$$\int_{-\infty}^{\infty} e^{-j(\omega - \alpha)x} dx = 2\pi \delta(\omega - \alpha), \quad (\text{B.26})$$

we have

$$U_B(\omega, l_0) = \int_{-\infty}^{\infty} \frac{j}{4\pi} \frac{1}{\beta} e^{j\beta l_0} O(\alpha, \beta - k_0) 2\pi \delta(\omega - \alpha) d\alpha. \quad (\text{B.27})$$

or

$$U_B(\alpha, l_0) = \frac{j}{2(k_0^2 - \alpha^2)^{\frac{1}{2}}} e^{j(k_0^2 - \alpha^2)^{\frac{1}{2}} l_0} O(\alpha, (k_0^2 - \alpha^2)^{\frac{1}{2}} - k_0). \quad (\text{B.28})$$

This equation which is valid for $|\alpha| < k_0$, relates the two-dimensional Fourier transform of the object to the one-dimensional Fourier transform of the field at the receiver line.

Using the scattering theory from Chapter 4, the scattered S_0 field from a point scatterer can be calculated. Then using this as the Green's function and our incident S_0 wave from Chapter 4, we can calculate an expression for the scattered S_0 Lamb wave field at the receiver line location. Taking the Fourier transform of this field and using Equation B.28, the two-dimensional Fourier transform of the object function can be determined. Finally, by taking the inverse two-dimensional Fourier transform of this expression, the object function can be determined. Thus, the scattering theory of Chapter 4 can be used to develop a tomographic algorithm that takes diffraction effects into account.

Appendix C

*S*0 Scattering Between Adjacent Plates

In this appendix, the scattering of the lowest order symmetric Lamb wave mode from a boundary between two adjacent plates with different material parameters is considered. We again use the theory of Kane and Mindlin.

Consider a plate lying in the xy -plane bounded by air at the planes $z = +h$ and $z = -h$. Because the thickness is small the components of displacement for dilatational plate waves can be approximated by [7]

$$u_x = v_x(x, y, t) \quad u_y = v_y(x, y, t) \quad u_z = \frac{z}{h} v_z(x, y, t)$$

where v_x , v_y , v_z are not functions of z . They can then be expressed in terms of three independent scalar potentials, $\phi_1(x, y)$, $\phi_2(x, y)$, $H(x, y)$ as

$$v_x = \left(\frac{\partial \phi_1}{\partial x} + \frac{\partial \phi_2}{\partial x} + \frac{\partial H}{\partial y} \right) \exp -i\omega t$$

$$v_y = \left(\frac{\partial \phi_1}{\partial y} + \frac{\partial \phi_2}{\partial y} - \frac{\partial H}{\partial x} \right) \exp -i\omega t$$

$$v_z = (\sigma_1 \phi_1 + \sigma_2 \phi_2) \exp -i\omega t$$

These potentials are chosen to satisfy the equations of motion

$$(\nabla^2 + \delta_1^2)\phi_1 = 0 \quad (\nabla^2 + \delta_2^2)\phi_2 = 0 \quad (\nabla^2 + \delta_3^2)H = 0$$

where ∇^2 is the 2-D Laplacian and δ_i are the effective wavenumbers given by

$$\delta_i^2 = \frac{3k^2}{2\beta h} \left[(\alpha + \beta) \frac{\omega^2}{\omega_0^2} - 1 - (-1)^i \psi \right] \quad (i = 1, 2) \quad \delta_3^2 = \frac{\omega^2}{c_T^2}$$

In the above equations,

$$\sigma_i = \frac{h(\lambda + 2G)}{k\lambda} \left(\delta_i^2 - \frac{\omega^2}{c_L^2} \right), \quad (i = 1, 2)$$

$$\psi = \left[\left((\alpha + \beta) \frac{\omega^2}{\omega_0^2} - 1 \right)^2 + 4\alpha\beta \frac{\omega^2}{\omega_0^2} \left(1 - \frac{\omega^2}{\omega_0^2} \right) \right]^{\frac{1}{2}}$$

$$\alpha = \frac{c_L^2}{c_P^2} \quad \beta = \frac{c_T^2}{c_P^2} \quad \omega_0^2 = \frac{\pi^2(\lambda + 2G)}{4h^2\rho}$$

$$c_L^2 = \frac{\lambda + 2G}{\rho} \quad c_T^2 = \frac{G}{\rho} \quad c_P^2 = \frac{4G(\lambda + G)}{\rho(\lambda + 2G)}$$

where ρ is the mass density of the plate material, λ and G are the Lamé parameters, and c_L , c_T and c_P are the compressional, shear, and plate wave speeds in isotropic media. Also ω_0 is the frequency corresponding to the first mode of pure thickness vibration of an infinite plate, and the parameter $k^2 = \frac{\pi^2}{12}$ is inserted to improve the results [7].

Now consider the general case of two plates in welded contact in the xy -plane, with material parameters λ , G , ρ , h for the first plate, and λ_1 , G_1 , ρ_1 , h_1 for

the second plate. We choose the potentials in order to represent an incident slow dilatational wave at angle ϵ_1 to the boundary, which is in the yz -plane, and we write

$$\phi_1^{inc} = \exp i\delta_1\mu \quad \phi_2^{inc} = 0 \quad H^{inc} = 0$$

with $\mu = y \sin \epsilon_1 - x \cos \epsilon_1$. The reflected and transmitted waves are assumed to be of the form

$$\phi_1^{ref} = R_1 \exp i\delta_1\mu_1, \quad \phi_2^{ref} = R_2 \exp i\delta_1\mu_2, \quad H^{ref} = R_3 \exp i\delta_1\mu_3,$$

with $\mu_i = y \sin \epsilon_i + x \cos \epsilon_i$ for $i = 1, 2, 3$

$$\phi_1^{trans} = T_1 \exp i\delta_1\mu'_1, \quad \phi_2^{trans} = T_2 \exp i\delta_1\mu'_2, \quad H^{trans} = T_3 \exp i\delta_1\mu'_3.$$

with $\mu'_j = y \sin \epsilon'_j - x \cos \epsilon'_j$ for $j = 1, 2, 3$. The quantities $R_1, R_2, R_3, T_1, T_2, T_3$ are the unknown amplitudes of the reflected and transmitted waves respectively. The angles of incident, reflection and transmission $\epsilon_1, \dots, \epsilon_6$ are related by a Snell's law.

In order to solve for the unknown amplitudes, we consider continuity of plate displacements and plate stresses at the boundary, $x = 0$. The plate displacements are as defined above and the plate stresses are given by

$$N_x = 2h \left[(\lambda + 2G) \frac{\partial v_x}{\partial x} + \lambda \frac{\partial v_y}{\partial y} + \frac{k\lambda}{h} v_z \right]$$

$$R_x = \frac{2h^2G}{3} \left(\frac{\partial v_z}{\partial x} \right)$$

$$N_{xy} = 2hG \left(\frac{\partial v_y}{\partial x} + \frac{\partial v_x}{\partial y} \right)$$

where N_x and N_{xy} are the usual forces per unit length which appear in the elementary theory of plates acted upon by forces in the middle plane, and R_x is a component of "pinching" shear [7]. The continuity of displacement gives three equations

$$v_x^{inc} + v_x^{ref} = v_x^{trans} \quad v_y^{inc} + v_y^{ref} = v_y^{trans} \quad v_z^{inc} + v_z^{ref} = v_z^{trans}$$

and the continuity of plate stresses gives three more equations

$$N_x^{inc} + N_x^{ref} = N_x^{trans} \quad R_x^{inc} + R_x^{ref} = R_x^{trans} \quad N_{xy}^{inc} + N_{xy}^{ref} = N_{xy}^{trans}$$

Substituting the above expressions into these six equations and rewriting in matrix form we have

$$\begin{pmatrix} \delta_1 \cos \epsilon_1 & \delta_2 \cos \epsilon_2 & \delta_3 \sin \epsilon_3 & \delta_4 \cos \epsilon_4 \\ \delta_1 \sin \epsilon_1 & \delta_2 \sin \epsilon_2 & -\delta_3 \cos \epsilon_3 & -\delta_4 \sin \epsilon_4 \\ \sigma_1 & \sigma_2 & 0 & -\sigma_4 \\ 2G\delta_1^2 \sin \epsilon_1^2 - \rho\omega^2 & 2G\delta_2^2 \sin \epsilon_2^2 - \rho\omega^2 & -\delta_3^2 G \sin 2\epsilon_3 & -\frac{h_1}{h}(2G_1\delta_4^2 \sin \epsilon_4^2 - \rho_1\omega^2) \\ \sigma_1\delta_1 \cos \epsilon_1 & \sigma_2\delta_2 \cos \epsilon_2 & 0 & \frac{h_1^2 G_1}{h^2 G}(\sigma_4\delta_4 \cos \epsilon_4) \\ \delta_1^2 \sin 2\epsilon_1 & \delta_2^2 \sin 2\epsilon_2 & -\delta_3^2 \cos 2\epsilon_3 & \frac{h_1 G_1}{hG}\delta_4^2 \sin 2\epsilon_4 \\ & \delta_5 \cos \epsilon_5 & -\delta_6 \sin \epsilon_6 & \\ & -\delta_5 \sin \epsilon_5 & -\delta_6 \cos \epsilon_6 & \\ & -\sigma_5 & 0 & \\ -\frac{h_1}{h}(2G_1\delta_4^2 \sin \epsilon_4^2 - \rho_1\omega^2) & -\frac{h_1}{h}\delta_6^2 G_1 \sin 2\epsilon_6 & & \\ \frac{h_1^2 G_1}{h^2 G}(\sigma_5\delta_5 \cos \epsilon_5) & 0 & & \\ \frac{h_1 G_1}{hG}\delta_5^2 \sin 2\epsilon_5 & \frac{h_1 G_1}{hG}\delta_6^2 \cos 2\epsilon_6 & & \end{pmatrix} \cdot \begin{pmatrix} R_1 \\ R_2 \\ R_3 \\ T_1 \\ T_2 \\ T_3 \end{pmatrix} = \begin{pmatrix} \delta_1 \cos \epsilon_1 \\ -\delta_1 \sin \epsilon_1 \\ -\sigma_1 \\ -2G\delta_1^2 \sin \epsilon_1^2 + \rho\omega^2 \\ \sigma_1\delta_1 \cos \epsilon_1 \\ \delta_1^2 \sin 2\epsilon_1 \end{pmatrix}$$

The six unknown amplitudes for the reflected and transmitted waves can be determined by solving the above system of equations. This provides an analytic

solution for the reflection and transmission of the lowest order symmetric Lamb wave mode from a boundary between two plates, which allows the behavior of the scattering to be explored as a function of frequency, thickness, material parameters, and incident angle.

In order to incorporate ray bending effects into CBT, it is necessary to calculate the refracted angle across each cell boundary defined in the reconstruction algorithm. The results of this appendix provide that necessary formula.

Bibliography

- [1] H. Lamb. On waves in an elastic plate. *Proc. Roy. Soc. Lon..* A XCIII:114. October 1917.
- [2] L. Balamuth. A new method for measuring elastic moduli and the variation with temperature of the principal Young's modulus of rocksalt between 78K and 273K. *Phys. Rev.*, 45:715, May 1934.
- [3] M.F.M. Osborne and S.D. Hart. Transmission, reflection, and guiding of an exponential pulse by a steel plate in water. I. Theory. *J. Acoust. Soc. Am.*, 17(1):1, 1945.
- [4] R.D. Mindlin. Influence of rotatory inertia and shear on flexural motions of isotropic elastic plates. *J. Appl. Mech.*, page 31. March 1951.
- [5] T.R. Kane. Reflection of flexural waves at the edge of a plate. *J. Appl. Mech.*, page 213, September 1954.
- [6] T.R. Kane. High-frequency extensional vibrations of plates. *J. Appl. Mech.*, page 277, June 1956.
- [7] T.R. Kane. Reflection of dilatational waves at the edge of a plate. *J. Appl. Mech.*, page 219, June 1957.

- [8] D.C. Worlton. Ultrasonic testing with Lamb waves. *Nondestructive Testing*, 158(4):218, July - August 1957.
- [9] R.D. Mindlin and M.A. Medick. Extensional vibrations of elastic plates. *J. Appl. Mech.*, page 561. December 1959.
- [10] D.C. Gazis. Three-dimensional investigation of the propagation of waves in hollow circular cylinders. I. Analytical foundation. *J. Acoust. Soc. Am.*, 31(5):568, 1959.
- [11] D.C. Gazis. Three-dimensional investigation of the propagation of waves in hollow circular cylinders. II. Numerical results. *J. Acoust. Soc. Am.*, 31(5):573, 1959.
- [12] D.C. Gazis, R. Herman, and R.F. Wallis. Surface elastic waves in cubic crystals. *Phys. Rev.*, 119(2):533, 1960.
- [13] D.C. Worlton. Experimental confirmation of Lamb waves at megacycle frequencies. *J. Appl. Phys.*, 32(6):967, 1961.
- [14] J.P. Jones. Wave propagation in a two-layered medium. *J. Appl. Mech.*, page 213. June 1964.
- [15] L.S. Gournay. Conversion of electromagnetic to acoustic energy by surface heating. *J. Acoust. Soc. Am.*, 40(6):1322, 1966.
- [16] I.A. Viktorov. Rayleigh and Lamb waves: Physical theory and applications. *Plenum Press*, 1967.
- [17] J.P. Jones and J.S. Whittier. Waves at a flexibly bonded interface. *J. Appl. Mech.*, page 905, December 1967.

- [18] P.J. Torvik. Reflection of wave trains in semi-infinite plates. *J. Acoust. Soc. Am.*, 41(2):346, 1967.
- [19] C.-L. Hu. Spherical model of an acoustical wave generated by rapid laser heating in a liquid. *J. Acoust. Soc. Am.*, 46(3):728, 1969.
- [20] Y.S. Kim and R.T. Smith. Thermal expansion of lithium tantalate and lithium niobate single crystals. *J. Appl. Phys.*, 40(11):4637, 1969.
- [21] N.C. Anderholm. Laser-generated stress waves. *Appl. Phys. Lett.*, 16(3):113, 1970.
- [22] J.D. O'Keefe and C.H. Skeen. Laser-induced stress-wave and impulse augmentation. *Appl. Phys. Lett.*, 21(10):464, 1972.
- [23] B.P. Fairand, B.A. Wilcox, W.J. Gallagher, and D.N. Williams. Laser shock induced microstructural and mechanical property changes in 7075 aluminum. *J. Appl. Phys.*, 43(9):3893, 1972.
- [24] L.R. Dragonette. Schlieren visualization of radiation caused by illumination of plates with short acoustical pulses. *J. Acoust. Soc. Am.*, 51(3):920, 1972.
- [25] R.E. Smith. Ultrasonic elastic constants of carbon fibers and their composites. *J. Appl. Phys.*, 43(6):2555, 1972.
- [26] S.A. Rybak. Waves in a plate containing random inhomogeneities. *Sov. Phys.-Acoust.*, 17(3):345, 1972.
- [27] S.A. Rybak. Randomly coupled flexural and longitudinal vibrations of plates. *Sov. Phys.-Acoust.*, 18(1):76, 1972.

- [28] W.G. Neubauer. Ultrasonic reflection of a bounded beam at Rayleigh and critical angles for a plane liquid-solid interface. *J. Appl Phys.*, 44(1):48, 1973.
- [29] R.B. Nelson and S.B. Dong. High frequency vibrations and waves in laminated orthotropic plates. *J. of Sound and Vibration*, 30(1):33, 1973.
- [30] T.K. Lockett. Lamb and torsional waves and their use in flaw detection in tubes. *Ultrasonics*, page 31, January 1973.
- [31] L.P. Solie and B.A. Auld. Elastic waves in free anisotropic plates. *J. Acoust. Soc. Am.*, 54(1):50, 1973.
- [32] O.A. Germogenova. Geometrical theory for flexure waves in shells. *J. Acoust. Soc. Am.*, 53(2):535, 1973.
- [33] B.P. Fairand, A.H. Clauer, R.G. Jung, and B.A. Wilcox. Quantitative assessment of laser-induced stress waves generated at confined surfaces. *Appl. Phys. Lett.*, 25(8):431, 1974.
- [34] J.A. Fox. Effect of water and paint coatings on laser-irradiated targets. *Appl. Phys. Lett.*, 24(10):461, 1974.
- [35] J.A. Garber and A.V. Granato. Theory of the temperature dependence of second-order elastic constants in cubic materials. *Phys. Rev. B*, 11(10):3990, 1975.
- [36] L.E. Pitts, T.J. Plona, and W.G. Mayer. Theoretical similarities of Rayleigh and Lamb modes of vibration. *J. Acoust. Soc. Am.*, 60(2):374, 1976.
- [37] R.J. von Gutfeld and R.L. Melcher. 20MHz acoustic waves from pulsed thermoelastic expansions of constrained surfaces. *Appl. Phys. Lett.*, 30(6):257, 1977.

- [38] R.L. Rosenberg and R.N. Thurston. Relationship between plate and surface modes of a tube. *J. Acoust. Soc. Am.*, 61(6):1499, 1977.
- [39] B.A. Auld and E.M. Tsao. A variational analysis of edge resonance in a semi-infinite plate. *IEEE Trans. Sonics, Ultrason. SU-24*, 5:317, 1977.
- [40] A.H. Nayfeh and E.A.-A.M. Nassar. Simulation of the influence of bonding materials on the dynamic behavior of laminated composites. *J. Appl. Mech.*, 45:822, December 1978.
- [41] W. Sachse and Y.-H. Pao. On the determination of phase and group velocities of dispersive waves in solids. *J. Appl. Phys.*, 49(8):4320, 1978.
- [42] R. Fiorito, W. Madigosky, and H. Uberall. Resonance theory of acoustic waves interacting with an elastic plate. *J. Acoust. Soc. Am.*, 66(6):1857, 1979.
- [43] R.J. von Gutfeld and H.F. Budd. Laser-generated MHz elastic waves from metallic-liquid interfaces. *Appl. Phys. Lett.*, 34(10):617, 1979.
- [44] R.O. Claus and R.A. Kline. Adhesive bondline interrogation using Stoneley wave methods. *J. Appl. Phys.*, 50(12):8066, 1979.
- [45] C.C. Habeger, R.W. Mann, and G.A. Baum. Ultrasonic plate waves in paper. *Ultrasonics*, page 57, March 1979.
- [46] J.D. Achenbach and J.G. Harris. Acoustic emission from a brief crack propagation event. *J. Appl. Mech.*, 46:107, March 1979.
- [47] C.B. Scruby, R.J. Dewhurst, D.A. Hutchins, and S.B. Palmer. Quantitative studies of thermally generated elastic waves in laser-irradiated metals. *J. Appl. Phys.*, 51(12):6210, 1980.

- [48] S.I. Rokhlin. Diffraction of Lamb waves by a finite crack in an elastic layer. *J. Acoust. Soc. Am.*, 67(4):1157, 1980.
- [49] M. Schoenberg. Elastic wave behavior across linear slip interfaces. *J. Acoust. Soc. Am.*, 68(5):1516, 1980.
- [50] S.I. Rokhlin, M. Hefets, and M. Rosen. An elastic interface wave guided by a thin film between two solids. *J. Appl. Phys.*, 51(7):3579, 1980.
- [51] D.A. Hutchins, R.J. Dewhurst, and S.B. Palmer. Directivity patterns of laser-generated ultrasound in aluminum. *J. Acoust. Soc. Am.*, 70(5):1362, 1981.
- [52] S.I. Rokhlin, M. Hefets, and M. Rosen. An ultrasonic interface-wave method for predicting the strength of adhesive bonds. *J. Appl. Phys.*, 52(4):2847, 1981.
- [53] A.M. Aindow, R.J. Dewhurst, D.A. Hutchins, and S.B. Palmer. Laser-generated ultrasonic pulses at free metal surfaces. *J. Acoust. Soc. Am.*, 69(2):449, 1981.
- [54] A.H. Nayfeh, D.E. Chimenti, A. Adler, and R.L. Crane. Ultrasonic leaky waves in the presence of a thin layer. *J. Appl. Phys.*, 52(8):4985, 1981.
- [55] R. Parnes. Dispersion relations of waves in a rod embedded in an elastic medium. *J. Sound Vibr.*, 76(1):65, 1981.
- [56] G.Z. Voyiadjis and M.H. Baluch. Refined theory for flexural motions of isotropic elastic plates. *J. Sound Vibr.*, 76(1):57, 1981.
- [57] Y. Bar-Cohen and R.L. Crane. Acoustic backscattering imaging of subcritical flaws in composites. *Mat. Eval.*, 40:970, August 1982.

- [58] A.V. Clark and S.D. Hart. Measurement of ultrasound reflected from liquid layers of submicron thickness. *Mat. Eval.*, 40:866. July 1982.
- [59] D.E. Chimenti, A.H. Nayfeh, and D.L. Butler. Leaky Rayleigh waves on a layered halfspace. *J. Appl. Phys.*, 53(1):170, 1982.
- [60] P.D. Jackins and G.C. Gaunard. Radar resonance reflection from sets of plane dielectric layers. *J. Appl. Phys.*, 53(10):6663. 1982.
- [61] S.K. Datta, A.H. Shah, and C.M. Fortunko. Diffraction of medium and long wavelength horizontally polarized shear waves by edge cracks. *J. Appl. Phys.*, 53(4):2895, 1982.
- [62] G.C. Knollman and J.J. Hartog. Shear modulus gradients in adhesive interfaces as determined by means of ultrasonic Rayleigh waves. *J. Appl. Phys.*, 53(3):1516, 1982.
- [63] R.J. Dewhurst, D.A. Hutchins, S.B. Palmer, and C.B. Scruby. Quantitative measurements of laser-generated acoustic waveforms. *J. Appl. Phys.*, 53(6):4064, 1982.
- [64] G. Veith and M. Kowatsch. Optical generation of continuous 76-MHz surface acoustic waves on YZ LiNbO₃. *Appl. Phys. Lett.*, 40(1):30, 1982.
- [65] A.H. Shah and S.K. Datta. Harmonic waves in a periodically laminated medium. *Int. J. Solids Structures*, 18(5):397, 1982.
- [66] M. Houze, B. Nongaillard, M. Gazalet, J.M. Rouvaen, and C. Bruneel. Measurement of the thickness of thin layers by ultrasonic interferometry. *J. Appl. Phys.*, 55(1):194, 1984.

- [67] D. Royer and E. Dieulesaint. Analysis of thermal generation of Rayleigh waves. *J. Appl. Phys.*, 56(9):2507, 1984.
- [68] A.C. Tam. Pulsed-laser generation of ultrashort acoustic pulses: Application for thin-film ultrasonic measurements. *Appl. Phys. Lett.*, 45(5):510, 1984.
- [69] M. Koshiha, S. Karakida, and M. Suzuki. Finite-element analysis of Lamb wave scattering in an elastic plate waveguide. *IEEE Trans. Sonics. Ultrason. SU-31*, page 18, 1984.
- [70] N. Vasudevan and A.K. Mal. Response of an elastic plate to localized transient sources. *J. Appl. Mech.*, 52:356, June 1985.
- [71] A. Pilarski. Ultrasonic evaluation of the adhesion degree in layered joints. *Mat. Eval.*, 43:765, May 1985.
- [72] D.E. Chimenti and A.H. Nayfeh. Leaky Lamb waves in fibrous composites. *J. Appl. Phys.*, 58(12):4531, 1985.
- [73] G.M. Sessler, R. Gerhard-Multhaupt, J.E. West, and H. Von Seggern. Optoacoustic generation and electrical detection of subnanosecond acoustic pulses. *J. Appl. Phys.*, 58(1):119, 1985.
- [74] H. Sontag and A.C. Tam. Optical monitoring of photoacoustic pulse propagation in silicon wafers. *Appl. Phys. Lett.*, 46(8):725, 1985.
- [75] S.B. Dong and K.H. Huang. Edge vibrations in laminated composite plates. *J. Appl. Mech.*, 52:433, June 1985.
- [76] G. Maze, J.L. Izbicki, and J. Ripoche. Resonances of plates and cylinders: Guided waves. *J. Acoust. Soc. Am.*, 77(44):1352, 1985.

- [77] S.I. Rokhlin and D. Marom. Study of adhesive bonds using low-frequency obliquely incident ultrasonic waves. *J. Acoust. Soc. Am.*, 80(2):585, 1986.
- [78] R.A. Crosbie, R.J. Dewhurst, and S.B. Palmer. Flexural resonance measurements of clamped and partially clamped disks excited by nanosecond laser pulses. *J. Appl. Phys.*, 59(6):1843, 1986.
- [79] A.C. Tam and G. Ayers. Ultrasonic imaging of layered structures utilizing nondestructive subnanosecond photoacoustic pulse generation. *Appl. Phys. Lett.*, 49(21):1420, 1986.
- [80] D.E. Chimenti and A.H. Nayfeh. Anomalous ultrasonic dispersion in fluid-coupled, fibrous composite plates. *Appl. Phys. Lett.*, 49(9):492, 1986.
- [81] C. Thomsen, H.T. Grahn, H.J. Maris, and J. Tauc. Surface generation and detection of phonons by picosecond light pulses. *Phys. Rev. B*, 34(6):34, 1986.
- [82] J.M. Liu. The frequency dependence of ultrasonic wave propagation in metal-matrix composite plates. *Symposium on Nondestructive Evaluation 15th, San Antonio, TX, April 23-25, 1985, Proceedings (A86-47129 22-38), San Antonio, TX, Nondestructive Testing Information Analysis Center, page 303, April 1986.*
- [83] Y. Bar-Cohen and D.E. Chimenti. NDE of defects in composites using leaky Lamb waves. *Symposium on Nondestructive Evaluation 15th, San Antonio, TX, April 23-25, 1985, Proceedings (A86-47129 22-38), San Antonio, TX, Nondestructive Testing Information Analysis Center, page 202, April 1986.*
- [84] Y.C. Angel. Scattering of Love waves by a surface-breaking crack. *J. Appl. Mech.*, 53:587, September 1986.

- [85] A.H. Shah, Y.F. Chin, and S.K. Datta. Elastic wave scattering by surface-breaking planar and nonplanar cracks. *J. Appl. Mech.*, 54:761, December 1987.
- [86] R.J. Dewhurst, C. Edwards, A.D.W. McKie, and S.B. Palmer. Estimation of the thickness of thin metal sheet using laser generated ultrasound. *Appl. Phys. Lett.*, 51(14):1066, 1987.
- [87] S.W. Lang, A.L. Kurkjian, J.H. McClellan, C.F. Morris, and T.W. Parks. Estimating slowness dispersion from arrays of sonic logging wave-forms. *Geophysics*, 52(4):530, 1987.
- [88] L. Adler, W.R. Rose, S.I. Rokhlin, and P.B. Nagy. Lamb wave and leaky Lamb wave characterization of fiber reinforced composites. *Advance Composites the Latest Developments, proceedings of the Second Conference on Advanced Composites Dearborn, Michigan*, page 263, November 1987.
- [89] M. Caslini, C. Zanotti, and T.K. O'Brien. Study of matrix cracking and delamination in glass/epoxy laminates. *Journal of Composites Technology & Research*, 9(4):121, Winter 1987.
- [90] S.Y. Zhang, J.Z. Shen, and C.F. Ying. The reflection of the Lamb wave by a free plate edge: Visualization and theory. *Mat. Eval.*, 46:638, April 1988.
- [91] A.H. Nayfeh and D.E. Chimenti. Propagation of guided waves in fluid-coupled plates of fiber-reinforced composite. *J. Acoust. Soc. Am.*, 83(5):1736, 1988.
- [92] M. de Billy and I. Molinero. On the nonobservance of nonspecular bounded beam reflection effects of Lamb modes. *J. Acoust. Soc. Am.*, 83(4):1249, 1988.

- [93] A. Pilarski and J.L. Rose. A transverse-wave ultrasonic oblique-incidence technique for interfacial weakness detection in adhesive bonds. *J. Appl. Phys.*, 63(2):300, 1988.
- [94] A.H. Nayfeh and D.E. Chimenti. Ultrasonic wave reflection from liquid-coupled orthotropic plates with application to fibrous composites. *J. Appl. Mech.*, 55:863, December 1988.
- [95] A.K. Mal. Guided waves in layered solids with interface zones. *Int. J. Engng Sci.*, 26(8):873, 1988.
- [96] S.K. Datta, A.H. Shah, R.L. Bratton, and T. Chakraborty. Wave propagation in laminated composite plates. *J. Acoust. Soc. Am.*, 83(6):2020, June 1988.
- [97] P.B. Nagy, A. Jungman, and L. Adler. Measurements of backscattered leaky Lamb waves in composite plates. *Mat. Eval.*, 46:97, January 1989.
- [98] G.D. Dean. The use of plate bending waves for elastic property determination of polymers. *NPL Report DMA (A)*, 166, August 1988.
- [99] A.K. Mal and Y. Bar-Cohen. Ultrasonic characterization of composite laminates. *Wave Propagation In Structural Composites AMD*, 90:1, 1988.
- [100] A.K. Mal and Y. Bar-Cohen. Stress waves in layered composite laminates. *Proceedings of the Fourth Japan-U.S. Conference on Composite Materials Washington D.C.*, page 361, June 1988.
- [101] D.A. Hutchins and K. Lundgren. A laser study of transient Lamb waves in thin materials. *J. Acoust. Soc. Am.*, 85(4):1441, 1989.
- [102] B. Tang and E.G. Henneke. Lamb-wave monitoring of axial stiffness reduction of laminated composites plates. *Mat. Eval.*, 47:928, August 1989.

- [103] Y. Tsukahara and K. Ohira. Detection of smooth bondings of polymer coatings by ultrasonic spectroscopy. *Ultrasonics*, 27:3, 1989.
- [104] F.A. McDonald. Practical quantitative theory of photoacoustic pulse generation. *Appl. Phys. Lett.*, 54(16):1504, 1989.
- [105] V. Dayal and V.K. Kinra. Leaky Lamb waves in an anisotropic plate. I: An exact solution and experiments. *J. Acoust. Soc. Am.*, 85(6):2268, 1989.
- [106] Y. Bar-Cohen and A.K. Mal. Leaky Lamb wave phenomena in composites using pulses. *Rev. Prog. in QNDE*, 8:1671, 1989.
- [107] R.A. Kline and M.M. Doroudian. Ultrasonic evaluation of adhesively bonded composites using guided waves. *Advances in composite materials and structures (A91-23701 08-24)*, page 63, 1989.
- [108] A.H. Nayfeh and D.E. Chimenti. Free wave propagation in plates of general anisotropic media. *J. Appl. Mech.*, 56:881, December 1989.
- [109] R.A. Kline, M.M. Doroudian, and C.P. Hsiao. Plate wave propagation in transversely isotropic materials. *J. Comp. Mat.*, 23:505, May 1989.
- [110] V. Dayal, V. Iyer, and V.K. Kinra. Ultrasonic evaluation of microcracks in composites. *Advances in Fracture Research Proceedings of the 7th International Conference on Fracture (IF7)*, page 3291, March 1989.
- [111] D. Noiret and J. Roget. Calculation of wave propagation in composite materials using the Lamb wave concept. *J. Comp. Mat.*, 23:195, February 1989.
- [112] J.S. Epstein, V.A. Deason, M.A. Abdallah, and H. Murakami. Lamb wave propagation in AS4 carbon fiber 3501-6 epoxy plates exhibiting microstructure. *Inst. Phys. Conf. series 102 session 8*, page 419, 1989.

- [113] B. Tang and E.G. Henneke. Long wavelength approximation for Lamb wave characterization of composite laminates. *Res. Nondestr. Eval.*, 1:51, 1989.
- [114] R.K. Kapania and S. Raciti. Recent advances in analysis of laminated beams and plates. Part II: Vibrations and wave propagation. *AIAA Journal*, 27(7):935, 1989.
- [115] E.P. Papadakis. The measurement of ultrasonic velocity. *Physical Acoustics*, XIX:81, 1990.
- [116] E.P. Papadakis. The measurement of ultrasonic attenuation. *Physical Acoustics*, XIX:107, 1990.
- [117] D.A. Hutchins and G. Hayward. Radiated fields of ultrasonic transducers. *Physical Acoustics*, XIX:1, 1990.
- [118] K. Balasubramaniam and J.L. Rose. Guided wave potential for damage analysis of composite materials. *Rev. Prog. in QNDE*, 9:1505, 1990.
- [119] M.R. Karim, A.K. Mal, and Y. Bar-Cohen. Inversion of leaky Lamb wave data by simplex algorithm. *J. Acoust. Soc. Am.*, 88(1):482, 1990.
- [120] J.B. Spicer, A.D.W. McKie, and J.W. Wagner. Quantitative theory for ultrasonic waves in a thin plate. *Appl. Phys. Lett.*, 57(18):1882, 1990.
- [121] P.-C. Xu and S.K. Datta. Guided waves in a bonded plate: A parametric study. *J. Appl. Phys.*, 67(11), 1990.
- [122] F.A. McDonald. On the precursor in laser-generated ultrasound waveforms in metals. *Appl. Phys. Lett.*, 56(3):230, 1990.

- [123] J.B. Deaton, A.D.W. McKie, J.B. Spicer, and J.W. Wagner. Generation of narrow-band ultrasound with a long cavity mode-locked Nd:YAG laser. *Appl. Phys. Lett.*, 56(24):2390, 1990.
- [124] D.E. Chimenti and A.H. Nayfeh. Ultrasonic reflection and guided wave propagation in biaxially laminated composite plates. *J. Acoust. Soc. Am.*, 87(4):1409, April 1990.
- [125] C.F. Burger, C. Duffer, and N. Schumacher. Non-contact evaluation of quality in FRP composites. *Composite Material Technology Thirteenth annual energy-sources technology conference and exhibition New Orleans, Louisiana*, page 193, January 1990.
- [126] A.H. Nayfeh and D.E. Chimenti. Elastic wave propagation in multilayered anisotropic media. *Elastic waves and ultrasonic nondestructive evaluation*, page 241, 1990.
- [127] S.I. Rokhlin and W. Wang. Nondestructive measurements of elastic constants of composite materials by ultrasonic methods. *Elastic waves and ultrasonic nondestructive evaluation*, page 249, 1990.
- [128] M. Bouden and S.K. Datta. Rayleigh and Love waves in cladded anisotropic medium. *J. Appl. Mech.*, 57:398, June 1990.
- [129] D.P. Jansen and D.A. Hutchins. Lamb wave tomography. *1990 Ultrasonics Symposium*, page 1017, 1990.
- [130] D. Alleyne and P. Cawley. A 2-dimensional Fourier transform method for the quantitative measurement of Lamb modes. *Rev. Prog. in QNDE*, 10:201, 1991.

- [131] R. Bratton, S. Datta, and A. Shah. Scattering of Lamb waves in a composite plate. *Rev. Prog. in QNDE*, 10:1507, 1991.
- [132] S.K. Datta and A.H. Shah. Lamb wave scattering by a surface-breaking crack in a plate. *Rev. Prog. in QNDE*, 10:97, 1991.
- [133] H. Nakano and S. Nagai. Laser generation of antisymmetric Lamb waves in thin plates. *Ultrasonics*, 29:230, 1991.
- [134] V. Dayal and V.K. Kinra. Leaky Lamb waves in an anisotropic plate. II: Nondestructive evaluation of matrix cracks in fiber-reinforced composites. *J. Acoust. Soc. Am.*, 89(4):1590, 1991.
- [135] D. Alleyne and P. Cawley. A two-dimensional Fourier transform method for the measurement of propagating multimode signals. *J. Acoust. Soc. Am.*, 89(3):1159, 1991.
- [136] S.I. Rokhlin and Y.J. Wang. Analysis of boundary conditions for elastic wave interaction with an interface between two solids. *J. Acoust. Soc. Am.*, 89(2):503, 1991.
- [137] A. Vary. Acousto-ultrasonics: Retrospective exhortation with bibliography. *Mat. Eval.*, page 581, May 1991.
- [138] D.E. Chimenti and R.W. Martin. Nondestructive evaluation of composite laminates by leaky Lamb waves. *Ultrasonics*, 29:13, 1991.
- [139] A.H. Nayfeh and D.E. Chimenti. Elastic wave propagation in fluid-loaded multiaxial anisotropic media. *J. Acoust. Soc. Am.*, 89(2):542, February 1991.

- [140] K. Yamanaka, Y. Nagata, and T. Koda. Selective excitation of single-mode acoustic waves by phase velocity scanning of a laser beam. *Appl. Phys. Lett.*, 58(15):1591, 1991.
- [141] A.H. Neyfeh. The general problem of elastic wave propagation in multilayered anisotropic media. *J. Acoust. Soc. Am.*, 89(4):1521, April 1991.
- [142] S.E. Bobbin, J.W. Wagner, and R.C. Cammarata. Determination of the flexural modulus of thin films for measurement of the first arrival of the symmetric Lamb wave. *Appl. Phys. Lett.*, 59(13):1544, September 1991.
- [143] S.I. Rokhlin. Lamb wave interactions with lap-shear adhesive joints: Theory and experiment. *J. Acoust. Soc. Am.*, 89(6):2758, June 1991.
- [144] K. Balasubramaniam and J.L. Rose. Physically based dispersion curve feature analysis in the NDE of composites. *Res. Nondestruct. Eval.*, 3:41, 1991.
- [145] S.K. Datta, W.M. Karunasena, and A.H. Shah. Guided waves in a multilayered composite and ultrasonic nondestructive evaluation. *Composites: Proceedings of the 8th International Conference on Composite Materials (ICCM8)*, (30-39 (A92-32535 13-39)):39-E-1, July 1991.
- [146] A.K. Mal, C.-C. Yin, and Y. Bar-Cohen. Ultrasonic nondestructive evaluation of cracked composite laminates. *Composites Engineering*, 1(2):85, 1991.
- [147] S.W. Liu, S.K. Datta, and T.H. Ju. Transient scattering of Rayleigh-Lamb waves by a surface-breaking crack: Comparison of numerical simulation and experiment. *J. Nondestruct. Eval.*, 10(3):111, 1991.
- [148] Y.N. Al-Nassar, S.K. Datta, and A.H. Shah. Scattering of Lamb waves by a normal rectangular strip weldment. *Ultrasonics*, 29:125, March 1991.

- [149] A. Nayfeh and H.-T. Chien. The influence of piezoelectricity on free and reflected waves from fluid-loaded anisotropic plates. *J. Acoust. Soc. Am.*, 91(3):1250, March 1992.
- [150] A. Nayfeh and H.-T. Chien. Wave propagation interaction with free and fluid-loaded piezoelectric substrates. *J. Acoust. Soc. Am.*, 91(6):3126, June 1992.
- [151] J. Laperre and W. Thys. Experimental and theoretical study of elastic wave dispersion in a liquid bilayer. *J. Acoust. Soc. Am.*, 92(2):908, August 1992.
- [152] S.E. Bobbin, J.W. Wagner, and R.C. Cammarata. Interpretation of laser-generated low-order Lamb waves for elastic modulus measurements in thin films. *Ultrasonics*, 30(2):87, 1992.
- [153] M.R. Karim, M.A. Awal, and T. Kundu. Elastic wave scattering by cracks and inclusions in plates: in-plane case. *Int. J. Solids Structures*, 29(19):2355, 1992.
- [154] D.N. Alleyne and P. Cawley. Optimization of Lamb wave inspection techniques. *NDT&E International*, 25(1):11, 1992.
- [155] H.E. Kautz. Detecting Lamb waves with broadband acousto-ultrasonic signals in composite structures. *NASA Tech Briefs: Using ultrasonic Lamb waves to measure moduli of composites*, LEW(15907), 1992.
- [156] J.J. Ditri, J.L. Rose, and G. Chen. Mode selection criteria for defect detection optimization using Lamb waves. *Rev. Prog. in QNDE*, 11:2109, 1992.

- [157] I.N. Komsky, I.M. Daniel, and Y.-C. Lee. Ultrasonic determination of layer orientation in multilayer multidirectional composite laminates. *Rev. Prog. in QNDE*. 11:1615, 1992.
- [158] N.A. Schumacher, P.H. Gien, and C.P. Burger. Analysis of transient Lamb waves on metal plates, composite panels, and curved members. *Rev. Prog. in QNDE*. 11:1569, 1992.
- [159] N. Guo and P. Cawley. Lamb waves for the nde of composite laminates. *Rev. Prog. in QNDE*. 11:1443, 1992.
- [160] J. Wu and Z. Zhu. The interfacial mass detection with Lamb-wave sensors. *Rev. Prog. in QNDE*, 11:1051, 1992.
- [161] K. Yamanaka, Y. Nagata, and T. Koda. Generation of dispersive acoustic waves by the phase velocity scanning of a laser beam. *Rev. Prog. in QNDE*. 11:633, 1992.
- [162] A.K. Mal and S.-S. Lih. Wave field produced in a composite laminate by a concentrated surface force. *Rev. Prog. in QNDE*, 11:137, 1992.
- [163] G.S. Verdict, P.H. Gien, and C.P. Burger. Finite element study of Lamb wave interactions with holes and through thickness defects in thin metal plates. *Rev. Prog. in QNDE*, 11:97, 1992.
- [164] S.W. Liu, S.K. Datta, and A.H. Shah. Transient scattering of Rayleigh-Lamb waves by surface breaking and buried cracks in a plate. *Rev. Prog. in QNDE*, 11:73, 1992.
- [165] K.J. Sun. Application of guided acoustic waves to delamination detection. *Rev. Prog. in QNDE*, 11:1213, 1992.

- [166] P.N. Dwen and P. Cawley. An ultrasonic technique for the quantitative determination of the cohesive properties of adhesive joints. *Rev. Prog. in QNDE*, 11:1253, 1992.
- [167] A.K. Mal, M.R. Gorman, and W.H. Prosser. Material characterization of composite laminates using low-frequency plate wave dispersion data. *Rev. Prog. in QNDE*, 11:1451, 1992.
- [168] D.A. Hutchins. Pulsed lasers for quantitative ultrasonic nde. *Rev. Prog. in QNDE*, 11:561, 1992.
- [169] N.J. Fergusson and W.D. Pilkey. Frequency-dependent element mass matrices. *J. Appl. Mech.*, 59:136, March 1992.
- [170] D.N. Alleyne and P. Cawley. The interaction of Lamb waves with defects. *IEEE Trans. Ultrason., Ferroelectr., and Freq. Contr.*, 39(3):381, 1992.
- [171] D.P. Jansen and D.A. Hutchins. Immersion tomography using Rayleigh and Lamb waves. *Ultrasonics*, 30(4):245, 1992.
- [172] A. Pilarski, J.L. Rose, J. Ditri, D. Jiao, and K. Rajana. Lamb wave mode selection for increased sensitivity to interfacial weaknesses of adhesive bonds. *Rev. Prog. in QNDE*, 12:1579, 1993.
- [173] H.-T. Chien, S.-H. Sheen, and A.C. Raptis. An acousto-ultrasonic NDE technique for monitoring material anisotropy. *Rev. Prog. in QNDE*, 12:1225, 1993.
- [174] R.D. Costley and Y.H. Berthelot. Laser generation of Rayleigh and Lamb waves for ultrasonic nondestructive testing. *Rev. Prog. in QNDE*, 12:579, 1993.

- [175] C. Edwards, A. Al-Kassim, and S.B. Palmer. Laser ultrasound for the study of thin sheets. *Rev. Prog. in QNDE*, 12:539, 1993.
- [176] I.N. Komsky and J.D. Achenbach. Application of a self-calibrating ultrasonic technique to the detection of fatigue cracks by the use of Lamb waves. *Rev. Prog. in QNDE*, 12:2167, 1993.
- [177] D.A. Hutchins, D.P. Jansen, and C. Edwards. Lamb-wave tomography using non-contact transduction. *Ultrasonics*, 31(3):97, 1993.
- [178] D.N. Alleyne, T.P. Pialucha, and P. Cawley. A signal regeneration technique for long-range propagation of dispersive Lamb waves. *Ultrasonics*, 31(3):201, 1993.
- [179] L. Noui and R.J. Dewhurst. A laser beam deflection technique for the quantitative detection of ultrasonic Lamb waves. *Ultrasonics*, 31(6):425, 1993.
- [180] S.R. Rao, A.H. Sheikh, and M. Mukhopadhyay. Large-amplitude finite element flexural vibration of plates/stiffened plates. *J. Acoust. Soc. Am.*, 93(6):3250, 1993.
- [181] S.W. Liu and S.K. Datta. Scattering of ultrasonic wave by cracks in a plate. *J. Appl. Mech.*, 60:352, June 1993.
- [182] T.K. Eto, B.J. Costello, S.W. Wenzel, R.M. White, and B. Rubinsky. Viscosity sensing with Lamb-wave microsensor: dimethylsulfoxide solution viscosity as a function of temperature. *J. Biomedical Eng.*, 115:329, August 1993.
- [183] T. Kundu and B. Maxfield. A new technique for measuring Rayleigh waves and Lamb wave speeds. *J. Acoust. Soc. Am.*, 93(6):3066, 1993.

- [184] N.A. Schumacher, C.P. Burger, and P.H. Gien. A laser-based investigation of higher-order modes in transient Lamb waves. *J. Acoust. Soc. Am.*, 93(5):2981, 1993.
- [185] A. Pilarski, J.J. Ditri, and J.L. Rose. Remarks on symmetric Lamb waves with dominant longitudinal displacements. *J. Acoust. Soc. Am.*, 93(4):222, 1993.
- [186] J.L. Rose, A. Pilarski, K. Rajana, and J.J. Ditri. Coating influence on generation and reception of ultrasonic Lamb type plate waves. *Rev. Prog. in QNDE*, 13:1903, 1994.
- [187] P.J. Shull, D.E. Chimenti, S.K. Datta, and J.H. Ju. Considerations for elastic plate wave inspection of bilayered plates. *Rev. Prog. in QNDE*, 13:1407, 1994.
- [188] A.K. Mal, S. Lih, and Y. Bar-Cohen. Characterization of the elastic constants of unidirectional laminates using oblique-incidence pulsed data. *Rev. Prog. in QNDE*, 13:1149, 1994.
- [189] H.-T. Chien, S.-H. Sheen, and A.C. Raptis. Theoretical studies of wave propagation in multilayered piezoelectric media. *Rev. Prog. in QNDE*, 13:219, 1994.
- [190] C.L. Yapura and V.K. Kinra. Lamb waves in an isotropic solid-fluid bi-layer. *Rev. Prog. in QNDE*, 13:1149, 1994.
- [191] A. Pilarski, J.J. Ditri, K. Rajana, and J.L. Rose. Utilization of non zero-order symmetric Lamb wave modes at the first critical angle. *Rev. Prog. in QNDE*, 13:173, 1994.

- [192] V. Dayal. Automated Lamb wave measurements. *Rev. Prog. in QNDE*, 13:189, 1994.
- [193] N.A. Schumacher and C.P. Burger. Frequency based analysis methods for laser generated and detected transient Lamb waves. *Rev. Prog. in QNDE*, 13:157, 1994.
- [194] D. Alleyne and P. Cawley. The practical excitation and measurement of Lamb waves using piezoelectric transducers. *Rev. Prog. in QNDE*, 13:181, 1994.
- [195] J.J. Ditri, A. Pilarski, B. Pavlakovic, and J.L. Rose. Generation of guided waves in a plate by axisymmetric normal surface loading. *Rev. Prog. in QNDE*, 13:133, 1994.
- [196] M.D. Seale, B.T. Smith, W.H. Prosser, and J.E. Masters. Lamb wave response of fatigued composite samples. *Rev. Prog. in QNDE*, 13:1261, 1994.
- [197] K.J. Sun and P.H. Johnston. Disbond detection in bonded aluminum joints using Lamb wave amplitude and time-of-flight. *Rev. Prog. in QNDE*, 13:1507, 1994.
- [198] Y.J. Lee, B.T. Khuri-Yakub, and K.C. Saraswat. Temperature measurement in rapid thermal processing using acoustic techniques. *Rev. Sci. Instrum.*, 65(4):974, April 1994.
- [199] M.J.S. Lowe and P. Cawley. The applicability of plate wave techniques for the inspection of adhesive and diffusion bonded joints. *J. NDE*, 13(4):185, 1994.
- [200] R.D. Costley and Y.H. Berthelot. Dispersion curve analysis of laser-generated Lamb waves. *Ultrasonics*, 32(4):249, 1994.

- [201] Z. Wang, C.K. Jen, and J.D.N. Cheeke. Mass sensitivity of two-layer shear horizontal plate wave sensors. *Ultrasonics*, 32(3):209, 1994.
- [202] Z. Wang, C.K. Jen, and J.D.N. Cheeke. Mass sensitivities of two-layer sagittal plane plate wave sensors. *Ultrasonics*, 32(3):201, 1994.
- [203] D.E. Chimenti. Lamb waves in microstructured plates. *Ultrasonics*, 32(4):255, 1994.
- [204] D.P. Jansen, D.A. Hutchins, and J.T. Mottram. Lamb wave tomography of advanced composite laminates containing damage. *Ultrasonics*, 32(2):83, 1994.
- [205] J.J. Ditri and J.L. Rose. Excitation of guided waves in generally anisotropic layers using finite sources. *J. Appl. Mech.*, 61:330, June 1994.
- [206] F.L. Degertekin, J. Pei, B.T. Khuri-Yakub, and K.C. Saraswat. In situ acoustic temperature tomography of semiconductor wafers. *Appl. Phys. Lett.*, 64(11):1338, 1994.
- [207] A.D. Pierce. Influence of structural wave dispersion on scattering patterns with application to scattering from structures with fuzzy internals. *Acoustic Radiation and Wave Propagation ASME NCA-17*, page 9, 1994.
- [208] D.M. Manos. Interface structural integrity evaluation using ultrasonic Lamb waves-aircraft application. *Proposal to NASA*, 1995.
- [209] D. Alleyne and P. Cawley. The long range detection of corrosion in pipes using Lamb waves. *Rev. Prog. in QNDE*, 14:2073, 1995.
- [210] G.G. Krauss, J. Chen, and P.E. Barbone. Use of guided waves for detection of interior flaws in layered materials. *Rev. Prog. in QNDE*, 14:1869, 1995.

- [211] M. Oksanen, J. Stor-Pellinen, and M. Luukkala. Determining mechanical properties of cardboard from photoacoustic Lamb wave transmission data. *Rev. Prog. in QNDE*, 14:1649, 1995.
- [212] W.M.D. Wright, D.A. Hutchins, A. Gachagan, and G. Hayward. Evaluation of fiber-reinforced composites using a non-contact laser/air-transducer system. *Rev. Prog. in QNDE*, 14:1333, 1995.
- [213] S.P. Pelts and J.L. Rose. Acousto-ultrasonic source influence in an anisotropic layer. *Rev. Prog. in QNDE*, 14:1257, 1995.
- [214] M.K.T. Hansch, K.M. Rajana, and J.L. Rose. Flaw classification potential in tubing with guided waves. *Rev. Prog. in QNDE*, 14:803, 1995.
- [215] Y. Nagata, J. Huang, J.D. Achenbach, and S. Krishnaswamy. Lamb wave tomography using laser-based ultrasonics. *Rev. Prog. in QNDE*, 14:561, 1995.
- [216] R.C. Addison and A.D.W. McKie. Generation and detection of single mode Lamb waves using laser based ultrasound. *Rev. Prog. in QNDE*, 14:521, 1995.
- [217] J.L. Rose, A. Pilarski, and K.M. Rajana. Ultrasonic guided waves for lap joint inspection in aging aircraft. *Rev. Prog. in QNDE*, 14:1417, 1995.
- [218] K.J. Sun and P.H. Johnston. Effect of rivet rows on propagation of Lamb waves in mechanically fastened two-layer aluminum plates. *Rev. Prog. in QNDE*, 14:1569, 1995.
- [219] J.C. Johnson, R.B. Thompson, and E.E. Jamieson. Determination of Rayleigh and Lamb wave velocities in diamond films using an acoustic microscope. *Rev. Prog. in QNDE*, 14:1805, 1995.

- [220] A. Safaeinili and D.E. Chimenti. Floquet analysis of Lamb waves propagating in periodically-layered composites. *Rev. Prog. in QNDE*, 14:179, 1995.
- [221] J.J. Ditri and K.M. Rajana. Analysis of the wedge method of generating guided waves. *Rev. Prog. in QNDE*, 14:163, 1995.
- [222] M. Lowe and P. Cawley. Comparison of reflection coefficient minima with dispersion curves for ultrasonic waves in embedded layers. *Rev. Prog. in QNDE*, 14:1505, 1995.
- [223] K.M. Rajana, D. Hongerholt, and J.L. Rose. Analysis of the generation of guided waves using finite sources: an experimental approach. *Rev. Prog. in QNDE*, 14:171, 1995.
- [224] J. Pei, F.L. Degertekin, B.T. Khuri-Yakub, and K.C. Saraswat. In situ film thickness measurement with acoustic Lamb waves. *Appl. Phys. Lett* 66(17), 24:2177, April 1995.
- [225] W. Huang, S. Brisuda, and S.I. Rokhlin. Ultrasonic wave scattering from fiber-matrix interphases. *J. Acoust. Soc. Am.*, 97(2):807, February 1995.
- [226] W. Karunasena, K.M. Liew, and S. Kitipornchai. Reflection of plate waves at the fixed edge of a composite plate. *J. Acoust. Soc. Am.*, 98(1):644, July 1995.
- [227] E. Phipps. Lamb wave measurements for the nondestructive evaluation of disbonds. *NSF Research Experiences for Undergraduates*, 1995.
- [228] K. Yamada and B.T. Khuri-Yakub. Point contact transducer of waveguiding structure for high-frequency operation. *Ultrasonics*, 1995.

- [229] D.A. Rebinsky and A.N. Norris. Acoustic and flexural wave scattering from a three-member junction. *J. Acoust. Soc. Am.*, 98(6):3309, 1995.
- [230] A. Gachagan, S.G. Pierce, W.R. Philip, A. McNab, G. Hayward, and B. Culshaw. Detection of ultrasonic Lamb waves in composite plates using optical-fibres. *Ultrasonics*, page 803, 1995.
- [231] W.P. Rogers. Elastic property measurement using Rayleigh-Lamb waves. *Res. Nondestr. Eval*, 6:185, 1995.
- [232] K.S. Tan, N. Guo, B.S. Wong, and C.G. Tui. Experimental evaluation of delaminations in composite plates by the use of Lamb waves. *Composites Science and Technology*, 53:77, 1995.
- [233] K.S. Tan, N. Guo, B.S. Wong, and C.G. Tui. Comparison of Lamb waves and pulse echo in determination of near-surface defects in laminate plates. *NDT&E International*, 28(4):215, 1995.
- [234] U. Bork and R.E. Challis. Non-destructive evaluation of the adhesive fillet size in a T-peel joint using ultrasonic Lamb waves and a linear network for data discrimination. *Meas. Sci. Technol.*, 6:72, 1995.
- [235] Z. Zhu and J. Wu. The propagation of Lamb waves in a plate bordered with a viscous liquid. *J. Acoust. Soc. Am.*, 98(2):1057, 1995.
- [236] D. Opie. Tomographic imaging for Lamb wave ultrasonic NDE systems. *SBIR proposal*, 1995.
- [237] D.M. Manos. Multilayer structural integrity evaluation using ultrasonic Lamb waves. *Proposal to NASA*, January 1996.

- [238] N. Guo and M.K. Lim. Lamb waves propagation in aluminum honeycomb structures. *Rev. Prog. in QNDE*, 15:323, 1996.
- [239] M.D. Seale and B.T. Smith. Lamb wave propagation in thermally damaged composites. *Rev. Prog. in QNDE*, 15:261, 1996.
- [240] J.C. Cheng and S.Y. Zhang. Lamb wave modes propagating along arbitrary directions in an orthotropic plate. *Rev. Prog. in QNDE*, 15:253, 1996.
- [241] K.M. Rajana, Y. Cho, and J.L. Rose. Utility of Lamb waves for near surface crack detection. *Rev. Prog. in QNDE*, 15:239, 1996.
- [242] M. Hirao and K. Yokota. Leaky Lamb wave along VCR magnetic tapes. *Rev. Prog. in QNDE*, 15:247, 1996.
- [243] T. Kundu, P. Karpur, T.E. Matikas, and P.D. Nicolaou. Lamb wave mode sensitivity to detect various material defects in multilayered composite plates. *Rev. Prog. in QNDE*, 15:231, 1996.
- [244] Y. Ji, R. Sullivan, and Balasubramaniam. Guided wave behavior analysis in multi-layered inhomogeneous anisotropic plates. *Rev. Prog. in QNDE*, 15:217, 1996.
- [245] S. Hirose and M. Yamano. Scattering analysis and simulation for Lamb wave ultrasonic testing. *Rev. Prog. in QNDE*, 15:201, 1996.
- [246] C.-W. Chan and P. Cawley. The existence of low loss Lamb modes in highly attenuative media. *Rev. Prog. in QNDE*, 15:193, 1996.
- [247] Z. Chang, D. Guo, and A.K. Mal. Lamb wave propagation across a lap joint. *Rev. Prog. in QNDE*, 15:185, 1996.

- [248] J. Pei, I. Yousuf, F.L. Degertekin, B.V. Honein, and B.T. Khuri-Yakub. Lamb wave tomography and its application in pipe erosion/corrosion monitoring. *Res. Nondestr. Eval.*, 8:189, 1996.
- [249] M. Spies and M. Kroning. Green's function for Lamb's problem and Rayleigh wave propagation in general transversely isotropic materials. *Rev. Prog. in QNDE*, 15:161, 1996.
- [250] M.K. Hinders. Lamb wave scattering from rivets. *Rev. Prog. in QNDE*, 15:209, 1996.
- [251] T. Laurent and F. Bastien. Lamb and shear-horizontal wave production by interdigital transducers deposited on both sides of a piezoelectric plate. *J. Acoust. Soc. Am.*, 99(5):2876, May 1996.
- [252] D.N. Alleyne and P. Cawley. The excitation of Lamb waves in pipes using dry-coupled piezoelectric transducers. *J. Nondestr. Eval.*, 15(1):11, 1996.
- [253] W. Sweet. Better networks for test ban monitoring. *IEEE Spectrum*, page 24, February 1996.
- [254] C. Desmet, U. Kawald, A. Mourad, W. Lauriks, and J. Thoen. The behavior of Lamb waves in stressed polymer foils. *J. Acoust. Soc. Am.*, 100(3):1509, 1996.
- [255] T. Kundu, K. Maslov, P. Karpur, T.E. Matikas, and P.D. Nicolaou. A Lamb wave scanning approach for the mapping of defects in [0/90] titanium matrix composites. *Ultrasonics*, 34:43, 1996.

- [256] M.E. Read, S. Seiler, M. Hinders, B. Smith, and K. Sun. Nde of metallic and composite structures. *Phase I STTR Final Report prepared for the ONR*. March 1996.
- [257] S. Seiler and M.E. Read. NDE of metallic and composite structures. *SBIR Phase II Program Plan prepared for ONR*, February 1996.
- [258] M.L. Read. NDE of metallic and composite structures. *STTR Program Proposal for Phase II*, July 1996.
- [259] P.G. Young, J. Yuan, and S.M. Dickinson. Three-dimensional analysis of the free vibration of thick rectangular plates with depressions, grooves, and cutouts. *J. Vibr. Acoust.*, 118:184, April 1996.
- [260] J. Turner and R. Weaver. Diffuse energy propagation on heterogeneous plates: Structural acoustics radiative transfer theory. *J. Acoust. Soc. Am.*, 100(6):3686, 1996.
- [261] Y. Xiang, K.M. Liew, and S. Kitipornchai. Vibration of circular and annular Mindlin plates with internal ring stiffeners. *J. Acoust. Soc. Am.*, 100(6):3696, 1996.
- [262] M.H. Park, S. Kim, and Y.K. Yoon. Ultrasonic inspection of long steel pipes using Lamb waves. *NDT&E International*. 29(1):13, 1996.
- [263] M. Castaings and P. Cawley. The generation, propagation, and detection of Lamb waves in plates using air-coupled ultrasonic transducers. *J. Acoust. Soc. Am.*, 100(5):3070, 1996.

- [264] G. Khmelevskaja-Plotnikova and V. Pavlov. On transversal structure of finite amplitude Lamb waves in the atmosphere near the Earth's surface. *J. Acoust. Soc. Am.*, 100(2):734, 1996.
- [265] J.L. Rose Y. Cho. A boundary element solution for a mode conversion study on the edge reflection for Lamb waves. *J. Acoust. Soc. Am.*, 99(4):2097, 1996.
- [266] J.-C. Cheng and Y.H. Berthelot. Theory of laser-generated transient Lamb waves in orthotropic plates. *J. Phys. D Appl. Sci.*, 29(1):1857, 1996.
- [267] R. Balasubramanyam, D. Quinney, R.E. Challis, and C.P.D. Todd. A finite-difference simulation of ultrasonic Lamb waves in metal sheets with experimental verification. *J. Phys. D Appl. Sci.*, 29(1):147, 1996.
- [268] N.F.-S. Secora. Lamb wave scanning of next generation composite. *Senior honors thesis, College of William and Mary*, May 1996.
- [269] M.D. Seale. Propagation of guided acoustic waves in composite media. *Dissertation, Department of Physics, The College of William and Mary in Virginia*, 1996.
- [270] S.P. Pelts, J.P. Cysyk, and J.L. Rose. The boundary element method for flaw classification in wave guides. *Rev. Prog. in QNDE*, 16, 1997.
- [271] B. Pavlakovic, M. Lowe, D. Alleyne, and P. Cawley. DISPERSE: A general purpose program for creating dispersion curves. *Rev. Prog. in QNDE*, 16:185, 1997.
- [272] L. Singher, Y. Segal, and J. Shamir. Guided wave scattering by a cylindrical flaw. *Rev. Prog. in QNDE*, 16, 1997.

- [273] Y.C. Cho, D.D. Hongerholt, and J.L. Rose. Lamb wave scattering analysis for reflector characterization. *IEEE Trans. Ultrason., Ferroelect., and Freq. Contr.*, 44(1):44, 1997.
- [274] X. Jia. Model analysis of Lamb wave generation in elastic plates by liquid wedge transducers. *J. Acoust. Soc. Am.*, 102(2):834, 1997.
- [275] D.N. Alleyne and P. Cawley. Long range propagation of Lamb waves in chemical plant pipework. *Mat. Eval.*, page 54, April 1997.
- [276] K. Maslov and T. Kundu. Selection of Lamb modes for detecting internal defects in composite laminates. *Ultrasonics*, 35:141, 1997.
- [277] S.G. Pierce, B. Culshaw, W.R. Philip, F. Lecuyer, and R. Farlow. Broadband Lamb wave measurements in aluminum and carbon/glass fiber reinforced composite materials using non-contacting laser generation and detection. *Ultrasonics*, 35:105, 1997.
- [278] A.H. Nayfeh and P.B. Nagy. Excess attenuation of leaky Lamb waves due to viscous fluid loading. *J. Acoust. Soc. Am.*, 101(5):2649, 1997.
- [279] D. Cathignol, O.A. Sapozhnikov, and J. Zhang. Lamb waves in piezoelectric focused radiator as a reason for discrepancy between O'Neils formula and experiment. *J. Acoust. Soc. Am.*, 101(3):1286, 1997.
- [280] R. Briers, O. Leroy, and G. Shkerdin. A liquid wedge as generating technique for Lamb and Rayleigh waves. *J. Acoust. Soc. Am.*, 102(4):2117, 1997.
- [281] T. Kundu and K. Maslov. Material interface inspection by Lamb waves. *Int. J. Solids Structures*, 34(29):3885, 1997.

- [282] P. Kielczynski. Attenuation of Love waves in low-loss media. *J. Appl. Phys.*, 82(12):5932, 1997.
- [283] E. Moulin, J. Assaad, C. Delebarre, H. Kaczmarek, and D. Balageas. Piezoelectric transducer embedded in a composite plate: Application to Lamb wave generation. *J. Appl. Phys.*, 82(5):2049, 1997.
- [284] P. Zinin, O. Lefeuvre, G.A.D. Briggs, B.D. Zeller, P. Cawley, J. Kinloch, and G.E. Thompson. Anomalous behaviour of leaky surface waves for stiffening layer near cutoff. *J. Appl. Phys.*, 82(3):1031, 1997.
- [285] S.N. Makarov and A.L. Belkova. High velocity pseudosurface waves on LiNbO_3 with thin overlayers. *Appl. Phys. Lett.*, 70(16):2100, 1997.
- [286] X. Jia. Normal-mode theory of nonspecular phenomena for a finite-aperture ultrasonic beam reflected from layered media. *Appl. Phys. Lett.*, 70(3):309, 1997.
- [287] O. Poncelet and M. Deschamps. Lamb waves generated by complex harmonic inhomogeneous plane waves. *J. Acoust. Soc. Am.*, 102(1):292, 1997.
- [288] A.N. Darinskii. Leaky waves and the elastic wave resonance reflection on a crystal-thin solid layer interface. *J. Acoust. Soc. Am.*, 102(1):283, 1997.
- [289] T.K. Kapoor and H. Schmidt. Acoustic scattering from a three-dimensional proturbance on a thin, infinite, submerged elastic plate. *J. Acoust. Soc. Am.*, 102(1):256, 1997.
- [290] O.I. Lobkis and D.E. Chimenti. Elastic guided waves in plates with surface roughness. I. Model calculation. *J. Acoust. Soc. Am.*, 102(1):143, 1997.

- [291] O.I. Lobkis and D.E. Chimenti. Elastic guided waves in plates with surface roughness. II. Experiments. *J. Acoust. Soc. Am.*, 102(1):150, 1997.
- [292] M. de Billy. On the scattering of antisymmetric edge modes. *J. Acoust. Soc. Am.*, 101(6):3261, 1997.
- [293] N.A. Losin. Asymptotics of flexural waves in isotropic elastic plates. *J. Appl. Mech.*, 64:337, June 1997.
- [294] R.S.C. Monkhouse, P.D. Wilcox, and P. Cawley. Flexible interdigital PVDF transducers for the generation of Lamb waves in structures. *Ultrasonics*, 35:489, 1997.
- [295] L. Wang and J. Shen. Scattering of elastic waves by a crack in a isotropic plate. *Ultrasonics*, 35:451, 1997.
- [296] Z. Guo, J.D. Achenbach, and S. Krishnaswamy. EMAT generation and laser detection of single Lamb wave modes. *Ultrasonics*, 35:423, 1997.
- [297] L. Singher. Bond strength measurement by ultrasonic guided waves. *Ultrasonics*, 35:305, 1997.
- [298] L. Singher, Y. Segal, and J. Shamir. Interaction of a guided wave with a nonuniform adhesion bond. *Ultrasonics*, 35:385, 1997.
- [299] D.W. Schindel, D.S. Forsyth, D.A. Hutchins, and A. Fahr. Air-coupled ultrasonic NDE of bonded aluminum lap joints. *Ultrasonics*, 35:1, 1997.
- [300] W. Hassan and P.B. Nagy. Feasibility of fatigue crack detection in fluid-filled cylindrical holes using circumferential creeping waves. *Rev. Prog. in QNDE*, 16:43, 1997.

- [301] A. Mal and Z. Chang. Interaction of Lamb waves with defects in a semi-infinite plate. *Rev. Prog. in QNDE*, 16:153, 1997.
- [302] C. Pecorari. Rayleigh wave dispersion due to one-dimensional interacting cracks. *Rev. Prog. in QNDE*, 16:161, 1997.
- [303] D.E. Chimenti and O.I. Lobkis. Effect of rough surfaces on guided waves in plates. *Rev. Prog. in QNDE*, 16:169, 1997.
- [304] C.-H. Yang and C. Gung. Acoustic waves in a piezoelectric plate immersed in a conductive fluid. *Rev. Prog. in QNDE*, 16:193, 1997.
- [305] M. Evans and P. Cawley. Generation of diffuse Lamb waves in plates. *Rev. Prog. in QNDE*, 16:389, 1997.
- [306] D. Guo, A. Mal, K. Ono, and M. Gorman. Lamb waves from microfractures in composite plates. *Rev. Prog. in QNDE*, 16:397, 1997.
- [307] P. Wilcox, M. Castaings, R. Monkhouse, P. Cawley, and M. Lowe. An example of the use of interdigital PVDF transducers to generate and receive a high order Lamb wave mode in a pipe. *Rev. Prog. in QNDE*, 16:919, 1997.
- [308] Y. Yang, J.N. Caron, J.B. Mehl, and K.V. Steiner. Laser generation and detection of Lamb waves in graphite/epoxy composite laminates. *Rev. Prog. in QNDE*, 16:1123, 1997.
- [309] J.L. Rose, J.N. Barshinger, and M. Zaidi. Guided waves for the inspection of titanium diffusion bonds. *Rev. Prog. in QNDE*, 16:1223, 1997.
- [310] H.J. Shin, M.J. Quarry, and J.L. Rose. Non-axisymmetric guided waves for tubing inspection. *Rev. Prog. in QNDE*, 16:1253, 1997.

- [311] M. Lowe, D. Alleyne, and P. Cawley. Mode conversion of guided waves by defects in pipes. *Rev. Prog. in QNDE*, 16:1261, 1997.
- [312] D.N. Alleyne, P. Cawley, A.M. Lank, and P.J. Mudge. The Lamb wave inspection of chemical plant pipework. *Rev. Prog. in QNDE*, 16:1269, 1997.
- [313] J.L. Rose, D. Jiao, and J. Spanner. Ultrasonics guided waves for piping inspection. *Rev. Prog. in QNDE*, 16:1285, 1997.
- [314] A. El-Azab, A.K. Mal, Y. Bar-Cohen, and S.-S. Lih. Measurement of thickness and elastic properties of electroactive thin polymer films using plate wave dispersion data. *Rev. Prog. in QNDE*, 16:1617, 1997.
- [315] K. Kawashima, I. Fujii, T. Sato, and M. Okade. Measurement of acoustoelastic coefficient with leaky surface wave. *Rev. Prog. in QNDE*, 16:1663, 1997.
- [316] W. Li, J.D. Achenbach, and A. Cheng. A time-resolved line-focus acoustic microscopy technique for surface-breaking crack depth determination. *Rev. Prog. in QNDE*, 16:1823, 1997.
- [317] W. Wright, D. Hutchins, D. Jansen, and D. Schindel. Air-coupled Lamb wave tomography. *IEEE Trans. Ultrason., Ferroelect., and Freq. Contr.*, 44(1):53, 1997.
- [318] A.A. Mesquida, J.A. Otero, and R.R. Ramos. Wave propagation in layered piezoelectric structures. *J. Appl. Phys.*, 83(9):4652, 1998.
- [319] S.G. Pierce, B. Culshaw, and Q. Shan. Laser generation of ultrasound using a modulated continuous wave laser diode. *Appl. Phys. Lett.*, 72(9):103, 1998.

- [320] A.N. Darinskii. Leaky waves and the elastic wave resonance reflection on a crystal-thin solid layer interface. II. Leaky waves given rise to by exceptional bulk waves. *J. Acoust. Soc. Am.*, 103(4):1845, 1998.
- [321] C. Pecorari. Rayleigh wave dispersion due to a distribution of semi-elliptical surface-breaking cracks. *J. Acoust. Soc. Am.*, 103(3):138, 1998.
- [322] Y.-S. Wang and Z.-M. Zhang. Propagation of Love waves in a transversely isotropic fluid-saturated porous layered half-space. *J. Acoust. Soc. Am.*, 103(2):695, 1998.
- [323] B. Zhang, W. Xiong, M. Yu, C.Q. Lan, and L. Li. Study of energy distribution of guided waves in multilayered media. *J. Acoust. Soc. Am.*, 103(1):125, 1998.
- [324] C. Bescond and M. Deschamps. Dynamical surface response of a semi-infinite anisotropic elastic medium to an impulsive force. *J. Acoust. Soc. Am.*, 103(1):114, 1998.
- [325] E. Moreno and P. Acevedo. Thickness measurement in composite materials using Lamb waves. *Ultrasonics*, 35:581, 1998.
- [326] T. Kundu, A. Maji, T. Ghosh, and K. Maslov. Detection of kissing bonds by Lamb waves. *Ultrasonics*, 35:573, 1995.
- [327] J.L. Rose, W. Zhu, and M. Zaidi. Ultrasonic NDT of titanium diffusion bonding with guided waves. *Mat. Eval.*, page 535, April 1998.
- [328] J. Radon. Über die Bestimmung von Funktionen durch ihre Integralwerte längs gewisser Mannigfaltigkeiten. *Berichte Saechsische Akademie der Wissenschaften*, 69:262, 1917.

- [329] R.N. Bracewell and A.C. Riddle. Inversion of fan-beam scans in radio astronomy. *The Astrophysical Journal*, 150:427, 1967.
- [330] R. Gordon, R. Bender, and G.T. Herman. Algebraic reconstruction techniques (ART) for three-dimensional electron microscopy and X-ray photography. *J. Theor. Biol.*, 29:471, 1970.
- [331] G.N. Ramachandran and A.V. Lakshminarayanan. Three-dimensional reconstruction from radiographs and electron micrographs: Applications of convolutions instead of Fourier transforms. *Proc. Natl. Acad. Sci. USA*, 68(9):2236, 1971.
- [332] R. Gordon. A tutorial on ART (Algebraic Reconstruction Techniques). *IEEE Trans. Nucl. Sci.*, NS-21(3):78, 1974.
- [333] T.F. Budinger and G.T. Gullberg. Three-dimensional reconstruction in nuclear medicine emission imaging. *IEEE Trans. Nucl. Sci.*, NS-21(3):2, 1974.
- [334] L.A. Shepp and B.F. Logan. The Fourier reconstruction of a head section. *IEEE Trans. Nucl. Sci.*, NS-21(3):21, 1974.
- [335] A.V. Lakshminarayanan. Reconstruction from divergent ray data. Technical Report 92, Dept. Comp. Sci. SUNY Buffalo, 1975.
- [336] E. Tanaka and T.A. Iinuma. Correction functions for optimizing the reconstructed image in transverse section scan. *Phys. Med. Bio.*, 20(5):789, 1975.
- [337] G.T. Herman and A. Lent. Iterative reconstruction algorithms. *Comput. Bio. Med.*, 6:273, 1976.
- [338] P. Dreike and D.P. Boyd. Convolution reconstruction of fan beam projections. *Comput. Graph. Imag. Process.*, 5:459, 1976.

- [339] T.M. Peters and R.M. Lewitt. Computed tomography with fan beam geometry. *J. Comp. Assist. Tomography*, 1(4):429, 1977.
- [340] G.T. Herman and A. Naparstek. Fast image reconstruction based on a radon inversion formula appropriate for rapidly collected data. *SIAM J. Appl. Math.*, 33(3):511, 1977.
- [341] L.Wang. Cross-section reconstruction with a fan-beam scanning geometry. *IEEE Trans. Comput.*, C-26:264, 1977.
- [342] S.J. Wernecke and L.R. D'Addario. Maximum entropy image reconstruction. *IEEE Trans. Comput.*, C-26:351, 1977.
- [343] K.A. Dines and R.J. Lytle. Computerized geophysical tomography. *Proc. IEEE*, 67(7):1065, 1979.
- [344] S.K. Kenue and J.F. Greenleaf. Efficient convolution kernels for computerized tomography. *Ultrasonic Imaging*, 1:232, 1979.
- [345] R.J. Lytle and K.A. Dines. Iterative ray tracing between boreholes for underground image reconstruction. *IEEE Trans. Geosci. Rem. Sens.*, GE-18(3):234, 1980.
- [346] C.J. Thompson and T.M. Peters. A fractional address accumulator for fast back-projection. *IEEE Trans. Nucl. Sci.*, NS-28(4):3648, 1981.
- [347] Y. Censor. Finite series-expansion reconstruction methods. *Proc. IEEE*, 71(3):409, 1983.
- [348] R.M. Lewitt. Reconstruction algorithms: Transform methods. *Proc. IEEE*, 71(3):390, 1983.

- [349] R.H.T. Bates, K.L. Garden, and T.M. Peters. Overview of computerized tomography with emphasis on future developments. *Proc. IEEE*, 71(3):356, 1983.
- [350] J. Wong, P. Hurley, and G.F. West. Crosshole seismology and seismic imaging in crystalline rocks. *Geophys. Res. Lett.*, 10(8):686, 1983.
- [351] G.A. McMechan. Seismic tomography in boreholes. *Geophys. J. R. ast. Soc.*, 74:601, 1983.
- [352] N. Ichida, T. Sato, and M. Linzer. Imaging the nonlinear ultrasonic parameter of a medium. *Ultrasonic Imaging*, 5:295, 1983.
- [353] W. Munk and C. Wunsch. Ocean acoustic tomography: Rays and modes. *Rev. Geophys. Space Phys.*, 21(4):777, 1983.
- [354] W. Menke. The resolving power of cross-borehole tomography. *Geophys. Res. Lett.*, 11(2):105, 1984.
- [355] A.J. Devaney. Geophysical diffraction tomography. *IEEE Trans. Geosci. Rem. Sens.*, GE-22(1):3, 1984.
- [356] J.E. Peterson, B.N.P. Paulsson, and T.V. McEvelly. Applications of algebraic reconstruction techniques to crosshole seismic data. *Geophys.*, 50(10):1566, 1985.
- [357] S. Ivansson. A study of methods for tomographic velocity estimation in the presence of low-velocity zones. *Geophys.*, 50(6):969, 1985.
- [358] R. Hartz, D. Bristow, and N. Mullani. A real-time TOFPET slice-backproject engine employing dual AM29116 microprocessors. *IEEE Trans. Nucl. Sci.*, NS-32(1):839, 1985.

- [359] J. Llacer and J.D. Meng. Matrix-based reconstruction methods for tomography. *IEEE Trans. Nucl. Sci.*, NS-32(1):855, 1985.
- [360] L.R. Testardi, S.J. Norton, and T. Hsieh. Acoustic dimensional resonance tomography: Some examples in one-dimensional systems. *J. Appl. Phys.*, 59(1):55, 1986.
- [361] S. Ivansson. Seismic borehole tomography-Theory and computational methods. *Proc. IEEE*, 74(2):328, 1986.
- [362] M. Gustavsson, S. Ivansson, P. Moren, and J. Pihl. Seismic borehole tomography - Measurement system and field studies. *Proc. IEEE*, 74(2):339, 1986.
- [363] W.-F. Chang and G.A. McMechan. Reverse-time migration of offset vertical seismic profiling data using the excitation-time imaging condition. *Geophys.*, 51(1):67, 1986.
- [364] M. Jones, T.M. Georges, and J. P. Riley. Inverting vertical-slice tomography measurements for asymmetric ocean sound-speed profiles. *Deep-Sea Research*, 33(5):601, 1986.
- [365] Y. Nakagawa, W. Hou, A. Cai, N. Arnold, G. Wade, M. Yoneyama, and M. Nakagawa. Nonlinear parameter imaging with finite-amplitude sound waves. *1986 Ultrasonics Symposium*, page 901, 1986.
- [366] J.M. Blackledge, R.E. Burge, K.I. Hopcraft, and R.J. Wombell. Quantitative diffraction tomography: II. Pulsed elastic waves. *J. Phys. D: Appl. Phys.*, 20:11, 1987.
- [367] J.A. Scales. Tomographic inversion via the conjugate gradient method. *Geophys.*, 52(2):179, 1987.

- [368] R.P. Bording, A. Gersztenkorn, L.R. Lines, J.A. Scales, and S. Treitel. Applications of seismic travelttime tomography. *Geophys. J. R. ast. Soc.*, 90:285, 1987.
- [369] C.-S. Chiu and J.F. Lynch. Tomographic resolution of mesoscale eddies in the marginal ice zone: A preliminary study. *J. Geophys. Res.*, 92(C7):6886, 1987.
- [370] J. Um and C. Thurber. A fast algorithm for two-point seismic ray tracing. *Bull. Seism. Soc. Am.*, 77(3):972, 1987.
- [371] R.G. Pratt and M.H. Worthington. The application of diffraction tomography to cross-hole seismic data. *Geophys.*, 53(10):1284, 1988.
- [372] B. Dyer and M.H. Worthington. Some sources of distortion in tomographic velocity images. *Geophys. Prosp.*, 36:209, 1988.
- [373] R.J.R. East, M.H. Worthington, and N.R. Goult. Convolutional back-projection imaging of physical models with crosshole seismic data. *Geophys. Prosp.*, 36:139, 1988.
- [374] T.-w. Lo, M.N. Toksoz, S.-h. Xu, and R.-S. Wu. Ultrasonic laboratory tests of geophysical tomographic reconstruction. *Geophys.*, 53(7):947, 1988.
- [375] L.R. Lines and E.D. LaFehr. Tomographic modeling of a cross-borehole seismic data set. *58th Ann. Intl. Mtg. Soc. Expl. Geophys. Expanded Abstracts*, page 1247, 1988.
- [376] W.F. Jones, L.G. Byars, and M.E. Casey. Positron emission tomographic images and expectation maximization: A VLSI architecture for multiple iterations per second. *IEEE Trans. Nucl. Sci.*, 35(1):620, 1988.

- [377] A.C. Kak and M. Slaney. *Principles of Computerized Tomographic Imaging*. IEEE Inc., New York, 1988.
- [378] L.R. Lines and E.D. LaFehr. Tomographic modeling of a cross-borehole data set. *Geophys.*, 54(10):1249, 1989.
- [379] N.D. Bregman, R.C. Bailey, and C.H. Chapman. Crosshole seismic tomography. *Geophys.*, 54(2):200, 1989.
- [380] S.T. Chen, L.J. Zimmerman, and J.K. Tugnait. Subsurface imaging using reversed vertical seismic profiling and crosshole tomographic methods. *Geophys.*, 55(11):1478, 1990.
- [381] R.G. Pratt and M.H. Worthington. Inverse theory applied to multi-source cross-hole tomography. Part 1: Acoustic wave-equation method. *Geophys. Prosp.*, 38:287, 1990.
- [382] R.G. Pratt. Inverse theory applied to multi-source cross-hole tomography. Part 2: Elastic wave-equation method. *Geophys. Prosp.*, 38:311, 1990.
- [383] R.G. Pratt. Short Note. Frequency-domain elastic wave modeling by finite differences: A tool for crosshole seismic imaging. *Geophys.*, 55(5):626, 1990.
- [384] C.M. Chen, S.-Y. Lee, and Z.H. Cho. A parallel implementation of 3-D CT image reconstruction on hypercube multiprocessor. *IEEE Trans. Nucl. Sci.*, 37(3):1333, 1990.
- [385] S. Barresi, D. Bollini, and A. Del Guerra. Use of a transputer system for fast 3-D image reconstruction in 3-D PET. *IEEE Trans. Nucl. Sci.*, 37(2):812, 1990.

- [386] R.G. Pratt and N.R. Goulyt. Combining wave-equation imaging with travel-time tomography to form high-resolution images from crosshole data. *Geophys.*, 56(2):208, 1991.
- [387] M.S. Atkins, D. Murray, and R. Harrop. Use of transputers in a 3-D positron emission tomograph. *IEEE Trans. Med. Imaging*, 10(3):276, 1991.
- [388] C.M. Chen, S.-Y. Lee, and Z.H. Cho. Parallelization of the EM algorithm for 3-D PET image reconstruction. *IEEE Trans. Med. Imaging*, 10(4):513, 1991.
- [389] T.J. Moser. Shortest path calculation of seismic rays. *Geophys.*, 56(1):59, 1991.
- [390] R. Snieder and M. Sambridge. Ray perturbation theory for traveltimes and ray paths in 3-D heterogeneous media. *Geophys. J. Intl.*, 109:294, 1992.
- [391] S.M. Huang, C.G. Xie, J.A. Salkeld, A. Plaskowski, R. Thorn, R.A. Williams, A. Hunt, and M.S. Beck. Process tomography for identification, design and measurement in industrial systems. *Powder Technol.*, 69:85, 1992.
- [392] S.D. Rajan, G.V. Frisk, J.A. Doust, and C.J. Sellers. Determination of compressional wave and shear wave speed profiles in sea ice by crosshole tomography-Theory and experiment. *J. Acoust. Soc. Am.*, 93(2):721, 1993.
- [393] O. Pade and A. Mandelis. Computational thermal-wave slice tomography with backprojection and transmission reconstructions. *Rev. Sci. Instr.*, 64(12):3548, 1993.
- [394] I. Agi, P.J. Hurst, and K.W. Current. An image processing IC for backprojection and spatial histogramming in a pipelined array. *IEEE J. Solid-State Circuits*, 28(3):210, 1993.

- [395] D.W. Vasco and E.L. Majer. Wavepath traveltime tomography. *Geophys. J. Intl.*, 115:1065, 1993.
- [396] G.T. Schuster and A. Quintus-Bosz. Wavepath eikonal traveltime inversion: Theory. *Geophys.*, 58(9):1314, 1993.
- [397] C.J. Ammon and J.E. Vidale. Tomography without rays. *Bull. Seism. Soc. Am.*, 83(2):509, 1993.
- [398] V. Farra. Ray tracing in complex media. *J. Appl. Geophys.*, 30:55, 1993.
- [399] E. Asakawa and T. Kawanaka. Seismic ray tracing using linear traveltime interpolation. *Geophys. Prosp.*, 41:99, 1993.
- [400] R. Fischer and J.M. Lees. Shortest path ray tracing with sparse graphs. *Geophys.*, 58(7):987, 1993.
- [401] V.V. Goncharov and A.G. Voronovich. An experiment on matched-field acoustic tomography with continuous wave signals in the Norway sea. *J. Acoust. Soc. Am.*, 93(4):1873, 1993.
- [402] R.M. Jones, E.C. Shang, and T.M. Georges. Nonperturbative modal tomography inversion. Part I. Theory. *J. Acoust. Soc. Am.*, 94(4):2296, 1993.
- [403] O. Isaksen and J.E. Nordtvedt. A new reconstruction algorithm for process tomography. *Meas. Sci. Technol.*, 4:1464, 1993.
- [404] D.W. Ratcliff and D.J. Weber. Mahogany salt images show key role of velocity model. *Oil & Gas Journal*, page 43, Oct. 24 1994.
- [405] D. Zhang and X. Gong. Computer simulation of acoustic nonlinear parameter tomography. *Chin. J. Acoust.*, 13(2):169, 1994.

- [406] T. Zhu and K.-Y. Chun. Complex rays in elastic and anelastic media. *Geophys. J. Intl.*, 119:269, 1994.
- [407] W.S. French. Improvements in 3-D seismic. *World Oil*, page 60, May 1994.
- [408] R.M. Jones and T.M. Georges. Nonperturbative ocean acoustic tomography inversion. *J. Acoust. Soc. Am.*, 96(1):439, 1994.
- [409] R.M. Jones, B.M. Howe, J.A. Mercer, R.C. Spindel, and T.M. Georges. Nonperturbative ocean acoustic tomography inversion of 1000-km pulse propagation in the Pacific ocean. *J. Acoust. Soc. Am.*, 95(5):3054, 1994.
- [410] Y.Q. Wang and R.A. Kline. Ray tracing in isotropic and anisotropic materials: Application to tomographic image reconstruction. *J. Acoust. Soc. Am.*, 95(5):2525, 1994.
- [411] E.C. Shang, Y.Y. Wang, and R.M. Jones. Nonperturbative modal tomography inversion. Part II. Numerical simulation. *J. Acoust. Soc. Am.*, 98(1):560, 1995.
- [412] F. Jalinoos, L.D. Olson, M.F. Aouad, and A.H. Balch. Acoustic tomography for qualitative nondestructive evaluation (QNDE) of structural concrete using a new ultrasonic scanner source. *Rev. Prog. in Quant. NDE*, 14:2177, 1995.
- [413] D. Zhang and X. Gong. The influence of ω filter on nonlinearity parameter imaging using filtered convolution method. *Chin. J. Acoust.*, 14(1):52, 1995.
- [414] F. Jalinoos, L.D. Olson, and M.F. Aouad. Ultrasonic crosshole and crossmedium tomography for the detection of defects in structural concrete. *SAGEEP, Orlando, Fl.*, page 45, 1995.
- [415] W. Daily and A. Ramirez. Environmental process tomography in the united states. *Chem. Eng. J.*, 56:159, 1995.

- [416] R.G. Green, N.M. Horbury, R.A. Rahim, F.J. Dickins, B.D. Naylor, and T.P. Pridmore. Optical fibre sensors for process tomography. *Meas. Sci. Technol.*, 6:1699, 1995.
- [417] B.S. Hoyle. Real-time ultrasonic process tomography of flowing mixtures. *Part. Part. Syst. Charact.*, 12:81, 1995.
- [418] F. Jalinoos and L.D. Olson. High speed tomography for the detection of flaws in concrete members. *First National Conference and Workshop on Research Into Practice, June 15-16, 1995, University of Maryland, College Park*, 1996.
- [419] C. Sullivan, R. Kline, R.B. Mignogna, and P.P. Delsanto. A parallel processing approach to acoustic tomography. *J. Acoust. Soc. Am.*, 99(4):2142, 1996.
- [420] D. Zhang, X. Gong, and S. Ye. Acoustic nonlinearity parameter tomography for biological specimens via measurements of the second harmonics. *J. Acoust. Soc. Am.*, 99(4):2397, 1996.
- [421] L.C. Ingesson and V.V. Pickalov. An iterative projection-space reconstruction algorithm for tomography systems with irregular coverage. *J. Phys. D: Appl. Phys.*, 29:3009, 1996.
- [422] M.S. Beck and R.A. Williams. Process tomography: a European innovation and its applications. *Meas. Sci. Technol.*, 7:215, 1996.
- [423] B.S. Hoyle. Process tomography using ultrasonic sensors. *Meas. Sci. Technol.*, 7:272, 1996.
- [424] P. Zhu, P. Duvauchelle, G. Pelx, and D. Babot. X-ray Compton backscattering techniques for process tomography: imaging and characterization of materials. *Meas. Sci. Technol.*, 7:281, 1996.

- [425] T. Dyakowski. Process tomography applied to multi-phase flow measurement. *Meas. Sci. Technol.*, 7:343, 1996.
- [426] S.J. Gibbs and L.D. Hall. What roles are there for magnetic resonance imaging in process tomography? *Meas. Sci. Technol.*, 7:827, 1996.
- [427] H.I. Schlaberg, M. Yang, and B.S. Hoyle. Real-time ultrasonic process tomography for two-component flows. *Electron. Lett.*, 32(17):1571, 1996.
- [428] T.A. Dickens and G.A. Winbow. Spatial resolution of diffraction tomography. *J. Acoust. Soc. Am.*, 101(1):77, 1997.
- [429] L.-J. Xu and L.-A. Xu. Ultrasound tomography system used for monitoring bubbly gas/liquid two-phase flow. *IEEE Trans. Ultrason., Ferroelect., and Freq. Contr.*, 44(1):67, 1997.
- [430] P.M.V. Subbarao, P. Munshi, and K. Muralidhar. Performance of iterative tomographic algorithms applied to non-destructive evaluation with limited data. *NDT&E International*, 30(6):359, 1997.
- [431] S. Mensah and J.-P. Lefebvre. Enhanced compressibility tomography. *IEEE Trans. Ultrason., Ferroelect., and Freq. Contr.*, 44(6):1245, 1997.
- [432] D. Ko and A. Meyyappan. Scanning tomographic acoustic microscopy using shear waves. *IEEE Trans. Ultrason., Ferroelect., and Freq. Contr.*, 44(2):425, 1997.
- [433] P. Wells, R. Smith, and G.B. Suparta. Sampling the sinogram in computed tomography. *Mat. Eval.*, page 772, July 1997.

- [434] V.L. Vengrinovich, Y.B. Denkevich, G.-R. Tillack, and C. Nockemann. Multi step 3D X-ray tomography for a limited number of projections and views. *Rev. Prog. in Quant. NDE*, 16:317, 1997.
- [435] E.C. Greenawald, L.J. Levenberry, C.F. Poranski, R.K. Everett, K.E. Simmonds, N.K. Batra, and D. Hu. X-ray backscatter evaluation of porosity distribution in low density porous magnesium. *Rev. Prog. in Quant. NDE*, 16:1495, 1997.
- [436] R. Reibold and P. Kwiek. Uncertainty considerations of ultrasonic field mapping by light-diffraction tomography. *Ultrasonics*, 35:187, 1997.
- [437] H.I. Schlaberg, M. Yang, B.S. Hoyle, M.S. Beck, and C. Lenn. Wide-angle transducers for real-time ultrasonic process tomography imaging applications. *Ultrasonics*, 35:213, 1997.
- [438] E. Hebbler, D. Oldenburg, T. Farnocombe, and A. Celler. Direct estimation of dynamic parameters in SPECT tomography. *IEEE Trans. Nucl. Sci.*, 44(6):2425, 1997.
- [439] T. Beyer, P.E. Kinahan, and D.W. Townsend. Optimization of transmission and emission scan duration in 3D whole-body PET. *IEEE Trans. Nucl.Sci.*, 44(6):2400, 1997.
- [440] T. Yuasa, M. Akiba, T. Takeda, M. Kazama, A. Hoshino, Y. Watanabe, K. Hyodo, and F.A. Dilmanian. Incoherent-scatter computed tomography with monochromatic synchrotron X ray: Feasibility of multi-CT imaging system for simultaneous measurement of fluorescent and incoherent scatter X rays. *IEEE Trans. Nucl. Sci*, 44(5):1760, 1997.

- [441] C. Schiepers, J. Nuyts, H.-M. Wu, and R. Verma. PET with ^{18}F -fluoride: Effects of iterative versus filtered backprojection reconstruction on kinetic modeling. *IEEE Trans. Nucl. Sci.*, 44(4):1591, 1997.
- [442] P.E. Kinahan, J.A. Fessler, and J.S. Karp. Statistical image reconstruction in PET with compensation for missing data. *IEEE Trans. Nucl. Sci.*, 44(4):1552, 1997.
- [443] W.G. Hawkins. Fourier transform resampling: Theory and application. *IEEE Trans. Nucl. Sci.*, 44(4):1543, 1997.
- [444] A. Celler, A. Sitek, and R. Harrop. Reconstruction of multiple line source attenuation maps. *IEEE Trans. Nucl. Sci.*, 44(4):1503, 1997.
- [445] X. Pan and C.E. Metz. Non-iterative methods and their noise characteristics in 2D SPECT image reconstruction. *IEEE Trans. Nucl. Sci.*, 44(3):1388, 1997.
- [446] D. Khosla and M. Singh. A maximum-entropy method for MEG source imaging. *IEEE Trans. Nucl. Sci.*, 44(3):1368, 1997.
- [447] J.A. Heanue, J.K. Brown, H.R. Tang, and B.H. Hasegawa. The effect of radionuclide scatter in emission-transmission CT. *IEEE Trans. Nucl. Sci.*, 44(3):1317, 1997.
- [448] F. Noo, R. Clack, and M. Defrise. Cone-beam reconstruction from general discrete vertex sets using Radon rebinning algorithms. *IEEE Trans. Nucl. Sci.*, 44(3):1309, 1997.

- [449] C.A. Johnson, J. Seidel, R.E. Carson, W.R. Gandler, A. Sofer, M.V. Green, and M.E. Daube-Witherspoon. Evaluation of 3D reconstruction algorithms for a small animal PET camera. *IEEE Trans. Nucl. Sci.*, 44(3):1303, 1997.
- [450] Y.-W. Chen, N. Miyanaga, M. Yamanaka, M. Nakai, T. Yamanaka, and S. Nakai. Three-dimensional imaging of laser-imploded targets using X-ray computed tomography technique. *IEEE Trans. Nucl. Sci.*, 44(3):890, 1997.
- [451] V.V. Nagarkar, J.S. Gordon, T.K. Gupta, S. Vasile, P. Gothoskar, M.R. Squillante, and G. Entine. CCD-based high resolution digital radiography system for non destructive evaluation. *IEEE Trans. Nucl. Sci.*, 44(3):885, 1997.
- [452] S.J. Glick and W. Xia. Iterative restoration of SPECT projection images. *IEEE Trans. Nucl. Sci.*, 44(2):204, 1997.
- [453] G.L. Zeng, Y. Weng, and G.T. Gullberg. Iterative reconstruction with attenuation compensation from cone-beam projections acquired via nonplanar orbits. *IEEE Trans. Nucl. Sci.*, 44(1):98, 1997.
- [454] T. Yuasa, M. Akiba, T. Takeda, M. Kazama, A. Hoshino, Y. Watanabe, K. Hyodo, F.A. Dimanian, T. Akatsuka, and Y. Itai. Reconstruction method for fluorescent X-ray computed tomography by least-squares method using singular value decomposition. *IEEE Trans. Nucl. Sci.*, 44(1):54, 1997.
- [455] R.P. Maguire, J.H. Missimer, F. Emert, D.W. Townsend, H. Dollinger, and K.L. Leenders. Positron emission tomography of large rock samples using a multiring PET instrument. *IEEE Trans. Nucl. Sci.*, 44(1):26, 1997.

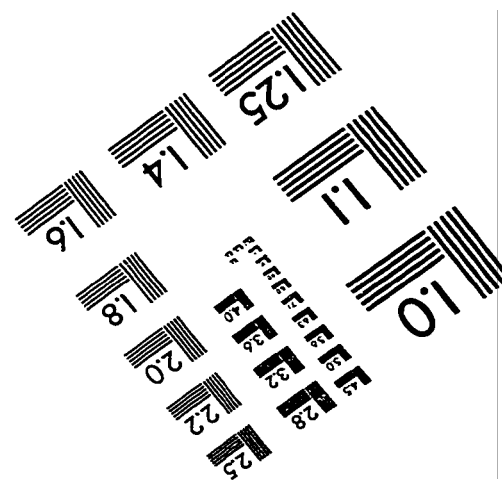
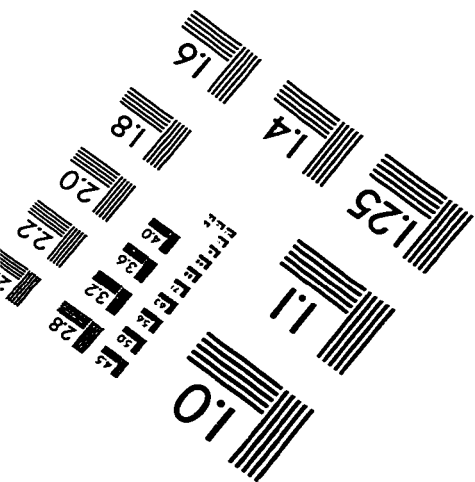
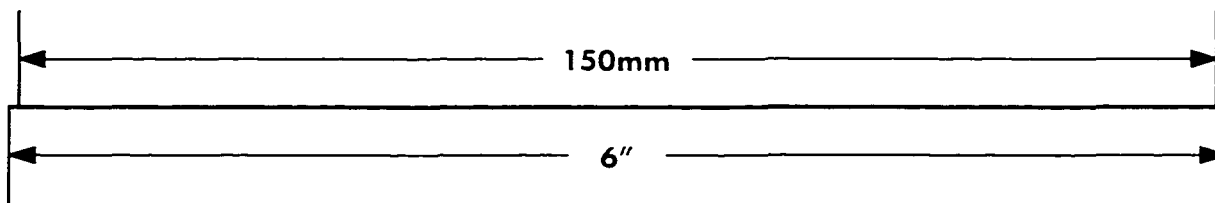
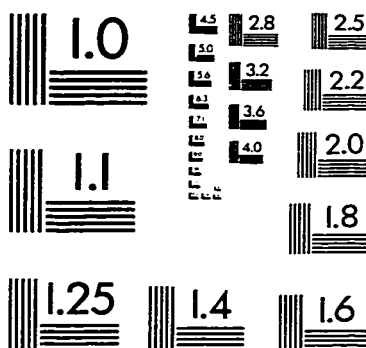
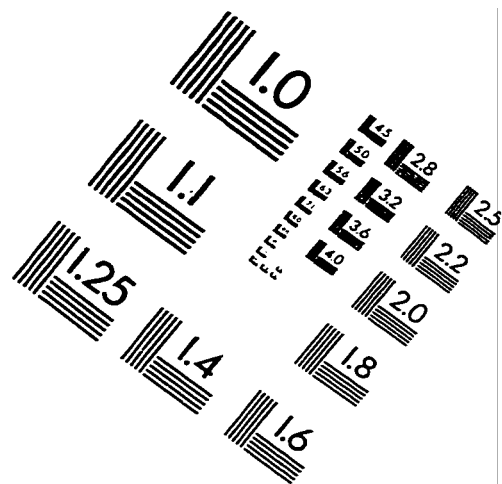
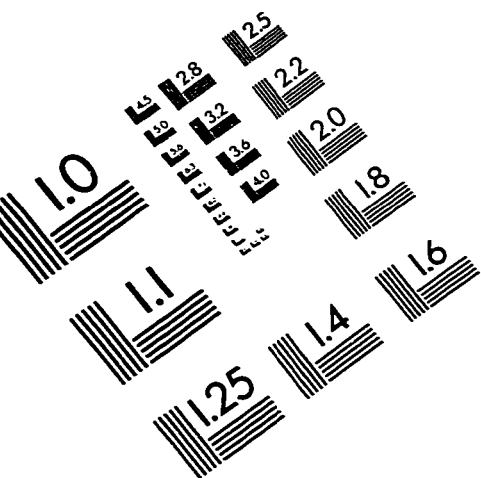
- [456] W. Li and B.S. Hoyle. Ultrasonic process tomography using multiple active sensors for maximum real-time eprformance. *Chem. Eng. Sci.*, 52(13):2161, 1997.
- [457] G.-F. Rust and J. Weigelt. X-ray fluorescent computer tomography with synchrotron radiation. *IEEE Trans. Nucl. Sci.*, 45(1):75, 1998.
- [458] Y.C. Fung. *A First Course in Continuum Mechanics*. Prentice Hall, 1994.
- [459] K.F. Graff. *Wave motion in Elastic Solids*. Dover Publications, Inc., 1991.
- [460] R. Millis. Pulse Phase Lock Loop Users Manual. *NASA-Langley Research Center*.
- [461] M.K. Hinders and D.M. Manos. Lamb wave ultrasonics for aircraft flaw detection. *Final technical report for NASA grant number NAG-1-1671*. April 1998.
- [462] Y.H. Pao and C.C. Mow. *Diffraction of elastic waves and dynamic stress concentrations*. Krane Russak, New York, 1973.
- [463] M. Mellody. Non-destructive evaluation Lamb-wave ultrasonic testing of aging aircraft. *Final paper for the NSF Research Encounter for Undergraduates program at the College of William and Mary, summer 1994*, 1994.

Vita

James Christopher Patrick McKeon

Jim was born in Plainfield, New Jersey on 07/17/72. In 1978 he moved from Piscataway, New Jersey to Richmond, Virginia. He attended Monacan High School there and graduated in June, 1990 with an advanced track degree. He received his Bachelor of Science degree in Physics with Highest Honors from The College of William and Mary in Williamsburg, Virginia in May, 1994, and that Fall he entered the Program in Applied Science of The College of William and Mary for graduate studies. Jim married Tracey Kristen Cesario on March 23, 1996 in the Wren Chapel of The College of William and Mary, and he received his Master of Science in Applied Science in May, 1996. Jim will begin a research scientist position with SONIX, Inc. in Springfield, Virginia on August 1st, 1998.

IMAGE EVALUATION TEST TARGET (QA-3)



APPLIED IMAGE . Inc
 1653 East Main Street
 Rochester, NY 14609 USA
 Phone: 716/482-0300
 Fax: 716/288-5989

© 1993, Applied Image, Inc., All Rights Reserved